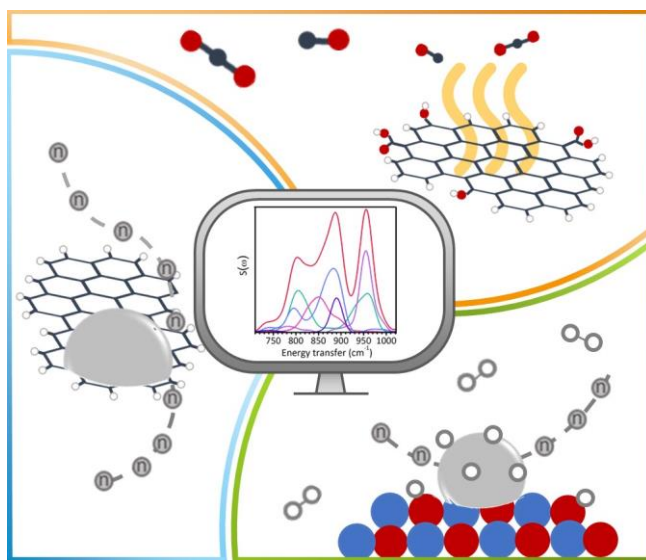




Università degli Studi di Torino
Doctoral School of the University of Torino
PhD Programme in Chemical and Materials Sciences XXXIII Cycle

Institut Laue-Langevin
ILL Graduate School

Nature, abundance and dynamics of surface species in noble metal nanoparticles catalysts and their supports: new experimental and computational insights



Eleonora Vottero

Supervisors:
Prof. Elena Groppo
Dr. Andrea Piovano



Università degli Studi di Torino

Doctoral School of the University of Torino

PhD Programme in Chemical and Materials Sciences XXXIII cycle

Nature, abundance and dynamics of surface species in noble metal nanoparticles catalysts and their supports: new experimental and computational insights

Candidate: **Eleonora Vottero**

Supervisor: Prof. **Elena Groppo**
Dr. **Andrea Piovano**

Jury Members: Dr. **Céline Chizallet**
IFP Énergies Nouvelles

Dr. **Stéphane Rols**
Institut Laue-Langevin

Prof. **Lorenzo Maschio**
University of Turin
Department of Chemistry

Head of the Doctoral School: Prof. Alberto Rizzuti
PhD Programme Coordinator: Prof. Bartolomeo Civalleri

Torino, 2020

TABLE OF CONTENTS

Preface	1
Chapter 1: Introduction	7
1.1: Supported metal nanoparticles in catalysis	7
1.1.1: Why employing metal nanoparticles	8
1.1.2: Preparation routes	10
1.1.3: Pt and Pd as hydrogenation catalysts	12
1.2: Supports	14
1.2.1: Role of supports	14
1.2.2. Activated carbon supports	15
1.2.3. Metal oxide supports	18
1.3. The complexity of heterogeneous catalyst	19
References	22
Chapter 2: Experimental and Methods	29
2.1: Samples	29
2.1.1: Activated carbon samples	29
2.1.2: Catalysts samples	30

2.2: Temperature Programmed	
Desorption Experiments	32
2.2.1: TPD instrumentation: state of the art	32
2.2.2: Home-made TPD-IR setup and experimental protocol	36
2.2.3: Data Analysis	39
2.2.4: Possibilities for improvements	43
2.3: Inelastic neutron scattering spectroscopy	44
2.3.1: Introduction to INS spectroscopy	44
2.3.2: INS measurements and data analysis	49
2.4: Computational simulations	52
2.4.1: DFT simulations of molecular and periodic systems	52
2.4.2: Simulation of the INS spectra of activated carbons and linear combination analysis	56
2.4.3: Simulation of the INS spectra of Pt-H	59
References	61
Chapter 3: Identification and quantification of	
functional groups in activated carbons	67
3.1 Functional groups in activated carbons	67
3.1.1: O-containing functional groups	68
3.1.2: Functional groups containing other heteroatoms	69
3.1.3: Characterization techniques	70
3.1.4: Temperature Programmed Desorption of Activated Carbons: state-of-the-art	73
3.2 Results and discussion	78
3.2.1 Qualitative analysis	78

3.2.1.1. Physically activated carbons	78
3.2.1.2. Chemically activated carbon	84
3.2.1.3. Oxidised carbons	86
3.2.2 Evaluation of secondary reactions	89
3.2.3 Quantitative analysis	93
3.2.3.1 Mass loss	93
3.2.3.2 Quantification of functional groups	94
3.3. Conclusions	99
References	101

Chapter 4: Hydrogen terminations in activated carbons and related catalysts	105
4.1 State of the art	105
4.2 Experimental spectra	111
4.2.1 Physically activated carbons and related catalysts	111
4.2.2 Carbons containing a high amount of functional groups	115
4.3 Simulation of INS spectra	118
4.3.1 Regular terminations	118
4.3.2 Physical defects	126
4.3.3 Functional groups	131
4.4 Identification and quantification of C-H terminations	136
4.4.1 Quantification of the C-H terminations in physically activated carbons	137
4.4.2 Qualitative evaluation on the effect of functional groups	143
4.5 Conclusions	145

References	149
Chapter 5: Characterization of Pt-H species in γ-Al₂O₃ supported catalysts	151
5.1 Introduction	151
5.2 State-of-the-art	152
5.2.1 Previous experiments on the Pt(NR)/Alu catalyst	152
5.2.2 Computational evidences for the H ₂ -induced reconstruction of γ -Al ₂ O ₃ supported Pt nanoparticles	158
5.3. Results and discussion	163
5.3.1. Pt ₁₃ H _x nanoparticles supported at the γ -Al ₂ O ₃ (100) surface: simulation of the INS spectra	163
5.3.2. Pt ₁₃ H _x nanoparticles supported at the γ -Al ₂ O ₃ (110) surface: simulation of the INS spectra	166
5.3.3 PtH _x species at larger nanoparticles: simulation of the INS spectra	168
5.3.4 Effect of the γ -Al ₂ O ₃ support on the INS spectra	168
5.3.5 Extended Pt surfaces: simulation of the INS spectra	173
5.3.6. Tentative interpretation of the experimental INS spectrum of Pt(NR)/Alu in excess of H ₂	175
5.4 Outlook and conclusion	177
References	179
Chapter 6: Conclusions and Perspectives	183
Acknowledgements	189
Appendix A: Input files and scripts	191
Appendix B: Regular aromatic platelets models	207

Appendix C: Linear combination fits	211
Appendix D: Simulated INS spectra of γ -Al ₂ O ₃ /Pt ₁₃ H _x	215
Appendix E: Publications	219

PREFACE

My PhD project is focused on the characterization of industrial catalysts based on supported metal nanoparticles for hydrogenation reactions and of their supports, combining experimental techniques (infrared and inelastic neutron scattering spectroscopies) and computational methods.

Many institutions were involved in this PhD project. The main actors are the University of Turin (UniTO) and the Institut Laue-Langevin (ILL) in Grenoble, which agreed on a joint PhD position under the supervision of prof. Elena Groppo (UniTO) and of Dr. Andrea Piovano (ILL). Accordingly, the first half of the activities related to the project were located in Turin, and the second half in Grenoble. The third main actor is Chimet S.p.A. (<https://www.chimet.com/en/home>), Italian company leader in the sector of the recovery and refinement of precious metals, and in particular the manager of the R&D laboratory, Dr. Riccardo Pellegrini. With the aim of gaining a better understanding of the physico-chemical properties of the supported precious metal catalysts they produce and sell, they developed a long-lasting

collaboration with the Chemistry department of UniTO and, more recently, also with the ILL.

Heterogeneous catalysts are very complex systems, requiring a multi-techniques approach in order to obtain a complete picture of the system. In the past years many people worked on the characterization of these catalysts, and also this PhD thesis project was inserted into this framework.

A large part of my PhD project was focused on the characterization of various activated carbons employed as catalytic supports by Chimet, and on their modification upon the metal nanoparticles deposition. At first, the functional groups content was investigated by means of Temperature Programmed Desorption (TPD) paired with infrared spectroscopy. Afterwards, the combination of Inelastic Neutron Scattering (INS) spectroscopy and DFT simulations was applied to the characterization of the C-H groups terminating the graphenic domains in the activated carbons, providing information about their morphology and their modifications upon interaction with Pd and Pt nanoparticles. These results are the topics of Chapter 3 and Chapter 4 of this thesis, respectively. Finally, in the last year a new collaboration was established with Dr. Céline Chizallet and Dr. Pascal Raybaud from IFP Énergies Nouvelles (IFPEN) in Solaize, France, with the aim to shed new light on the dynamics of Pt nanoparticles supported on γ -Al₂O₃ in the presence of H₂ and the nature of the hydride species formed. For this part I compared experimental INS results and supported nanoparticle DFT simulations, as described in Chapter 5 of this thesis.

In more details, the structure and content of this thesis is summarised here in the following:

Chapter 1 – Introduction

The chapter covers the main features of supported metal nanoparticles in heterogeneous catalysis. A relevant focus is given to the nature of Pd and Pt and on their ability to activate the H₂ molecule and organic substrates, as well as to the preparation routes of the metal nanoparticles and of their deposition upon a support. Then, the nature and the role of the supports are discussed, with a particular focus on the metal-support interaction and on two classes of support materials, activated carbons and metal oxidic supports. Finally, the new directions of contemporary heterogeneous catalyst research are introduced.

Chapter 2 – Experimental and Methods

The chapter provides an overview over the samples investigated during this thesis work, as well as the description of the experimental and computational techniques, of the instrumental setups, of the experimental protocols and of the methods I employed for the data analysis.

Chapter 3 – Identification and quantification of functional groups in activated carbons

This chapter deals with the quantification of functional groups in activated carbon supports by employing Temperature Programmed Desorption (TPD) coupled with infrared spectroscopy. An introductory overview over the nature of the heteroatoms-containing functionalities in activated carbons is provided, together with a brief comparison of the techniques that can be employed for their identification and quantification. Then, the principles of TPD and of its application to activated carbons are described. The core of the chapter covers the qualitative and quantitative results of the TPD experiments I performed with the new TPD-IR setup we developed for this purpose, providing the differences in the concentration and nature of the functional

groups in activated carbons prepared starting from different precursors or following different activation routes, or samples subjected to a post-activation oxidative treatment.

Chapter 4 - Hydrogen terminations in activated carbons and related catalysts

The chapter covers the characterization of the C-H terminations in the graphenic domains constituting activated carbons by the combined use of Inelastic Neutron Scattering (INS) spectroscopy and DFT simulations. The chapter first introduces the state of the art on this topic, then presents the analysis of the experimental INS spectra of the activated carbon supports and of the correspondent catalysts, and finally discuss their interpretation on the basis of DFT simulations on model systems. A large part of the study was devoted to the study of physically activated carbons and of the corresponding Pt and Pd catalysts, for which a linear combination fit analysis of the simulated contribution to the experimental spectra allowed the identification and quantification of the main C-H termination geometries and their modifications upon the metal nanoparticles deposition. Finally, the cases of a chemically activated sample and of two oxidised samples were examined, allowing me to point out the perturbation on the spectral features caused by the presence of heteroatom containing functional groups.

Chapter 5 – Characterization of Pt-H species in γ -Al₂O₃ supported catalysts

This chapter reports the results of the characterization of the Pt-H species in Pt/ γ -Al₂O₃ samples performed by comparing experimental and simulated INS spectra, as part of the collaboration with IFPEN. The chapter is introduced by an overview over the previous INS experiments on the same catalyst, and on the previous DFT simulation work performed at IFPEN on the dynamic of γ -

Al_2O_3 supported Pt nanoparticles in H_2 atmosphere. In the frame of this thesis work it was possible to directly compare these experimental and computational data through the simulation of the INS spectra of each model and comparing them with the experimental data. The effect of the H coverage, of the nanoparticles dimension and of the $\gamma\text{-Al}_2\text{O}_3$ surface were considered, as well as the case of extended Pt surfaces.

Chapter 6 - Conclusions and Perspectives

Finally, this chapter summarises the ensemble of the results obtained during this PhD thesis work and states the future perspectives of research on these topics.

CHAPTER 1

Introduction

1.1. Supported metal nanoparticles in catalysis

A catalyst is a substance or material able to accelerate the rate of a chemical reaction by lowering its activation energy barrier, without being consumed in the process. The employment of catalysts is fundamental for the industrial production, as it allows for the conversion of the raw materials to valuable products or chemicals in more economically and/or environmentally sustainable ways. Their importance is clear looking at numbers, since it is estimated that about the 85-90% of the industrial chemical syntheses employ a catalyst in some step of their processes [1]. The most of the catalysts employed in the industrial processes belong to the class of heterogeneous catalysts, which typically consist in solid materials catalysing reactions in the gas or in the liquid phase. More detailed information about this typology of catalysts can be found in references [2-4].

Noble metals such as Pt, Pd, Ru and others, are well known for exhibiting a strong catalytic activity for reactions such as the hydrogenation

or the oxidation of organic compounds. In most cases, the most efficient way of employing these metals in catalysis consists in their dispersion into small nanoparticles immobilised at the surface of large surface area supports. The resulting systems are defined supported metal nanoparticle catalysts [5].

The characterization of supported Pd and Pt nanoparticles for the catalysis is one of the main focuses of this thesis work, and a general overview over the main features of these systems and their employment in catalysis will be readily provided.

1.1.1. Why employing metal nanoparticles

Most sources agree on defining nanoparticles as atomic aggregates whose dimension ranges between 1 and 100 nm [6]. The employment of metal nanoparticles presents several advantages in respect with the correspondent bulk material, which often makes them much more suitable for catalytic applications.

One first property of nanoparticles relevant for the catalysis is the high surface to area ratio resulting from their very small dimension. This quantity is usually expressed in terms of the metal dispersion, corresponding to the fraction of atoms exposed at the nanoparticle surface. Considering that the catalytic activity of metals generally occurs at their surface [7], high dispersion also corresponds to a much higher fraction of metal atoms available for the catalysis, and thus with a more efficient exploitation of the available material. The surface of metal nanoparticles also exposes a large fraction of atoms at borders and edges in comparison with the extended surfaces exposed by the bulk material. These sites present a lower coordination, which result in a higher reactivity [8].

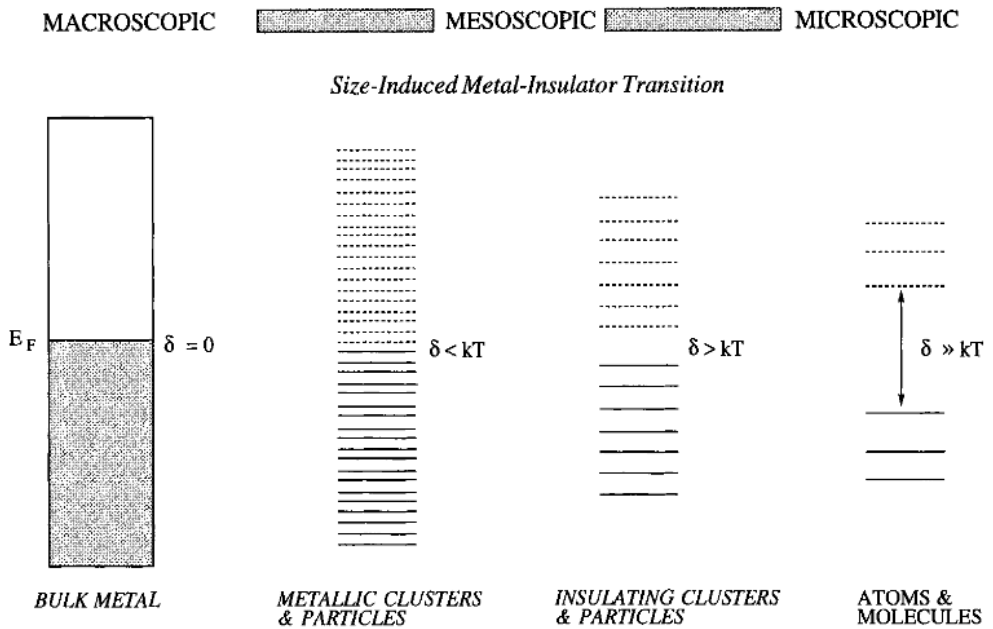


Figure 1. 1: evolution of the electronic structure when reducing the dimension of the system. From reference [9].

However, these considerations alone are not sufficient to justify the different reactivity between metal nanoparticles and the corresponding bulk material. For instance, they do not explain why gold nanoparticles sized a few nanometres exhibit a strong reactivity, while the corresponding bulk material is inert [10-12]. These peculiar properties can be ascribed to the characteristic electronic structure of nano-sized materials, whose features range from the continuous bands of bulk solid systems toward the discrete energy levels characterizing molecules when decreasing the size of the particles, as shown in Figure 1. 1. This phenomenon is usually referred to as quantum size effect or quantum confinement [9, 13, 14], and strongly affects the material thermal [15], optical [16] and magnetic [17] properties, and its reactivity as well. The quantum size effect is the main reason why gold turns into a highly active catalyst when reduced into a few nanometres large particles, but it also

modifies the reactivity of other metals which display a catalytic behaviour in their bulk form, such as platinum or palladium.

1.1.2. Preparation routes

There are two main classes of approaches for the preparation of metal nanoparticles [18, 19]:

- Physical approaches, also referred to as top-down methods: the metal nanoparticles are obtained by disintegrating the bulk metal. This is achieved by employing mechanical procedures, vaporization, ultrasonication, laser ablation and many others.
- Chemical approaches, also referred to as bottom-up methods: the metal nanoparticles are obtained from the reduction or decomposition of a soluble precursor (for instance, a soluble salt or metal complex) and the consequent nucleation and aggregation of the metal into nanoparticles.

Because of their relatively high surface energy, free metal nanoparticles tend to be instable in reaction conditions and display a tendency toward sintering with the consequent formation of larger and less catalytically active aggregates [20]. To avoid this process, metal nanoparticles can be synthesized in the presence of capping agents (such as polymeric molecules or surfactants) which inhibit the interaction between nanoparticles (Figure 1. 2a). However, for heterogeneous catalysts, in most cases the stabilization of metal nanoparticles is achieved by immobilizing them over a large surface area support (Figure 1. 2b), which also has a fundamental role in determining the final catalytic properties.

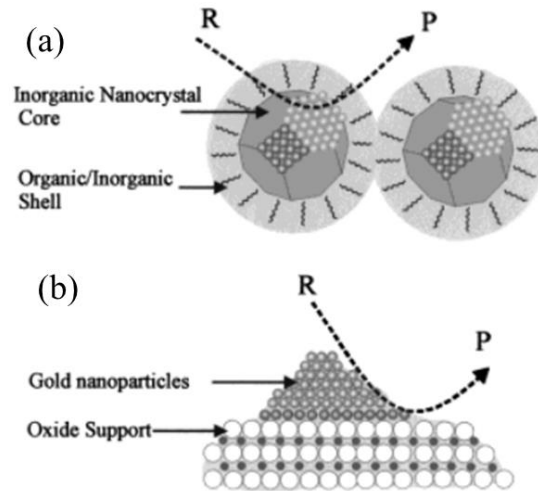


Figure 1. 2: schematic representation of metal nanoparticles for catalysis. (a) colloidal nanoparticles stabilised by capping agents, (b) nanoparticle stabilised via immobilization over a large surface area support. Adapted from reference [21].

The preparation of immobilised nanoparticles on a support is commonly achieved by three main preparation methods [19]:

- Impregnation: the support is impregnated with a solution of the metal precursor (chloride or nitrate salts, generally) and then calcinated.
- Deposition-precipitation: the salt or complex used as the metal precursor is dissolved in the solution where the support is suspended into a slurry by agitation, and then precipitated by changing the pH of the solution.
- Co-precipitation: this method consists in the simultaneous precipitation of the metal nanoparticles and of the support. This approach is often employed in the case of mesoporous supports.

In either case, when organic residues are present a calcination step is often employed for their removal. Moreover, the formed nanoparticles are generally in their oxidized state and require a reduction step to convert them into their reduced form. The reduction can be performed with gaseous reactants (i.e. H_2) or in the liquid phase with e.g. sodium formate or hydrazine solutions. At

the end of the procedure, the catalyst is washed and then dried to remove the solvent (generally water).

1.1.3. Pt and Pd as hydrogenation catalysts

Interaction with H_2 The catalytic activity of Pt group metals for the hydrogenation of organic molecules is recognised since the end of the XIX century, following the experiments of Paul Sabatier and Jean-Baptiste Senderens on the hydrogenation of ethylene on Ni [22]. Thanks to their electronic structure, these metals (both single atoms within complexes and solid surfaces) are able to activate the H_2 molecule by splitting its hydrogen-hydrogen bond with the resulting formation of metal hydride species [7]. Similarly, they are also able to activate and chemisorbed organic compounds such as olefins or aromatics [7]. These adsorbed species at the metal surface are the ones reacting, resulting in the evolution of the hydrogenated product [23, 24].

Pd and Pt belong to the same group of the periodic table, and they exhibit a very similar reactivity toward H_2 that makes them some of the most active catalysts for hydrogenation reactions. However, albeit the significant analogies, their behaviour in the presence of H_2 also exhibits evident differences. Pd is able to rapidly solubilize hydrogen, leading to the formation of bulk PdH where H atoms occupy the octahedral interstices of its fcc lattice. Two different phases, α or β -PdH, are formed depending on the amount of H introduced into the lattice [25]. At last, Pd is also able to adsorb H at its surface [25]. In the case of Pt, instead, the solubility of H_2 is almost negligible under ambient conditions [26], leading only to the formation of surface and sub-surface Pt-H species. In this case, a large variety of surface species can be formed depending on the geometry of the exposed surfaces, steps and edges of the metal.

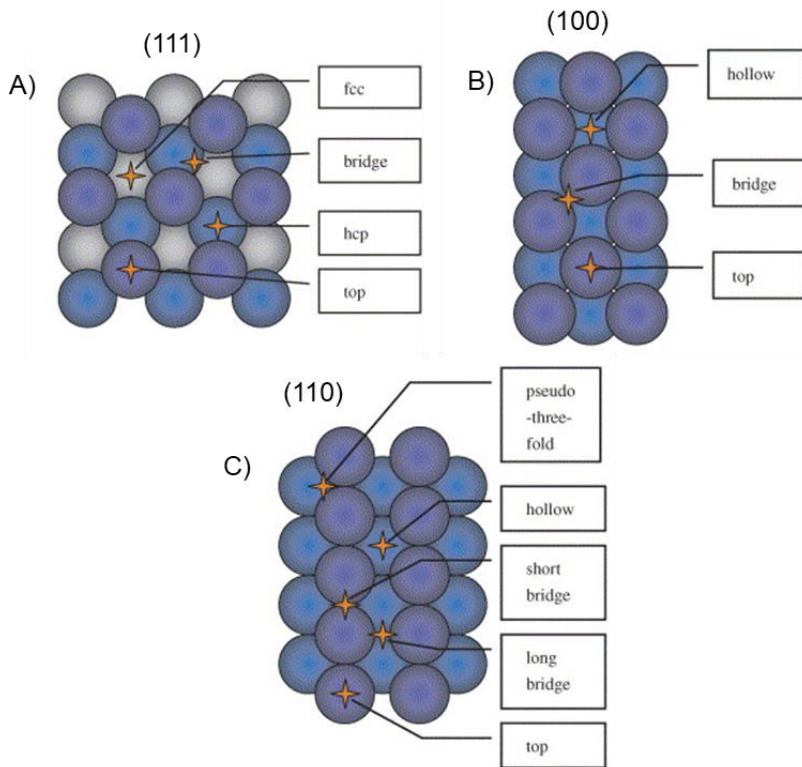


Figure 1. 3: exposed adsorption sites at the (111), (100) and (110) surfaces of fcc metals such as Pd and Pt. Adapted from reference [25].

As an example, the available adsorption sites on the (111), (100) and (110) surfaces of fcc metals are shown in

. The typologies of Pd and Pt hydrides may thus vary depending on the morphology of the Pd and Pt nanoparticles, but also on the reaction conditions (such as temperature, reactants concentration, solvent, and so forth). Not all the hydride species present the same reactivity, and it is thus fundamental to obtain a precise characterization with the aim to understand the optimal conditions for the catalysis [27, 28].

Industrial applications Catalysis is one of the main sectors in which Pd and Pt are applied, in most cases in the form of supported metal nanoparticles.

Thanks to their ability to activate the H₂ molecule, they are largely employed for industrial chemical processes requiring hydrogenation and dehydrogenation steps of organic molecules, in sectors ranging from the food and pharmaceutical industry to petroleum refining [29]. For example, Pd based catalysts are used for the purification of terephthalic acid [30] or for the selective hydrogenation of acetylene to ethylene [29], while Pt is present in the catalyst for the catalytic reforming of gasoline [31], and it is also often employed as the electrodes for electrochemical applications and fuel cells [32]. Other than for hydrogenation processes, Pt and Pd can also be employed as oxidation catalysts [33] and also find large application as components of the three-way catalytic converter for exhaust vehicles emissions [34].

1.2. Supports

1.2.1. Role of supports

As previously stated, one of the main methods for stabilizing metal nanoparticles is to immobilize them over a large surface area support. At a first sight, supports could appear like components of secondary importance with respect to the metal phase. With a better look, however, one can soon recognize their fundamental role in determining the final properties of the catalyst. The main phenomena related to the metal-support interactions (MSI) consist in [35, 36]:

- **Charge transfer:** the bonding between the metal nanoparticle can lead to the redistribution of electrons between the two phases. The extent of the phenomenon depends on the nature of both the support and the metal nanoparticle and can have important repercussions on their catalytic behaviour.
- **Interfacial sites:** atoms at the interface between the nanoparticle and the support tend to be the most affected by the MSI, and often exhibit peculiar

features and reactivity. The creation of unique conditions favouring the catalytic processes is thus possible.

- **Modification of the nanoparticles morphology:** the shape of the metal nanoparticle and the nature of the exposed surfaces are strongly influenced by the strength of the support-nanoparticle adhesion energy, with strong interactions favouring large contact areas and vice-versa. Relevant mismatches between the lattice parameters of the support and of the metal nanoparticles can also lead to strains and/or defects in the latter.
- **Strong metal-support interaction (SMSI):** specific kind of oxidic supports exhibiting a particularly strong interaction with the metal nanoparticles. In this case, it is possible to observe the migration of some ions from the support to partially or totally encapsulate the metal nanoparticles. Since the process reduces the amount of exposed catalytic centres, this phenomenon tends to be detrimental for the catalysis.
- **Spillover** [37, 38]: the migration of surface species from the metal nanoparticle to the support, or the opposite (reverse spillover), is well documented in some classes of catalysts, and may cover a fundamental role in the reaction mechanism.

It is thus evident that the choice of the right support can be fundamental for determining the catalytic properties of the final catalyst [35].

Two main classes of catalytic supports are the carbonaceous materials and the metal oxides, whose properties and effects in catalysis will be now discussed.

1.2.2. Activated carbon supports

Several carbonaceous materials have been employed as catalytic supports, ranging from carbon black to carbon nanotubes and to graphene [39, 40].

Among this class of materials, the most employed are activated carbons. These materials, obtained by the pyrolysis and following activation of organic precursors, are characterized by very large surface area values which easily exceed 1000 m²/g and high porosity [41]. In comparison with other supports, they are characterized by relatively low cost of production, by chemical and physical stability under reaction condition, and by the easy recovery of the metal phase in the spent catalyst by combustion. All these characteristics contributed to make activated carbons some of the most common supports in heterogeneous catalysis. Other than in catalysis, their features also make them suitable for the application as adsorbent, for gas storage and for separation [42, 43].

Activated carbons can be obtained from various carbonaceous precursors, such as wood, peat, coconut shells, agricultural wastes and many others [41, 44]. Their preparation methods are generally classified into two main categories [41, 44]:

- **Physical activation:** the carbon precursor is preventively pyrolyzed under inert atmosphere at high temperature, typically in the 800-1000°C range. Following, the char is activated in the presence of mild oxidising agents such as CO₂ or steam with the aim of increasing its surface area and porosity.
- **Chemical activation:** the precursor is impregnated in a solution of a dehydrating agent such as H₃PO₄, KOH or ZnCl₂ and then heated under inert atmosphere, typically at lower temperatures than in the previous case (400-600°C range). At the end of the process the product is washed to remove the residual chemicals.

In addition, the properties of activated carbons can be further tuned by post-activation processes, such as oxidizing treatment in the gas or in the

liquid phase aimed to the introduction of oxygen containing functional groups [45, 46], or the functionalization with nitrogen [47, 48].

The high temperature pyrolysis of their carbonaceous precursors leads to the loss of the heteroatoms containing species in the form of light gaseous and liquid compounds such as H_2O , CO_2 or CH_4 , and to the increase of the carbon content of the chars [49]. The microstructure of the precursor is partially retained in the process, as evident in the SEM micrograph shown as an example in Figure 1. 4A. As the pyrolysis proceeds, the material progressively undergoes a graphitization process, with the formation of small and disorderly stacked graphenic domain, as shown in Figure 1. 4B.

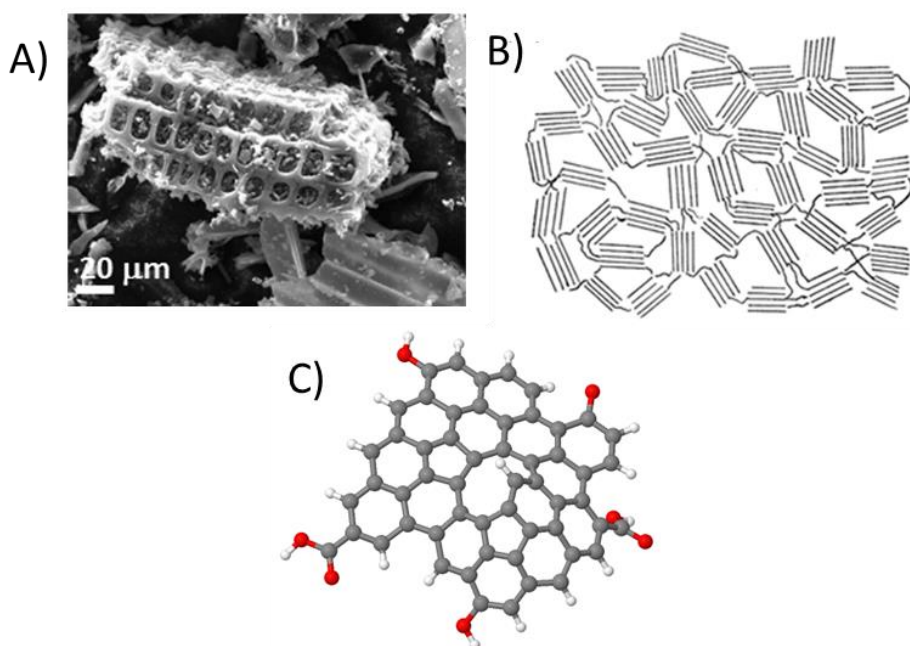


Figure 1. 4: A) SEM micrograph of a physically activated carbon of wood origin. From reference [50] B) structure of a non-graphitizable carbon proposed by R. Franklin in 1951 [51]. C) Representation of the defective graphenic domains in activated carbons.

This kind of structure is confirmed by their XRD patterns, which show reflections at the same angles as for regular graphite, but with much broader peaks due to the very small lateral dimension of the periodic domains [51, 52].

The intrinsic disorder and defectivity which characterize activated carbons is also evident at the atomic scale: in fact, the aromatic pattern of each graphenic domain is anything but perfect, with the frequent presence of defects which can also lead to the local curvature of the geometry [53]. Small residual amounts of other heteroatoms are generally also present in the form of functional groups, that are mostly localized at the platelet borders [45, 46, 54] (Figure 1. 4C), and have repercussions on both the surface polarity and the reactivity of activated carbons. The presence of defects and functional groups in activated carbons also has relevant consequences when employing them as catalytic supports, as they are reported to provide stronger bonding sites for the metal nanoparticle in respect with the graphenic basal plane [55]. The reactivity arising from the presence of functional groups and defects is also associated to the possibility of employ activated carbons as catalysts on their own [56].

Both the nature of the precursors and the activation conditions can strongly affect the final textural and compositional properties of the activated carbon [57-59], with the possibility of covering a very wide range of different features. The choice of the right activated carbon for each application is thus fundamental in order to optimize the performances [54].

1.2.3. Metal oxide supports

The second class of materials which are often employed as supports in heterogeneous catalysts are metal oxides such as Al_2O_3 , TiO_2 , ZrO_2 , MgO , SiO_2 and others [60]. They are employed thanks to their stability under harsh

reaction conditions, but also because of their varied surface chemistry, which often contributes to the activity of the catalyst for specific reactions. In fact, the surface of oxides tend to be saturated by the formation of hydroxyl groups, which can provide Brønsted acid-base properties to the material [61-63]. In addition, the presence of low-coordinated metal cations at the surface can also introduce Lewis acidity into the surface [61, 63, 64]. Metal oxides can also present different redox behaviour: supports exhibiting a facile modification of the metal redox state under reaction conditions, such as TiO₂, ZrO₂ or CeO₂, are generally labelled as reducible supports, while the ones with a stable redox state such as MgO, Al₂O₃ or SiO₂ are defined as not-reducible [61]. The surface of oxidic supports thus presents a relevant reactivity, which is important for the interaction between the metal nanoparticle and the support [64, 65], and that can also provide active centres that contribute to the total catalytic activity or even permit their employ as catalysts on their own [61, 62, 66]. For most of the catalytic applications, the employ of metal oxides supports at large surface area is generally preferred. For instance, the high surface area transition alumina (γ , δ , η , θ), with a surface area of few hundreds of m²/g, are much more likely to find application in catalysis than the thermodynamically stable α -Al₂O₃ phase (surface area of few m²/g) [63, 67].

1.3. The complexity of heterogeneous catalyst

In the previous sections, the main components constituting supported metal nanoparticles catalysts were reviewed. This section, instead, focuses on these catalysts as a single entity. Supported metal nanoparticles catalysts are characterized by a relevant structural heterogeneity and complexity, as summarized in Figure 1. 5.

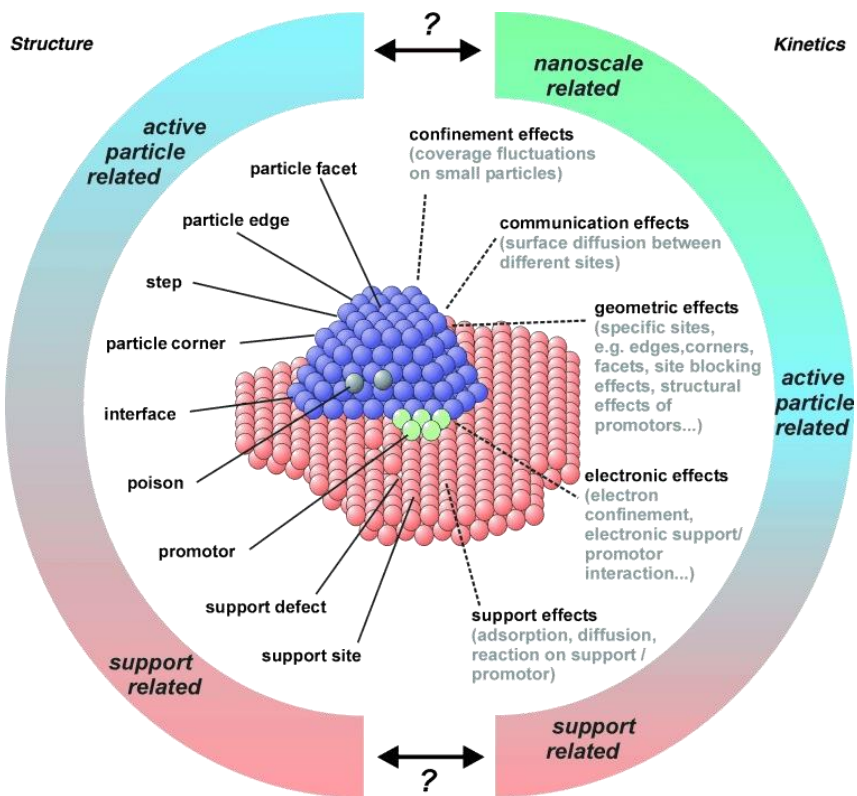


Figure 1. 5: Example of structural and chemical complexity of an oxide supported metal nanoparticles catalyst, with focus on the structure and on the reaction kinetic related effects. From reference [68].

Many different aspects can contribute to determine the final features of a heterogeneous catalyst. For example, it is possible to choose among several different metal phases and supports compositions, which can be modified by introducing dopants, mixed phases or alloys [60, 69]. Also the introduction of promoters enhancing the catalytic activity or the formation of poisoning substances able to suppress it have to be taken into account [70]. In addition, the structure of both the metal nanoparticles and the support can be very variable, with differences in the size, shape and exposed facets of the metal nanoparticles [71] or in the morphology of the support [35]. One should also take into account the fact that these catalysts are not static systems, but that

they can undergo significant changes and reconstructions under reaction conditions [28, 72], making it challenging to individuate the active species for the catalysis.

Due to the intrinsic complexity of these systems and the difficulties in their characterization, a relevant part of their development so far was based on an empirical trials and errors approach, and many aspects are still unclear. The current direction of the scientific research on heterogeneous catalysis is largely focused in filling this knowledge gap, aiming to be able to rationally design new and more efficient catalysts in terms of activity and selectivity toward the target reaction [35, 73-75], as well as applicable in more environmental friendly and less energetically demanding processes [76]. In order to achieve this level of comprehension, a much more detailed characterization of heterogeneous catalysts down to the atomic scale is required. So that there is not a single technique able to provide all the necessary information, the complementary application of several experimental and computational methods is fundamental [50, 75], and this is the frame in which this thesis work is inserted.

References

1. Chorkendorff I. and Niemantsverdriet J., *Introduction to Catalysis. Concepts of Modern Catalysis and Kinetics*, 2003: p. 1-21.
2. Ertl G., Knözinger H., and Weitkamp J., *Handbook of Heterogeneous Catalysis*. Vol. 1-5. 2008: Wiley.
3. Lloyd L., *Handbook of Industrial Catalysts*. 2011: Springer.
4. Chorkendorff I. and Niemantsverdriet H., *Concepts of modern catalysis and kinetics* 2005: Wiley.
5. Ndolomingo M.J., Bingwa N., and Meijboom R., *Review of supported metal nanoparticles: synthesis methodologies, advantages and application as catalysts*. Journal of Materials Science, 2020. **55**(15): p. 6195-6241.
6. Standardization I.O.f., *ISOTS 80004-1:2015 Nanotechnologies -- Vocabulary - - Part 1: Core terms*. 2015, Geneva, Switzerland.
7. Saillard J.Y. and Hoffmann R., *Carbon-hydrogen and hydrogen-hydrogen activation in transition metal complexes and on surfaces*. Journal of the American Chemical Society, 1984. **106**(7): p. 2006-2026.
8. Ni B. and Wang X., *Face the Edges: Catalytic Active Sites of Nanomaterials*. Advanced Science, 2015. **2**(7): p. 1500085.
9. Edwards P.P., Johnston R.L., and Rao C.N.R., *On the Size-Induced Metal-Insulator Transition in Clusters and Small Particles*. Metal Clusters in Chemistry, 1999: p. 1454-1481.
10. Sankar M., He Q., Engel R.V., Sainna M.A., Logsdail A.J., Roldan A., Willock D.J., Agarwal N., Kiely C.J., and Hutchings G.J., *Role of the Support in Gold-Containing Nanoparticles as Heterogeneous Catalysts*. Chemical Reviews, 2020. **120**(8): p. 3890-3938.
11. Haruta M., Kobayashi T., Sano H., and Yamada N., *Novel Gold Catalysts for the Oxidation of Carbon Monoxide at a Temperature far Below 0 °C*. Chemistry Letters, 1987. **16**(2): p. 405-408.
12. Daniel M.C. and Astruc D., *Gold Nanoparticles: Assembly, Supramolecular Chemistry, Quantum-Size-Related Properties, and Applications Toward Biology, Catalysis, and Nanotechnology*. Chemical Reviews, 2004. **104**(1): p. 293-346.
13. Halperin W.P., *Quantum size effects in metal particles*. Reviews of Modern Physics, 1986. **58**(3): p. 533-606.

14. Rao C.N.R., Kulkarni G.U., Thomas P.J., and Edwards P.P., *Metal nanoparticles and their assemblies*. Chemical Society Reviews, 2000. **29**(1): p. 27-35.
15. Gao F. and Gu Z., *Melting Temperature of Metallic Nanoparticles*, in *Handbook of Nanoparticles*, Aliofkhaezrai M., Editor. 2016, Springer International Publishing: Cham. p. 661-690.
16. Alivisatos A.P., *Semiconductor Clusters, Nanocrystals, and Quantum Dots*. Science, 1996. **271**(5251): p. 933.
17. Nealon G.L., Donnio B., Greget R., Kappler J.-P., Terazzi E., and Gallani J.-L., *Magnetism in gold nanoparticles*. Nanoscale, 2012. **4**(17): p. 5244-5258.
18. Toshima N., *Metal Nanoparticle Catalysts*, in *Dekker Encyclopedia of Nanoscience and Nanotechnology*, Contescu C., Editor. 2008, CRC Press: Boca Raton. p. 2052-2063.
19. Campelo J.M., Luna D., Luque R., Marinas J.M., and Romero A.A., *Sustainable Preparation of Supported Metal Nanoparticles and Their Applications in Catalysis*. ChemSusChem, 2009. **2**(1): p. 18-45.
20. Phan H.T. and Haes A.J., *What Does Nanoparticle Stability Mean?* The Journal of Physical Chemistry C, 2019. **123**(27): p. 16495-16507.
21. Zhong C.J. and Maye M.M., *Core-Shell Assembled Nanoparticles as Catalysts*. Advanced Materials, 2001. **13**(19): p. 1507-1511.
22. Sabatier P. and Senderens J.-B., *Action du nickel sur l'éthylène. Synthèse de l'éthane*. Comptes rendus de l'Académie des Sciences, 1897. **124**: p. 1358-1360.
23. Horiuti I. and Polanyi M., *Exchange reactions of hydrogen on metallic catalysts*. Transactions of the Faraday Society, 1934. **30**(0): p. 1164-1172.
24. Zaera F., *Key unanswered questions about the mechanism of olefin hydrogenation catalysis by transition-metal surfaces: a surface-science perspective*. Physical Chemistry Chemical Physics, 2013. **15**(29): p. 11988-12003.
25. Jewell L.L. and Davis B.H., *Review of absorption and adsorption in the hydrogen-palladium system*. Applied Catalysis A: General, 2006. **310**: p. 1-15.
26. Katsuta H. and McLellan R.B., *Diffusivity permeability and solubility of hydrogen in platinum*. Journal of Physics and Chemistry of Solids, 1979. **40**(9): p. 697-699.
27. Teschner D., Borsodi J., Wootsch A., Révay Z., Hävecker M., Knop-Gericke A., Jackson S.D., and Schlögl R., *The Roles of Subsurface Carbon and Hydrogen in Palladium-Catalyzed Alkyne Hydrogenation*. Science, 2008. **320**(5872): p. 86.

28. Zhou Y., Jin C., Li Y., and Shen W., *Dynamic behavior of metal nanoparticles for catalysis*. Nano Today, 2018. **20**: p. 101-120.
29. Lloyd L., *Hydrogenation Catalysts*, in *Handbook of Industrial Catalysts. Fundamental and Applied Catalysis*. 2011, Springer: Boston.
30. Pernicone N., Cerboni M., Prelazzi G., Pinna F., and Fagherazzi G., *An investigation on Pd/C industrial catalysts for the purification of terephthalic acid*. Catalysis Today, 1998. **44**(1): p. 129-135.
31. *Catalytic Naphtha Reforming*. 2nd ed. 2004, Boca Raton: CRC Press
32. Ren X., Lv Q., Liu L., Liu B., Wang Y., Liu A., and Wu G., *Current progress of Pt and Pt-based electrocatalysts used for fuel cells*. Sustainable Energy & Fuels, 2020. **4**(1): p. 15-30.
33. Schwartz A., Holbrook L.L., and Wise H., *Catalytic oxidation studies with platinum and palladium*. Journal of Catalysis, 1971. **21**(2): p. 199-207.
34. Heck R., Farrauto R., and Gulati S., *Automotive Catalyst*, in *Catalytic Air Pollution Control*. 2009. p. 101-175.
35. van Deelen T.W., Hernández Mejía C., and de Jong K.P., *Control of metal-support interactions in heterogeneous catalysts to enhance activity and selectivity*. Nature Catalysis, 2019. **2**(11): p. 955-970.
36. Liu J.J., *Advanced Electron Microscopy of Metal-Support Interactions in Supported Metal Catalysts*. ChemCatChem, 2011. **3**(6): p. 934-948.
37. Prins R., *Hydrogen Spillover. Facts and Fiction*. Chemical Reviews, 2012. **112**(5): p. 2714-2738.
38. Karim W., Spreafico C., Kleibert A., Gobrecht J., VandeVondele J., Ekinici Y., and van Bokhoven J.A., *Catalyst support effects on hydrogen spillover*. Nature, 2017. **541**(7635): p. 68-71.
39. Auer E., Freund A., Pietsch J., and Tacke T., *Carbons as supports for industrial precious metal catalysts*. Applied Catalysis A: General, 1998. **173**(2): p. 259-271.
40. Rodríguez-Reinoso F. and Sepúlveda-Escribano A., *Carbon as Catalyst Support*, in *Carbon Materials for Catalysis*. 2008. p. 131-155.
41. Rodríguez-Reinoso F., *Production and Applications of Activated Carbons*. Handbook of Porous Solids, 2002: p. 1766-1827.
42. Sircar S., Golden T.C., and Rao M.B., *Activated carbon for gas separation and storage*. Carbon, 1996. **34**(1): p. 1-12.

43. Fierro V., Torné-Fernández V., Montané D., and Celzard A., *Adsorption of phenol onto activated carbons having different textural and surface properties*. Microporous and Mesoporous Materials, 2008. **111**(1): p. 276-284.
44. González-García P., *Activated carbon from lignocellulosics precursors: A review of the synthesis methods, characterization techniques and applications*. Renewable and Sustainable Energy Reviews, 2018. **82**: p. 1393-1414.
45. Figueiredo J.L., Pereira M.F.R., Freitas M.M.A., and Órfão J.J.M., *Modification of the surface chemistry of activated carbons*. Carbon, 1999. **37**(9): p. 1379-1389.
46. Moreno-Castilla C., Carrasco-Marín F., Maldonado-Hódar F.J., and Rivera-Utrilla J., *Effects of non-oxidant and oxidant acid treatments on the surface properties of an activated carbon with very low ash content*. Carbon, 1998. **36**(1): p. 145-151.
47. Jia Y.F., Xiao B., and Thomas K.M., *Adsorption of metal ions on nitrogen surface functional groups in activated carbons*. Langmuir, 2002. **18**(2): p. 470-478.
48. Pietrzak R., *XPS study and physico-chemical properties of nitrogen-enriched microporous activated carbon from high volatile bituminous coal*. Fuel, 2009. **88**(10): p. 1871-1877.
49. Kawamoto H., *Lignin pyrolysis reactions*. Journal of Wood Science, 2017. **63**(2): p. 117-132.
50. Lazzarini A., Piovano A., Pellegrini R., Leofanti G., Agostini G., Rudić S., Chierotti M.R., Gobetto R., Battiato A., Spoto G., Zecchina A., Lamberti C., and Groppo E., *A comprehensive approach to investigate the structural and surface properties of activated carbons and related Pd-based catalysts*. Catalysis Science & Technology, 2016. **6**(13): p. 4910-4922.
51. Franklin R.E. and Randall J.T., *Crystallite growth in graphitizing and non-graphitizing carbons*. Proceedings of the Royal Society of London. Series A. Mathematical and Physical Sciences, 1951. **209**(1097): p. 196-218.
52. Lazzarini A., Piovano A., Pellegrini R., Agostini G., Rudić S., Lamberti C., and Groppo E., *Graphitization of Activated Carbons: A Molecular-level Investigation by INS, DRIFT, XRD and Raman Techniques*. Physics Procedia, 2016. **85**: p. 20-26.
53. Harris P.J.F., Liu Z., and Suenaga K., *Imaging the atomic structure of activated carbon*. Journal of Physics: Condensed Matter, 2008. **20**(36): p. 362201.
54. Lazzarini A., Pellegrini R., Piovano A., Rudić S., Castan-Guerrero C., Torelli P., Chierotti M.R., Gobetto R., Lamberti C., and Groppo E., *The effect of surface chemistry on the performances of Pd-based catalysts supported on activated carbons*. Catalysis Science & Technology, 2017. **7**(18): p. 4162-4172.

55. Gerber I.C. and Serp P., *A Theory/Experience Description of Support Effects in Carbon-Supported Catalysts*. Chemical Reviews, 2020. **120**(2): p. 1250-1349.
56. Figueiredo J.L. and Pereira M.F.R., *The role of surface chemistry in catalysis with carbons*. Catalysis Today, 2010. **150**(1): p. 2-7.
57. Prauchner M.J. and Rodríguez-Reinoso F., *Chemical versus physical activation of coconut shell: A comparative study*. Microporous and Mesoporous Materials, 2012. **152**: p. 163-171.
58. Wu F.-C., Tseng R.-L., and Juang R.-S., *Comparisons of porous and adsorption properties of carbons activated by steam and KOH*. Journal of Colloid and Interface Science, 2005. **283**(1): p. 49-56.
59. Tiryaki B., Yagmur E., Banford A., and Aktas Z., *Comparison of activated carbon produced from natural biomass and equivalent chemical compositions*. Journal of Analytical and Applied Pyrolysis, 2014. **105**: p. 276-283.
60. Misono M., *Chapter 2 - Chemistry and Catalysis of Mixed Oxides*, in *Studies in Surface Science and Catalysis*, Misono M., Editor. 2013, Elsevier. p. 25-65.
61. Hu J., Chen L., and Richards R., *Properties, Synthesis and Applications of Highly Dispersed Metal Oxide Catalysts*. Metal Oxide Catalysis, 2008: p. 613-663.
62. Pines H. and Haag W.O., *Alumina: Catalyst and Support. I. Alumina, its Intrinsic Acidity and Catalytic Activity*. Journal of the American Chemical Society, 1960. **82**(10): p. 2471-2483.
63. Busca G., *Chapter Three - Structural, Surface, and Catalytic Properties of Aluminas*, in *Advances in Catalysis*, Jentoft F.C., Editor. 2014, Academic Press. p. 319-404.
64. Kwak J.H., Hu J Fau - Mei D., Mei D Fau - Yi C.-W., Yi Cw Fau - Kim D.H., Kim Dh Fau - Peden C.H.F., Peden Ch Fau - Allard L.F., Allard Lf Fau - Szanyi J., and Szanyi J., *Coordinatively unsaturated Al³⁺ centers as binding sites for active catalyst phases of platinum on gamma-Al₂O₃*. Science, 2009. **325**(5948): p. 1670-1673.
65. Hu C.H., Chizallet C., Toulhoat H., and Raybaud P., *Structural, energetic, and electronic trends in low-dimensional late-transition-metal systems*. Physical Review B, 2009. **79**(19): p. 195416.
66. Gorte R.J., *Ceria in catalysis: From automotive applications to the water-gas shift reaction*. AIChE Journal, 2010. **56**(5): p. 1126-1135.
67. Busca G., *The surface of transitional aluminas: A critical review*. Catalysis Today, 2014. **226**: p. 2-13.

68. Libuda J., *Molecular Beams and Model Catalysis: Activity and Selectivity of Specific Reaction Centers on Supported Nanoparticles*. ChemPhysChem, 2004. **5**(5): p. 625-631.
69. Loza K., Heggen M., and Epple M., *Synthesis, Structure, Properties, and Applications of Bimetallic Nanoparticles of Noble Metals*. Advanced Functional Materials, 2020. **30**(21).
70. Koel B.E. and Kim J., *Promoters and Poisons*, in *Handbook of Heterogeneous Catalysis*. 2008, Wiley. p. 1593-1624.
71. Rongchao J., *The impacts of nanotechnology on catalysis by precious metal nanoparticles*. Nanotechnology Reviews, 2012. **1**(1): p. 31-56.
72. Mager-Maury C., Bonnard G., Chizallet C., Sautet P., and Raybaud P., *H₂-Induced Reconstruction of Supported Pt Clusters: Metal–Support Interaction versus Surface Hydride*. ChemCatChem, 2011. **3**(1): p. 200-207.
73. Jin R., Li G., Sharma S., Li Y., and Du X., *Toward Active-Site Tailoring in Heterogeneous Catalysis by Atomically Precise Metal Nanoclusters with Crystallographic Structures*. Chemical Reviews, 2020.
74. Ahmadi M., Mistry H., and Roldan Cuenya B., *Tailoring the Catalytic Properties of Metal Nanoparticles via Support Interactions*. The Journal of Physical Chemistry Letters, 2016. **7**(17): p. 3519-3533.
75. Zaera F., *New Challenges in Heterogeneous Catalysis for the 21st Century*. Catalysis Letters, 2012. **142**(5): p. 501-516.
76. Kalidindi S.B. and Jagirdar B.R., *Nanocatalysis and Prospects of Green Chemistry*. ChemSusChem, 2012. **5**(1): p. 65-75.

CHAPTER 2

Experimental and Methods

2.1. Samples

2.1.1. Activated carbon samples

Several activated carbons employed as catalytic supports have been deeply investigated regarding their functional groups content (Chapter 3) and the nature of their C-H terminations (Chapter 4). All the samples were provided by Chimet S.p.A. [1], and differ in their precursors, activation procedure and post-activation treatment. The samples labels, precursor, activation method, post activation treatment, Specific Surface Area (SSA_{BET}) and micropore volume (V_{micro}) are summarised in Table 2.1. The oxidation was performed by treating the carbon samples in concentrated HNO_3 (67% w/w) at room temperature for 24 h, followed by washing in distilled water until reaching a neutral pH.

Table 2. 1. Four of the activated carbons were physically activated by steam, starting from two different wood precursors (CwA and CwB) and from two

peat ones (CpA and CpB). Following, Cchemi was obtained by a chemical activation in H_3PO_4 on a wood precursor. Finally, two samples were obtained by a post-activation oxidation procedure in HNO_3 of samples CwA and Cchemi, resulting in the CwA-ox and Cchemi-ox samples, respectively. The oxidation was performed by treating the carbon samples in concentrated HNO_3 (67% w/w) at room temperature for 24 h, followed by washing in distilled water until reaching a neutral pH.

Table 2. 1: summary of the activated carbon samples investigated in this work. The type of precursor, the activation method, the post-activation treatment, the specific surface area (SSA_{BET}) and the micropore volume (V_{micro}) are reported. The two latter were measured by means of N_2 physisorption at 77 K.

Label	Precursor	Activation method	Post-activation	SSA_{BET} (m^2g^{-1})	V_{micro} (cm^3g^{-1})
CwA	Wood	Physical, steam	-	1018	0.63
CwB	Wood	Physical, steam	-	1325	0.65
CpA	Peat	Physical, steam	-	903	0.49
CpB	Peat	Physical, steam	-	882	0.52
Cchemi	Wood	Chemical, H_3PO_4	-	1508	1.11
CwA-ox	Wood	Physical, steam	CwA + HNO_3	949	0.59
Cchemi-ox	Wood	Chemical, H_3PO_4	Cchemi + HNO_3	1442	1.13

2.1.2. Catalysts samples

Six carbon-supported Pt and Pd-based catalysts and a $\gamma\text{-Al}_2\text{O}_3$ supported Pt one have been investigated regarding the effect of the metal deposition on the C-H terminations of the carbon support (Chapter 4) and the nature of the Pt-H species formed under hydrogenation conditions (Chapter 5). All the investigated catalysts were prepared in the laboratories of Chimet S.p.A. [1] Their names, the employed support, the metal constituting the nanoparticles,

the eventual presence of a pre-reduction step and the dispersion values evaluated by CO chemisorption [2] are reported in Table 2. 2.

Two samples were prepared by depositing Pd nanoparticles on CwA (5 wt% Pd loading), following the deposition-precipitation method described in references [3, 4], using Na_2PdCl_4 as precursor and Na_2CO_3 as basic agent. The metal phase precipitates in the form of PdO and/or $\text{Pd}(\text{OH})_2$ [3], which is then reduced to obtain Pd^0 . One of the two samples was pre-reduced via reaction with a HCOONa solution at 55°C for 1 h, leading to reduced Pd^0 nanoparticles with an external passivated layer [5]. In both cases, the sample was finally washed in distilled water to remove the residual Cl^- and then dried at 120°C overnight. The two catalysts are labelled Pd(NR)/CwA and Pd(R)/CwA, where NR and R stand for “non pre-reduced” and “pre-reduced”, respectively.

Table 2. 2: summary of the catalysts investigated in the frame of this work. The support, the metal (Pt or Pd), the metal loading, the presence of a pre-reduction step, and the metal dispersion evaluated by CO chemisorption are reported.

Sample	Support	Metal	Loading	Pre-reduced	Dispersion (%)
Pd(NR)/CwA	CwA	Pd	5 wt%	No	24
Pd(R)/CwA	CwA	Pd	5 wt%	Yes	24
Pt(R)/CwA	CwA	Pt	5 wt%	Yes	72
Pt(R)/CwB	CwB	Pt	5 w %	Yes	77
Pt(R)/CpA	CpA	Pt	5 wt%	Yes	71
Pt(R)/CpB	CpB	Pt	5 wt%	Yes	69
Pt(NR)/Alu	$\gamma\text{-Al}_2\text{O}_3$	Pt	5 wt%	No	80

The supported Pt catalysts were prepared by depositing the Pt phase on four of the previously described activated carbon supports (CwA, CwB, CpA and CpB) and on a transition alumina support. The latter is a commercial

transition alumina characterised by a specific surface area of $121 \text{ m}^2\text{g}^{-1}$ and a micropore volume of $0.62 \text{ cm}^3\text{g}^{-1}$. Also in this case, the metal loading is of 5 wt% for all the samples. The Pt deposition was performed following a deposition-precipitation method similar to the one described in reference [6]. All the samples, apart for the $\gamma\text{-Al}_2\text{O}_3$ supported one, were pre-reduced with a HCOONa solution at 80°C for one hour. The samples were labelled as Pt(R) followed by the label of the employed support for the carbon supported samples, and as Pt(NR)/Alu for the alumina supported one.

2.2. Temperature Programmed Desorption Experiments

Temperature Programmed Desorption (TPD) is a powerful technique to study the interaction of adsorbates at the surface of a material [7, 8]. It consists in a controlled heating of the sample in a gas flow or in vacuum, and in the measurement of the desorption of the adsorbed species as a function of the temperature. In the frame of this thesis work, it was employed for the characterization of the functional groups in activated carbons. For this class of samples, the controlled heating in inert atmosphere triggers the thermal decomposition of the heteroatom-containing functional groups into small gaseous products such as CO, CO₂ or H₂O, whose measurement allows for an indirect characterization and quantification of the original functional groups [9-12]. The interpretation of the TPD results will be largely discussed in Chapter 3, while the current section will focus on the description of the available experimental setups and approaches, as well as in showing the details, pros and cons of the home-made TPD-IR approach used during this PhD project.

2.2.1. TPD instrumentation: state of the art

Very different setups can be employed for TPD experiments, but the basic requirements are always the same: a sample holder section equipped with an

oven or a furnace able to heat the sample at a controlled rate; a device for detecting and quantify the gaseous products; and a mean to bring the gaseous products from the sample to the detector. Two main strategies are commonly adopted: vacuum lines or inert gas flow ones. The former, for which an example is shown in Figure 2. 1a, consists in a sample holder inserted into a furnace and directly interfaced with a vacuum line and a mass spectrometer (MS). In the reported example, the pressure is maintained at values lower than 10^{-3} Pa to avoid the accumulation of the gases and assure that the values read by the MS are representative of the instantaneous gas evolution rate. Figure 2. 1b instead shows an example of TPD setup operating in inert gas flow conditions. In this case, the gaseous decomposition products of the TPD are carried to the MS unit by a constant flow of ultrapure He. The most commonly employed detection unit in TPD experiments consists in a mass spectrometer (MS), as in the two examples shown in Figure 2. 1. This technique permits to identify molecular compounds by measuring the masses and amounts of their ionization fragments. This instrumentation is very sensible to very low concentrations, but needs to operate in almost vacuum conditions. Through a careful calibration with a reference gas feed, it is also possible to quantify the released gases by MS. This calibration could be challenging because of the overlap of ionization fragments with the same m/z values generated from different molecules: for example, CO is quantified from the intensity of the MS peak at $m/z = 28$ but, on the other hand, the same value is also read for N_2 and for a fragment of CO_2 . In these cases, a completely quantitative analysis can require a quite complex data treatment, as shown in reference [13]. These drawbacks can be reduced by coupling MS with a separative technique such as Gas Chromatography (GC) [14], at the cost of a more complex instrumentation and a lower sampling frequency.

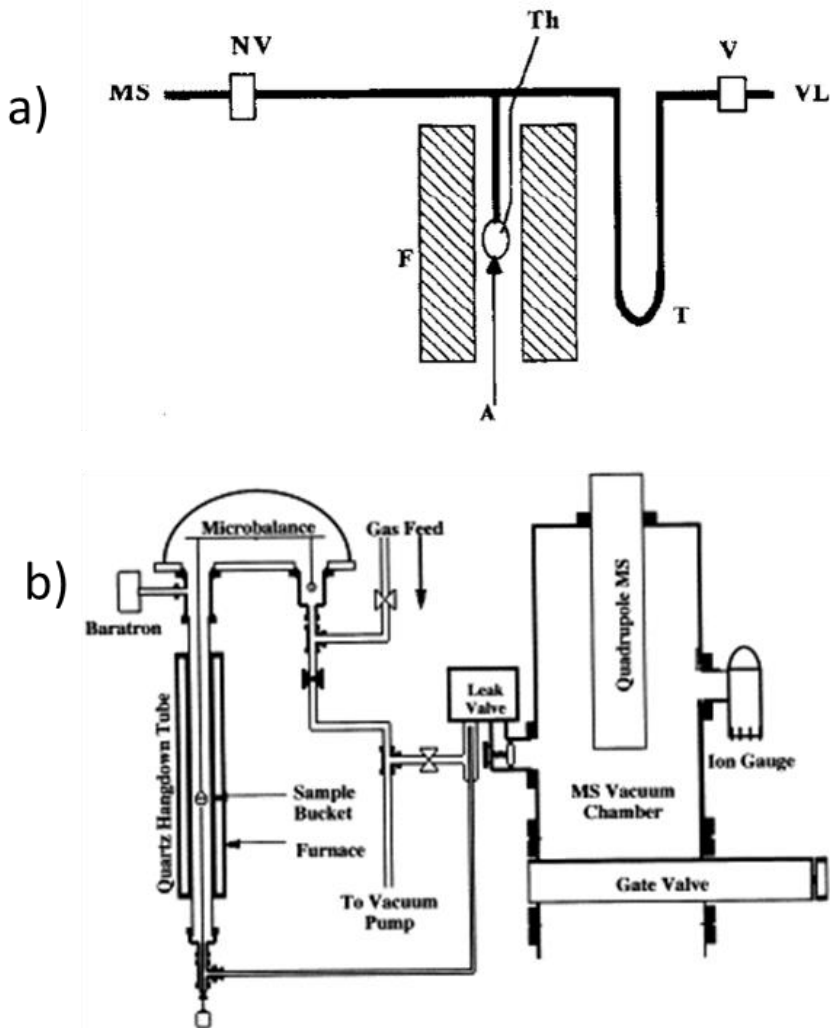


Figure 2. 1: two representative examples of TPD apparatus employed for the characterization of activated carbons. Part a) representative example of TPD-MS apparatus operating in vacuum, from reference [15]. The system is composed by: A) quartz bulb containing the sample; Th) thermocouple; F) furnace; VL) Vacuum line; MS) mass spectrometer; T) liquid N₂ trap; NV) needle valve. The pressure in the apparatus is kept below 10^{-3} Pa in order to avoid the accumulation of the decomposition products. Part b) representative example of TPD-MS apparatus operating in inert gas flow conditions, from reference [16]. The inert gas flows through the sample all along the experiment, carrying the gaseous products toward the leak valve interfacing with the mass spectrometer. The microbalance allows to operate in both TGA and TPD modes. This system was designed to operate with a gas flux at a reduced pressure of 25 Torr.

The second most employed detection system in TPD experiments for activated carbons is Infrared Spectroscopy (FT-IR) [17-19], which makes it possible to identify all the infrared-active molecules (i.e. molecules which undergo a change in dipole moment when vibrating).

It is commonly used in TPD setups operating in gas flux conditions, where the carrier gas continuously pass through the IR gas cell. FT-IR spectroscopy is generally less sensitive to very low concentration of gases than MS, but it allows for a more straightforward identification and quantification of the gaseous products. In fact, the roto-vibrational profiles are specific for each molecule, and the relation between the concentration and the measured absorbance values simply follow the Lambert-Beer law.

Ideally, a TPD setup should be able to reach a sufficient temperature to allow the complete decomposition of the O-containing functional groups in the activated carbon. Typically when the temperature exceeds 1000°C the decomposition rate rapidly decreases [20] meaning that, for a complete characterization of all the functional groups, attaining this temperature would be required. The heating rate of the experiment is another important parameter to keep into consideration. Heating rates in between 5 and 50 °C/min are the most commonly reported in the literature [10, 21]. Lower heating rates are usually preferred to improve the temperature resolution. However, the influence of the heating rate on secondary reactions should also be taken into account [16, 22], as it will be discussed in Chapter 3, Section 3.2.2. It is important to optimise both the heating rate and the gas flow to maintain the optimal concentration range for the detection of the species, to keep a good temperature resolution and to limit the delays between the gases evolution and their detection. Most of the TPD systems operating in flux conditions are designed to work at ambient pressure, even if it has been reported that systems operating with a reduced pressure flux of He (25 Torr)

are able to reduce the occurrence of secondary reactions [16]. In the case of vacuum systems, instead, the pressure ranges are generally optimised to avoid the accumulation of the decomposition products and to allow an easy interfacing with the MS detection unit [15].

2.2.2. Home-made TPD-IR setup and experimental protocol

For the quantification of functional groups in the activated carbons investigated for this PhD project, a new home-made TPD-IR setup was optimised, presenting several innovative characteristics in comparison with the commonly used setups discussed in Section 2.2.1. A photo of the apparatus is shown in Figure 2. 2a, while part b and c show the details of some of the main components. In addition, part d reports a simplified scheme of its main parts. The sample is contained in a quartz tube (A), which is inserted within an oven (B). The temperature is constantly monitored by a thermocouple placed close to the sample in the external part of the quartz tube, as shown in Figure 2. 2b. The tube is connected via Swagelok plastic tubes to the IR gas cell (C), which is a custom-made 17 cm long cell equipped with KBr optical windows. The IR cell is inserted within the infrared spectrometer (C'), a Nicolet 6700 instrument with a MCT detector. Finally, the other end of the IR cell is connected to the vacuum line (E). It is possible to completely isolate the setup volume by closing the valve D, while opening it the line can be degassed. The setup is designed to operate in static vacuum conditions, allowing the accumulation of the decomposition products in the available volume and their continuous detection via FT-IR spectroscopy. This setup, unlike the flux operating ones, permits to work within the optimal absorbance range for a precise quantification of the main products.

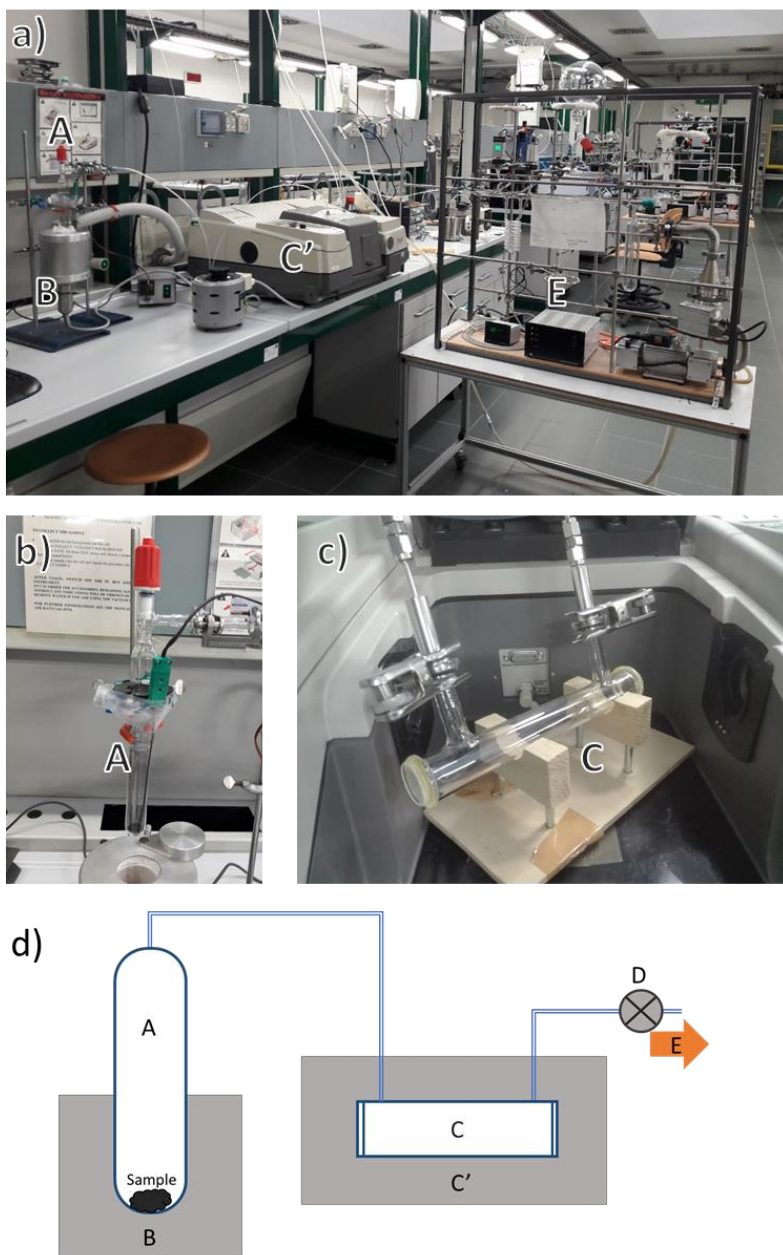


Figure 2. 2: part a) photo of the home-made TPD setup. Part b) detail over the quartz tube and the thermocouple. Part c) detail over the IR cell for detection of gases. Part d) schematic representation of the whole setup. The labels indicate: A) the quartz tube in which the sample is inserted, B) the electric oven, C) the gas infrared cell, C') the infrared spectrophotometer, D) the valve isolating the apparatus from the vacuum line, E) vacuum line.

In addition, with this setup it is possible to collect high resolution IR spectra (0.5 cm^{-1} and 32 scans), which is fundamental for the precise identification of several trace products, whose spectral features appeared extremely well resolved despite the very low absorbance values.

The setup presents however some drawbacks, related to the fact that the most of the employed components were not specifically designed and optimised for this experiment. This is particularly evident for the quartz tube (Figure 2. 2b), which is composed by two sections hold together by an O-ring. From previous experiments made in the lab, it was concluded that leaks from this O-ring were possible when the sample was heated at a temperature higher than 700°C , invalidating the result of the experiments. Moreover the employed oven cannot reach higher temperatures safely. For this reason, it was decided to interrupt all the experiments once reaching this temperature, even if it is not sufficient for the complete decomposition of all the functional groups in activated carbons.

To ensure the repeatability of the measurements it is fundamental to avoid the movement of any element of the setup, in particular of the thermocouple and of the IR cell, which have been carefully fixated at the beginning of any experiment.

The typical experimental protocol can be summarised into three main steps:

- **Sample activation:** a weighed amount of sample (between 0.2 and 0.8 g) was placed in the quartz tube, and then heated up to 120°C overnight in dynamic vacuum in order to remove the majority of physisorbed water.
- **TPD run:** the TPD apparatus was isolated from the vacuum line by closing valve D in Figure 2. 2, and then a linear heating ramp of $5^{\circ}\text{C}/\text{min}$ up to 700°C was set. During this part of the experiment, the evolution of gases was monitored by collecting FT-IR spectra every 20°C (we collected 64 scans for the background and 32 for the sample, with a resolution of

0.5 cm⁻¹). When 700°C were reached, the temperature was kept constant for 40 further minutes and one spectrum every 5 min was collected.

- **End of the experiment:** at the end of the experiment, the system was carefully outgassed. When the sample cooled down, it was weighted again in order to evaluate the mass loss underwent during the experiment.

2.2.3. Data analysis

The data analysis aimed at quantifying the gases released during each TPD experiment starting from the information contained in the FT-IR spectra. As the experiment is performed accumulating the decomposition gases in the apparatus, the infrared spectra's absorbance progressively increases along the experiment (Figure 2. 3A). To evaluate the amount of gases present in the system in correspondence with each spectrum, we measured known pressures of pure reference gases with the same setup and used those spectra to calculate the pressure vs absorbance calibration lines, as shown in Figure 2. 3, reporting the calibration lines for CO (B), CO₂ (C), H₂O (D), CH₄ (E) and NO (F). Each line was calculated by using the absorbance values of a single roto-vibrational peak for each species. Also notice that the plastic connections were not heated to prevent the condensation of H₂O, whose quantification is thus considered to be semi-quantitative.

Once the partial pressures of the decomposition products have been measured, it was possible to calculate the corresponding number of moles by using the perfect gas law ($pV = nRT$). The apparatus volume was simply calibrated by means of gas expansion from a known volume. The temperature dependence instead was more challenging to evaluate, as it was not constant in all the parts of the system, nor it remained constant during the experiment (as the sample follows a temperature ramp from 120 to 700°C, while the IR cell remains at about room temperature for all the time).

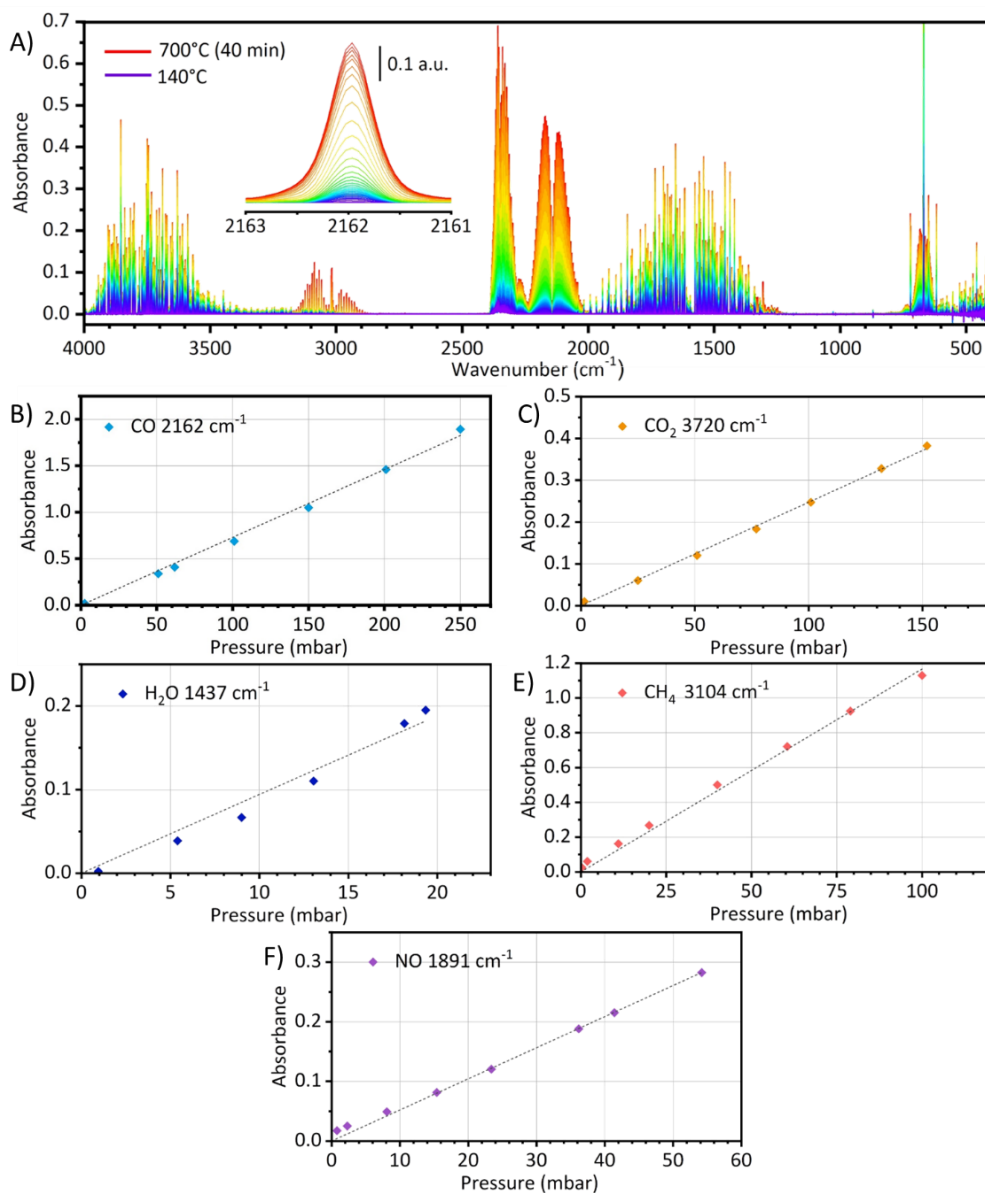


Figure 2. 3 example of the increase in the IR absorbance during the TPD experiments (A) and calibration lines pressure vs absorbance for CO (B), CO₂ (C), H₂O (D), CH₄ (E) and NO (F). The wavenumber value of the roto-vibrational peaks used for calculating the calibration lines are reported in each plot. Dotted lines are obtained by a linear fit procedure.

To empirically evaluate this effect, some reference measurements were made filling the system with a known amount of CO or CO₂ and proceeding with the same protocol as a normal TPD run. As shown in Figure 2. 4A, the infrared intensity progressively increases during this experiment, up to ~10% when the base of the quartz tube reached 700°C. It was also observed that the entity of this effect was strongly related to the position of the oven with respect to the quartz tube: for this reason, to keep the comparability among the results, we always placed these components at the same position. The effect of the temperature on the absorbance could not be ignored. We decided to evaluate empirically the relation between the relative increase in absorbance (Abs/Abs_0 , where Abs_0 is the value measured at room temperature) as a function of the temperature. The points collected during the four reference measurements were then fitted through a non-linear least-squares procedures, whose best solution was given by a third degree polynomial (Figure 2. 4B).

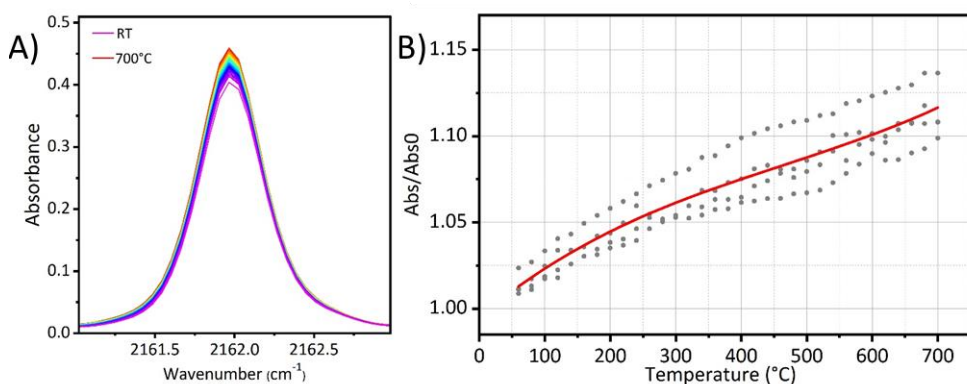


Figure 2. 4: effect of the temperature on the measured infrared spectra, an increase up to the 10% in absorbance is observed as the temperature increases (part A shows as an example a detail of the rotational peak used for quantifying the amount of CO). Part B: third degree polynomial describing the empirical relation between the relative increase in absorbance Abs/Abs_0 and the temperature.

Dividing the absorbance values of the spectra measured during the TPD run by the $Abs(T)/Abs_0$ value calculated from the regression polynomial, it was possible to evaluate the expected value of absorbance as if the whole system was at room temperature. At this point, the corrected absorbance values were used to calculate the corresponding partial pressures, and then the perfect gas law was applied to calculate the amounts of moles considering $T = 20^\circ\text{C}$.

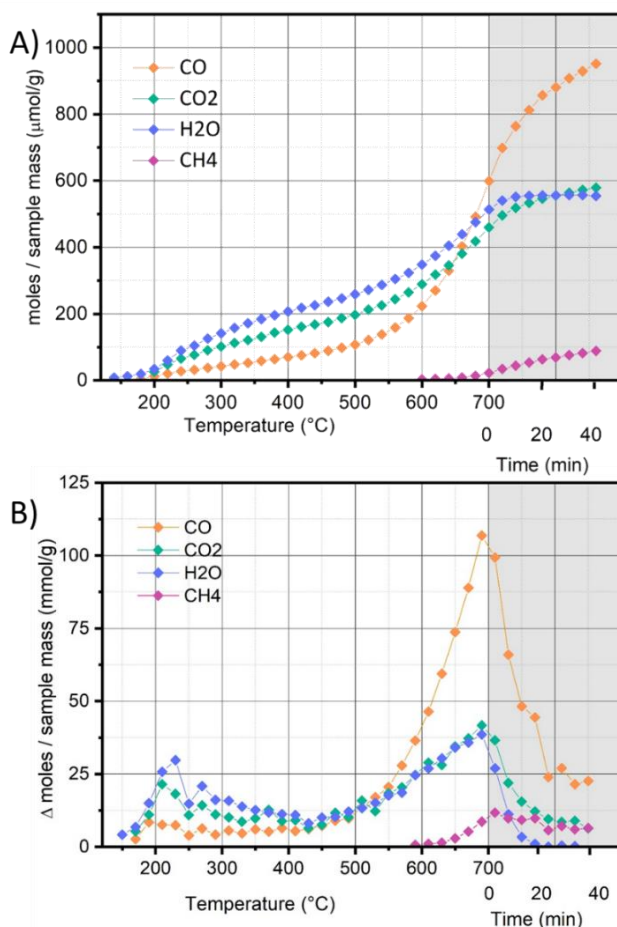


Figure 2. 5: Part A) Example of the cumulative TPD plot calculated for Cchemi, following the increasing amount of gases inside the apparatus. Part B) Example of differential TPD plot for Cchemi, each point corresponds to the difference between two consecutive points in the previous plot. In both cases, white background refers to the temperature ramp, and grey background to the isotherm.

As an example, the results obtained for Cchemi are reported in Figure 2. 5A. It shows the amounts of moles of the main decomposition products from each independent IR spectrum. These data reflect the accumulation of the gaseous products in the apparatus, and we can observe that each component increases at variable rate. The different decomposition rates can be better visualised in the differential plot reported in Figure 2. 5B, where each point of this corresponds to the difference between two consecutive points in the cumulative plots, and thus to the amount of gases evolved between the measurement of two subsequent infrared spectra. All the TPD results that will be discussed in Chapter 3 will be shown in the form of differential TPD plots.

2.2.4. Possibilities for improvements

The development of the home-made TPD-IR setup allowed to gain important details about the heteroatoms content of the activated carbon samples under exam and of their functional groups. However, some improvements are still possible. First of all, to update the setup components in order to be able to exceed the temperature of 700°C, ideally to reach 1000°C, would allow to access the complete decomposition of the O-containing functional groups, allowing also for the quantification of the most thermoresistant ones. Following, to introduce a heating system to the connections between the quartz tube and the IR cell would completely avoid the condensation of H₂O on the walls of the apparatus, thus making its evaluation completely quantitative. The setup could also be improved reducing the dead volumes, which would permit a faster diffusion of the gasses through the system. Finally, the quantification of all the thermal decomposition products was not possible because of the lack of the reference gases for making a calibration lines in our labs. Thus, to retrieve those reference gases (such as SO₂ or NO₂)

would provide a more complete picture of the occurring thermal decomposition processes.

2.3. Inelastic neutron scattering spectroscopy

Inelastic Neutron Scattering (INS) spectroscopy has been employed in this PhD project to characterize the nature of the C-H terminations in activated carbons and of the Pt-H species formed upon H₂ exposure of the catalysts. In the following, the theoretical background of this technique will be briefly summarised, and the details of the instrumentation and of the data analysis will be commented.

2.3.1. Introduction to INS spectroscopy

Neutrons are subatomic particles characterised by a null charge, a mass of $\sim 1.67 \cdot 10^{-27}$ kg and a spin of $\frac{1}{2}$. They interact weakly with matter, principally by short-range nuclear and magnetic interactions, and they are a versatile probe for characterizing many properties of materials. Many neutron-based techniques exist, ranging from diffraction to spectroscopies to imaging. Very extensive description of the theory describing the neutron-matter interactions, its mathematical treatment, and the details of the main techniques and instrumentations can be found elsewhere [23-27]. In the following, instead, the discussion will be centred on the main concepts required to understand the INS spectroscopy.

INS spectroscopy is a technique which allows to measure the vibrational spectra of a material or molecule. The technique exploits the inelastic scattering of neutrons with the sample, as summarised in Figure 2. 6. The neutrons in the incident beam present an initial energy E_0 and momentum k_0 . When interacting with the sample, part of the neutrons are inelastically scattered by the sample with exchange of both energy and momentum, resulting in the final values of E_1 and k_1 .

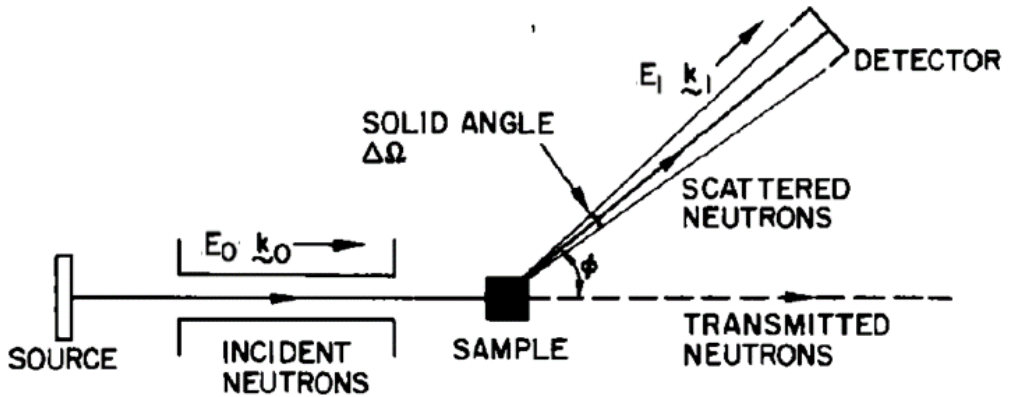


Figure 2. 6: general scheme of a neutron scattering event, adapted from reference [23]. The incident neutron beam (with an energy of E_0 and momentum of k_0) travel from the neutron source to the sample, where it can either be transmitted without interacting or being scattered. The neutrons are scattered within a solid angle $\Delta\Omega$ to the detector, with a final energy E_1 and momentum k_1 .

The variation in energy $E_1 - E_0$ corresponds to the energy required for a vibrational transition in the sample, $\hbar\omega$. Thus, from the information provided by the change in energy and momentum of the neutron beam, it is possible to obtain vibrational spectra of the sample.

The amount of neutrons scattered in the solid angle $\Omega + d\Omega$ and the energy range of $E + dE$ is expressed in terms of the double differential cross section, which is obtained by applying the Fermi's Golden rule and corresponds to [23, 24, 26]:

$$\left(\frac{d^2\sigma}{d\Omega dE} \right)_{l_0 \rightarrow l_1} = \frac{k_1}{k_0} \left(\frac{m}{2\pi\hbar^2} \right)^2 |\langle \mathbf{k}_1 l_1 | V | \mathbf{k}_0 l_0 \rangle \delta(\hbar\omega + E_0 - E_1) \quad (2.1)$$

where l_i and l_f are the initial and final quantum states of the system, and V is the interaction potential between neutrons and sample.

Not all the atomic nuclei scatter neutrons in the same way, and this can be expressed by defining their neutron scattering cross sections. It is necessary to distinguish between the coherent scattering, providing

information about the cooperative effects arising from atoms of a same type, and incoherent scattering, which instead describes the individual nuclei. It is thus possible to define the coherent neutron scattering cross section, σ_{coh} , and the incoherent one, σ_{inc} , as [23-27]:

$$\sigma_{\text{coh}} = 4\pi(\bar{b})^2 \tag{2.3}$$

$$\sigma_{\text{inc}} = 4\pi(\overline{b^2} - \bar{b}^2) \tag{2.4}$$

where b is the scattering length of an element. The scattering cross sections of different elements varies erratically in the periodic table, as well as differs from isotope to isotope, as shown by the examples in Table 2. 3. Comparing these numbers, we can observe that ^1H has the largest scattering cross section and that it is mostly an incoherent scatterer ($\sigma_{\text{inc}} = 80.27 \text{ b}$) while, on the other hand, ^2H , ^{12}C and ^{16}O have much lower scattering cross sections and mostly show a coherent scattering. The last example, ^{27}Al , has a very low neutron scattering cross section and also a very limited absorption, which makes it a suited material for the sample holders used in neutron experiments.

Table 2. 3: comparison among the coherent and incoherent scattering cross sections of some relevant isotopes, expressed in b. Values from ref [25].

Isotope	σ_{coh}	σ_{inc}	σ_{tot}
^1H	1.76	80.27	82.03
^2H	5.9	2.05	7.64
^{12}C	5.56	0	5.56
^{16}O	4.23	0	4.23
^{27}Al	1.49	0.01	1.50

The INS spectra are often plotted in terms of the scattering function $S(\mathbf{Q}, \omega)$, where \mathbf{Q} is the exchanged momentum $\mathbf{k}_1 - \mathbf{k}_0$, and ω is directly proportional to the exchanged energy following the relation $E_1 - E_0 = \hbar\omega$. This quantity is related to the double differential cross section by the formula [26, 27]:

$$\left(\frac{d^2\sigma}{d\Omega dE} \right) = N \frac{k_0}{k_1} \frac{\sigma}{4\pi} S(\mathbf{Q}, \omega) \quad (2.5)$$

Where N is the number of atoms in the sample and σ the neutron scattering cross section of the element.

In INS spectroscopy, the scattering function is commonly expressed in the form [27]:

$$S(\mathbf{Q}, \omega_\nu)_l^n = \sigma_l \frac{(\mathbf{Q} \cdot \nu \mathbf{u}_l)^{2n}}{n!} \exp \left[- \left(\mathbf{Q} \cdot \sum_\nu \nu \mathbf{u}_l \right)^2 \right] \quad (2.6)$$

where ν is the vibrational mode involved, l is the atom, n is the order of the transition, and $\nu \mathbf{u}_l$ is the mean square displacement for the atom l in the vibrational mode ν . These experiments are generally conducted assuming the validity of the incoherent approximation, and thus treating all the scattering as if it was incoherent [27].

This formulation points out the two main factors determining the final intensity of INS spectra: the neutron scattering cross section σ_l and the atomic mean square displacement \mathbf{u}_l . The highest neutron scattering cross section is the one of ^1H , as already shown in Table 2. 3, and in addition the light weight of the isotope provides to ^1H large displacement values. Consequently, the INS spectra of hydrogenous samples are dominated by the bands of vibrational modes involving hydrogen atoms. Another main characteristic of INS is the absence of real selection rules, with the consequence that all the

vibrational modes are in principle visible (although some can present very weak intensities). All these characteristics makes INS a vibrational spectroscopy complementary to other techniques such as FT-IR or Raman spectroscopies, as it can be easily observed from Figure 2. 7. The comparison also makes it evident that INS spectra tend to contain a larger number of bands than FT-IR and Raman ones, making their interpretation more challenging. These issues are often solved by coupling the experimental INS spectra with computational simulations [28-30], which is the reason why INS spectroscopy was coupled with simulations also in the frame of this PhD project.

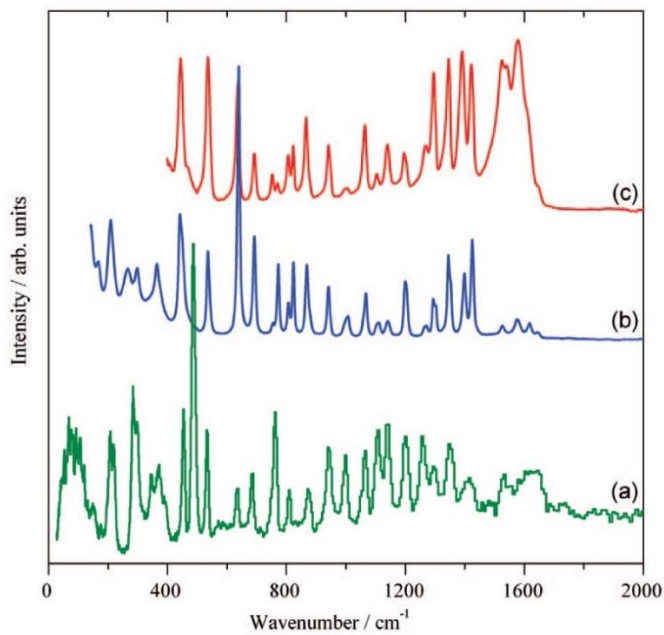


Figure 2. 7: comparison between the vibrational spectra of L-cysteine measured by means of INS (a), Raman (b) and FT-IR spectroscopies. From reference [31].

2.3.2. INS measurements and data analysis

The IN1-Lagrange instrument. All the INS measurements commented in this thesis were collected on the IN1-Lagrange instrument at the ILL, Grenoble [32]. The instrumental layout is shown in Figure 2. 8. The instrument is downstream to a hot neutron source, allowing for the measurement of energy exchange values up to $\sim 4000 \text{ cm}^{-1}$ (500 meV). Different monochromators are available for selecting the energy of the incoming neutrons E_0 , each one covering different energy ranges. Three monochromators were used, Si(111) for the $45 - 160 \text{ cm}^{-1}$ (5.5 - 20 meV) range, Si(311) in the $135 - 240 \text{ cm}^{-1}$ (16 - 30 meV) range and Cu(220) for the $220 - 4030 \text{ cm}^{-1}$ (27 - 500 meV) range. Following, the monochromatic neutron beam reaches the sample and is scattered. The final energy E_1 is selected by the combination of a Be filter (absorbing all the neutrons with an energy higher than $\sim 40 \text{ cm}^{-1}$, or 5 meV) and of a graphite filter, which converges on the ^3He gas detector neutrons with a final fixed energy of 4.5 meV (36.3 cm^{-1}). The instrument was optimized to increase the neutron counts in comparison with the past instrument, allowing to collect high signal to noise spectra with an energy good resolution of $\Delta E/E = 2\%$. This instrumental geometry allows scanning the initial values of the neutron momentum (k_0) while keeping fix the final k_1 only permitting to explore one specific Q value at each value of exchanged energy, analogously with the indirect geometry TOF spectrometers. For this reason, the spectra measured on Lagrange will be reported in terms of $S(\omega)$ only in the following. In the following the unity of measure chosen for the x axis is cm^{-1} .

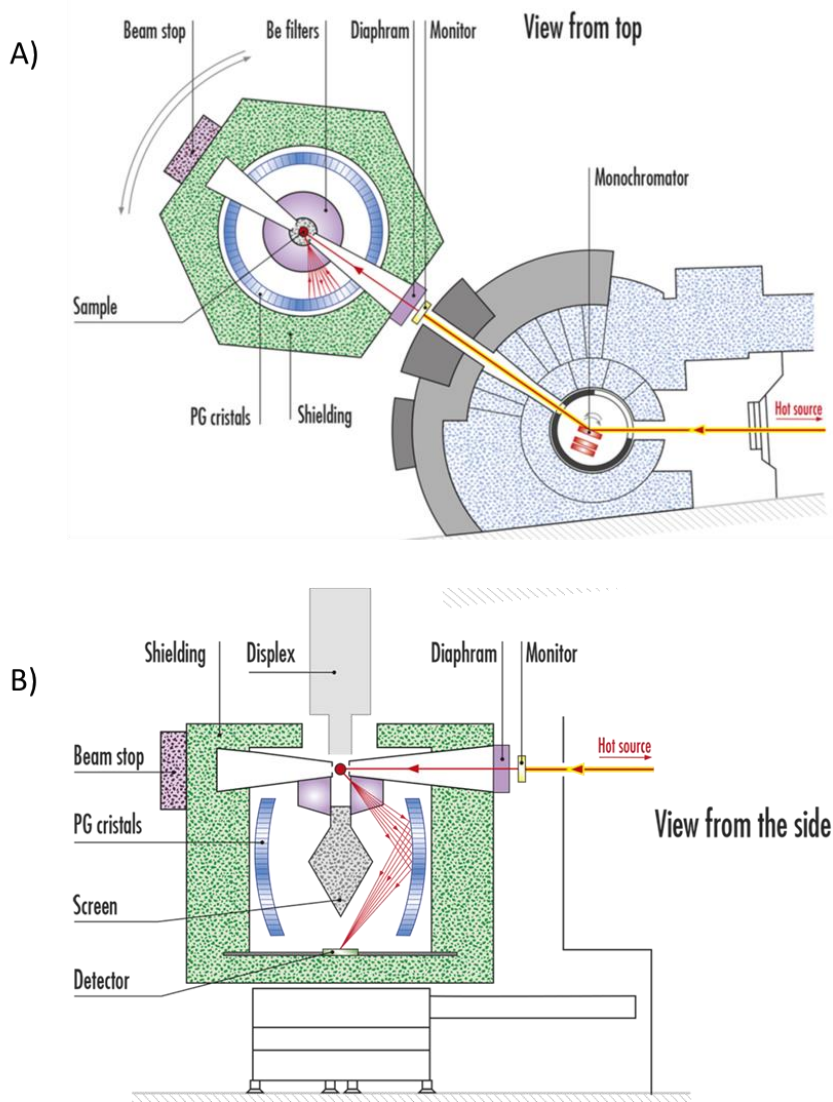


Figure 2. 8: instrumental layout of the IN1-Lagrange spectrometer at the ILL, Grenoble. From reference [33]

Sample preparation and measurements procedure. Samples CwA, Pt(R)/CwA, Alu and Pt(NR)/Alu were measured as such and in the presence of H_2 (proposal nr 7-05-466 [34]), while all the other supports and catalysts listed in Section 2.1 of this chapter have been measured as such in a following experiment (proposal nr 7-04-162 [35]). For the first experiment the spectra

were collected in the 24-3000 cm^{-1} range, while for the second we focused on the 24-1020 cm^{-1} region only. All the samples have been pre-treated in dynamic vacuum at 120°C in order to eliminate most of the physisorbed water. This step is particularly critical due to the fact that even small amounts of water may contribute with intense bands in spectral regions of interest, obscuring minor features due to the sample vibrational modes. In addition, the catalysts measured during the first experiment have also been pre-reduced in H_2 . All the samples manipulation following the activation procedure were made in an Ar-filled glovebox, to avoid any contamination from air moisture. Weighted amounts of sample were introduced in cylindrical Al cells (diameter 16 mm, height 4 cm) sealed with In wire. For the first experiment a sample sticks equipped for gas injection was used, while for the second one simple sample holder was employed. The samples were then introduced into the instrument and cooled down to about 20 K by a CCR cryostat. Measurement at such low temperatures is required to reduce the thermal broadening of the spectra. Finally, for the first experiment, the H_2 dosing and sample evacuation was performed with a Hiden Isochema gas volumetric device.

Data treatment. The raw data were elaborated with the software Lamp [36]. The first data elaboration consisted in the normalization to the incoming neutron flux, the subtraction of the spectrum of the empty cell and the correction for the presence of water. The spectra collection was split on three monochromators (Si(111), Si(311) and Cu(220)), resulting in three spectra covering different energy ranges. Thus, the following step consisted in merging the three segments into a single spectrum as described in reference [37]. Finally, the intensities of the spectra of the catalysts were normalized to the one of their supports to match the intensity of the latter at 1020 cm^{-1} and the ones of the oxidized samples to their parent carbon at 220 cm^{-1} , where

only the background is contributing to the spectra. This last step was required because of some difficulties arose from the measurement of the catalysts' INS spectra, whose intensity was systematically higher than the expected value for reasons that we are not yet able to explain.

2.4. Computational simulations

Computational simulations demonstrated to be very useful to overcome the intrinsic difficulties in the interpretation of the experimental INS spectra [28-30]. In particular, Density Functional Theory (DFT) methods are particularly popular thanks to their ability to provide reliable results with a reasonable computational cost. In this section, a brief overlook over the main characteristics of DFT calculations will be presented, followed by the computational details for the simulations made.

2.4.1. DFT simulations of molecular and periodic systems

DFT methods. They belong to the category of quantum-mechanics *ab initio* computational methods for the simulation of molecular and solid systems. The complete description of the theory and the mathematical formalisms can be quite complex, and just a brief summary will be reported in the following. The complete treatment can be found in many literature works, such as for example refs [38-40]

The basis for DFT is the Hohenberg and Kohn theorems, according to which the energetic ground state of a system can be completely determined on the base of the electron density $\rho(\mathbf{r})$ only [41]. The most used DFT formalism is the one later proposed by Kohn and Sham [42], which partially re-introduces the wavefunctions into the equations. In this formulation, the DFT energy of the system can be written as:

$$E_{\text{DFT}} = T_s[\rho] + E_{\text{ne}}[\rho] + J[\rho] + E_{\text{xc}}[\rho] \quad (2.7)$$

where T_s is the kinetic energy of the system, calculated in the approximation of non-interacting electrons, E_{ne} is the potential energy between nuclei and electrons, J is the Coulomb term, and E_{xc} contains the contributions for the electrons correlation and exchange energy. This last one is the only term which cannot be calculated exactly, and the available DFT functionals differ in the method employed for approximating it.

On the base of the level of approximation employed for defining the E_{xc} term, DFT functionals are generally classified into:

- Local Density Approximation (LDA) functionals: $\rho(\mathbf{r})$ is locally treated as a uniform electron gas. It allows for an exact solution, but this approximation is generally valid only for metallic systems.
- Generalized Gradient Approximation (GGA) functionals: the first derivative of $\rho(\mathbf{r})$ is introduced in the calculation of the E_{xc} term. Various of the most popular functionals for simulating molecules and solids (PBE, PW91) belong to this category.
- Meta-GGA functionals: extension of the previous group, in this case also the second derivative of $\rho(\mathbf{r})$ is introduced in the calculation of E_{xc} . The quality of the result increases, but also the computational cost.
- Hybrid functionals: the electron exchange part comprehended in E_{xc} can be exactly calculated by the Hartree-Fock method (HF). Thus, hybrid functionals introduce parametrically the exact HF exchange term to the DFT exchange and correlation energy. Some of the most popular DFT functionals, such as B3LYP and PBE0, belong to this category.

Geometry optimization and frequency calculation. Once the DFT functional is set, the DFT energy is calculated following an iterative Self Consistent Field (SCF) algorithm, similar to the Hartree-Fock method. This step is the base for more complex algorithms routinely used in computational chemistry

simulations, such as the geometry optimization or the calculation of the vibrational frequencies of molecules and solids. The geometry optimization of a structure consists in iterative algorithms aimed to the individuation of the minimum energy geometry. For this purpose, the most of the computational chemistry software implement minimization algorithms such as the quasi-Newton method to explore the Potential Energy Surface (PES) and find the geometry corresponding to the energy minimum. The procedure converges when the change in energy and/or atomic position between two consecutive steps falls below a set threshold [40].

To simulate the vibrations of one system, instead, it is at first necessary to calculate the Hessian matrix, corresponding to the second derivatives matrix of the PES in respect with the atomic displacements [43]. The elements of this matrix correspond to:

$$H_{ij} = \frac{1}{2} \left(\frac{\partial^2 E(\mathbf{x})}{\partial u_i \partial u_j} \right) \quad (2.8)$$

where u_i and u_j correspond to the displacements along the directions i and j , respectively. The Hessian matrix is generally calculated with the method of the finite displacements of the atoms. From this matrix, it is possible to calculate the dynamic matrix, simply obtained by weighting its elements by the masses of the atoms:

$$W_{ij} = \frac{H_{ij}}{\sqrt{w_i w_j}} \quad (2.9)$$

where w_i and w_j correspond to the mass of the atoms i and j , respectively. The eigenvalues obtained from the diagonalization of the dynamic matrix correspond to the force constant of the vibrational modes of the system κ_j which, in turn, can be used for calculating the vibrational frequencies following the equation 2.10. The corresponding eigenvector instead

correspond to the atomic displacements corresponding to each vibrational modes.

$$\omega_j = \frac{\sqrt{K_j}}{2\pi} \quad (2.10)$$

It also worth noticing that the vibrational frequencies and the atomic displacements provide a sufficient information for the simulation of INS spectra (following equation 2.6), and thus the simulation of INS spectra starting from a DFT frequency calculation is generally straightforward.

This method is based on the harmonic approximation, and thus represents the energy in the proximity of the minima as quadratic functions. This approximation leads to systematic overestimation of the vibrational frequencies, which can be corrected by introducing a scaling factor on the calculated frequencies [44].

From the simulation of atomic to periodic systems. For modelling a molecular system, the starting point is the definition of the initial geometry of the isolated molecule. In the case of period systems (3D, 2D, 1D) instead it is necessary to define the unit cell, which will be repeated to infinity along the period directions (periodic boundaries condition). A more complete description of the theoretical background of the modelling of periodic systems can be found in ref [45].

On a practical standpoint, when setting up a molecular or a periodic simulation one of the main differences is the definition of a basis set describing the atomic orbitals. For molecular simulations, the most common strategy is the use of Gaussian Type Orbitals (GTO), where the atomic orbitals are represented by a linear combination of gaussian functions [40]. In order to improve the results of the simulations, these basis sets are often augmented with polarization functions (extra orbitals with larger angular momentum) or with diffuse functions (functions with small exponents, to

describe effects further from the nuclei). In the case of periodic systems instead, the mathematical formalism employed favors the use of plane waves basis sets consisting in linear combinations of several plane waves functions, which have the advantage to be naturally able to describe the periodicity of the system. On the other hand, plane waves basis sets struggle to describe the high electronic density in the proximity of the nuclei and for this reason in the most of the cases they are paired with the definition of Effective Core Pseudopotential (ECP) for the description of core electrons.

2.4.2. Simulation of the INS spectra of activated carbons and linear combination analysis

As commented in Section 2.3, computational simulations were performed in order to better interpret the experimental INS spectra. Activated carbons are very heterogeneous in nature, making it difficult to choose a representative model of their structure. Since INS is mostly sensible to the vibrational modes involving H, the spectra contain information about the vibrations of the terminal C-H groups at the edges of the graphenic domains. Thus, the simulated models should be able to give a good representation of the variety of the terminal C-H species. As demonstrated by previous works in the literature [28, 30, 46], and as confirmed by our first simulations, it is possible to obtain a good agreement between simulated and experimental vibrational spectra of activated carbons by simulating relatively simple polyaromatic models. Consequently, we were able to model the variety of the C-H terminations in activated carbons by considering a wide range of polyaromatic models with variable borders geometries. A total of 17 regular models, 13 defective ones and 34 featuring heteroatom-containing functional groups were modelled. They are reported in Chapter 4 and Appendix B, while three representative examples are shown in Figure 2. 9.

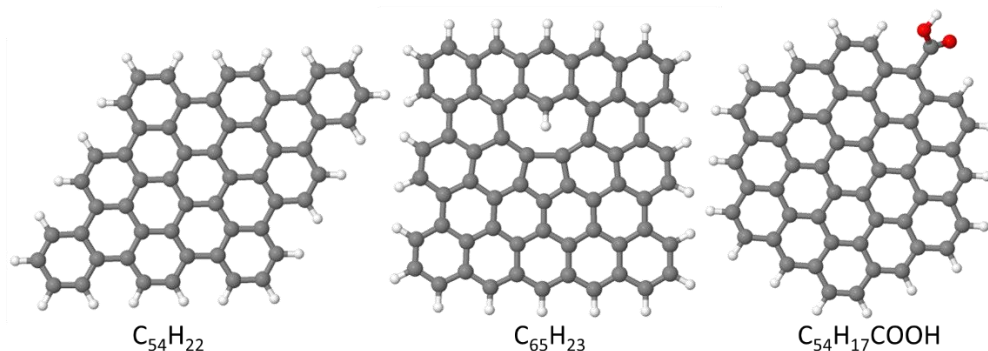


Figure 2. 9: three examples of aromatic models simulated in the present work.

All the simulations were run with the CRYSTAL17 [47, 48] software on the ILL computational clusters. CRYSTAL17 is an *ab initio* computational chemistry software for the simulation of 0D, 1D, 2D and 3D systems whose algorithms are based in the use of GTO basis sets. On the basis of the references in the literature [46, 49] and of the benchmark simulations performed during my master thesis work, I observed that the B3LYP hybrid DFT functional [50, 51] coupled with the Pople's 6-31G** basis set provided a good compromise between the reliability of the results and the computational cost. Some of the simulated models present an open shell electronic configuration, which required the use of the unrestricted UB3LYP method. The geometry of all the models was at first optimised (SCF convergence set at 10^{-8} Ha) and then the frequencies calculations were performed (SCF convergence 10^{-10} Ha). It was possible to classify all the geometries as true minima from the absence of imaginary frequencies. In order to ensure the stability of the SCF cycles, it was necessary to set very thight values for the integrals screening tolerance (8 8 8 25 50). The typical input files for both the geometry optimization and frequency calculation are reported in Appendix A.

It is also worth noticing that many of the discussed defective models feature an odd number of electrons, requiring open-shell calculations. The simulation of many of these models resulted particularly challenging, as their electronic configuration tended to converge into electronic configuration with high spin polarization over the basal plane, which is not a physically correct description. It was generally observed that models constructed starting from a hexagonal shape were much less affected by this issue than the rectangular ones.

The simulated INS spectra were calculated using the software aClimax [52], which uses the calculated frequencies and vibrational modes obtained from the dynamic matrix read from the frequency calculation output to calculate the $S(\mathbf{Q},\omega)$ following equation 2.6. The required *.aclimax file is automatically created every time that the output file of a frequency calculation run with CRYSTAL is open with the visualization software Moldraw [53]. With aClimax we also simulated the contribution from higher order transitions and phonon wings, but they were not included in the final discussion since they gave rise to features not observed in the experimental spectra. In addition, with aClimax it was also possible to calculate the contribution of the vibration of a few atoms to the total INS spectrum by manually setting to 0 barn the scattering cross section of the atoms not comprehended in the portion of the model under investigation. In this way, it was possible to find out the characteristic INS fingerprint of each portion of the C-H terminations in the models and to classify them, as it will be discussed in Chapter 4. To better compare the simulated spectra to the experimental ones, a scaling factor on the frequencies was introduced. The chosen scaling factor was obtained by a least squares linear regression of the experimental and simulated frequencies of the benzene molecule, as proposed in reference [44], resulting in the scaling function $\nu_{\text{scaled}} = 22.1 + 0.9543\nu_{\text{calculated}}$.

In order to quantify the amounts of each of the C-H terminations, a linear combination fit analysis was performed. The functions used for the fit were obtained by averaging the contributions of C-H terminations displaying similar geometries in different models, and their intensity was normalised to correspond to the contribution of a single H atom. The experimental spectra were fitted by a linear combination of these contributions following a least squares minimization algorithm. The values of the multiplicative coefficients for each contribution obtained at the end of the fit is proportional to their amount in the sample. For a better comparison, these values were normalised so that the sum of these coefficients corresponded to 1 for the activated carbon supports, while the catalysts were normalised in the same way as their supports. In addition, a small multiplicative scaling factor on the frequencies ($0.99 < s < 1.01$) was introduced as a variable in the fit to adjust for small shifts along the horizontal axis. All the fits were run using Mathematica 10, and an example of the script used is reported in Appendix A.

2.4.3. Simulation of the INS spectra of Pt-H

The simulation of INS spectra was also used to interpret the experimental results obtained from the Pt(NR)/Alu catalysts and its modifications upon interaction with hydrogen [37].

The models used for the simulation of the INS spectra were all provided by the IFPEN group, and many of them were already object of previous publications [54-56]. They consist in Pt₁₃ nanoparticles supported at the γ -Al₂O₃ (100) and (110) surfaces (12 and 6 models, respectively) at variable degrees of hydrogenation, in two larger nanoparticles (Pt₃₄H₅₄ and Pt₅₅H₄₄) supported on the γ -Al₂O₃ (100) surface, and in 6 models of extended Pt (100) and Pt (111) surfaces. All the calculations were run with the VASP software [57] using the PBE functional [58] for the supported nanoparticles models and

the PW91 one [59] for the extended surfaces. The basis set was described by means of the Projector Augmented Wave (PAW) method [60], with a cut-off energy of 400 eV. All the systems were modelled as periodic slabs. More details about the simulations conducted at IFPEN can be found in the corresponding publications [54, 55, 61].

Regarding the simulation of their INS spectra, the first step is the conversion of the OUTCAR file obtained from a frequency calculation in VASP to an *.aclimax file. For some of the models, we directly received the final OUTCAR file from the frequency calculation performed at IFPEN, while for the others we got the optimised geometry and we performed the frequency calculation. From early tests, it appears that performing the frequency calculation on the Pt_xH_y nanoparticle alone or together with the first layers of the support does not change the spectral features of the PtH species. To perform the conversion from OUTCAR to *.aclimax file I wrote a specific script in Python 3, which is reported in Appendix A. The resulting file was then elaborated using aClimax [52] to simulate the INS spectra of the whole model and of the contributions of the single Pt-H sites, following the same procedure described for the activated carbons in Section 2.4.2. Unlike the case of the activated carbons simulations, for these spectra no scaling factor was used to correct the calculated frequencies.

References

1. <https://www.chimet.com>.
2. Anderson J.R. and Pratt K.C., *Introduction to Characterization and Testing of Catalysts*. 1986, Sydney, Australia: Academic Press.
3. Agostini G., Groppo E., Piovano A., Pellegrini R., Leofanti G., and Lamberti C., *Preparation of Supported Pd Catalysts: From the Pd Precursor Solution to the Deposited Pd²⁺ Phase*. *Langmuir*, 2010. **26**(13): p. 11204-11211.
4. Pellegrini R., Leofanti G., Agostini G., Groppo E., Rivallan M., and Lamberti C., *Pd-Supported Catalysts: Evolution of Support Porous Texture along Pd Deposition and Alkali-Metal Doping*. *Langmuir*, 2009. **25**(11): p. 6476-6485.
5. Agostini G., Lamberti C., Pellegrini R., Leofanti G., Giannici F., Longo A., and Groppo E., *Effect of Pre-Reduction on the Properties and the Catalytic Activity of Pd/Carbon Catalysts: A Comparison with Pd/Al₂O₃*. *ACS Catalysis*, 2014. **4**(1): p. 187-194.
6. Kaprielova K.M., Yakovina O.A., Ovchinnikov I.I., Koscheev S.V., and Lisitsyn A.S., *Preparation of platinum-on-carbon catalysts via hydrolytic deposition: Factors influencing the deposition and catalytic properties*. *Applied Catalysis A: General*, 2012. **449**: p. 203-214.
7. Lónyi F. and Valyon J., *On the interpretation of the NH₃-TPD patterns of H-ZSM-5 and H-mordenite*. *Microporous and Mesoporous Materials*, 2001. **47**(2): p. 293-301.
8. Marchon B., Carrazza J., Heinemann H., and Somorjai G.A., *TPD and XPS studies of O₂, CO₂, and H₂O adsorption on clean polycrystalline graphite*. *Carbon*, 1988. **26**(4): p. 507-514.
9. de la Puente G., Pis J.J., Menéndez J.A., and Grange P., *Thermal stability of oxygenated functions in activated carbons*. *Journal of Analytical and Applied Pyrolysis*, 1997. **43**(2): p. 125-138.
10. Figueiredo J.L., Pereira M.F.R., Freitas M.M.A., and Órfão J.J.M., *Modification of the surface chemistry of activated carbons*. *Carbon*, 1999. **37**(9): p. 1379-1389.
11. Moreno-Castilla C., Carrasco-Marín F., Maldonado-Hódar F.J., and Rivera-Utrilla J., *Effects of non-oxidant and oxidant acid treatments on the surface properties of an activated carbon with very low ash content*. *Carbon*, 1998. **36**(1): p. 145-151.
12. Silva A.M.T., Machado B.F., Figueiredo J.L., and Faria J.L., *Controlling the surface chemistry of carbon xerogels using HNO₃-hydrothermal oxidation*. *Carbon*, 2009. **47**(7): p. 1670-1679.

13. Hotová G. and Slovák V., *Quantitative TG-MS analysis of evolved gases during the thermal decomposition of carbon containing solids*. *Thermochimica Acta*, 2016. **632**: p. 23-28.
14. Keshet U., Alon T., Fialkov A.B., and Amirav A., *Open Probe fast GC-MS — combining ambient sampling ultra-fast separation and in-vacuum ionization for real-time analysis*. *Journal of Mass Spectrometry*, 2017. **52**(7): p. 417-426.
15. Haydar S. and Joly J.P., *Study of the Evolution of Carbon Dioxide from Active Carbon by a Threshold Temperature-Programmed Desorption Method*. *Journal of Thermal Analysis and Calorimetry*, 1998. **52**(2): p. 345-353.
16. Zhang L.H. and Calo J.M., *Thermal desorption methods for porosity characterization of carbons and chars*. *Colloids and Surfaces A: Physicochemical and Engineering Aspects*, 2001. **187-188**: p. 207-218.
17. Diyuk V.E., Zaderko A.N., Grishchenko L.M., Yatsymyrskiy A.V., and Lisnyak V.V., *Efficient carbon-based acid catalysts for the propan-2-ol dehydration*. *Catalysis Communications*, 2012. **27**: p. 33-37.
18. Skodras G., Diamantopoulou I., Zabaniotou A., Stavropoulos G., and Sakellaropoulos G.P., *Enhanced mercury adsorption in activated carbons from biomass materials and waste tires*. *Fuel Processing Technology*, 2007. **88**(8): p. 749-758.
19. Zielke U., Hüttinger K.J., and Hoffman W.P., *Surface-oxidized carbon fibers: I. Surface structure and chemistry*. *Carbon*, 1996. **34**(8): p. 983-998.
20. Ishii T. and Kyotani T., *Chapter 14 - Temperature Programmed Desorption*, in *Materials Science and Engineering of Carbon*, Inagaki M. and Kang F., Editors. 2016, Butterworth-Heinemann. p. 287-305.
21. Moreno-Castilla C., Carrasco-Marín F., and Mueden A., *The creation of acid carbon surfaces by treatment with (NH₄)₂S₂O₈*. *Carbon*, 1997. **35**(10): p. 1619-1626.
22. Hall P.J. and Calo J.M., *Secondary interactions upon thermal desorption of surface oxides from coal chars*. *Energy & Fuels*, 1989. **3**(3): p. 370-376.
23. Skold K. and Price D.L., *Neutron Scattering, part A Methods of Experimental Physics*. Vol. 23. 1986, Academic Press: London.
24. Squires G.L., *Introduction to the Theory of Thermal Neutron Scattering*. 3 ed. 2012, Cambridge: Cambridge University Press.
25. Dianoux A.J. and Lander G.H., *Neutron data booklet*. 2002: S.I. : s.n.
26. Piovano A., *Inelastic neutron scattering applied to materials for energy*. EPJ Web of Conferences, 2015. **104**.

27. Mitchell P.C.H., Parker S.F., Ramirez-Cuesta A.J., and Tomkinson J., *Vibrational Spectroscopy with Neutrons*. Series on Neutron Techniques and Applications. Vol. Volume 3. 2005: WORLD SCIENTIFIC. 668.
28. Albers P.W., Pietsch J., Krauter J., and Parker S.F., *Investigations of activated carbon catalyst supports from different natural sources*. Physical Chemistry Chemical Physics, 2003. **5**(9): p. 1941-1949.
29. Cavallari C., Pontiroli D., Jiménez-Ruiz M., Johnson M., Aramini M., Gaboardi M., Parker S.F., Riccò M., and Rols S., *Hydrogen motions in defective graphene: the role of surface defects*. Physical Chemistry Chemical Physics, 2016. **18**(36): p. 24820-24824.
30. Piovano A., Lazzarini A., Pellegrini R., Leofanti G., Agostini G., Rudić S., Bugaev A.L., Lamberti C., and Groppo E., *Progress in the Characterization of the Surface Species in Activated Carbons by means of INS Spectroscopy Coupled with Detailed DFT Calculations*. Advances in Condensed Matter Physics, 2015. **2015**.
31. Parker S.F., Lennon D., and Albers P.W., *Vibrational spectroscopy with neutrons: A review of new directions*. Applied Spectroscopy, 2011. **65**(12): p. 1325-1341.
32. Jiménez-Ruiz M., Ivanov A., and Fuard S., *LAGRANGE - the new neutron vibrational spectrometer at the ILL*. Journal of Physics: Conference Series, 2014. **549**: p. 012004.
33. <https://www.ill.eu/users/instruments/instruments-list/in1-taslagrange/description/instrument-layout/> Accessed in date 20/8/20.
34. [dataset] Piovano A., Agostini G., Carosso M., Groppo E., Jimenez Ruiz M., Lamberti C., Lazzarini A., Manzoli M., Morandi S., Pellegrini R., and Vottero E., *Study of the Pt-hydride formation and spillover effect on Pt/Al₂O₃ and Pt/C catalysts* DOI:10.5291/ILL-DATA.7-05-466, 2016.
35. [dataset] Vottero E., Carosso M., Groppo E., Jimenez Ruiz M., Lamberti C., Pellegrini R., and Piovano A., *Exploring the surface chemistry of activated carbons by INS and DFT calculations* DOI:10.5291/ILL-DATA.7-04-162, 2018.
36. Richard D., Ferrand M., and Kearley G.J., *Analysis and Visualisation of Neutron-Scattering Data*. Journal of Neutron Research, 1996. **4**: p. 33-39.
37. Carosso M., Vottero E., Lazzarini A., Morandi S., Manzoli M., Lomachenko K.A., Ruiz M.J., Pellegrini R., Lamberti C., Piovano A., and Groppo E., *Dynamics of Reactive Species and Reactant-Induced Reconstruction of Pt Clusters in Pt/Al₂O₃ Catalysts*. ACS Catalysis, 2019. **9**(8): p. 7124-7136.

38. Gross E.K.U. and Dreizler R.M., *Density Functional Theory*, ed. Gross E.K.U. and Dreizler R.M. 1995, New York: Springer US.
39. Robert G.P. and Yang W., *Density-Functional Theory of Atoms and Molecules*. 1989, New York: Oxford University Press.
40. Jensen F., *Introduction to Computational Chemistry*. Second Edition ed. 2007: Wiley.
41. Hohenberg P. and Kohn W., *Inhomogeneous Electron Gas*. Physical Review, 1964. **136**(3B): p. B864-B871.
42. Kohn W. and Sham L.J., *Self-Consistent Equations Including Exchange and Correlation Effects*. Physical Review, 1965. **140**(4A): p. A1133-A1138.
43. Pascale F., Zicovich-Wilson C.M., López Gejo F., Civalleri B., Orlando R., and Dovesi R., *The calculation of the vibrational frequencies of crystalline compounds and its implementation in the CRYSTAL code*. Journal of Computational Chemistry, 2004. **25**(6): p. 888-897.
44. Alcolea Palafox M., *Scaling Factors for the Prediction of Vibrational Spectra. I. Benzene Molecule*. International Journal of Quantum Chemistry, 2000. **77**(3): p. 661-684.
45. Dovesi R., Civalleri B., Roetti C., Saunders V.R., and Orlando R., *Ab Initio Quantum Simulation in Solid State Chemistry*. Reviews in Computational Chemistry, 2005: p. 1-125.
46. Kar T., Scheiner S., Adhikari U., and Roy A.K., *Site Preferences of Carboxyl Groups on the Periphery of Graphene and Their Characteristic IR Spectra*. The Journal of Physical Chemistry C, 2013. **117**(35): p. 18206-18215.
47. Dovesi R., Erba A., Orlando R., Zicovich-Wilson C.M., Civalleri B., Maschio L., Rérat M., Casassa S., Baima J., Salustro S., and Kirtman B., *Quantum-mechanical condensed matter simulations with CRYSTAL*. Wiley Interdisciplinary Reviews: Computational Molecular Science, 2018. **8**(4).
48. Dovesi R., Saunders V.R., Roetti C., Orlando R., Zicovich-Wilson C.M., Pascale F., Civalleri B., Doll K., Harrison N.M., Bush I.J., D'Arco P., Llunell M., Causà M., Noël Y., Maschio L., Erba A., Rerat M., and Casassa S., *CRYSTAL17 User's Manual 2017*, Turin: University of Turin.
49. Maschio L., Lorenz M., Pullini D., Sgroi M., and Civalleri B., *The unique Raman fingerprint of boron nitride substitution patterns in graphene*. Physical Chemistry Chemical Physics, 2016. **18**(30): p. 20270-20275.
50. Becke A.D., *Density-functional thermochemistry. III. The role of exact exchange*. The Journal of Chemical Physics, 1993. **98**(7): p. 5648-5652.

51. Lee C., Yang W., and Parr R.G., *Development of the Colle-Salvetti correlation-energy formula into a functional of the electron density*. Physical Review B, 1988. **37**(2): p. 785-789.
52. Ramirez-Cuesta A.J., *aCLIMAX 4.0.1, The new version of the software for analyzing and interpreting INS spectra*. Computer Physics Communications, 2004. **157**(3): p. 226-238.
53. Ugliengo P., Viterbo D., and Chiari G., *MOLDRAW: Molecular graphics on a personal computer*. Zeitschrift fur Kristallographie - New Crystal Structures, 1993. **207**(Part-1): p. 9-23.
54. Hu C.H., Chizallet C., Mager-Maury C., Corral-Valero M., Sautet P., Toulhoat H., and Raybaud P., *Modulation of catalyst particle structure upon support hydroxylation: Ab initio insights into Pd13 and Pt13/ γ -Al₂O₃*. Journal of Catalysis, 2010. **274**(1): p. 99-110.
55. Mager-Maury C., Bonnard G., Chizallet C., Sautet P., and Raybaud P., *H₂-Induced Reconstruction of Supported Pt Clusters: Metal-Support Interaction versus Surface Hydride*. ChemCatChem, 2011. **3**(1): p. 200-207.
56. Gorczyca A., Moizan V., Chizallet C., Proux O., Net W.D., Lahera E., Jean-Louis H., Raybaud P., and Joly Y., *Monitoring morphology and hydrogen coverage of nanometric Pt/ γ -Al₂O₃ particles by in situ HERFD-XANES and quantum*. Angewandte Chemie - International Edition, 2014. **53**(46): p. 12426-12429.
57. Kresse G. and Furthmüller J., *Efficient iterative schemes for ab initio total-energy calculations using a plane-wave basis set*. Physical Review B, 1996. **54**(16): p. 11169-11186.
58. Perdew J.P., Burke K., and Ernzerhof M., *Generalized Gradient Approximation Made Simple*. Physical Review Letters, 1996. **77**(18): p. 3865-3868.
59. Perdew J.P. and Wang Y., *Accurate and simple analytic representation of the electron-gas correlation energy*. Physical Review B, 1992. **45**(23): p. 13244-13249.
60. Kresse G. and Joubert D., *From ultrasoft pseudopotentials to the projector augmented-wave method*. Physical Review B, 1999. **59**(3): p. 1758-1775.
61. Raybaud P., Chizallet C., Mager-Maury C., Digne M., Toulhoat H., and Sautet P., *From γ -alumina to supported platinum nanoclusters in reforming conditions: 10 years of DFT modeling and beyond*. Journal of Catalysis, 2013. **308**: p. 328-340.

CHAPTER 3

Identification and quantification of functional groups in activated carbons

3.1. Functional groups in activated carbons

Activated carbons are mainly constituted by H-terminated graphenic domains, but other elements are present at lower and variable concentrations in the form of functional groups bonded to the carbon platelets borders. Heteroatoms-containing functionalities are well known to introduce modification in the surface polarity of carbons, and consequently to affect their adsorption and reactive properties [1, 2]. In order to optimize the activated carbon properties for specific applications, large research efforts have been directed to introduce specific types of functional groups by choosing the most suited precursor, activation procedure or *ad-hoc* post-activation treatments. Several different types of functional groups can be present and will be discussed in the following.

3.1.1. O-containing functional groups

Oxygen is the most frequent heteroatom in activated carbons and related materials, and can be present in a wide range of different functional groups, such as ethers, lactones, anhydrides, carboxylic acids, ketones, lactols, pyrones, ethers and quinones [3]. A sketch of the listed functional groups is reported in Figure 3. 1.

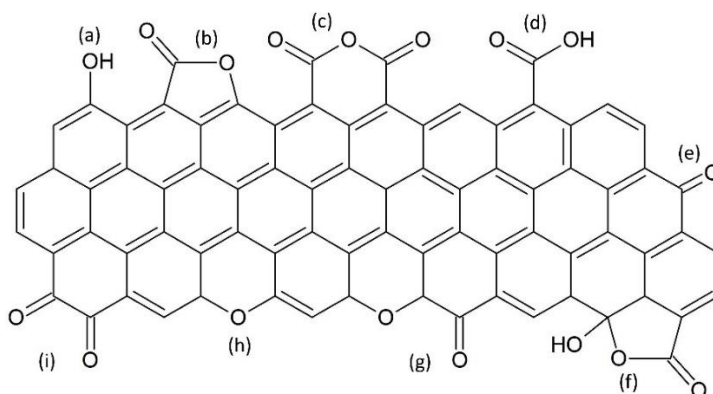


Figure 3. 1: main oxygen-containing functional groups observed in activated carbons: (a) phenols, (b) lactones, (c) anhydrides, (d) carboxylic acids, (e) ketones, (f) lactoles, (g) pyrones, (h) ethers, (i) quinones.

The carbon basal plane shows a low polarity and a mostly hydrophobic character that limits the efficiency in the absorption of water and other polar molecules. The oxidation of the carbon, instead, introduces hydrophilic O-containing functionalities on the surface that increase its overall polarity. This modification is able to increase the affinity of activated carbons to adsorbates such as water, polar organic molecules or metal ions, with important repercussions on their applications as adsorbents [1, 4-6]. The polarity of the carbon can also play a fundamental role in the field of catalysis, since it was proven to influence the yield of a target reaction. In the work by Lazzarini *et al* [7], it was shown that polar carbon supports enhance the hydrogenation activity of Pd/C catalysts toward polar substrates, while they are detrimental in the hydrogenation of nonpolar ones, and vice-versa.

Several methods have been proposed to introduce O-containing functional groups in carbon-based samples, but all of them can be considered as controlled oxidation processes. In the literature both dry oxidation treatments in air [8], O₂ [9] or stronger oxidising gases such as O₃ [10] were proposed, as well as liquid oxidations performed in solution of HNO₃ [8, 9, 11], H₂O₂ [9], (NH₄)₂S₂O₈ [12, 13] and many others. It was observed that the distribution of functional groups varies in function of the chosen oxidative reaction. For example, it has been reported that HNO₃ introduces acid functionalities and reduces the basic ones, while O₃ introduces acidic sites without altering the basic ones [14].

3.1.2. Functional groups containing other heteroatoms

Other heteroatoms can be present in activated carbons, or can be introduced following specific treatments. The second most studied heteroatom in carbonaceous materials is probably nitrogen. Due to the wide range of possible oxidation states of the N atom (from -3 to +5), there are many possible nitrogen based functional groups in carbonaceous materials, as highlighted in the sketch shown in Figure 3. 2. The introduction of N in activated carbons is particularly interesting for those applications requiring basic surface functional groups (such as amines or pyridine), which show stronger adsorption of acidic compounds such as CO₂ [15, 16] or of metal ions [17]. Nitrogen can be introduced by reaction with N-containing compounds: for example, NH₃ can be used to generate amides, imines, lactames, pyridines or pyrroles (depending on the temperature) [18, 19], while HNO₃ in a strong acid solution has been proposed to introduce nitro groups [20]. An alternative route may consist in the direct use of a N-containing precursor for the preparation of the carbon [15, 21].

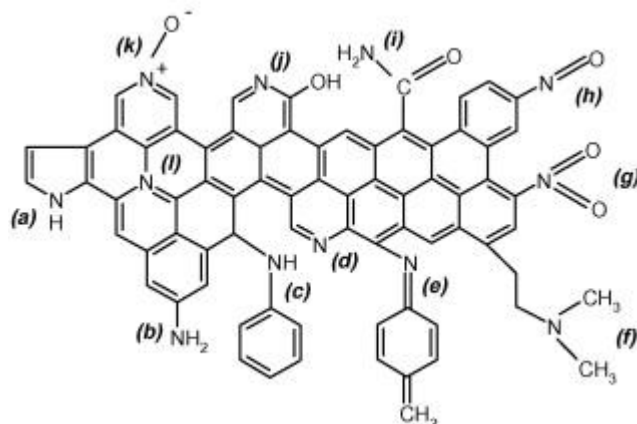


Figure 3. 2: summary of the main N-containing functional groups that can be found in an activated carbon, as reported in reference [22]: (a) pyrrole, (b) primary amine, (c) secondary amine, (d) pyridine, (e) imine, (f) tertiary amine, (g) nitro, (h) nitroso, (i) amide, (j) pyridone, (k) pyridine-N-oxide, (l) quaternary nitrogen.

Sulphur is another heteroatom often observed in activated carbons, since it is commonly present in lignocellulosic precursors of wood or peat and traces of it can remain in the activated carbons. On the other hand, the introduction of these functionalities was proposed for specific applications: for example, the reaction of carbons with H_2S was proposed as a method to produce a material for Hg^{2+} removal from water [23].

Another heteroatom found in activated carbons is phosphorous, since it is present in all living matter and thus in any lignocellulosic precursor. However, the most common origin of P-containing functional groups is the chemical activation procedure with H_3PO_4 , which is known to introduce a non-negligible amount of these functional groups within the carbon sample [24].

3.1.3. Characterization techniques

The identification and quantification of functional groups in carbon-based materials acquires a pivotal importance when optimising their properties for specific applications. Several different techniques have been proposed for their characterization, each one exhibiting strengths and drawbacks.

- **Boehm titration** [25, 26]: this method allows for the precise quantification of all the functional groups exhibiting acid (carboxylic acids, phenols, lactones, anhydrides) or basic (quinones, pyrones) properties and for their classification on the base of the acidic strength. However, it is blind to neutral species.
- **FT-IR spectroscopy** [7, 26, 27]: the vibrations of O-containing functional groups have strong dipole moments and, consequently, give origin to strong IR absorptions, making in principle FT-IR spectroscopy a solid technique to identify these functionalities. However, activated carbons show a very strong infrared absorption in the whole Mid-IR region and uneven light scattering, which make the measurement very challenging. Better results can be obtained in DRIFT mode, which however does not allow a quantitative evaluation.
- **XPS** [28]: this technique measures the electronic binding energy of the core electrons, providing details about the elemental composition of the investigated material and the oxidation states of each element. Upon deconvolution of the signals characteristic for C and O it is possible to get quantitative information about an activated carbon composition and also to discriminate among different functional groups. On the other hand, due to the low penetration of the electrons probing the material, the obtained results are descriptive of the surfaces and not of the bulk.
- **Raman spectroscopy** [29]: it is a vibrational spectroscopy that demonstrated to be a particularly sensible tool for studying the extension of the aromaticity and the defectivity of carbonaceous samples. However, it is not very sensible toward heteroatoms-containing functional groups.
- **INS spectroscopy** [30]: this vibrational spectroscopy allows for a precise characterization of the terminal C-H groups at the edges of the aromatic domains in carbonaceous materials. It can also provide indirect

information about functional groups. Further details about the application of this technique to activated carbons will be reported in Chapter 4.

- **Magnetic resonances** [31]: Nuclear Magnetic Resonance (NMR) provides details about the chemical surroundings of nuclei such as ^1H , ^{13}C or ^{31}P . Nevertheless, the signals intensity is proportional to the concentration of the species in the samples, making it challenging to study traces species such as the heteroatoms-containing functional groups in activated carbons. Electronic Paramagnetic Resonance (EPR) instead provides important information about the unpaired spins in a sample, but it is almost blind to spin-free functional groups. In addition, both techniques suffer the presence of small traces of metal ions with spin $\neq 0$, often present in activated carbons mineral ashes.
- **Temperature Programmed Desorption** [8, 9, 32-34]: this techniques allows for the indirect identification and quantification of functional groups in an activated carbon by measuring their thermal decomposition products. Its application requires a careful study regarding the setup, the data analysis and the assignments.

In order to obtain a complete characterization of an activated carbon it is necessary to use several complementary techniques. In the past this approach was extensively employed in our group, in particular in the frame of the PhD thesis work of Dr. Andrea Lazzarini [7, 26, 35]. Several of the activated carbon samples under investigation in this work were thus characterized by means of DRIFT, Raman, INS, XPS, NEXAFS, N_2 physisorption, Boehm titration, XRD and NMR, providing a good general understanding about the structure and surface properties of the samples. However, a clear picture relative to the concentration and distribution of heteroatom-containing functional groups is still missing, and this is the reason why we decided to focus on the

characterization of these samples by TPD. This technique is thus going to be the main focus of the rest of this chapter.

3.1.4. Temperature Programmed Desorption of Activated Carbons: state-of-the-art

Temperature Programmed Desorption (TPD) technique has been widely employed for the study of species adsorbed at solids surfaces. The typical experiment consists in heating the sample following a controlled temperature ramp in an inert atmosphere, and in the real-time measurement of the gases desorbed from the surface. In the fields of surface science and catalysis this technique is often employed to study the energetic distribution of the active sites for adsorption, as low desorption temperatures correspond to weak interactions and vice-versa. For example, TPD has been employed to evaluate the acid sites distribution in zeolites by following the desorption of NH_3 [36], or to study the interaction of metal surfaces or nanoparticles with adsorbates such as H_2O or CO [37, 38].

In the case of activated carbons and related carbonaceous materials, instead, the controlled heating of the sample in inert atmosphere leads to the thermal decomposition of the heteroatoms-containing functional groups present at the surface, which are converted into gaseous products detectable by mass spectrometry (MS) or infrared spectroscopy (FT-IR). Since the direct identification and quantification of functional groups in activated carbons is not straightforward, as discussed in the previous Section 3.1.3, the TPD approach has become a popular alternative for their indirect characterization. In fact, each functional group thermally decomposes within a specific temperature range generating known gaseous products, whose identification and quantification is easier than the direct characterization of the original functional groups bonded to activated carbons.

For these reasons, TPD is nowadays a solid method for the identification and quantification of functional groups in carbonaceous materials.

The assessment of O-containing functional groups is the best-established methodology and is the main focus of the TPD measurements on carbonaceous systems and finds many examples in the literature. As a representative example of the application of the technique to activated carbons, the result of a TPD study from Figueiredo *et al* is reported in Figure 3. 3. The plots report the formation rates of the two main decomposition products (CO and CO₂) released by a series of activated carbons as a function of the temperature, comparing samples differing in their post-activation treatments [9]. It is immediately evident that the plots differ in the absolute amounts of the two decomposition products (integrated area), but also in the decomposition temperature (position of the peaks). These differences undoubtedly point to variations in the functional groups' nature and concentration. However, to interpret the data a method to univocally attribute each of these signals to specific functional groups is required.

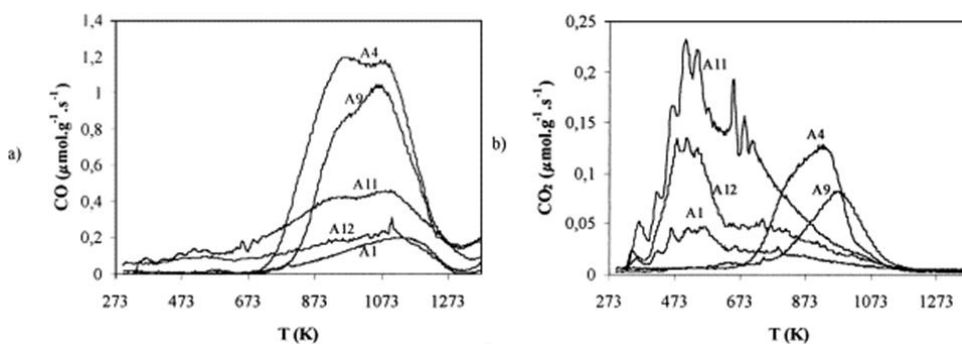


Figure 3. 3 example of the typical result of a TPD experiment on various activated carbons, taken from reference [9]. Part a) CO evolution curves; part b) CO₂ evolution curves. A1 is the parent activated carbon, while the other plots refer to samples oxidised following various post-activation treatments.

Assignment of CO and CO₂ Thanks to the seminal works of several research groups, among which Otake *et al* [8], de la Puente *et al* [32], Figueiredo *et al*

[9, 33] and Moreno-Castilla *et al* [34], a solid assignment of O-containing functional groups to specific gaseous products and decomposition temperatures was settled. To do so, they performed complementary measurements such as Boehm titration, DRIFT or XPS on activated carbons after their pyrolysis at various temperatures, to retrieve the decomposition temperature range of each functional group.

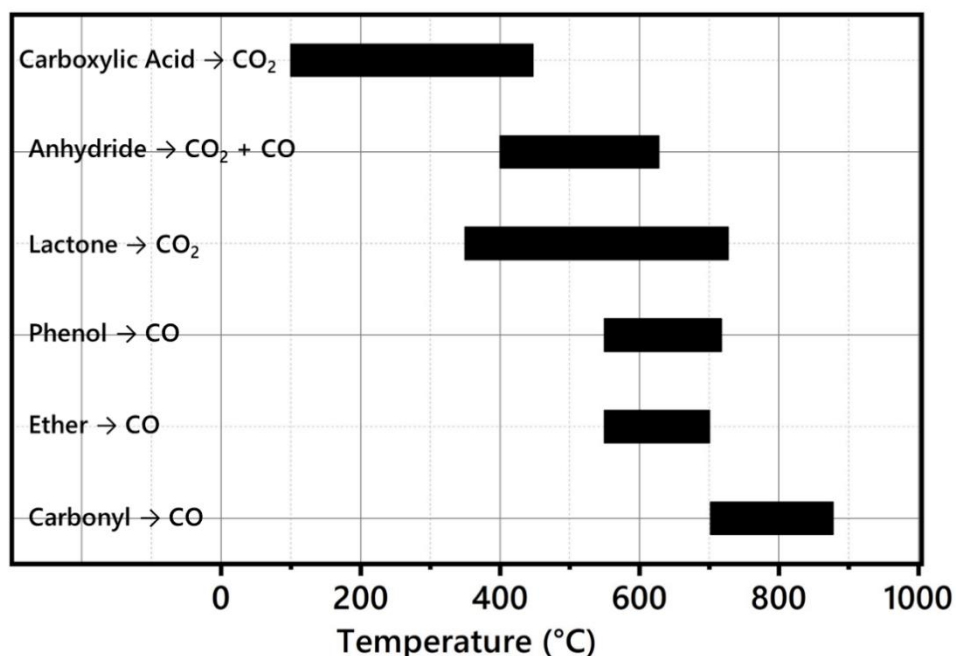


Figure 3. 4: main thermal decomposition reactions of O-containing functional groups in activated carbons and their temperature ranges, from references [8, 9, 32-34].

The main assignments of the gaseous products to functional groups are summarised in Figure 3. 4. It is possible to notice that:

- Carboxylic acids are the most thermolabile groups, as their decomposition is almost completed at about 400°C [8, 9, 32, 34]. Most of the early literature associates them with the release of CO₂ only but, more recently, alternative decomposition routes have been proposed. In particular, Li *et al* [12] observed the evolution of equimolar amounts CO

and H₂O at ca 240 and 330°C, concluding that these last products were the result of an alternative decomposition route for carboxylic acids. Similarly, Vivo-Vilches *et al* [39] observed the contemporary release of CO₂, CO and H₂O at ca 280°C, which was interpreted as the condensation of two vicinal carboxylic acid groups to an anhydride and to its immediate decomposition. In the earlier literature, the formation of CO at temperature lower than 400°C was often attributed to the decomposition of α -substituted carbonyl, following the proposition of Surygala *et al* in 1993 [40].

- Anhydrides and lactones are expected to decompose in an intermediate temperature interval, ranging from about 400°C to around 650°C [8, 9, 32, 33]. Anhydrides decompose to both CO and CO₂, while lactones to CO₂ only. On one hand the temperature range reported in Figure 3. 4 reflects the energetic heterogeneity of the considered functional groups, but on the other it also reflects possible mismatch of such ranges in literature. This is particular evident in the case of lactones, which are assigned to the 350-550°C range by de la Puente *et al* [32] and in the 627-727°C range by Figueiredo *et al* [33].

- Ethers and phenols are expected to decompose at temperature higher than 550°C forming CO [9, 33, 41]. Since they decompose within the same temperature range and form the same product, it is generally challenging to discriminate among them using TPD.

- Carbonyl-containing functional groups (such as ketones or quinones) decompose at the higher temperature, above 700°C [9, 32, 34].

Assignment of H₂O Water is generally observed during TPD experiments of carbonaceous materials, but rarely discussed in details. Signals at the very beginning of the TPD run, at temperatures lower than 200°C, are generally

attributed to the removal of weakly physisorbed water [13, 42]. The appearance of this signal can be avoided or strongly suppressed performing a pre-treatment of the sample in dynamic vacuum or in a flow of inert gas and/or by heating the sample at 150°C. More strongly bound H₂O molecules, such as the ones hydrogen-bonded to the functional groups, were also reported to desorb at higher temperatures (up to 400°C) [8, 13, 42]. Alternatively, water could also originate by a condensation reaction between two adjacent functional groups, such as two carboxylic acids giving an anhydride, a carboxylic acid and a phenol giving a lactone, or two phenols giving an ether [32]. It is also worth noticing that this last reaction would imply the conversion of thermolabile groups (carboxylic acids) into more thermoresistant ones (anhydrides and lactones), and this phenomenon should not be neglected when interpreting TPD results. Finally, H₂O is one of the products of the alternative decomposition paths for carboxylic acids proposed by Li *et al* [12] and Vivo-Vilches *et al* [39] previously discussed. Consequently, the evolution of H₂O observed in the low temperature range (T < 400°C) could also be attributed to the decomposition of these functional groups. The possibility of the condensation of vicinal groups and of the direct decomposition of carboxylic acids also underline that at least part of the H₂O released during a TPD run should be accounted for the total amount of O in the sample, together with CO and CO₂ [12].

Other heteroatoms Other heteroatoms, such as N or S, are known to thermally decompose into gaseous products detectable by a TPD approach, but the literature in this regard is much scarcer than in the case of O-containing functional groups. Some studies pointed out the evolution of NO, HCN, HCNO or C₂N₂ during the TPD run of N-containing carbons [18, 21, 43], or of SO₂ for S-containing samples [41], but a complete assignation of all functional groups to the corresponding thermal decomposition products is still missing.

3.2 Results and discussion

In the following, the results of the TPD-IR experiments performed on the activated carbons summarized in Table 2.1 in Chapter 2 will be reported and interpreted. Firstly, the main gaseous products identified by FT-IR and their origin will be commented. Secondly, the TPD plots of the main released gases (CO, CO₂, H₂O, CH₄ and NO) will be presented, allowing to point out important differences regarding the functional groups energetic distribution and decomposition rates. Finally, the total mass loss of the samples will be discussed and an evaluation of the functional groups concentrations will be proposed, pointing out significant differences in the distribution and amount of O-containing functional groups in different carbons.

3.2.1. Qualitative analysis

The measurement of high-resolution infrared spectra for each point of the TPD runs in static conditions allowed for the precise identification of several decomposition products, both the majoritarian and the minoritarian ones. Then, using the data analysis procedure described in Chapter 2, section 2.2.3, it was possible to calculate the moles of the released gases in correspondence with each infrared spectrum. The resulting TPD plots permitted to better visualize the temperature at which the thermal decomposition of functional groups was happening, and at which rate.

3.2.1.1. Physically activated carbons

The last acquired FT-IR spectra of the TPD-IR experiments for the four steam activated samples is reported in Figure 3. 5 for CwA and CwB, and in Figure 3. 6 for CpA and CpB. To ensure comparability among the samples, all the absorbance values were normalised to the sample mass.

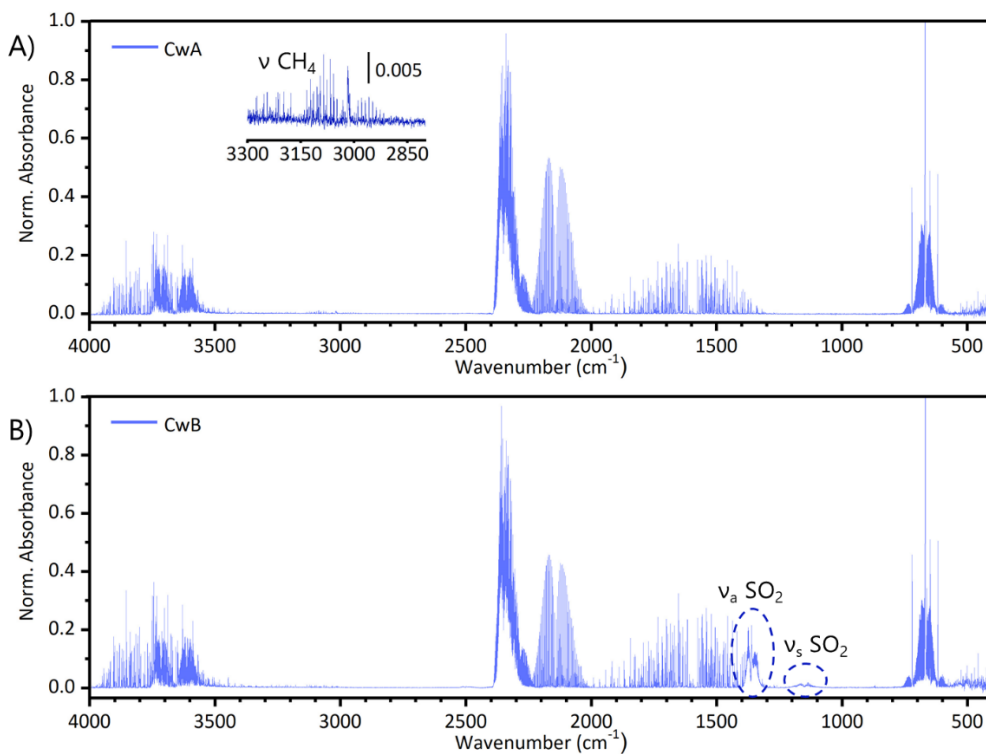


Figure 3. 5: Last infrared spectra recorded during the TPD run of CwA (part A) and CwB (part B). The absorbance values are normalised to the mass of measured sample. The weakest signals are magnified within an inset, and the peaks arising from species other than CO, CO₂ and H₂O are indicated.

The experiment was run accumulating the gaseous products inside the setup volume all along the TPD run, so that the last spectra contain the fingerprint of all the gases evolved during the experiment. It is immediately evident that the main decomposition products are CO, CO₂ and H₂O for all the samples, as expected for the decomposition of O-containing functional groups in carbonaceous materials. However, other gases are also observable in the spectra. The first additional gaseous product observed is CH₄ (3018 cm⁻¹) in the spectrum of CwA (Figure 3. 5A) and CpB (Figure 3. 6B), which appears at temperature above 600°C.

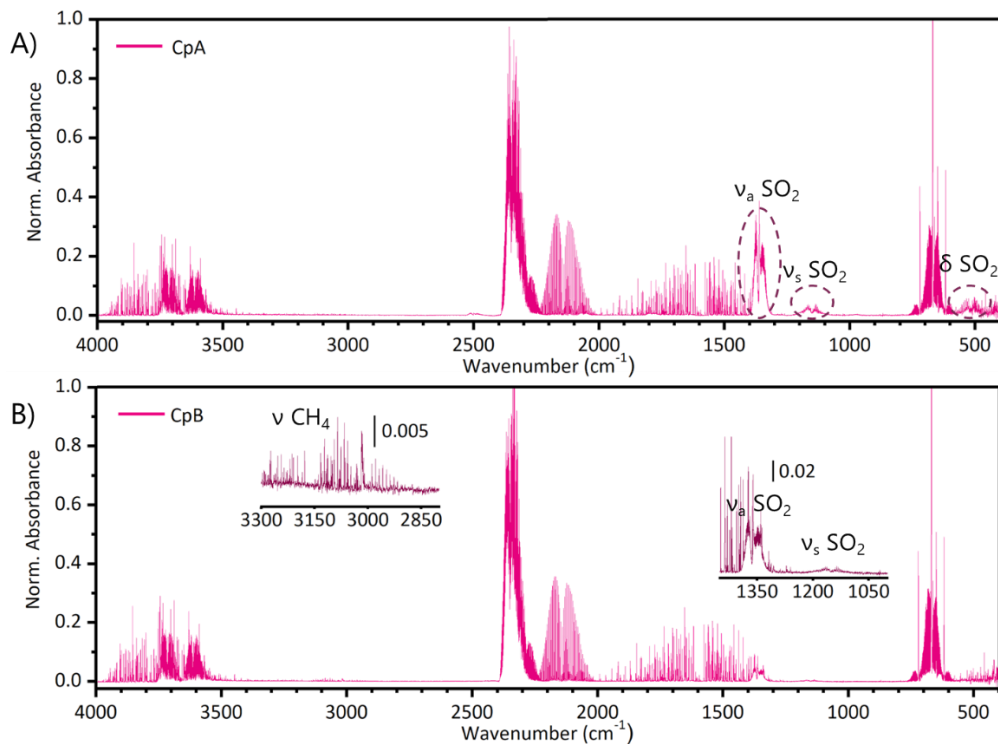


Figure 3. 6: Last infrared spectra recorded during the TPD run of CpA (part A) and CpB (part B). The absorbance values are normalised to the mass of measured sample. The weakest signals are magnified within an inset, and the peaks arising from species other than CO, CO₂ and H₂O are indicated.

These peaks show very low absorbance values, not useful for their quantification, and indicate the presence of low amount of not fully graphitised carbon in both these samples, most likely in the form of aliphatic terminations [44]. In addition, the spectra of CwB, CpA and CpB clearly present the characteristic IR peaks of SO₂ (Figure 3. 5B, Figure 3. 6A and B, respectively), which appear in the spectra at a temperature of about 400°C. These signals are quite intense and show three clear bands centred at 1361, 1150 and 518 cm⁻¹, but their quantification was not possible due to the lack of a reference pure gas to perform the calibration. Since these three samples are not expected to have undergone any treatment intended to introduce S-

containing functionalities, we attribute the formation of SO₂ to the natural content of sulphur in wood and peat [45].

The TPD plots for the Cw samples are reported in Figure 3. 7, and those of the Cp ones in Figure 3. 8. For all the samples, we can observe that the main decomposition product at low temperature is CO₂, with a peak centred at about 250°C. This peak is more pronounced for CwB, CpA and CpB than for CwA. CO₂ signals in this temperature range are assigned to the decomposition of carboxylic acid groups [8, 9, 32, 34], and the narrowness of the peak is connected to the energetic homogeneity of the sites. In parallel, we can also observe the presence of weaker CO and H₂O peaks centred at the same temperature. The release of CO at low temperature was proposed to be determined by the thermal decomposition of α -substituted carbonyls [40], while H₂O could be associated with strongly physisorbed water and/or to condensation reactions of vicinal functional groups [8, 32]. On the other hand, the contemporary release of the two gasses happening at the same temperature as CO₂ also appears in strong accordance with the alternative decomposition routes of carboxylic acid proposed by Li *et al* [12] and Vivo-Vilches *et al* [39] (as described in Section 3.1.4 of this chapter). However, the different amounts of moles do not fully support the proposed stoichiometry. In particular, H₂O always appear in excess in comparison with CO, making us hypothesise the contemporary occurrence of the alternative decomposition of carboxylic acids generating CO and H₂O and the release of strongly adsorbed water (for instance, the one H-bonded to the decomposing carboxylic acid groups) or the condensation of vicinal groups.

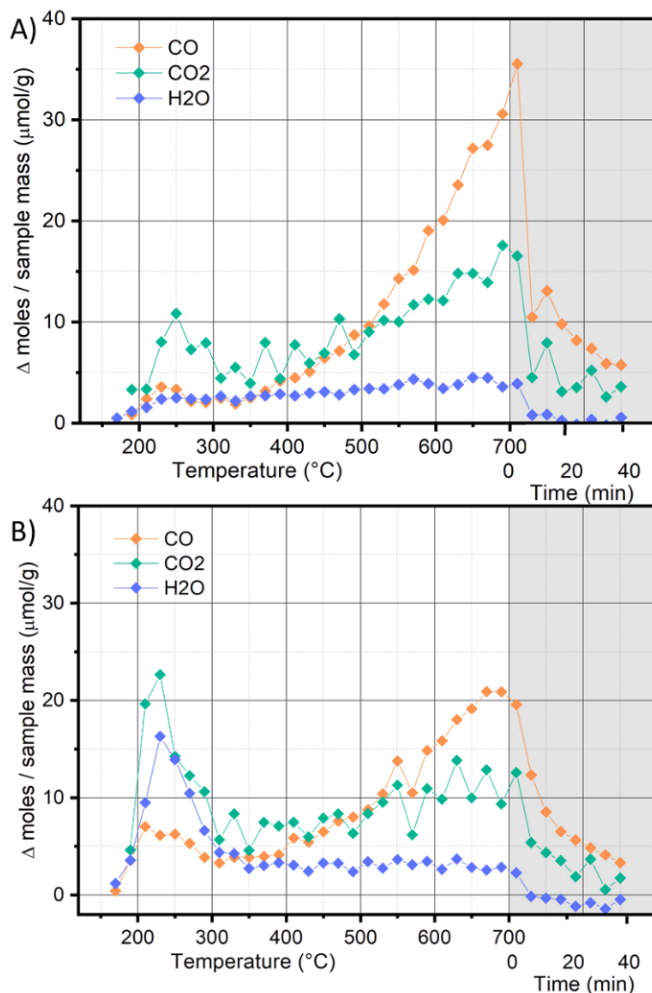


Figure 3. 7: differential TPD plots of CO, CO₂ and H₂O for the physically activated carbons of wood origin CwA (part A) and CwB (part B). The temperature ramp is on white background, while the isotherm at 700 $^{\circ}$ C on grey background.

For all the four samples, the thermal decomposition rate reaches a minimum at about 400 $^{\circ}$ C, followed by a steady rise in the formation rate of both CO and CO₂. In this high temperature range CO appears as the main decomposition product for the Cw samples, and in particular for CwA for which the amount of CO released at 700 $^{\circ}$ C is almost the double of CO₂ (Figure 3. 7A).

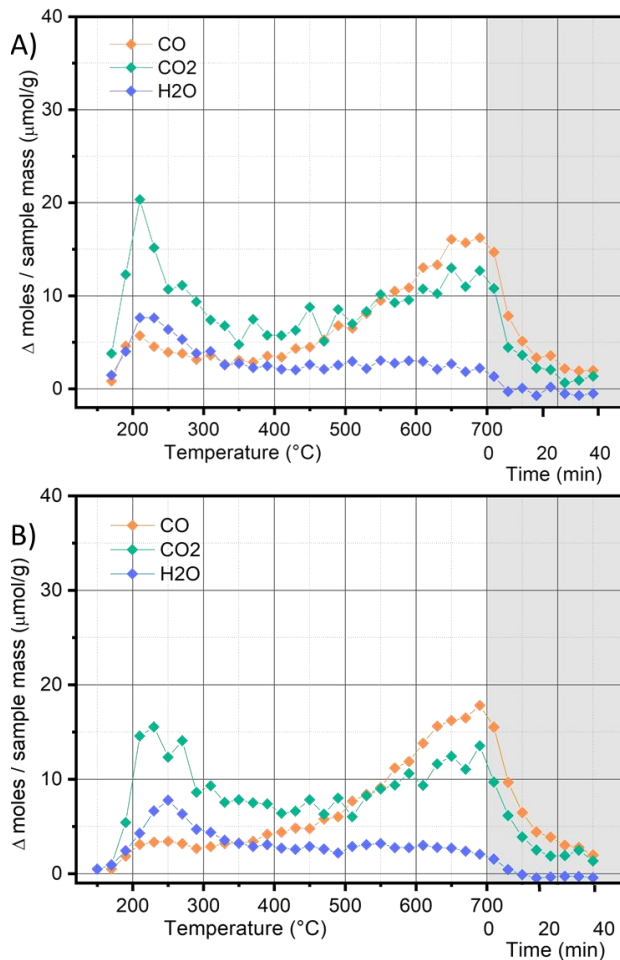


Figure 3. 8: differential TPD plots of CO, CO₂ and H₂O for the physically activated carbons of peat origin CpA (part A) and CpB (part B). The temperature ramp is on white background, while the isotherm at 700°C on grey background.

In the case of the Cp samples instead, CO remains the main decomposition product at high temperature, although its values is comparable to the CO₂ ones (Figure 3. 8).

The H₂O formation rate at temperature higher than 400°C is quite constant and low for all the four carbons. The formation of water in this interval can be explained in terms of the condensation of adjacent phenol

groups, and the very small amount suggest a low probability for such functional groups in vicinal position.

Further details about the kinetics of the processes involved can be gained by the analysis of the isotherm segment of the TPD run (intervals in grey backgrounds in Figure 3. 7 and Figure 3. 8). In fact, we can observe that the release rate of CO and CO₂ does not stop suddenly at the end of the temperature ramp, but needs about 20 minutes before approaching a stable value. This suggests that the thermal decomposition of functional groups is not a kinetically fast process, but some time is required before reaching the thermodynamic equilibrium. On the other hand, the signal of H₂O drops much more quickly, suggesting that the condensation of functional groups is a kinetically faster process.

3.2.1.2. Chemically activated carbon

The last infrared spectrum measured during the TPD run of Cchemi is reported in Figure 3. 9. Its features are similar to the ones observed for the steam activated samples, but the overall intensity of the mass-normalised spectrum is about the double of the previous ones. This observation already hints to an overall higher concentration of functional groups for Cchemi than for the physically activated samples.

In this spectrum, we could clearly observe the bands characteristic of CH₄ (at 3018 and 1306 cm⁻¹) for which, in this case, a quantification was possible. The formation of relevant amounts of CH₄ was attributed to the presence of a relatively large not-graphitic fraction within the sample, most likely in the form of aliphatic side chains [44]. The largest amount of CH₄ in comparison with the physically activated samples is explained considering the lower temperature of activation for this sample, leading to an only partial graphitization of the carbon.

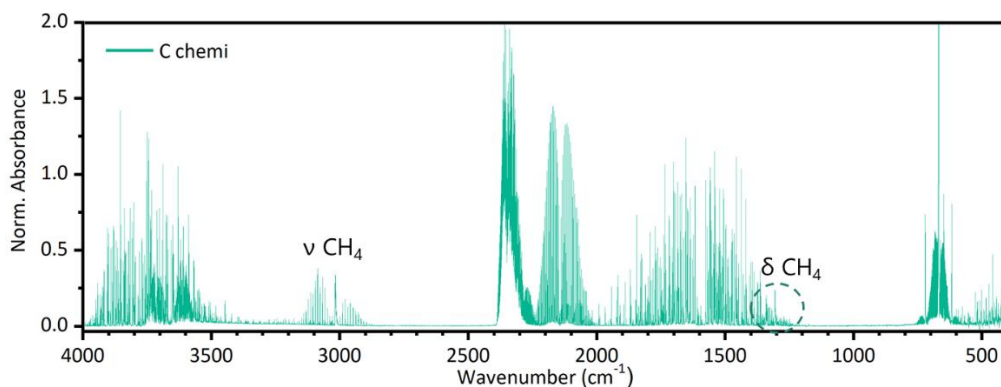


Figure 3. 9: Last infrared spectrum recorded during the TPD run of Cchemi. The absorbance values are normalised to the mass of measured sample. The peaks arising from species other than CO, CO₂ and H₂O are indicated.

The TPD plot for the Cchemi sample is shown in Figure 3. 10. The profiles of CO and CO₂ strongly resemble the one of CwA (Figure 3. 7A), apart from the absolute scale which is about three times larger as a consequence of the larger concentration of functional groups. The other main difference is the TPD plot of H₂O, that this time is released at an amount comparable to CO₂. Also in this case we can observe the contemporary formation of CO and H₂O at temperature lower than 400°C, and thus the alternative decomposition route for the carboxylic acids seems likely also for this sample [12, 39]. The excess of H₂O in the low temperature interval could be explained in part by the desorption of strongly adsorbed water. However, the phenomenon that better explains the evolution of H₂O all over the experiment is the condensation of vicinal functional groups, which appears particularly important in the 550-700°C range in this case. The comparison of the H₂O TPD plots pointed out that for Cchemi condensation reactions are much more likely than for CwA, which suggests a higher probability of functional groups in vicinal positions, and thus a higher occupancy of the carbon platelets borders.

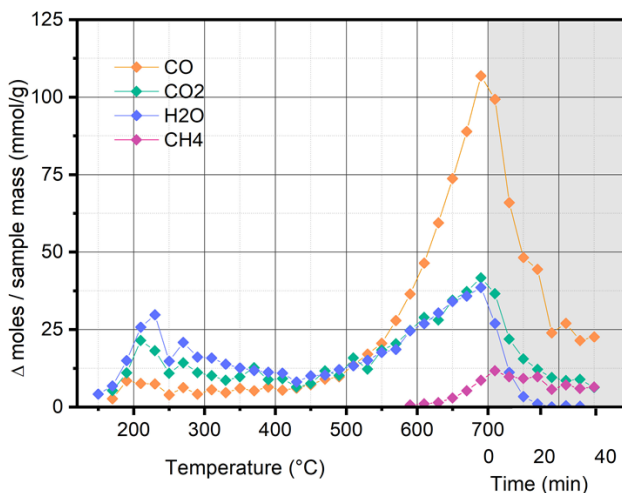


Figure 3. 10: differential TPD plots of CO, CO₂, H₂O and CH₄ for the chemically activated sample Cchemi. The temperature ramp is on white background, while the isotherm at 700°C on grey background.

The other distinctive aspect of the Cchemi TPD plot is the evolution of CH₄, clearly visible starting from 600°C. As previously commented, its formation is attributed to the graphitization processes underwent by the aliphatic fraction of the sample, triggered by a temperature higher than the activation one. From the TPD plot shown in Figure 3. 10, we can clearly observe that its formation rate increases starting from 600°C, and also that the rate seems to remain almost stable during the isotherm segment of the experiment (grey background in Figure 3. 10). This indicates that the kinetic of the graphitization reaction is very slow in comparison with the other processes, and that the thermodynamic equilibrium was not yet reached at the end of the experiment.

3.2.1.3. Oxidised carbons

The last infrared spectra measured during the TPD run of CwA-ox and Cchemi-ox are reported in Figure 3. 11A and B, respectively. A significant increase of the mass-normalised absorbance values of about five times is observed in comparison with their parent carbons. This modification in the

spectral intensities evidently points to the effectiveness of the oxidative treatment with HNO_3 in introducing O-containing functional groups in the carbon [8, 9, 11].

By analysing the spectra more carefully, it can be noticed that many new weak bands appeared in both spectra since the very beginning of the experiment. More in details, we observed for both samples the characteristic signals for NO (1875 cm^{-1}), N_2O (2223 and 1285 cm^{-1}) and NO_2 (1615 cm^{-1}), while for Cchemi-ox also HCN is clearly visible at 3310 cm^{-1} . An extra signal, centred at about 1370 cm^{-1} , is observed in the case of Cchemi-ox, but it was not possible to unambiguously assign it to a specific species.

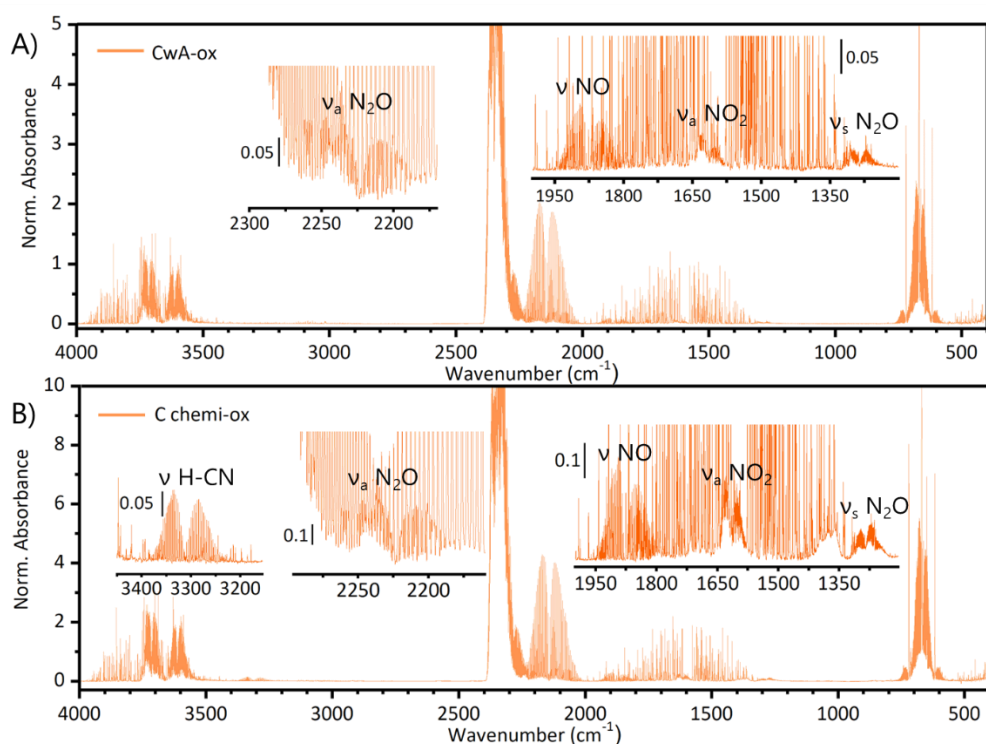


Figure 3. 11: Last infrared spectra recorded during the TPD run of CwA-ox (part A) and Cchemi-ox (part B). The absorbance values are normalised to the mass of measured sample. The weakest signals are magnified within an inset, and the peaks arising from species other than CO , CO_2 and H_2O are indicated.

The evolution of NO_x and HCN clearly indicates that the oxidative treatment in HNO_3 does not only introduce O-containing functionalities in the sample, as commonly assumed in the literature, but a certain amount of N are introduced as well. In the case of NO, which is the main NO_x released by both samples, the quantification was also possible. That allowed to partially estimate the amount of N introduced in the samples, evaluated to be at least 0.15% w/w for CwA-ox and 0.47% w/w for Cchemi-ox. Hence, the amount of N-containing functionalities introduced in the carbons are not negligible, but their concentrations is generally low. Finally, from the analysis of the FT-IR spectra, it is also possible to observe that the CH_4 signal disappears from the spectrum of Cchemi-ox, despite the fact that it was observed in the case of the parent carbons. This observation suggests that the aliphatic component responsible for the evolution of CH_4 was removed by the oxidative treatment in HNO_3 [46].

The TPD plots for the two oxidised samples are reported in Figure 3. 12. By the visual comparison with the parent carbons CwA (Figure 3. 7A) and Cchemi (Figure 3. 10), the changes in both the TPD profiles and the intensities is striking. The biggest modification is observed at temperatures lower than 400°C , where a considerable release of CO_2 is observed, while CO and H_2O are produced to a lower extent. Being the region of the carboxylic acids decomposition [8, 9, 32, 34], we deduce that the treatment in HNO_3 effectively introduced large amounts of these functional groups within the samples. The broadness of these signals in comparison with those observed in the spectra of their parent carbons also suggests a greater energetic heterogeneity of the introduced carboxylic acid groups. The fact that the TPD curves of CO and H_2O are very similar in this interval for both samples suggests that the alternative decomposition routes for the decomposition of carboxylic acids [12, 39] is significant in this interval.

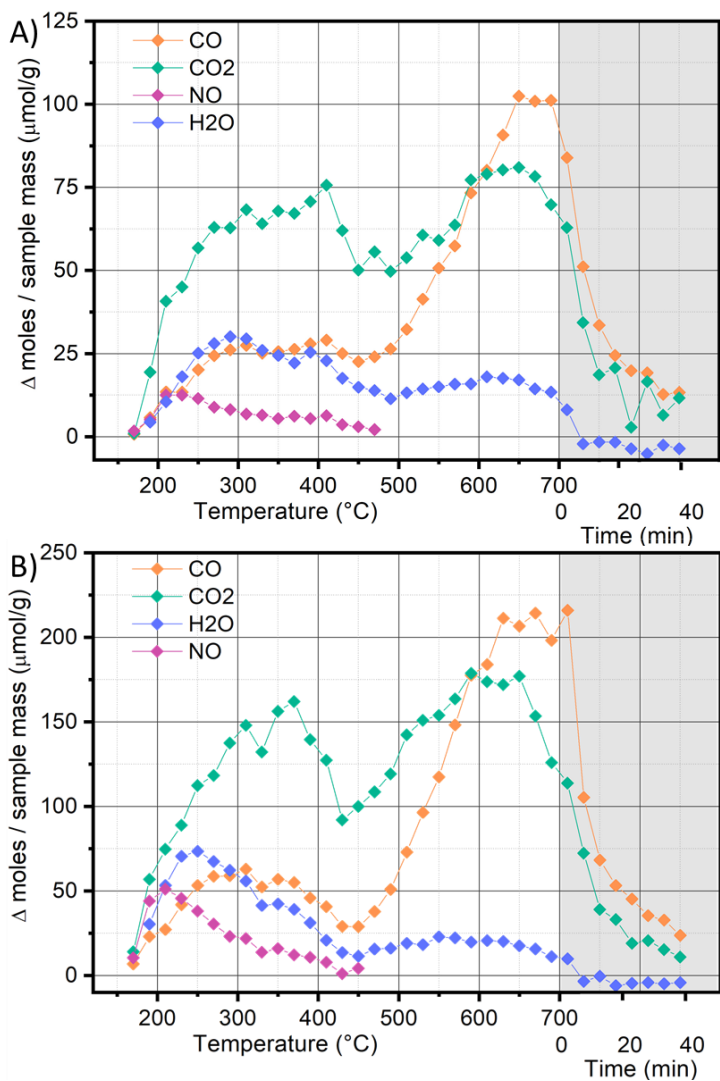


Figure 3. 12: differential TPD plots of CO, CO₂, H₂O and NO for the carbons oxidised in HNO₃ CwA-ox (part A) and Cchemi-ox (part B). The temperature ramp is on white background, while the isotherm at 700°C on grey background.

The TPD plots also show that the evolution of NO, associated with the decomposition of N-containing functionalities, reaches its maximum at very low temperatures (ca 200°C). We are not yet able to assign this signal to a specific functional group, but the TPD suggest that it is some kind of thermolabile N-containing group.

Both the TPD plots show a minimum at about 450°C, followed by a steady rise of the release of both CO and CO₂, with the former reaching a plateau at about 650°C and the latter a maximum at about 620°C. This indicates that the oxidative treatment in HNO₃ also introduced important amounts of more thermoresistant O-containing functional groups, such as lactones, anhydrides, phenols and ethers. The discussion about the assignation of the data contained in the TPD plots to specific functional groups will be done later in Section 3.2.3.

3.2.2. Evaluation of secondary reactions

Some further difficulties in the interpretation of TPD results could arise from the possibility of secondary reactions involving the gaseous decomposition products CO and CO₂ [8, 47]. The main secondary reaction proposed in the literature is:



where C(O) is an O-containing functional group at the activated carbon surface and C_f is a free carbon termination. This kind of reaction would alter the ratio between CO and CO₂ along the TPD experiment, affecting the interpretation of the data. The reaction is expected to take place inside the carbon pores, and thus is less important for samples exhibiting a low porosity [47]. Secondary reactions were also reported to be minimised when performing the experiment at reduced pressure (25 torr) instead of ambient pressure [48], which is the condition adopted in our experiments.

In case of a significant effect of secondary reactions, the final ratio between CO and CO₂ at the end of the experiment is expected to change as a function of the heating rate [8, 47, 48]. To verify this, we decided to repeat the TPD run on three representative activated carbons (CwA, Cchemi and

Cchemi-ox) with a temperature rate of 15°C/min instead of 5°C/min. The obtained results are compared in Figure 3. 13. We can observe that, in all the cases, the three TPD runs at 15°C/min are extremely similar to those at 5°C/min, apart from a slight shift at higher temperatures of the TPD measured at 15°C/min, which we ascribe to the diffusion time of the gasses from the sample to the IR cell. At first sight, also the first point of the isotherms is much higher for the TPD at 15°C/min, but this difference only depends on the frequency in the spectra collection in the two cases. Finally, it was also possible to compare the final ratio CO/CO₂ as obtained from the TPD at the two heating rates for all the three samples, as shown in Table 3. 1. Also in this case, the differences are minimal.

Table 3. 1: comparison on the final ratio CO/CO₂ at the end of the TPD run at 5°C/min and 15°C/min for CwA, Cchemi and Cchemi-ox.

Carbon	CO/CO₂ 5°C/min	CO/CO₂ 15°C/min
CwA	1.28	1.29
Cchemi	1.64	1.54
Cchemi-ox	0.77	0.79

We thus concluded that secondary reactions were negligible during our TPD-IR experiments. However, we cannot conclude whether this effect is a consequence of the intrinsic nature of the samples, of the instrumental setup, or both. However, the observation appears compatible with the previous reports in the literature, as secondary reactions were reported to be less severe when working at low pressures, such as in the case of our setup [48].

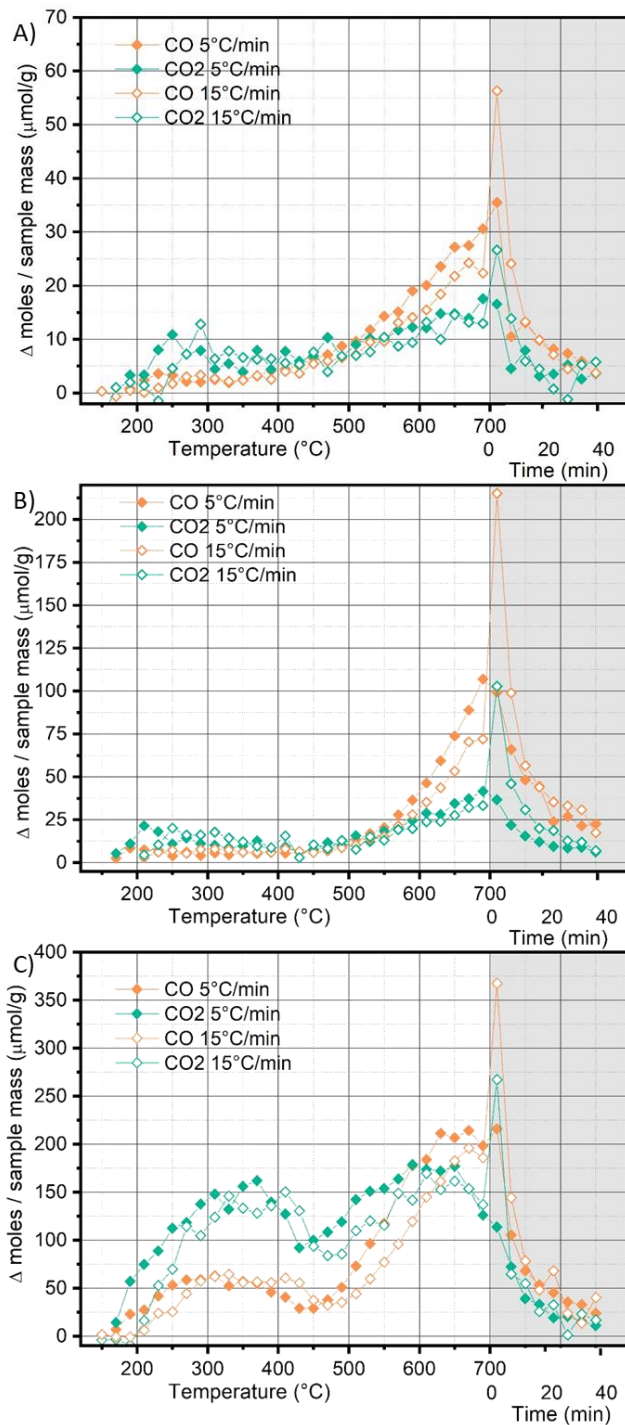


Figure 3. 13: Comparison between the TPD run at 5°C/min (full dots) and 15°C/min (empty dots) for CwA (partA), Cchemi (part B) and Cchemi-ox (part C).

3.2.3. Quantitative analysis

3.2.3.1. Mass loss

By weighting the samples before and after each TPD experiment, it was possible to calculate the mass lost by the samples during the TPD run. Additionally, from the quantification of the released CO, CO₂, H₂O, CH₄ and NO it was possible to calculate the mass percentage corresponding to the evolution of each of these species. A residual mass loss, not attributed to the gases measured during the TPD run, is still present, and it is mostly due to the physisorbed water removed during the samples' activation prior to the TPD experiment. Still, part of it must be ascribed to the not quantified species such as SO₂ or the other N-containing compounds. A summary of these results is reported in Table 3. 2.

Table 3. 2: mass lost during the TPD experiments for each carbon, expressed as wt% of the initial mass of the sample. The table reports the total mass lost and the fraction explainable in terms of the quantified CO, CO₂, H₂O, CH₄ and NO release. The "Others" column contains the fraction of the total lost mass not explained in terms of quantified species, and comprehends the physisorbed water removed during the activation phase and of the not-quantified species such as SO₂ or the other N-containing compounds.

CARBON	Mass lost (wt % on the initial sample mass)						
	total	CO	CO ₂	H ₂ O	CH ₄	NO	Others
CwA	6.0	1.0	1.2	0.3	-	-	3.5
CwB	9.3	0.8	1.3	0.4	-	-	6.8
CpA	12.6	0.6	1.2	0.3	-	-	10.5
CpB	8.9	0.7	1.2	0.3	-	-	6.8
Cchemi	13.6	2.7	2.5	1.7	0.1	-	6.6
CwA-ox	23.2	3.8	7.9	1.4	-	0.3	9.8
Cchemi-ox	41.7	8.2	16.8	2.5	-	1.0	13.2

For the steam-activated carbons the mass loss is generally modest, ranging between 6.0% for CwA to 12.6% for CpA. The fraction of mass loss not explained by the decomposition of functional groups is relatively high, and it is attributed to the physisorbed water and to the decomposition of S-containing functionalities into SO_2 , which was not quantified.

For Cchemi, instead, the total mass lost is about 1.5 times higher than the average observed for the physically activated carbons. The main difference lies in the distribution of the lost masses between the quantified products. In fact, the relative values of physisorbed water are comparable to the previous ones, while the mass loss associated with CO, CO_2 and H_2O is almost three times higher.

Finally, for the HNO_3 treated samples, the mass loss increased considerably, reaching the 41.7% in the case of Chemi-ox. The greatest increase was observed for the quantified decomposition products (CO, CO_2 and H_2O), compatibly with a massive introduction of O-functionalities.

3.2.3.2. Quantification of functional groups

With the data reported in the TPD plots in Section 3.2.1, it was possible to calculate the amount of gases released per gram of sample in three main temperature intervals ($T < 400^\circ\text{C}$, $400^\circ\text{C} < T < 560^\circ\text{C}$ and $T > 560^\circ\text{C}$), whose results are reported in Table 3. 3. This was the starting point for the evaluation of the concentration of functional groups in each sample, on the base of the general assignments discussed in Section 3.1.4. The results are summarised in Figure 3. 4 and discussed in the following.

Table 3. 3: amounts of gases released by the seven activated carbon in the $T < 400^{\circ}\text{C}$, $400^{\circ}\text{C} < T < 560^{\circ}\text{C}$ and $T > 560^{\circ}\text{C}$ temperature intervals.

	AMOUNT OF DECOMPOSITION PRODUCTS ($\mu\text{mol/g}$)											
	$T < 400^{\circ}\text{C}$				$400^{\circ}\text{C} < T < 560^{\circ}\text{C}$				$T > 560^{\circ}\text{C}$			
	CO	CO ₂	H ₂ O	NO	CO	CO ₂	H ₂ O	NO	CO	CO ₂	H ₂ O	CH ₄
CwA	29	68	28	-	68	67	26	-	259	144	35	-
CwB	52	116	80	-	66	65	24	-	185	107	19	-
CpA	43	117	53	-	48	60	20	-	136	103	16	-
CpB	35	111	53	-	51	58	22	-	151	108	18	-
Cchemi	70	152	207	-	89	92	98	-	793	335	249	89
CwA-ox	238	630	246	92	252	467	123	15	864	703	100	-
Cchemi-ox	546	1345	581	321	474	994	138	13	1920	1469	110	-

- **Temperature < 400°C:** In this interval, the decomposition of carboxylic acids to CO₂ is the main expected reaction [6, 7, 31, 33], but an alternative decomposition path with formation of CO + H₂O [12] or their condensation and immediate decomposition to CO₂ + CO + H₂O [39] were also proposed. We thus calculated the total concentration of carboxylic acids as the sum of the $\mu\text{mol/g}$ of CO and CO₂ released at temperatures lower than 400°C. The amount of H₂O is in excess with respect to CO for all the samples except for CwA (for which the values are almost the same), so it cannot be fully explained in terms of the decomposition of functional groups. The excess of H₂O in this range was thus explained as the desorption of strongly physisorbed water and/or the condensation of vicinal functional groups.
- **400°C < T < 560°C:** In this temperature range, only the decomposition of lactones to CO₂ and the one of anhydrides to CO + CO₂ are expected [8, 9, 32, 33]. It is thus possible to evaluate the amount of anhydrides decomposed in this range as equal to the $\mu\text{mol/g}$ of CO, while lactones correspond to the difference between the total amounts of CO₂ and CO.

We can notice that the concentration of lactones evaluated in this range varies among the classes of samples, being almost negligible for CwA, CwB, CpA, CpB and Cchemi, and having similar concentrations to anhydrides for CwA-ox and Cchemi-ox. All the H₂O evolved in this interval is attributed to the condensation of adjacent functionalities.

- **$T > 560^{\circ}\text{C}$** : as shown in Figure 3. 4, in addition to the decomposition of anhydrides and lactones, also the decomposition of phenols and ethers to CO is expected in this temperature range [9, 32, 33]. The problem corresponds to a linear system of two equations and four variables, for which an exact solution is not possible. In order to evaluate the concentration of functional groups is thus necessary to introduce some reasonable approximation. First of all, phenols and ethers decompose in the same temperature range releasing the same product, making it impossible to distinguish them. Consequently, the two of them were evaluated together as a single variable. The second approximation instead is based on the observed amounts of lactones calculated in the previous temperature interval. Since their amount was close to zero for the physically and chemically activated samples, the concentration of lactones was set to zero in the high temperature range for CwA, CwB, CpA, CpB and Cchemi. In the case of the oxidised samples instead the concentration of lactones in the previous interval was comparable to the one of anhydrides, and so for CwA-ox and Cchemi-ox the amounts of anhydrides and lactones released at $T > 560^{\circ}\text{C}$ were constrained to be equal. The H₂O released in this interval was attributed to the condensation of vicinal functional groups, most likely the thermoresistant phenols.
- **$T > 700^{\circ}\text{C}$** : our experiments were stopped at 700°C, so it was not possible to observe decomposition of ketones and quinones which is expected to start from this temperature [9, 33, 34].

The functional groups concentrations obtained with this procedure are shown in Figure 3. 14A. The difference in total concentration of functional groups among the samples is striking, with the steam activated carbons showing the lowest concentrations, which increases passing to the chemically activated carbons and even more so for the oxidised ones. Albeit the low concentrations, the differences among the physically activated carbons are clear, as displayed by Figure 3. 14B. The most different sample is CwA, for which the highest concentration is observed for anhydrides, followed by ethers + phenols and then carboxylic acids. For CwB, CpA and CpB instead anhydrides and carboxylic acids present similar concentrations. The phenols and ethers' concentration is comparable for CwA and CwB, and it is lower for CpA and CpB. The concentration of lactones is very low for all these samples, but the value is slightly higher for the Cp carbons than for the Cw ones. The amount of released H₂O assigned to the condensation of vicinal groups is relatively small for all the steam activated samples, and in particular for the Cp ones, indicating a general distancing among the functionalities and low chances for groups in adjacent position.

The chemically activated carbon Cchemi instead exhibits a sensibly higher concentration of functional groups (Figure 3. 14A). In this case the most present functional groups are phenols and ethers, followed by carboxylic acids and anhydrides at similar values. Also in this case the amount of lactones is negligible. Cchemi is also the sample which released the highest amount of H₂O generated by the condensation of vicinal groups, even higher than for the oxidised samples, indicating high chances for vicinal functional groups.

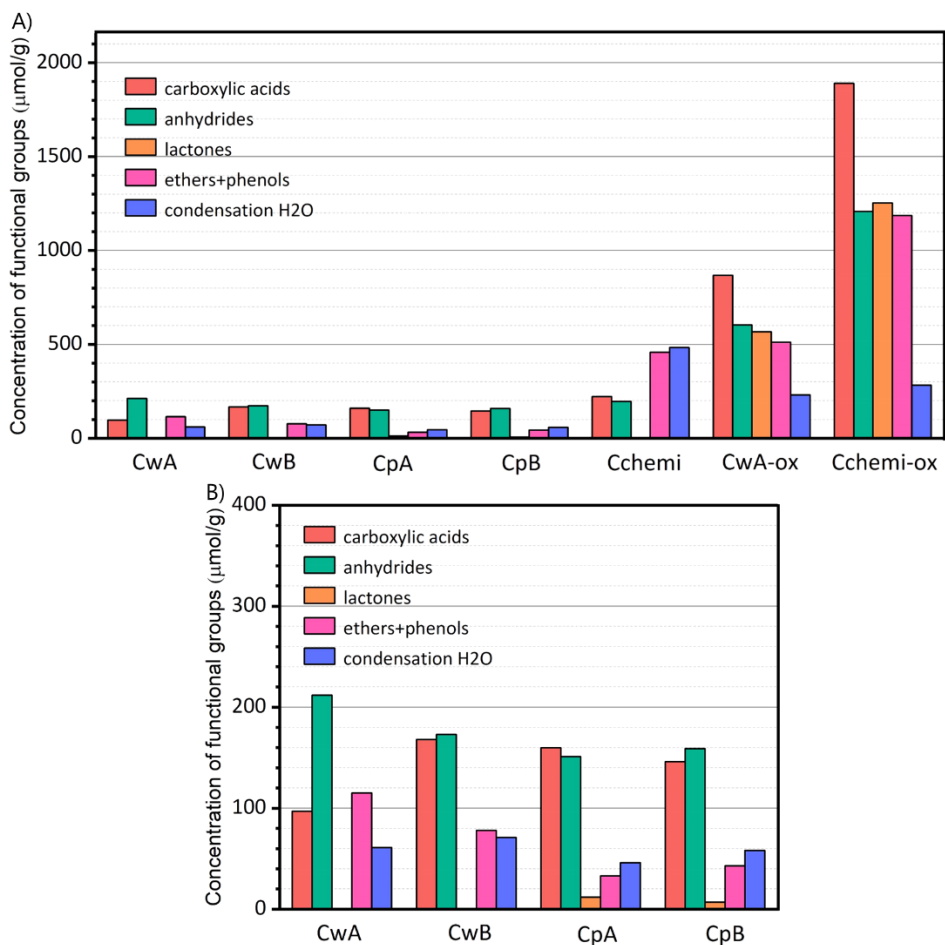


Figure 3. 14: A) evaluated concentrations of functional groups in the seven activated carbon samples. B) Detail over the physically activated carbon samples.

The oxidative treatment in HNO_3 strongly increased the concentration of functional groups and changed their relative distribution, as evident when comparing the TPD results of CwA with CwA-ox and of Cchemi with Cchemi-ox in Figure 3. 14A. In both cases the total amount of functional groups was about 6 times higher, with similar ratios for all the functional groups, indicating that the effectiveness in creating new O-containing functionalities was comparable for the two samples. The absolute difference in concentration of the two series of samples could be explained in terms of a variation in the

dimension of the graphenic domains, smaller for Cchemi than for CwA [26], which would reflect in the amount of available terminal sites for the formation of functional groups. Regarding the distribution of the functional groups, in this case the principal ones are carboxylic acids, followed by anhydrides, lactones and phenols + ethers at similar values. The values of released H₂O are small in relation to the concentration of the other functional groups, indicating that the functional groups that may undergo condensation are unlikely to sit in adjacent positions.

3.3. Conclusions

The application of TPD-IR allowed us to enlarge our previous knowledge about a wide range of activated carbons employed as catalytic supports, providing important details about the nature and the concentration of functional groups.

The development of a TPD setup centred around the accumulation of the decomposition products and their measurement by FT-IR spectroscopy demonstrated to be a winning strategy, allowing to identify precisely all the decomposition products, even at traces levels, and at the same time to quantify the main products with high precision. From the data collected during the TPD experiment, it was also possible to evaluate the nature and the concentration of the O-containing functional groups in all the activated carbons.

For the steam activated carbons, a low concentration of functional groups was generally observed, with anhydrides and carboxylic acids being the most present at similar amounts for most of them, apart from CwA for which anhydrides were the main group. Phenols and ethers are present at slightly higher concentrations for the Cw samples, while lactones are rare for all of them. Traces of CH₄ were observed for CwA and CpB, indicating the

presence of a small residual aliphatic fraction in the samples. The release of SO_2 was observed for the all of them apart CwA, pointing out the presence of small amounts of S intrinsic of the precursors of these samples.

The chemically activated carbon contains a higher concentration of functional groups than the steam activated ones. This can be partly explained in terms of a smaller size of the aromatic platelets and of the consequent higher availability of border terminations, but the greater chances for the condensation of vicinal functional groups also suggest a higher occupancy of the borders. The relative distribution of the functional groups also appears different, with phenols and ethers being the most present in the case of Cchemi. The presence of a non-negligible aliphatic fraction is indicated by the evolution of CH_4 above 600°C .

The oxidation treatment in HNO_3 introduced sensible amounts of O-containing functional groups, in particular carboxylic acids and lactones, but also the presence of tiny amounts of N-containing ones is clearly indicated by the evolution of NO , NO_2 , N_2O and HCN , among which NO was also quantifiable.

The better understanding of the amounts and the typologies of functional groups in the investigated activated carbons will help in better understanding their performances as catalytic supports. In this sense an improvement of the TPD-IR set-up to access temperatures above 700°C and the use of more calibration gases to assign minority species will be a great advantage.

References

1. Fierro V., Torné-Fernández V., Montané D., and Celzard A., *Adsorption of phenol onto activated carbons having different textural and surface properties*. Microporous and Mesoporous Materials, 2008. **111**(1): p. 276-284.
2. Figueiredo J.L. and Pereira M.F.R., *The role of surface chemistry in catalysis with carbons*. Catalysis Today, 2010. **150**(1): p. 2-7.
3. Boehm H.P., *Surface oxides on carbon and their analysis: a critical assessment*. Carbon, 2002. **40**(2): p. 145-149.
4. Fletcher A.J., Uygur Y., and Thomas K.M., *Role of Surface Functional Groups in the Adsorption Kinetics of Water Vapor on Microporous Activated Carbons*. The Journal of Physical Chemistry C, 2007. **111**(23): p. 8349-8359.
5. Cuervo M.R., Asedegbega-Nieto E., Díaz E., Ordóñez S., Vega A., Dongil A.B., and Rodríguez-Ramos I., *Modification of the adsorption properties of high surface area graphites by oxygen functional groups*. Carbon, 2008. **46**(15): p. 2096-2106.
6. Skodras G., Diamantopoulou I., Zabaniotou A., Stavropoulos G., and Sakellariopoulos G.P., *Enhanced mercury adsorption in activated carbons from biomass materials and waste tires*. Fuel Processing Technology, 2007. **88**(8): p. 749-758.
7. Lazzarini A., Pellegrini R., Piovano A., Rudić S., Castan-Guerrero C., Torelli P., Chierotti M.R., Gobetto R., Lamberti C., and Groppo E., *The effect of surface chemistry on the performances of Pd-based catalysts supported on activated carbons*. Catalysis Science & Technology, 2017. **7**(18): p. 4162-4172.
8. Otake Y. and Jenkins R.G., *Characterization of oxygen-containing surface complexes created on a microporous carbon by air and nitric acid treatment*. Carbon, 1993. **31**(1): p. 109-121.
9. Figueiredo J.L., Pereira M.F.R., Freitas M.M.A., and Órfão J.J.M., *Modification of the surface chemistry of activated carbons*. Carbon, 1999. **37**(9): p. 1379-1389.
10. Valdés H., Sánchez-Polo M., Rivera-Utrilla J., and Zaror C.A., *Effect of Ozone Treatment on Surface Properties of Activated Carbon*. Langmuir, 2002. **18**(6): p. 2111-2116.
11. Silva A.M.T., Machado B.F., Figueiredo J.L., and Faria J.L., *Controlling the surface chemistry of carbon xerogels using HNO₃-hydrothermal oxidation*. Carbon, 2009. **47**(7): p. 1670-1679.
12. Li N., Ma X., Zha Q., Kim K., Chen Y., and Song C., *Maximizing the number of oxygen-containing functional groups on activated carbon by using ammonium persulfate and improving the temperature-programmed desorption characterization of carbon surface chemistry*. Carbon, 2011. **49**(15): p. 5002-5013.

13. Moreno-Castilla C., Carrasco-Marín F., and Mueden A., *The creation of acid carbon surfaces by treatment with (NH₄)₂S₂O₈*. Carbon, 1997. **35**(10): p. 1619-1626.
14. Jaramillo J., Álvarez P.M., and Gómez-Serrano V., *Oxidation of activated carbon by dry and wet methods: Surface chemistry and textural modifications*. Fuel Processing Technology, 2010. **91**(11): p. 1768-1775.
15. Sevilla M., Valle-Vigón P., and Fuertes A.B., *N-doped polypyrrole-based porous carbons for CO₂ capture*. Advanced Functional Materials, 2011. **21**(14): p. 2781-2787.
16. Przepiórski J., Skrodzewicz M., and Morawski A.W., *High temperature ammonia treatment of activated carbon for enhancement of CO₂ adsorption*. Applied Surface Science, 2004. **225**(1): p. 235-242.
17. Jia Y.F., Xiao B., and Thomas K.M., *Adsorption of metal ions on nitrogen surface functional groups in activated carbons*. Langmuir, 2002. **18**(2): p. 470-478.
18. Jansen R.J.J. and van Bekkum H., *Amination and ammoxidation of activated carbons*. Carbon, 1994. **32**(8): p. 1507-1516.
19. Jansen R.J.J. and van Bekkum H., *XPS of nitrogen-containing functional groups on activated carbon*. Carbon, 1995. **33**(8): p. 1021-1027.
20. Cao H., Xing L., Wu G., Xie Y., Shi S., Zhang Y., Minakata D., and Crittenden J.C., *Promoting effect of nitration modification on activated carbon in the catalytic ozonation of oxalic acid*. Applied Catalysis B: Environmental, 2014. **146**: p. 169-176.
21. Boudou J.P., Parent P., Suárez-García F., Villar-Rodil S., Martínez-Alonso A., and Tascón J.M.D., *Nitrogen in aramid-based activated carbon fibers by TPD, XPS and XANES*. Carbon, 2006. **44**(12): p. 2452-2462.
22. Pietrzak R., *XPS study and physico-chemical properties of nitrogen-enriched microporous activated carbon from high volatile bituminous coal*. Fuel, 2009. **88**(10): p. 1871-1877.
23. Calahorra C.V., Garcia A.M., Garcia A.B., and Serrano V.G., *Study of sulfur introduction in activated carbon*. Carbon, 1990. **28**(2): p. 321-335.
24. Puziy A.M., Poddubnaya O.I., Gawdzik B., and Tascón J.M.D., *Phosphorus-containing carbons: Preparation, properties and utilization*. Carbon, 2020. **157**: p. 796-846.
25. Boehm H.P., *Some aspects of the surface chemistry of carbon blacks and other carbons*. Carbon, 1994. **32**(5): p. 759-769.
26. Lazzarini A., Piovano A., Pellegrini R., Leofanti G., Agostini G., Rudić S., Chierotti M.R., Gobetto R., Battiato A., Spoto G., Zecchina A., Lamberti C., and Groppo E., *A comprehensive approach to investigate the structural and surface properties of activated carbons and related Pd-based catalysts*. Catalysis Science & Technology, 2016. **6**(13): p. 4910-4922.

27. Dandekar A., Baker R.T.K., and Vannice M.A., *Characterization of activated carbon, graphitized carbon fibers and synthetic diamond powder using TPD and DRIFTS*. Carbon, 1998. **36**(12): p. 1821-1831.
28. Smith M., Scudiero L., Espinal J., McEwen J.-S., and Garcia-Perez M., *Improving the deconvolution and interpretation of XPS spectra from chars by ab initio calculations*. Carbon, 2016. **110**: p. 155-171.
29. Ferrari A.C. and Robertson J., *Interpretation of Raman spectra of disordered and amorphous carbon*. Physical Review B, 2000. **61**(20): p. 14095-14107.
30. Albers P.W., Pietsch J., Krauter J., and Parker S.F., *Investigations of activated carbon catalyst supports from different natural sources*. Physical Chemistry Chemical Physics, 2003. **5**(9): p. 1941-1949.
31. Cheng H.N., Wartelle L.H., Klasson K.T., and Edwards J.C., *Solid-state NMR and ESR studies of activated carbons produced from pecan shells*. Carbon, 2010. **48**(9): p. 2455-2469.
32. de la Puente G., Pis J.J., Menéndez J.A., and Grange P., *Thermal stability of oxygenated functions in activated carbons*. Journal of Analytical and Applied Pyrolysis, 1997. **43**(2): p. 125-138.
33. Figueiredo J.L., Pereira M.F.R., Freitas M.M.A., and Órfão J.J.M., *Characterization of Active Sites on Carbon Catalysts*. Industrial & Engineering Chemistry Research, 2007. **46**(12): p. 4110-4115.
34. Moreno-Castilla C., Carrasco-Marín F., Maldonado-Hódar F.J., and Rivera-Utrilla J., *Effects of non-oxidant and oxidant acid treatments on the surface properties of an activated carbon with very low ash content*. Carbon, 1998. **36**(1): p. 145-151.
35. Lazzarini A., *PhD Thesis: Structural and surface study of Metal nanoparticles-based catalysts and relative supports*, 2016, Università di Torino.
36. Lónyi F. and Valyon J., *On the interpretation of the NH₃-TPD patterns of H-ZSM-5 and H-mordenite*. Microporous and Mesoporous Materials, 2001. **47**(2): p. 293-301.
37. Joly J.P., Gaillard F., Peilleux E., and Romand M., *Temperature-programmed desorption (TPD) of water from iron, chromium, nickel and 304L stainless steel*. Vacuum, 2000. **59**(4): p. 854-867.
38. Foger K. and Anderson J.R., *Temperature programmed desorption of carbon monoxide adsorbed on supported platinum catalysts*. Applications of Surface Science, 1979. **2**(3): p. 335-351.
39. Vivo-Vilches J.F., Bailón-García E., Pérez-Cadenas A.F., Carrasco-Marín F., and Maldonado-Hódar F.J., *Tailoring the surface chemistry and porosity of activated carbons: Evidence of reorganization and mobility of oxygenated surface groups*. Carbon, 2014. **68**: p. 520-530.
40. Surygała J., Wandas R., and Śliwka E., *Oxygen elimination in the process of non-catalytic liquefaction of brown coal*. Fuel, 1993. **72**(3): p. 409-411.

41. Diyuk V.E., Zaderko A.N., Grishchenko L.M., Yatsymyrskiy A.V., and Lisnyak V.V., *Efficient carbon-based acid catalysts for the propan-2-ol dehydration*. Catalysis Communications, 2012. **27**: p. 33-37.
42. Haydar S., Moreno-Castilla C., Ferro-García M.A., Carrasco-Marín F., Rivera-Utrilla J., Perrard A., and Joly J.P., *Regularities in the temperature-programmed desorption spectra of CO₂ and CO from activated carbons*. Carbon, 2000. **38**(9): p. 1297-1308.
43. Friedel Ortega K., Arrigo R., Frank B., Schlögl R., and Trunschke A., *Acid-Base Properties of N-Doped Carbon Nanotubes: A Combined Temperature-Programmed Desorption, X-ray Photoelectron Spectroscopy, and 2-Propanol Reaction Investigation*. Chemistry of Materials, 2016. **28**(19): p. 6826-6839.
44. Hotová G., Slovák V., Soares O.S.G.P., Figueiredo J.L., and Pereira M.F.R., *Oxygen surface groups analysis of carbonaceous samples pyrolysed at low temperature*. Carbon, 2018. **134**: p. 255-263.
45. Nordin A., *Chemical elemental characteristics of biomass fuels*. Biomass and Bioenergy, 1994. **6**(5): p. 339-347.
46. Haghseresht F., Lu G.Q., and Whittaker A.K., *Carbon structure and porosity of carbonaceous adsorbents in relation to their adsorption properties*. Carbon, 1999. **37**(9): p. 1491-1497.
47. Hall P.J. and Calo J.M., *Secondary interactions upon thermal desorption of surface oxides from coal chars*. Energy & Fuels, 1989. **3**(3): p. 370-376.
48. Zhang L.H. and Calo J.M., *Thermal desorption methods for porosity characterization of carbons and chars*. Colloids and Surfaces A: Physicochemical and Engineering Aspects, 2001. **187-188**: p. 207-218.

CHAPTER 4

Hydrogen terminations in activated carbons and related catalysts

4.1. State of the art

Activated carbons are highly heterogeneous materials, consisting in disorderly stacked graphenic platelets terminated by C-H groups and small amounts of other heteroatoms-containing functional groups. The characterization of the morphology of their C-H terminations can provide fundamental details about the structure of the aromatic domains constituting the activated carbons and related materials at the atomic level, whose complete understanding is still missing [1-3], as well as provide a better understanding of the processes occurring at the edges of the platelets.

Among the available techniques for the characterization of carbonaceous materials, Inelastic Neutron Scattering (INS) spectroscopy is particularly sensible toward vibrations involving H atoms, as explained in Section 2.3, making it the methodology of choice to study the C-H terminations in carbonaceous materials [4-7].

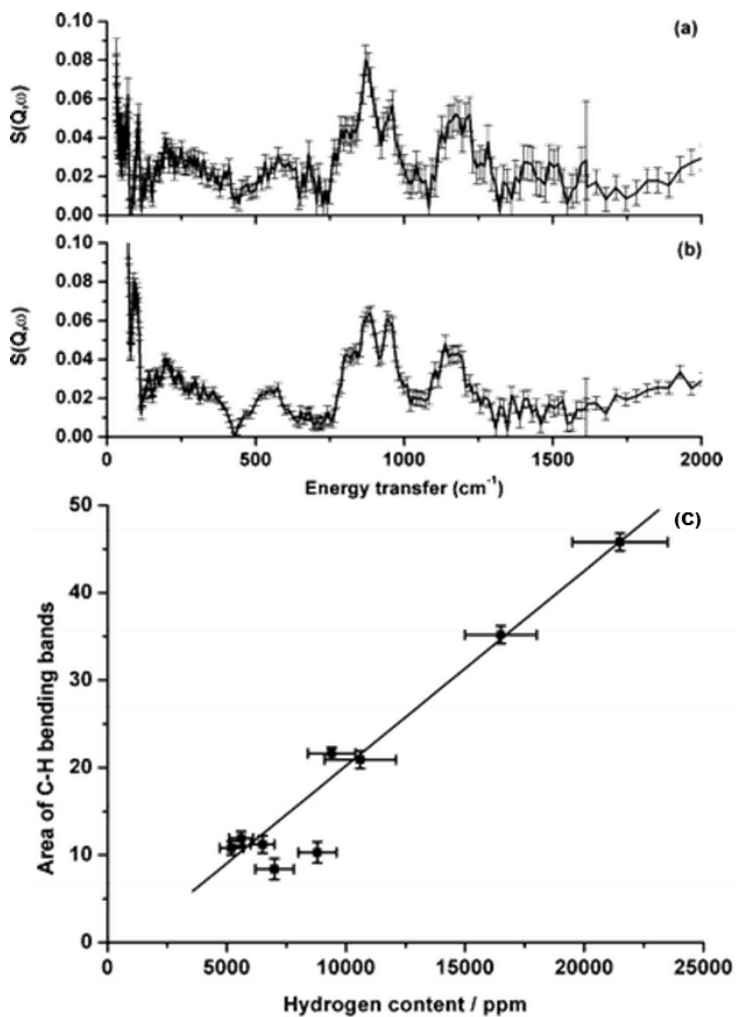


Figure 4. 1: INS spectrum of a bare activated carbon (a) and of the corresponding 5 wt% Pt catalysts (b). Part c: relation between the area below the spectra in the C-H bending region ($700\text{-}1400\text{ cm}^{-1}$) vs the hydrogen content determined by means of elemental analysis. From reference [4].

The INS instrumentation underwent relevant improvement over the last few decades, progressively increasing the level of detail of the spectra. A relevant example of early INS spectra of activated carbons and of related catalysts can be found in the work of Albers *et al* [4]. An example of their results is shown in Figure 4. 1a and b, reporting the spectrum of an activated

carbon support and of the corresponding catalyst, respectively. To overcome the low signal intensity of the instruments at that time, the measurements were performed on high amounts of sample, in the order of 20-50 g.

The bands observed in the vibrational spectra were attributed to: i) the out-of-plane bending modes of the terminal C-H groups (three sharp bands in the 700-1000 cm^{-1} region); ii) the corresponding in-plane bending modes (broad band at 1000-1600 cm^{-1}), and iii) the riding modes of hydrogen on top of the C-C vibrations (150-700 cm^{-1}) [4, 8]. In addition, Albers *et al* also demonstrated that the integrated area of the spectra in the C-H bending region is directly proportional to the hydrogen content as determined by elemental analysis (Figure 4. 1c). This observation means that it is also possible to evaluate the relative concentration of hydrogen in carbonaceous samples by comparing the integrated areas of their INS spectra.

Figure 4. 1 shows significant differences between the spectrum of the activated carbon and that of the corresponding catalyst, but the high noise level makes it difficult to proceed to a detailed comparison. This became much more straightforward as the signal-to-noise decreases. The spectra reported in Figure 4. 2 are those of CwA and Pt(R)/CwA recently collected by our group [6], measured on about 3 g of sample. The high counting statistic allowed to point out with certainty the small differences between the spectra of the support and the one of the catalyst. From this comparison, it is possible to notice that the intensity of the spectrum slightly decreases when passing from the activated carbon support to the catalyst, in particular in the C-H bending regions, but also that not all the signals are decreasing to the same extent. This is particularly evident for the three bands in the 700-1020 cm^{-1} region, where the central band is the most affected.

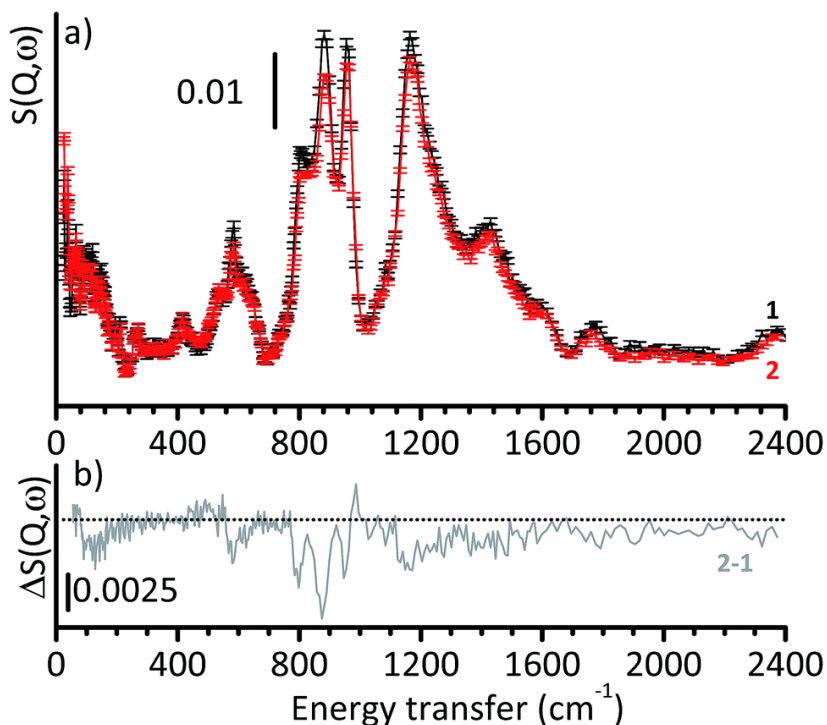


Figure 4. 2: INS spectrum of CwA (black), of Pt(R)/CwA (red) and their difference (grey), from a previous work of our group [6]. The much higher resolution of recently collected spectra permits to point out also very small variations in the spectra.

In the same experiment, by comparing the spectra of the catalyst as such and in the presence of hydrogen, it was possible to clearly observe modifications in the spectra related to the H-spillover from the Pt nanoparticles to the support.

In order to fully interpret these small changes, a precise assignment of the peaks to specific typologies of C-H terminations is essential. It was demonstrated that it is possible to shed more light on this assignment by comparing the experimental spectra with DFT simulations [4, 5, 8]. The first simulation works focused on relatively small aromatic models, whose INS spectral features are already very close to the experimental ones (Figure 4. 3).

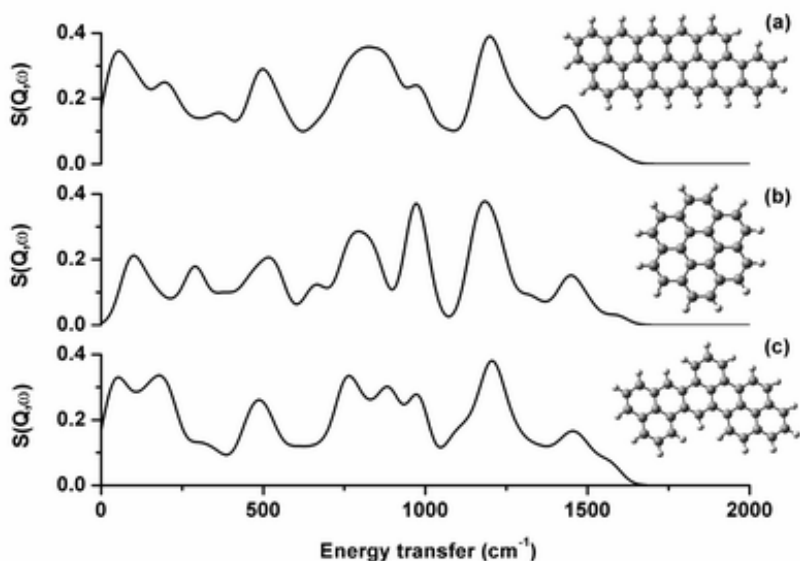


Figure 4. 3: Simulated INS spectra of three aromatic models featuring different geometries, from reference [4].

These simulations also pointed out that many spectral features, and in particular the ones in the 700-1000 cm^{-1} region, change dramatically with the geometry of the model.

In the following years, the DFT simulations focused on the assignment of the spectral signals to specific portions of the C-H terminations in activated carbons [5, 8, 9]. As an example, Piovano *et al* described the contributions to the INS spectra in terms of C-H terminations corresponding to benzene rings exposing one (*solo*), two (*duo*), three (*trio*) or four (*quatro*) H atoms [8]. Two models with different ratios among the four categories of border sites were simulated, as shown in Figure 4. 4. This analysis focused on the assignment of the vibrational modes in the 700-1000 cm^{-1} region, assigning the 873 cm^{-1} band to extended and regular *solo* borders, the 958 cm^{-1} one to defective borders featuring *duo*, *trio* and *quatro* terminations, and the bands at 820 and 761 cm^{-1} to *duo* and *trio* sites. The study also pointed out that carboxylic acid groups can contribute to the signal at 580 cm^{-1} .

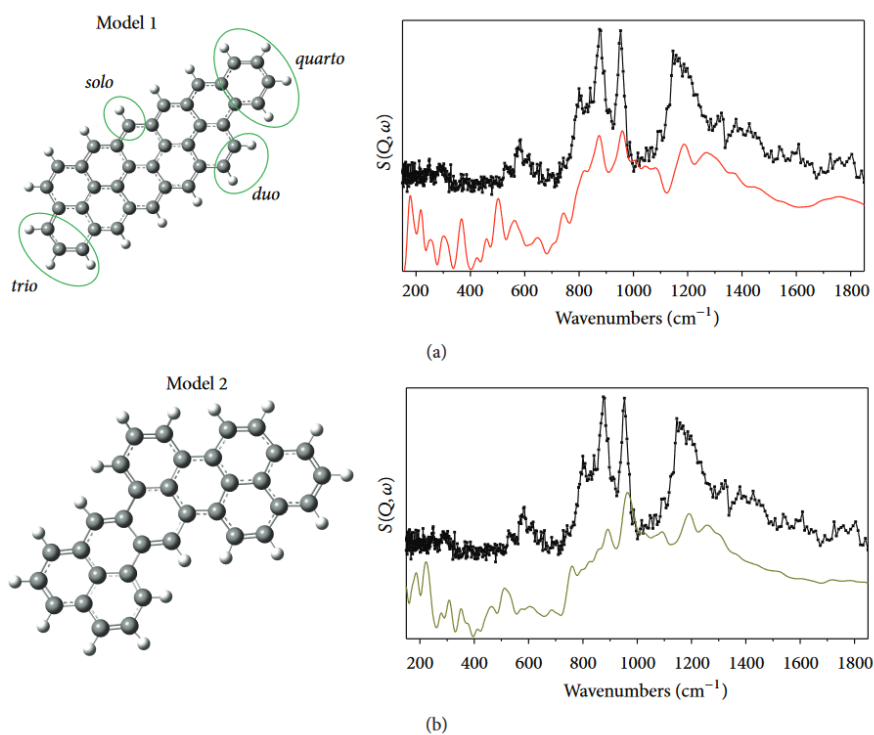


Figure 4. 4: simulated INS spectra of two models, including the effect of higher order transitions and phonon wings, compared to the experimental spectrum of CwA. From reference [8].

Albeit the constant improvements, none of these simulations were able to fully capture the true complexity of activated carbons, and consequently they were not able to completely describe the experimental spectra.

Nowadays the instrumentation suited for the measurement of high-resolution INS spectra is available, together with the computational resources to perform extended simulation works. In this framework, a large part of this PhD project was focused on the measurement of the INS spectra of a large number of activated carbons and related catalysts, and on their interpretation by means of a systematic DFT simulations on models featuring a large variety of regular C-H terminations, of defects and of functional groups.

4.2. Experimental spectra

The INS spectra of all the activated carbon samples and related catalysts considered in this work were measured at the LAGRANGE spectrometer at ILL, Grenoble, following the specifications described in Chapter 2. In the following sections, the different spectral features of the activated carbons will be discussed, together with the modifications they underwent due to the metal nanoparticles deposition and the oxidative treatment in HNO_3 .

4.2.1. Physically activated carbons and related catalysts

The INS spectra of CwA, CwB and their related catalysts are shown in Figure 4. 5, while those for CpA, CpB and their catalysts in Figure 4. 6. All the spectra exhibit the general features previously discussed, but variations in the total intensities, in the relative intensities of the bands and in their positions can be clearly observed.

The greatest differences are observed in the $690\text{-}1020\text{ cm}^{-1}$ region, corresponding to the out-of-plane $\delta(\text{C-H})$ modes, which was already indicated as the most sensible to the changes in the carbonaceous sample [4, 6, 7, 10]. This spectral range contains three main bands centred at about 800 , 880 and 955 cm^{-1} , with a tail extending at 750 cm^{-1} . Variations among the relative intensities of these bands, and in some cases also some small shifts in the frequencies, can be observed. By comparing the spectra of the parent carbons (black plots in Figure 4. 5 and Figure 4. 6), it is possible to observe significant variations among carbons prepared from different precursors (wood or peat), but also among samples having the same origin. In particular, when comparing CwA and CwB, it is possible to observe a very evident difference in the intensity of the band at 880 cm^{-1} . Also the absolute intensities of the spectra, which are proportional to the hydrogen content [4], are significantly different among the four samples, with CwA exhibiting the

highest hydrogen concentration, followed by CwB and CpA at similar values, and at last by CpB. This indicates that small changes in the composition of the precursor and/or in the activation procedure can introduce important variations in the hydrogen content and in the morphology of the C-H terminations.

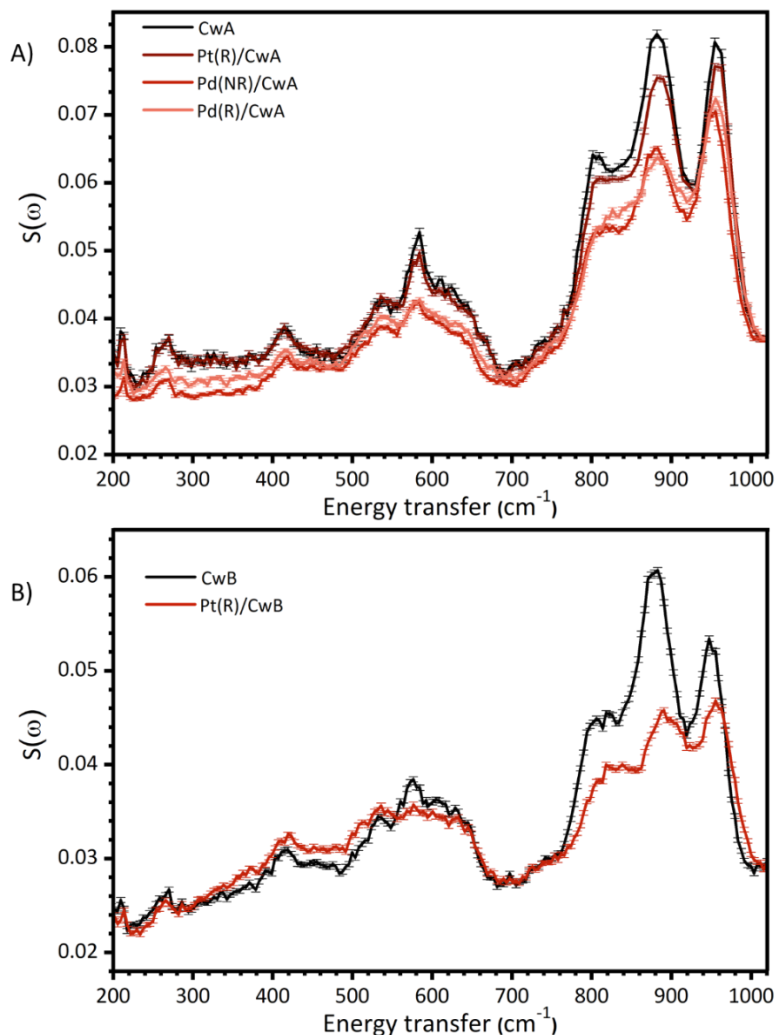


Figure 4. 5: INS spectra of CwA and the corresponding Pt and Pd-based catalysts (A), and of CwB and Pt(R)/CwB (B). All the spectra were measured at the LAGRANGE spectrometer at ILL. The intensity of the spectra of the catalysts was normalised to the one of the supports to match the background at 1020 cm⁻¹.

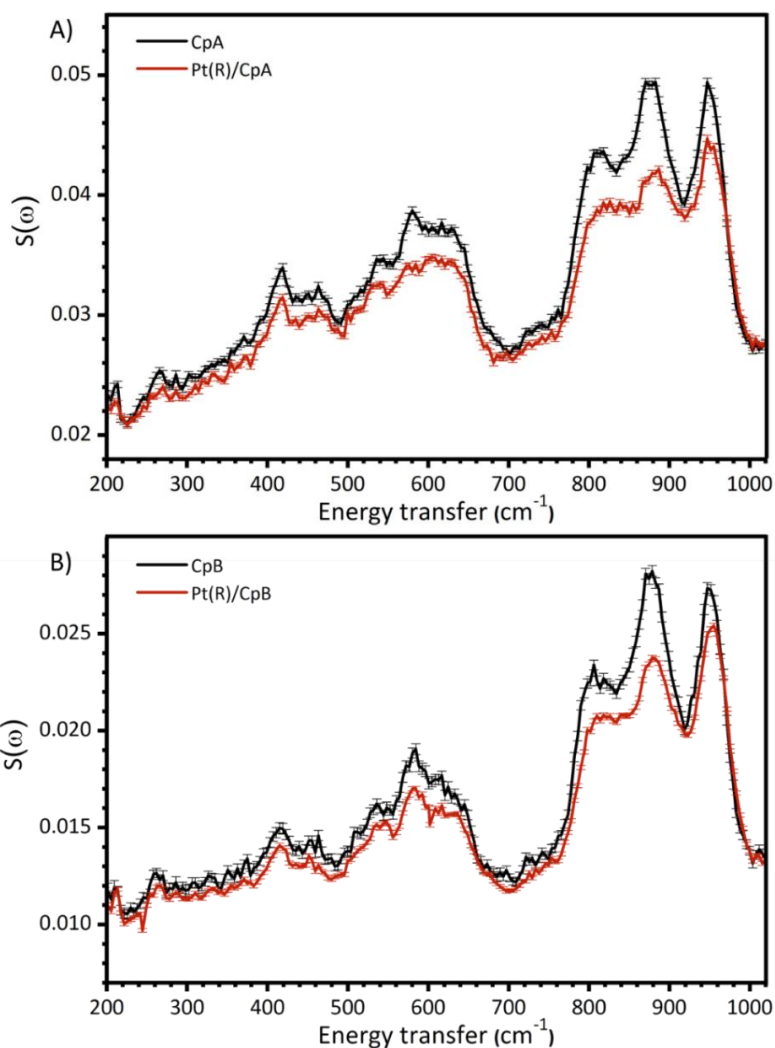


Figure 4. 6: INS spectra of CpA and Pt(R)/CpA (A), and of CpB and Pt(R)/CpB. All the spectra were measured at the LAGRANGE spectrometer at ILL. The intensity of the catalysts was normalised to the one of the supports to match the background at 1020 cm⁻¹.

Clear variations can also be observed when comparing the INS spectra of the Pt and Pd catalysts (red spectra in Figure 4. 5 and Figure 4. 6) with those of their parent carbons (black spectra). The first measurements, focusing on CwA and Pt/CwA, already pointed out that the Pt nanoparticles deposition tends to reduce the intensity of the spectra in the δ (C-H) region, and in

particular in correspondence with the 880 cm^{-1} band [6]. The observed reduction in the spectral intensities is even more important for the other catalysts hereby presented, and in particular for the Pt(NR)/CwB catalyst, for which a dramatic reduction in the intensity of all the three main bands and a slight blue-shift in the frequencies is observed. This modification in the spectra could be the result of the interaction of Pt and Pd nanoparticles with the C-H terminations of the support, and the fact that not all the bands decreased to the same extent suggests that some terminations are more affected than others. In the past, these observations were interpreted considering that the metal nanoparticles may be located at and interacting with the edges of the graphenic domains [6].

The observed decrease in the INS intensities when passing from the carbon support to the catalyst is evidently caused by a reduction in the hydrogen concentration of the sample. As previously mentioned, the integrated area of the INS spectra is directly proportional to the hydrogen content of the sample (Figure 4. 1c, ref [4]), and it was thus decided to evaluate this decrease in terms of variation in the integrated area in the $690\text{-}1020\text{ cm}^{-1}$ region. These data were plotted against the metal nanoparticles dispersion, as shown in Figure 4. 7. For the Pt catalysts (Figure 4. 7b) it is possible to observe that the decrease in integrated area (i.e. in the hydrogen content) is directly proportional to the metal nanoparticles dispersion. This suggests that smaller nanoparticles, exposing a higher percentage of atoms at their surfaces, give rise to a higher interaction with the C-H terminations of the support. The Pd nanoparticles instead cause a stronger reduction of the integrated area than the Pt ones albeit their much lower dispersion, suggesting that Pd can give rise to stronger perturbations of the support than Pt. However, it should be noticed that the two sets of samples are difficult to

compare, since the dispersion values as obtained from CO chemisorption measurements are not directly comparable.

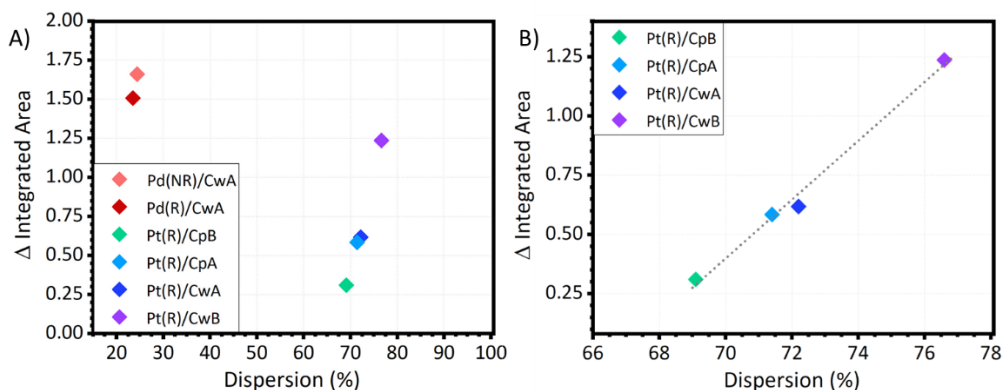


Figure 4. 7: A) difference in the integrated area in the $690\text{-}1020\text{ cm}^{-1}$ region between the activated carbon support and the corresponding catalysts, plotted against the metal nanoparticles dispersion. B) Detail over the supported Pt catalysts points. A linear trend can be observed.

4.2.2. Carbons containing a high amount of functional groups

As discussed in Chapter 3, the chemically activated sample Cchemi and the two samples oxidised in HNO_3 (CwA-ox and Cchemi-ox) present a higher concentration of O-containing functional groups than the steam-activated ones. These differences in the occupancy of the graphenic platelets terminations also reflect on their INS spectra, as shown in Figure 4. 8.

Figure 4. 8A compares the spectra of CwA and of the corresponding oxidized sample CwA-ox. The spectral features underwent dramatic changes, in particular in the $690\text{-}1020\text{ cm}^{-1}$ region. The integrated area diminished, indicating the removal of H atoms. The signals at 955 cm^{-1} and in particular the one at 800 cm^{-1} show the most significant decrease, while the 880 cm^{-1} signal both weakens and shifts at 910 cm^{-1} . A slight increase of the shoulder at 750 cm^{-1} can also be observed.

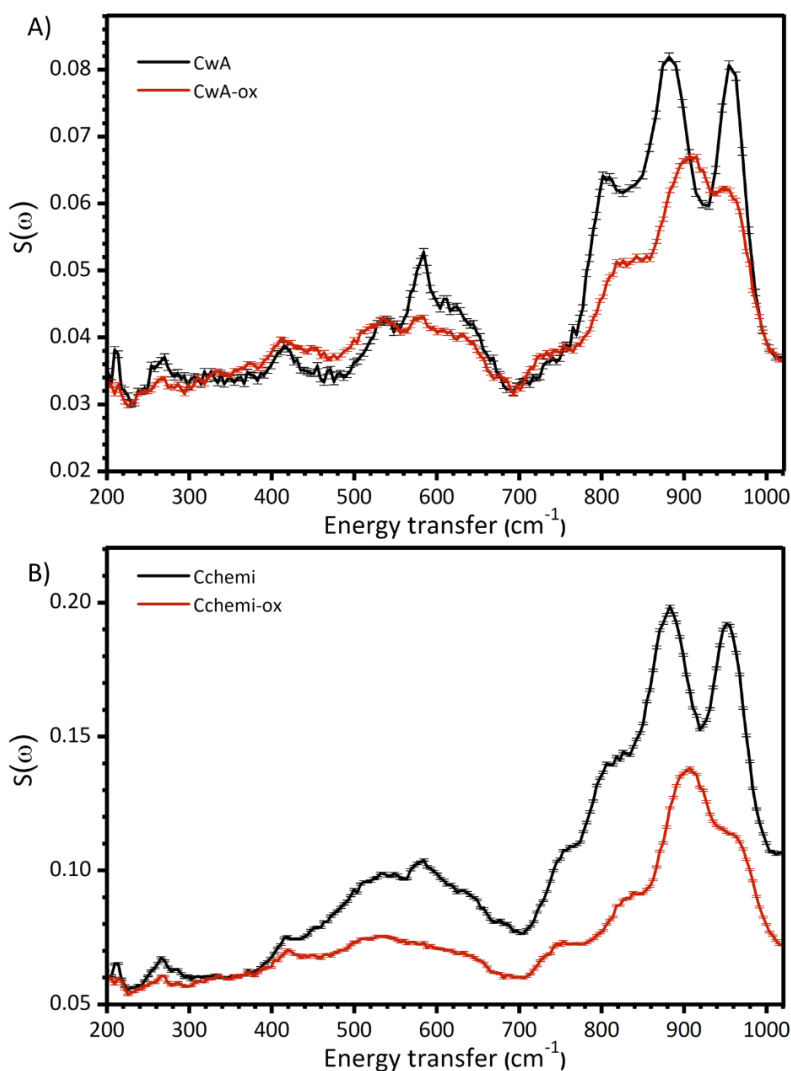


Figure 4. 8: INS spectra of CwA and CwA-ox (A), and of Cchemi and Cchemi-ox (B). The spectra were measured at the LAGRANGE spectrometer at ILL. The intensity of the oxidised samples was normalised to the one of the parent carbons to match the background at 220 cm⁻¹.

Figure 4. 8B instead shows the spectra of Cchemi and of the correspondent oxidised sample, Cchemi-ox. The parent carbon, Cchemi, displays many differences in comparison with the previously discussed steam activated samples. One first aspect that it is possible to observe is the peculiar

shape of the background, that appears to increase with the energy transfer unlike any other of the samples. This is evident because all the other spectra, when normalised to the same background intensity, match at both 220 and 1020 cm^{-1} (where only the background is expected to contribute to the spectrum), while for Cchemi this is not possible. Because of this issue, which was not yet completely explained, the interpretation of the Cchemi spectrum was more cautious. Albeit the difficulties in its interpretation, the INS spectrum of Cchemi evidently presents an intensity which is much higher than any of the previously discussed samples, indicating a significantly higher hydrogen content for this sample in respect with the steam-activated ones. The second aspect that we can notice is that the three main bands in the 690-1020 cm^{-1} region are still clearly visible also for Cchemi, but also broader than for the steam-activated samples, possibly indicating a higher heterogeneity of the C-H terminations. Also, the shoulder at 750 cm^{-1} is much more defined and intense than for the previous examples. The changes underwent by the sample following the HNO_3 oxidative treatment are even more evident than in the CwA-ox case: in fact, the overall spectral intensity drastically decreased, together with a significant change of the profile, in particular in the 690-1020 cm^{-1} region. The shift of the 880 cm^{-1} peak to 910 cm^{-1} is similar with the one previously discussed for CwA-ox, while the decrease of the 800 and 955 cm^{-1} signals is even more pronounced. Finally, as for Cchemi, also for Cchemi-ox the shoulder at 750 cm^{-1} is relatively intense and well-defined.

Analogous observations on many of the presented experimental INS spectra were already made in the past, on the base of lower quality spectra recorded on Tosca at ISIS [7, 8, 10], but in this case the higher signal to noise ratio permits to perform a much more detailed data analysis, and quantify the typologies of C-H terminations in the samples.

4.3. Simulation of INS spectra

In order to assign the bands in the experimental spectra to specific C-H terminations, we underwent a systematic DFT simulations work exploring the spectral contributions arising from regular terminations, physical defects and functional groups. For the steam-activated samples, it was eventually also possible to quantify the amount of the main terminations in the samples by mean of a linear combination fit analysis. These results will be commented in the following.

4.3.1. Regular terminations

Regular models were built as polyaromatic models featuring hexagonal rings only, where all the terminations are saturated by H atoms. These models display a regular geometry that can be described in terms of extended borders and corners, as summarised in Figure 4. 9. The formers comprehend zigzag (Z) edges, consisting in regular sequences of benzene rings exposing a single C-H group, or armchair (A) edges, consisting in benzene rings exposing two adjacent C-H groups. Corners instead are located at the intersection between two extended borders and, depending on the geometry of the model, can consist in a benzene ring exposing two, three or four adjacent C-H groups. In the following, they will be named *duo* (D), *trio* (T) and *quatro* (Q), respectively, following the nomenclature proposed by Zander for substituted benzenes [11, 12]. A total of 17 regular models have been simulated, by varying the ratios among the termination typologies previously described. The all of them are shown in Appendix B. For all these spectra, the total INS spectra and the partial contributions of the single C-H terminations were simulated.

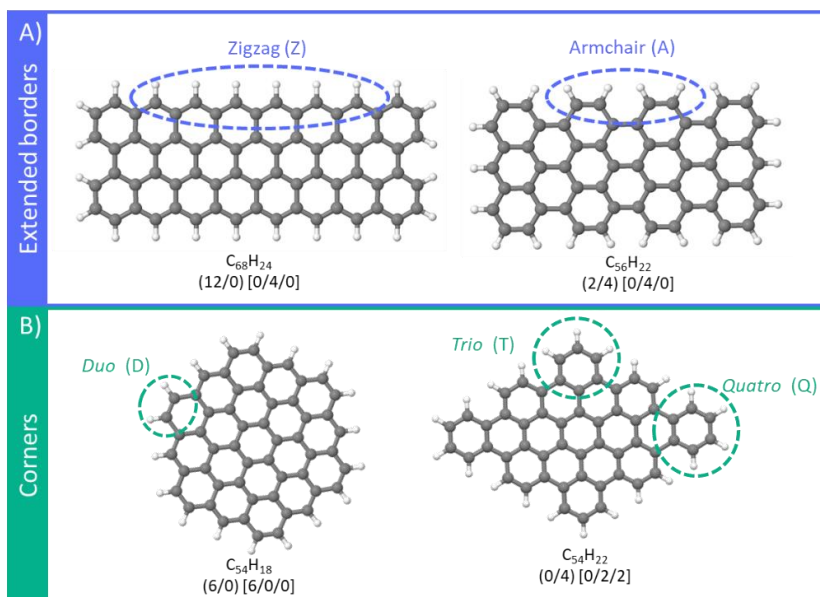


Figure 4. 9: representative example of regular models simulated in this work, indicating the defined typologies of extended borders (A) and of corners (B). The number of terminations of each type is summarised following the notation (Z/A) for the regular borders and [D/T/Q] for the corners.

The representative INS spectra of two different models, the hexagonal $C_{54}H_{18}$ and the rectangular $C_{66}H_{24}$, are shown in Figure 4. 10. In the following, the experimental spectrum of CwA is taken as the reference for the comparisons with the simulated spectra.

It is possible to observe that the two simulated spectra are able to describe the main spectral features, in particular in the out-of-plane $\delta(C-H)$ range ($690-1020\text{ cm}^{-1}$) and in the in-plane $\delta(C-H)$ one ($1020 - 1600\text{ cm}^{-1}$). It is also possible to notice that the simulated spectra tend to exhibit narrower bands, as a consequence of their molecular-like nature. The two spectra also show significant differences in the bands number, position and intensity. Consequently, this observation confirms that the INS spectra are strongly dependent on the geometry of the model [4, 8].

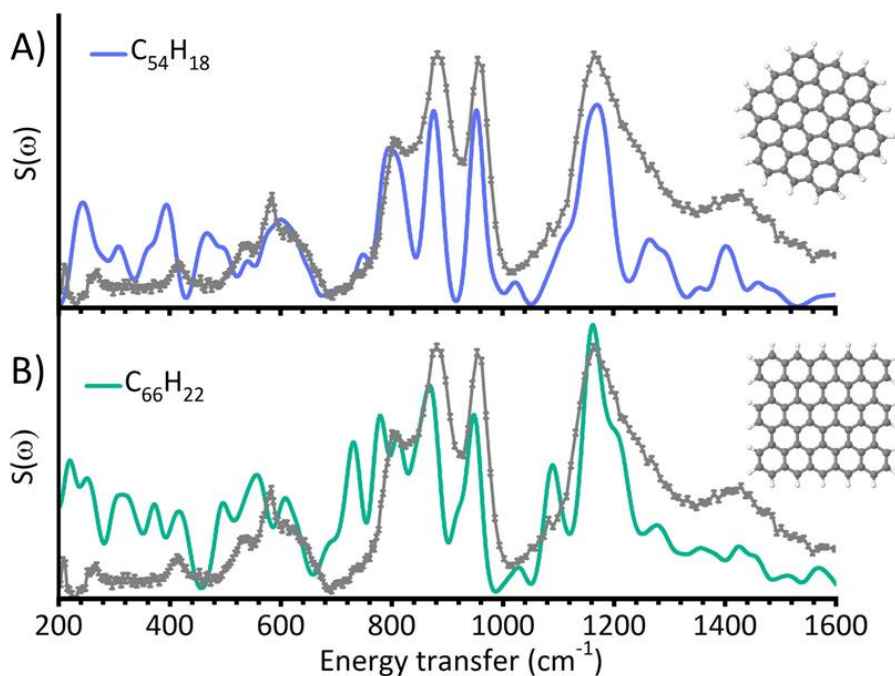


Figure 4. 10: Simulated INS spectra of $C_{54}H_{18}$ (A) and $C_{66}H_{22}$ (B), compared with the experimental spectrum of CwA. Both the simulated spectra can reasonably reproduce the experimental profile, and many features appear to be strongly dependent on the model's geometry.

To better investigate the relation between the geometry of the C-H terminations and the INS spectra, the partial contributions of each typology of C-H termination was calculated. As an example, model $C_{54}H_{18}$ contains two kind of borders, D corners and Z edges, whose contributions to the total INS spectra are shown in Figure 4. 11. The two terminations exhibit significantly different INS features, with the greatest variation observed in the 690-1020 cm^{-1} region. In this part of the spectra we can in fact observe that D sites (Figure 4. 11A) present two bands centred at 800 and 955 cm^{-1} , while the Z edges (Figure 4. 11B) give rise to a single band at 880 cm^{-1} . This same observation holds true also when comparing the partial INS spectra of the different C-H terminations in the other models.

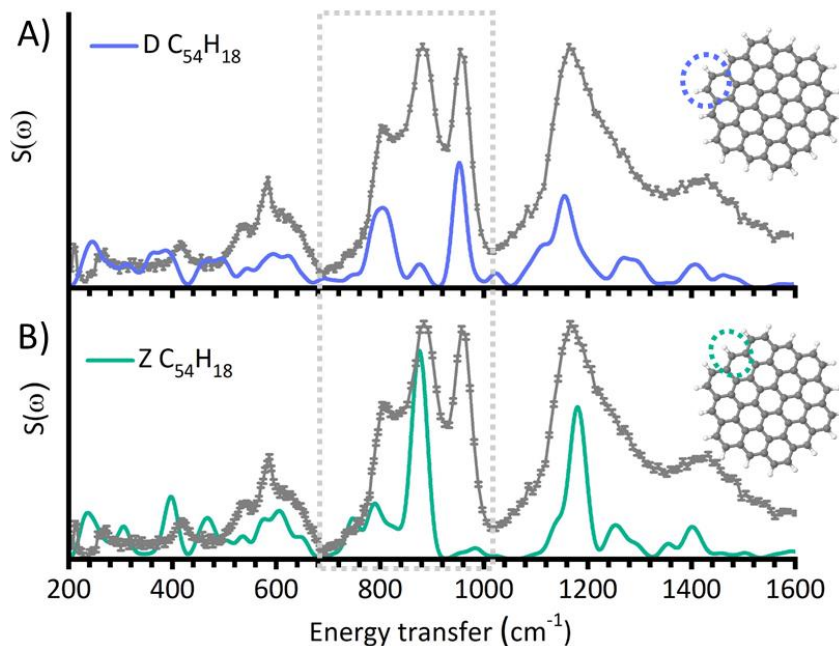


Figure 4. 11: contribution of the D sites (A) and of Z1D sites (B) on the total INS spectrum of $C_{54}H_{18}$. Different terminations on a same model give rise to different spectral features.

However, when comparing two terminations of the same kind belonging to two different models, the simulated INS spectra show a striking resemblance. An example of this can be seen in Figure 4. 12, which compares the INS fingerprint of D corners in model $C_{54}H_{18}$ and $C_{38}H_{18}$.

The similarity between the two spectra is particularly evident in the $690-1020\text{ cm}^{-1}$ region, where the D corners of both the models show the same two peaks. The two comparisons shown in Figure 4. 11 and Figure 4. 12 indicate that the out-of-plane $\delta(C-H)$ region of the spectra ($690-1020\text{ cm}^{-1}$) is the most affected by the local geometry of the C-H termination under exam, but also that it is the less affected by the rest of the geometry of the model. From the vibrational modes of these models, it is possible to see that this is the consequence of the little long-range mixing of the out-of-plane $\delta(C-H)$ modes, resulting in small portions of the C-H terminations that vibrate almost independently from the rest of the model.

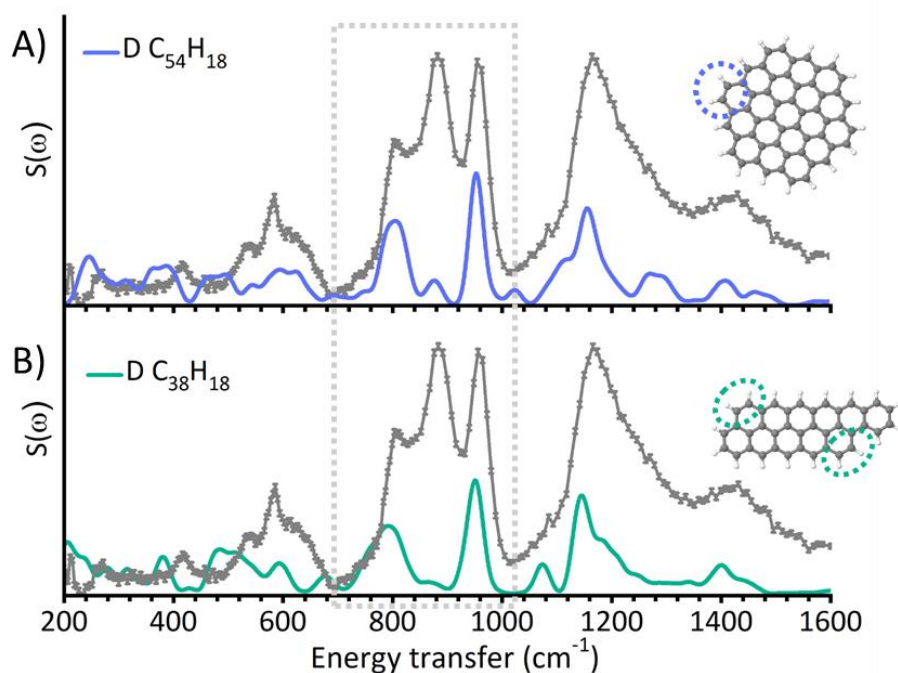


Figure 4. 12: comparison between the simulated spectrum of D sites in $\text{C}_{54}\text{H}_{18}$ (A) and of the same kind of D terminations in $\text{C}_{38}\text{H}_{18}$. The contribution of a same termination from different models is very similar, in particular in the region of the out of plane $\delta(\text{C-H})$ modes ($690\text{-}1020\text{ cm}^{-1}$).

In the rest of the spectral range instead a long-range combination of the vibrational modes is observed. On this basis, we decided to focus our analysis on the $690\text{-}1020\text{ cm}^{-1}$ range only, where it is possible to define the characteristic INS fingerprint of each typology of C-H local termination and hence to proceed with their classification.

By comparing the partial INS spectra of all the C-H terminations present in the regular models, it was possible to determine five different classes of terminations:

- **Extended zigzag borders:** the vibration of the adjacent C-H terminations along the zigzag edge are strongly correlated, giving rise to two main band centred at ~ 800 and 880 cm^{-1} , corresponding to the out-of-phase and in-

phase vibration of vicinal sites, respectively. The spectral features of the single C-H termination depend on the distance from the extremities of the regular border and, for the extremes, on the typology of adjacent corner site. Their contributions are shown in Figure 4. 13A and B, where each typology of C-H termination is labelled with a Z followed by a number indicating the distance with respect to the corner. In the case of sites next to a corner, an extra letter (D or T) is added to specify the nature of the adjacent corner. Z1 sites are those showing the highest variability with the model, as shown in Figure 4. 13A. For Z1D sites (i.e. for zigzag terminations adjacent to a *duo* corner), the spectra are dominated by a main peak at 880 cm^{-1} , while the 800 cm^{-1} band is much weaker. Instead, in the case of a Z1T site (i.e. a termination adjacent to a *trio* corner), the band at 880 cm^{-1} is generally split into two components, and the 800 cm^{-1} band is slightly lower in intensity. In the case of longer zigzag edges, the spectral features tend to converge as the distance from the corner increases, as particularly evident when comparing the Z3 and Z4 contributions (Figure 4. 13B). For these terminations the 800 cm^{-1} signal appears more intense than the 880 cm^{-1} one, while Z2 sites exhibit similar spectra slightly shifted at higher frequencies.

- **Extended armchair borders:** The spectra of armchair borders (A) are characterized by two bands centred at 810 and 920 cm^{-1} , corresponding to the in-phase and out-of-phase vibration of the two C-H terminations on the same benzene ring (Figure 4. 13C). Their features remain almost the same irrespectively of the length of the border.

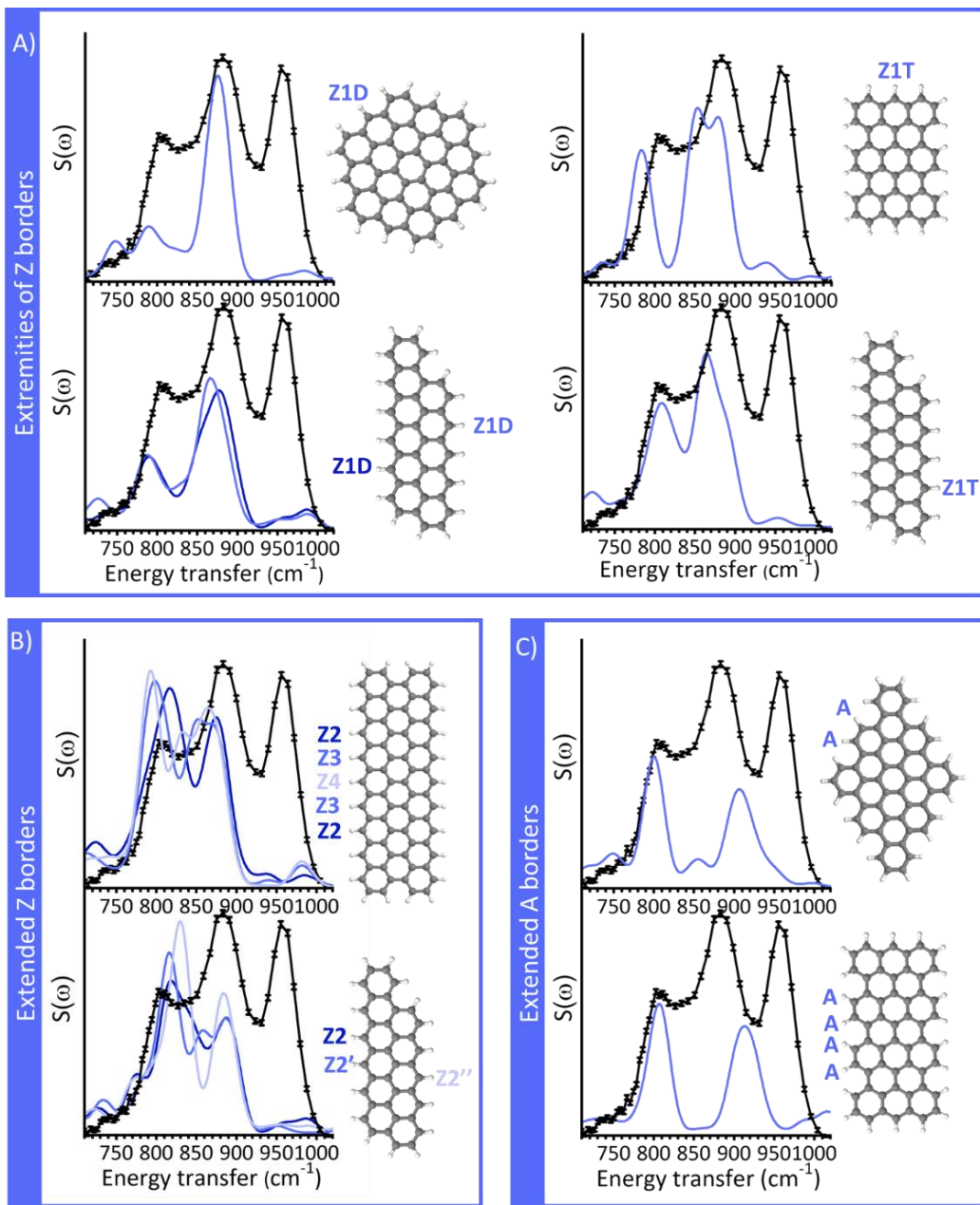


Figure 4.13: representative INS contributions for Z1D and Z1T sites at the extremities of Z edges (A), of extended Z edges (B), and of extended A edges (C).

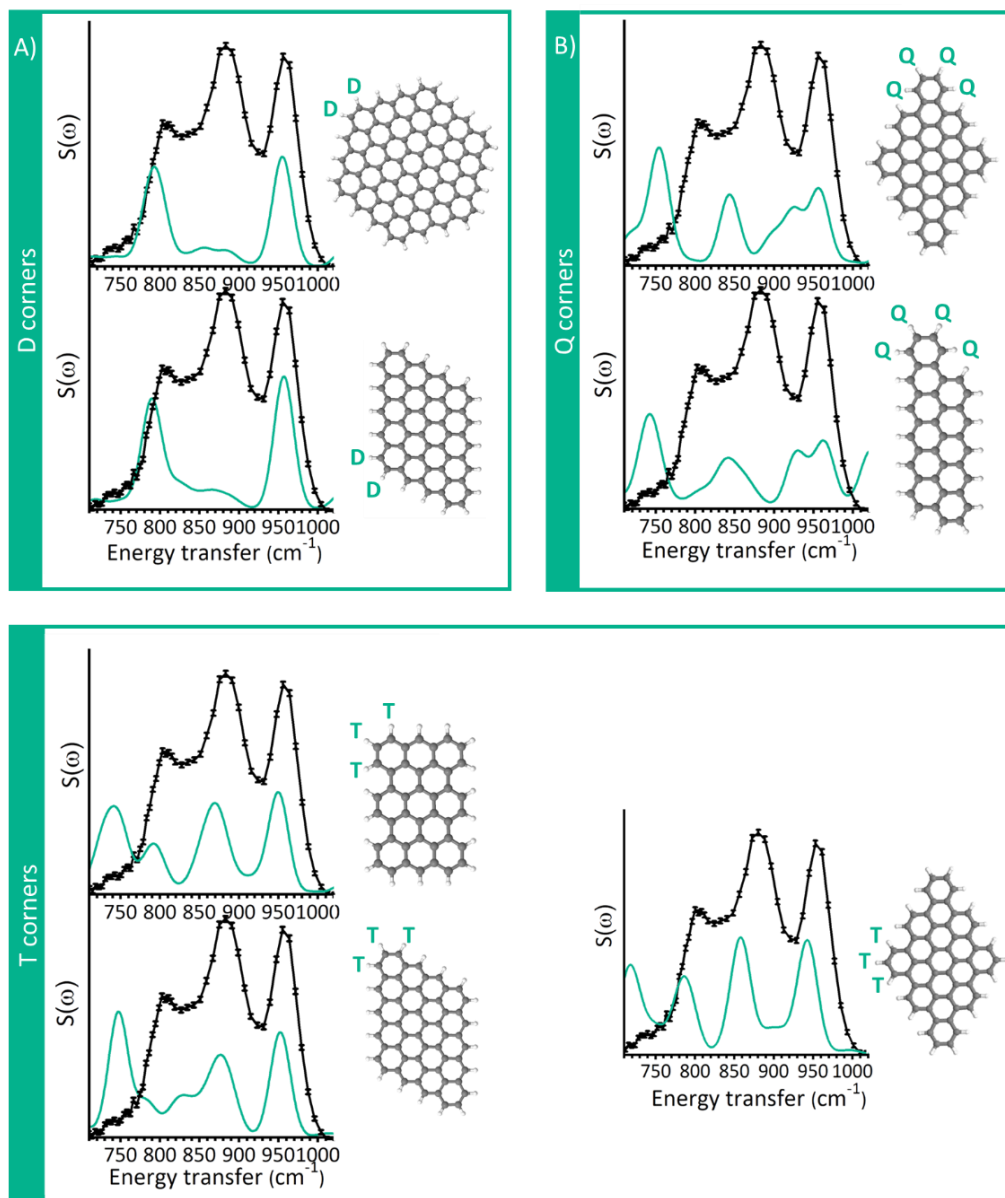


Figure 4. 14: representative INS contribution of A) D corners, B) Q corners and C) T corners.

- **Duo corners:** the spectral features of *duo* (D) corners comprehend two bands centred at 810 and 920 cm^{-1} (Figure 4. 14A). The vibrational modes

involved and the spectra are very similar to the A case, apart from the larger spacing between the bands.

- **Trio corners:** the INS spectra of *trio* (T) corners contain four main bands, the first two at 750 and 800 cm^{-1} (the latter can appear as a shoulder of the first one), one at 850 cm^{-1} and the last one at 950 cm^{-1} (Figure 4. 14C). The three C-H exposed on the same benzene ring vibrate collectively, transitioning from totally in-phase modes (low frequency) to completely in-phase modes (high frequency). Their spectral features, and in particular the relative intensities, seem to change depending on whether the adjacent edge is of Z or A type.
- **Quatro corner:** their INS spectra present four main bands centred at 740, 840, 930 and 960 cm^{-1} (Figure 4. 14B). Similarly to the T case, vibrational modes of the four C-H groups exposed by the benzene ring are correlated, and they progressively pass to totally in-phase vibrations to totally out-of-phase vibrational modes when increasing the frequency. Their spectra are minimally influenced by the rest of the model.

4.3.2. Physical defects

Other than regular C-H terminations, activated carbons are also expected to contain variable amounts of defects, which can arise from the introduction of heteroatoms (functional groups) or of ruptures of the regular aromatic domains (physical defects). In this section, the INS fingerprint of physical defects will be discussed, while functional groups will be treated in the following one.

The typologies of possible physical defects are very varied, since they comprehend every possible structure in which C atoms are missing from the aromatic platelet, or their bonds are rearranged into five or seven-membered rings. When simulating platelets in which the defect consisted only in a

rearrangement of the C-C bonds at the centre of the platelet, such as in the case of the Stone-Wales defect [13], the modifications of the INS spectra were generally negligible. It was thus concluded that INS is only sensible to defects directly affecting the model's terminations, or the ones containing new C-H bonds. The simulations on the physical defects were thus focused on these typologies of defects. The main typologies of defective C-H terminations that we have simulated are:

Disordered border: these terminations consist in portions of the C-H terminations which cannot be fully classified as any of the regular borders and corners previously discussed, and that exhibit sensibly different spectral features. The simulated models belonging to this category and some significant examples of their INS spectra are shown in Figure 4. 15A. In these models only small variations are observed for T and Q corners, probably as a consequence of their peripheral position. The greatest variations are instead observed in the cases of Z1 and D terminations. In fact, it can be observed that disordered Z1 terminations (Figure 4. 15A, first plot) give rise to broad bands, centred at about 830 cm^{-1} , in correspondence with one of the minima in the experimental spectrum. The disordered D terminations instead (Figure 4. 15A, second plot) exhibit two bands similar to the regular A and D terminations, but at an intermediate position (~ 800 and 935 cm^{-1}). When also consider the disordered terminations, it appears that the INS spectra of all the benzene rings exposing two C-H groups (A, D and disordered D) fall within a continuum of cases, of which the A and D cases correspond to the two extremes.

- **Holes:** models featuring holes within the aromatic platelet were built by removing a variable amount of C atoms, and by saturating the resulting dangling bonds with H atoms.

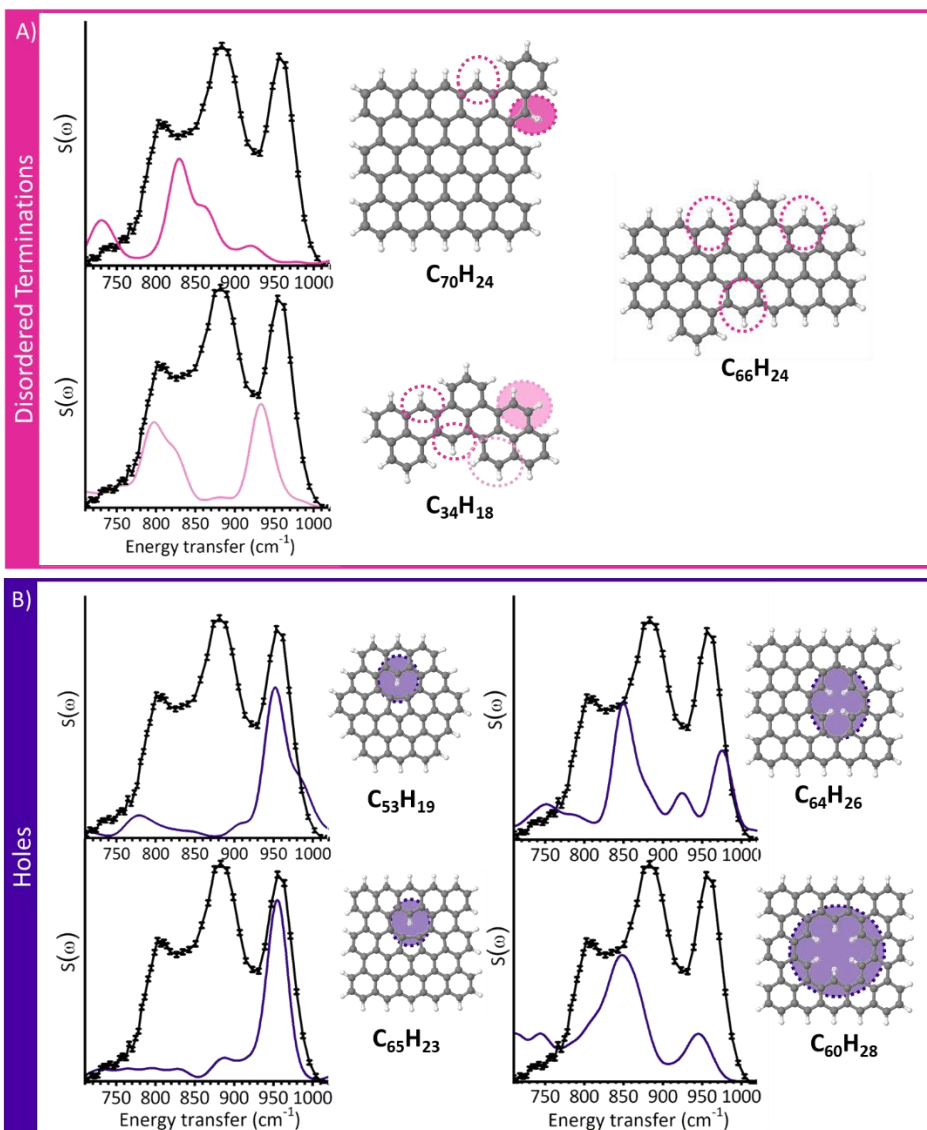


Figure 4. 15: Part A) disordered models and the simulated INS spectra of disordered zigzag terminations (dark pink) and disordered *duo* (light pink). The disordered sites are circled, and a whole circles indicate the sites whose simulated spectra was plotted. Part B) models containing holes within the aromatic platelet. The first two spectra correspond to single vacancies, obtained by removing a single C atom from the platelet, the third one a double vacancy, obtained by removing two adjacent C atoms, and the last one a larger hole generated by removing six C atoms. In all cases the dangling bonds were saturated with H atoms.

This kind of H-saturated holes were found in various carbonaceous materials, and in particular in defective graphene [9]. Our simulations pointed out that the C-H terminations exposed by holes present some very peculiar INS fingerprints, as shown in Figure 4. 15B. The first two models contain a single carbon vacancy, which is saturated by forming a five-member ring and a C-H termination on the opposite part of the hole. The dimension of the hole is too small to accommodate the C-H termination in a planar configuration, resulting in a projection of the C-H group out of the plane. In both the models this C-H termination gives rise to a single INS band centred at 950 cm^{-1} . The removal of two adjacent C atoms from the platelet instead creates a double vacancy, as that shown in Figure 4. 15B, third plot. In this case, all the four dangling bonds were saturated with H atoms. As in the previous case, the steric hindrance did not allow to accommodate the four C-H in a planar configuration, resulting in an optimised geometry in which the internal C-H groups sit, alternatively, above and below the plane of the model. The resulting INS spectrum displays two main bands centred at about 850 and 975 cm^{-1} . Finally, by removing a whole benzene ring from the centre of the platelet a larger hole was obtained, as shown in Figure 4. 15B, last plot. In this case, the space in between the C-H terminations allows for a flat configuration of the model. The resulting spectrum displays a broad band centred at 840 cm^{-1} , and quite similar to the fingerprint of disordered Z1 sites.

- **Curved models:** curvature was observed in the structure of non-graphitizable carbon samples [1, 3], and for this reason we decided to investigate its effect on the INS spectra. Curvature can be obtained by introducing five or seven member rings in the model.

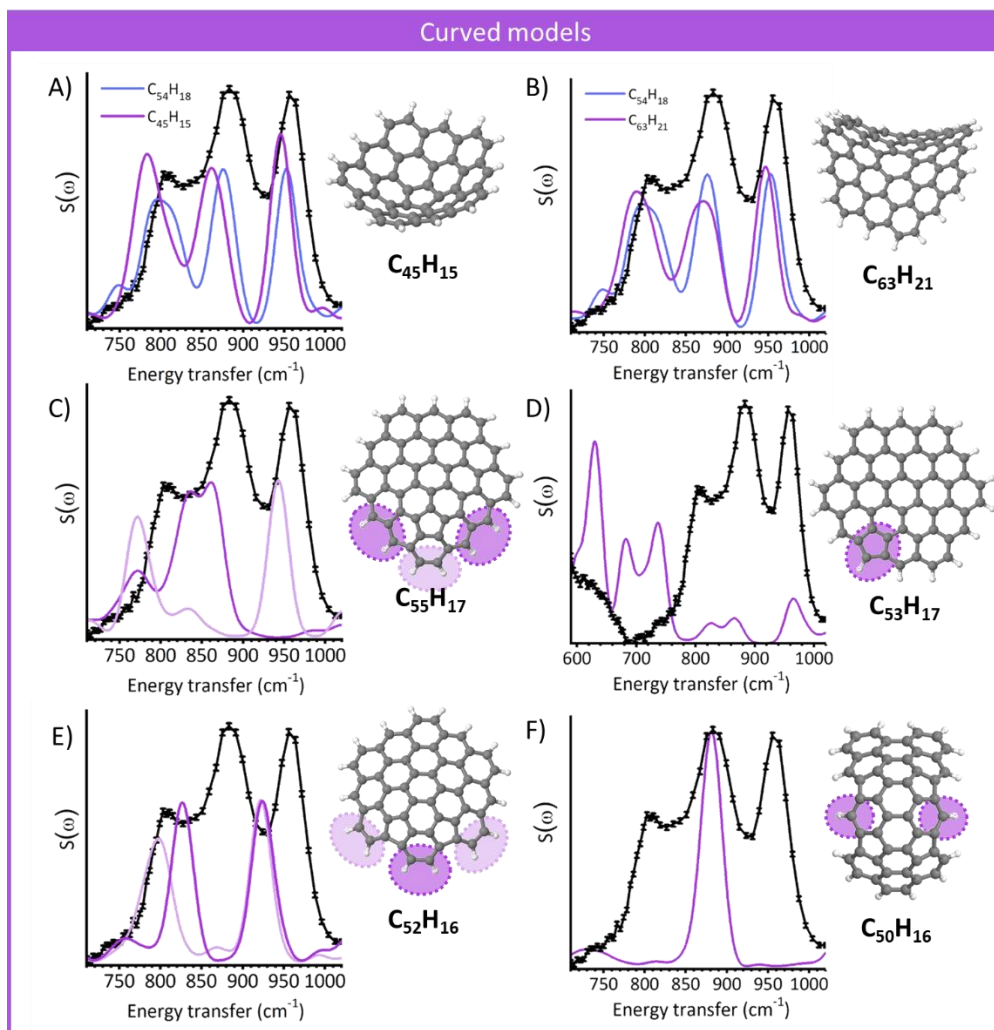


Figure 4. 16: simulated INS spectra of curved models. The introduction of a 5-membered ring (A) or of a 7-membered one (B) at the centre of the model only introduce small shifts in respect with the flat $C_{54}H_{18}$ model. The introduction of a pentagonal ring closer to the border (C) alters the INS fingerprint of the adjacent Z1D and D terminations, making them indistinguishable from the disordered terminations. A five-membered ring exposing a C-H (D) gives rise to a characteristic band at low frequencies, in correspondence with one of the minima of the experimental spectrum. The introduction of two 5-benzene rings at the border of the model to isolate a D corner (E) only causes small shifts in the signals position, which still fall within the range of the continuum of the D-all terminations. When isolating a Z1 termination instead (F), the INS spectra present a particularly sharp peak at 880 cm^{-1} .

Inserting a five member ring in the middle of the structure generate a fullerene-like curvature (Figure 4. 16A), while seven-member rings are source of saddle-like curvatures (Figure 4. 16B). In both these examples the source of sphericity is far from the C-H terminations, and the resulting INS spectra present almost negligible shifts in comparison with the corresponding flat model $C_{54}H_{18}$. The effect of the perturbation introduced by the curvature of the model tends to increase as the five-member ring is located closed to the edges of the model, as shown in Figure 4. 16C: in this case, both the adjacent Z1 and D terminations show similar features to the disordered Z1 and D ones. By placing the five-membered ring at the edge, it is possible to obtain models exposing a C-H group from a pentagonal ring. In this case the INS spectrum presents bands at very low frequencies, in correspondence with one of the minima of the experimental spectrum, indicating that this kind of termination is unlikely to be present at relevant amounts in our samples (Figure 4. 16D). Alternatively, five-membered rings at the edges could not expose any C-H group, resulting in the isolation of the adjacent terminations. When five-member rings isolate a D-corner, as in the model in Figure 4. 16E, the perturbed terminations show specific features in comparison with the original regular sites, but still belonging to the continuum of the D-all terminations. When instead five-member rings isolate a Z1 termination (Figure 4. 16F), the resulting spectra show a very sharp and isolated band at 880 cm^{-1} , caused by the complete lack of combination with the vibrational modes of the other terminations.

4.3.3. Functional groups

In Chapter 3, we demonstrated that functional groups are present in in all the activated carbons under exam, and in particular in Cchemi and in the oxidised carbons. Significant modifications were observed also in the INS

spectra of these samples, suggesting that some INS features could arise from the presence of functionalities. For this reason, the systematic DFT simulations work also included a wide range of O-containing functional groups. A total of 34 heteroatoms-containing models were simulated, featuring carboxylic acid groups, carboxylates, phenols, ketones, ethers (Figure 4. 17), anhydrides, lactones, pyrones and quinones (Figure 4. 18).

The simulation of the INS spectra of functional groups containing models pointed out significant changes in comparison with the regular ones.

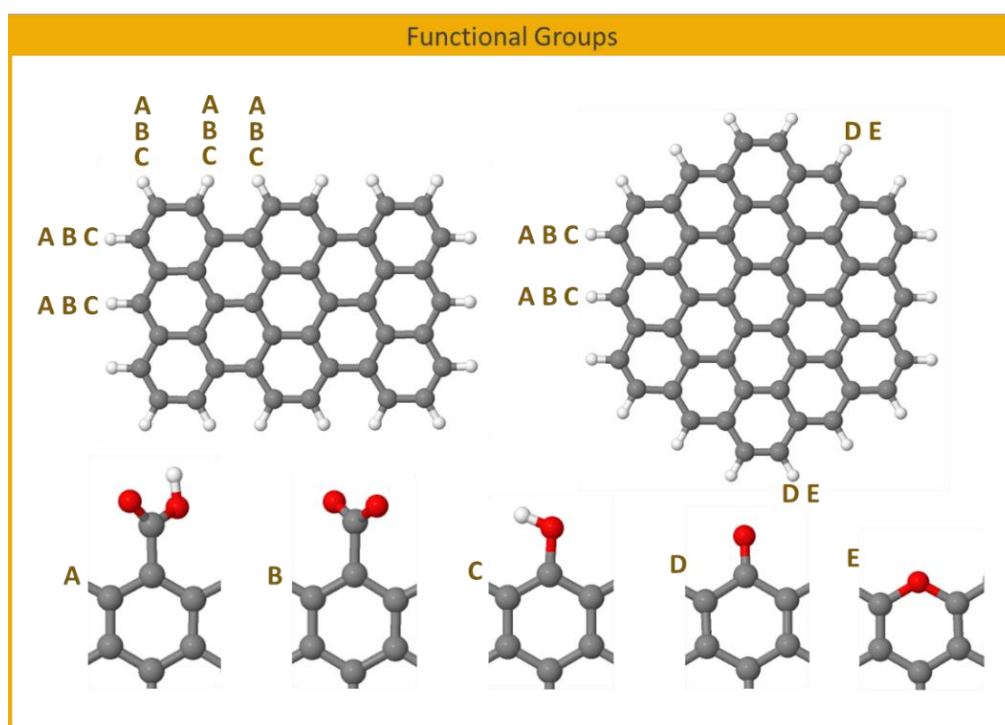


Figure 4. 17: carboxylic acid groups (A), carboxylates (B), phenols (C), ketones (D) and ethers (E) were introduced in models $C_{42}H_{18}$ and $C_{54}H_{18}$ in the positions indicated by the correspondent letters. When two non-equivalent conformations were possible, both of them were simulated. In the case of ketones and ethers on model $C_{54}H_{18}$, both the positions were occupied at the same time in order to obtain an overall closed-shell electronic configuration.

Functional Groups

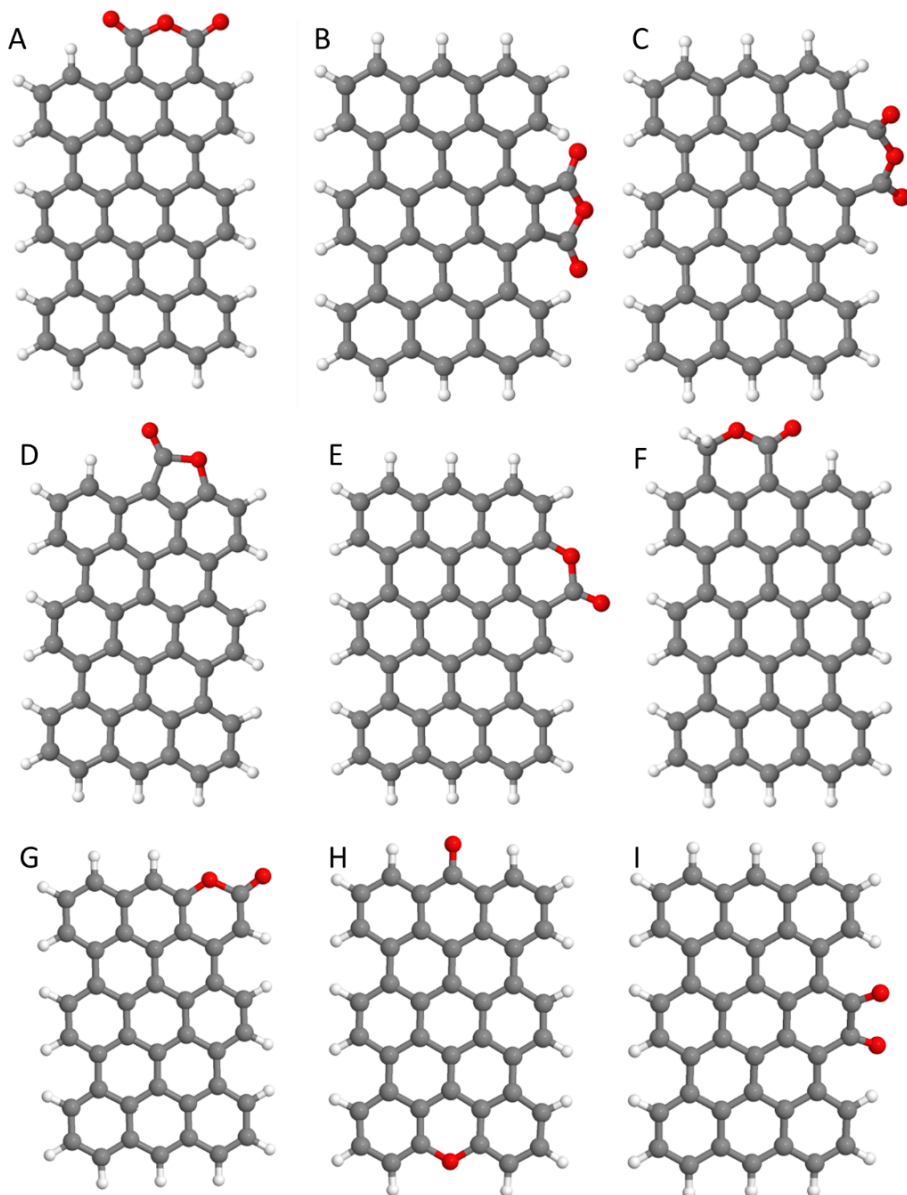


Figure 4.18: simulated models of anhydrides (A, B, C), lactones (D, E, F, G), pyrones (H) and quinone (I).

However, the rationalization of their effect is more challenging than in the case of regular borders or physical defects: in fact, significant variations were observed when comparing the INS features of a same functional group in similar positions, and sometimes even when modifying the spatial orientation of a functional group bonded in a same position.

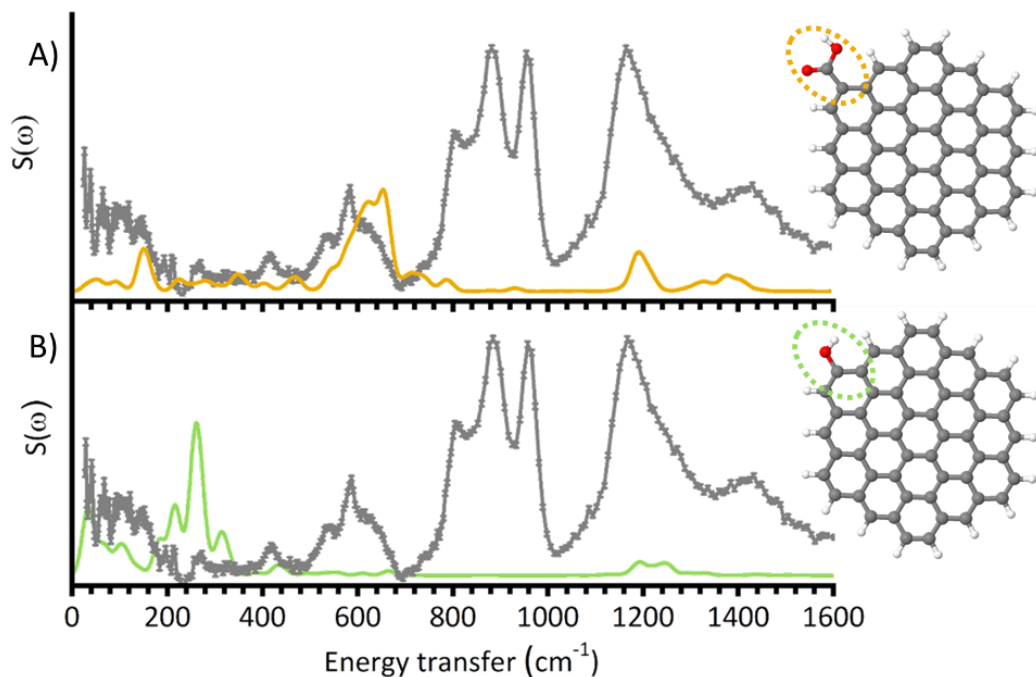


Figure 4. 19: specific INS fingerprint of the carboxylic acid group (A) and of the phenolic group (B) in D position on the $\text{C}_{54}\text{H}_{18}$ model.

Still, it was possible to point out that:

- The introduction of functional groups reduces the total intensity of the INS spectrum, as it involves the substitution of one or more H atoms in the model.
- H-containing functional groups give rise to their own characteristic INS spectra (Figure 4. 19). More in details, carboxylic acid groups tend to show their strongest signal at about 600 cm^{-1} (Figure 4. 19A), as already observed

in ref [8], while phenols give rise to strong bands at frequencies lower than 200 cm^{-1} (Figure 4. 19B). Instead, the direct contribution of functional groups on the $690\text{-}1020\text{ cm}^{-1}$ range in the spectra is almost negligible.

- The introduction of functional groups can also strongly perturb the vibrational modes of the vicinal C-H groups. When the functional group sits on the benzene ring next to a C-H group, the general INS fingerprint of the latter is maintained, but a shift in the frequency is observed in the most of the cases (Figure 4. 20A). Instead, when the functional group sits on the same benzene ring as the vicinal C-H group, the number of terminations contributing to the combined vibrational mode is reduced, resulting in a lower number of bands in the spectrum and a shift in frequency (Figure 4. 20B). Generally, when only one C-H group remains on the benzene ring, a single band is observed. When two adjacent C-H remain, instead, the spectrum contains two bands corresponding to the in-phase and out-of-phase combinations of their vibrational modes, and so forth. The number of the bands is usually predictable, while the frequency shift is much more variable.

In most cases, it was observed that groups with a C=O bond (carboxylic acids, carboxylates, ketones) are more likely to shift the signal at higher frequencies, while groups with a C-O bond (ethers, phenols) at lower frequencies. However, the observed shifts are too variable to really point out a specific fingerprint of the functional groups which is valid for all the models. In addition, the spectral profile and the band positions often overlap with the previously discussed disordered Z1 and D terminations, making it difficult to discriminate among them.

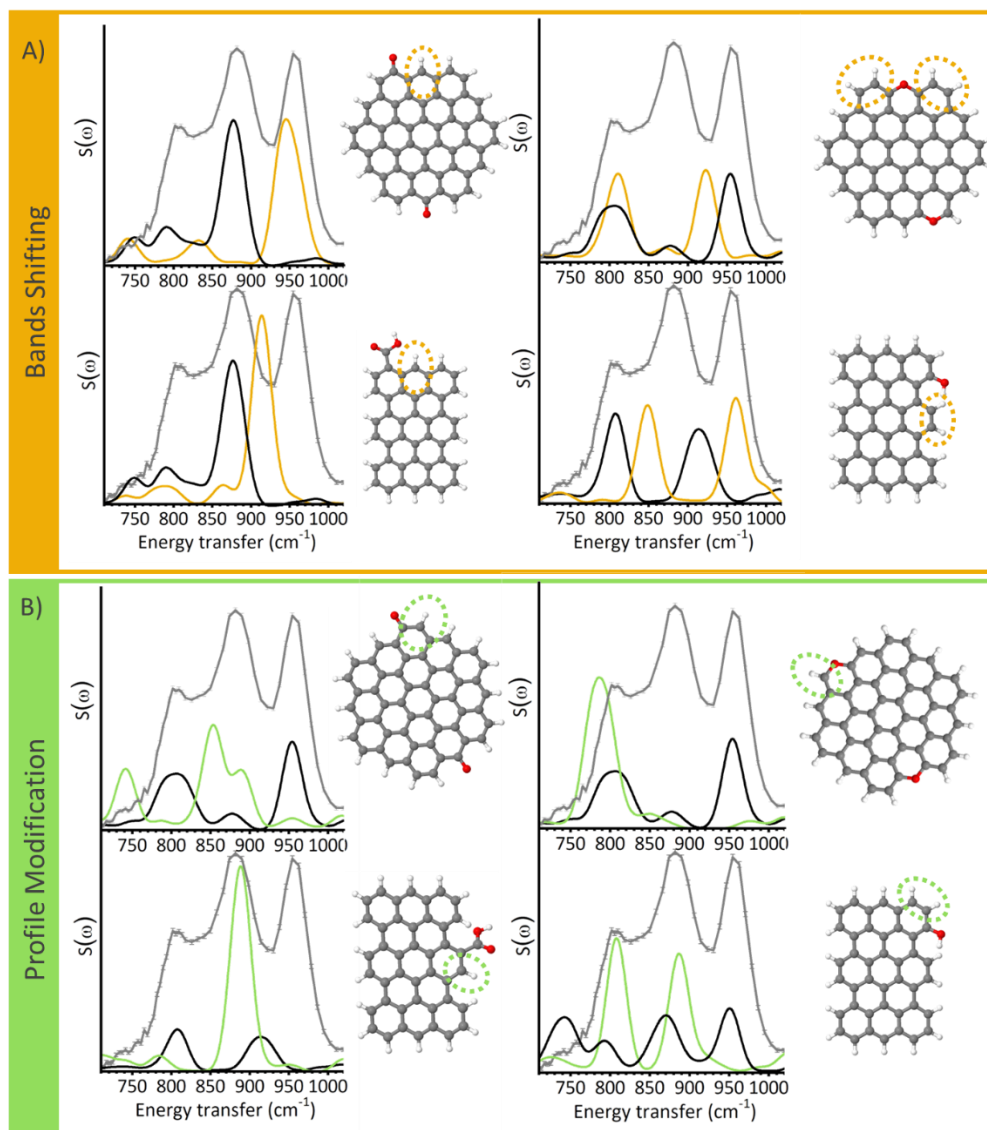


Figure 4. 20: perturbation on the INS fingerprint of C-H terminations caused by the introduction of a functional group. Part A) frequency shift, part B) modification in the whole spectral profile. In all the spectra, the reference spectrum of the corresponding unperturbed species is reported in black as a reference.

4.4. Identification and quantification of C-H terminations

The large number of simulated INS spectra of the previously described C-H terminations were compared with the experimental INS spectra for a detailed

assignment of the bands. In some cases it was also possible to quantify their relative concentrations by fitting the experimental spectra with a linear combination of the simulated ones. However, in order to ensure the reliability of a fit calculated on a limited number of experimental points, it is crucial to select a relatively small number of functions to be used in the fit. In the case of the steam-activated samples the amount of functional groups was evaluated to be very low, almost negligible in comparison with the amount of H terminations, as shown in Chapter 3. For this reason, for these samples it was possible to limit the linear combination fit analysis to the contributions of regular and defective terminations, and to proceed with their quantification. In the cases of Cchemi and of the oxidised samples instead it was not possible to neglect the effect of the functional groups, that in particular in the latter cases is fundamental to explain the spectral profiles. For these samples, consequently, the number of functions to introduce into the linear combination fit would have been too high to ensure the stability of the algorithm and the reliability of the result, limiting us to a qualitative evaluation.

4.4.1. Quantification of the C-H terminations in physically activated carbons

By comparing the INS spectra of the physically activated carbons with regular models such as $C_{54}H_{18}$ (Figure 4. 10), it is evident that fully regular models are able to describe the position of the main experimental features. For this reason, the first attempt of quantification of the C-H terminations in the physically activated samples was made by considering regular borders only. In order to reduce the number of functions, the contributions arising for analogous terminations on different models were averaged, resulting in eight contributions to the fit (Z1D, Z1T, Z2, Z3-Z4, A, D, T and Q). The spectra of T

and Q corners were excluded since they contribute in regions of the spectra where the experimental signal is weak, and are thus expected to be present in low amount. Extended zigzag borders (Z1T, Z2, Z3-Z4) were also excluded, as their contributions always resulted in negligible values in the preliminary calculations. Therefore, the final fit was run considering a linear combination of Z1D, A and D terminations, as shown in Figure 4. 21. Albeit this fit is able to describe the position of the experimental bands, the relative intensities evidently are not well reproduced. In fact, it can be observed that the band at 800 cm^{-1} is overestimated, while the one at 950 cm^{-1} and the two minima at 830 and 930 cm^{-1} are missing some intensity. Analogous results were also obtained for the other physically activated carbons and their catalysts. Hence, it is clear that the INS spectra of activated carbons cannot be fully described in terms of regular C-H terminations only.

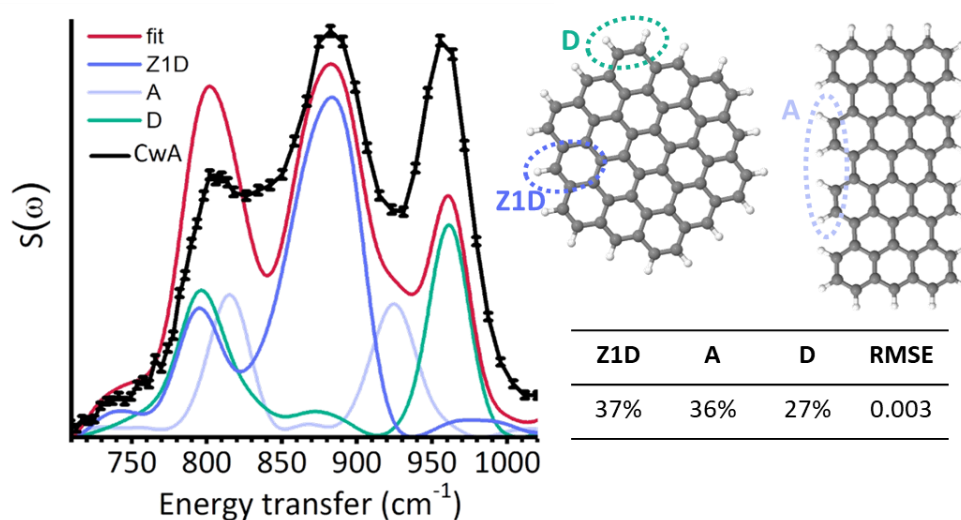


Figure 4. 21: fit of the INS spectra of CwA using a linear combination of regular C-H terminations contributions (Z1D, A and D). An example of the geometries of the considered terminations is reported for clarity, together with the table summarising the percentages of the three sites as calculated by the fit. The quality of the solution is evaluated by the RMSE (root mean square error) value.

Activated carbons are known for being heterogeneous and disordered systems. Therefore, we expected that physical defects could play a relevant role in the description of the INS spectra of the steam activated carbons. The second attempt to the linear combination analysis was thus made by introducing the contributions of some of the defective C-H terminations in the fit. Both the functions describing the disordered Z1 and D terminations were introduced in the fit. Since the simulations of the disordered models showed that D, A and disordered D terminations belong to a continuum of characteristic spectra, we decided to represent all of them with a single function, D-all, obtained by averaging these three functions. As for the holes in the platelets, the size of the graphenic platelets in activated carbons is expected to be small, and thus not able to accommodate large holes. We thus decided to focus on the contribution of Single Vacancies (S.V.). Regarding the curved models instead, the most of them gave rise to contributions almost indistinguishable from the regular models (Figure 4. 16A and B) or from the disordered terminations (Figure 4. 16C and E). In addition, peculiar contributions such as the C-H termination exposed by a pentagonal ring was found to contribute in correspondence with one of the minima of the experimental spectra (Figure 4. 16D). Among the curved models, the only contribution providing a distinguishable contribution in the frequency range of the experimental signal is the isolated Z1 site (Figure 4. 16F), which was thus introduced into the fit. Therefore, the final fit was calculated by considering a linear combination of Z1D, D-all, disordered Z1, single vacancies and isolated Z1 contributions.

In order to ensure the stability of the fit, it was necessary to introduce some further reasonable constrain. At first, following the observation that the position of the main experimental bands is better described by the regular terminations than by the defective ones, it was decided to impose that the

concentration of regular terminations should be higher than the one of the defective ones. Secondly, when passing from the activated carbon support to the corresponding catalyst we expect that C-H terminations can only be removed, and not created. Therefore, all the coefficients in the linear combination fit of the catalysts were constrained to be equal or lower than in the fit of the parent carbon. The result of the linear combination fit performed with these functions and constrains for CwA is shown in Figure 4. 22 and for the other samples in Appendix C, while Table 4. 1 summarises the results of the fit calculated on all the steam activated carbons and corresponding catalysts. The optimised coefficients in the fit were normalised so that their sum was equal to one for the supports, while the catalysts were normalised as their supports in order to allow for a direct evaluation of the loss of H as a consequence of the metal nanoparticles deposition.

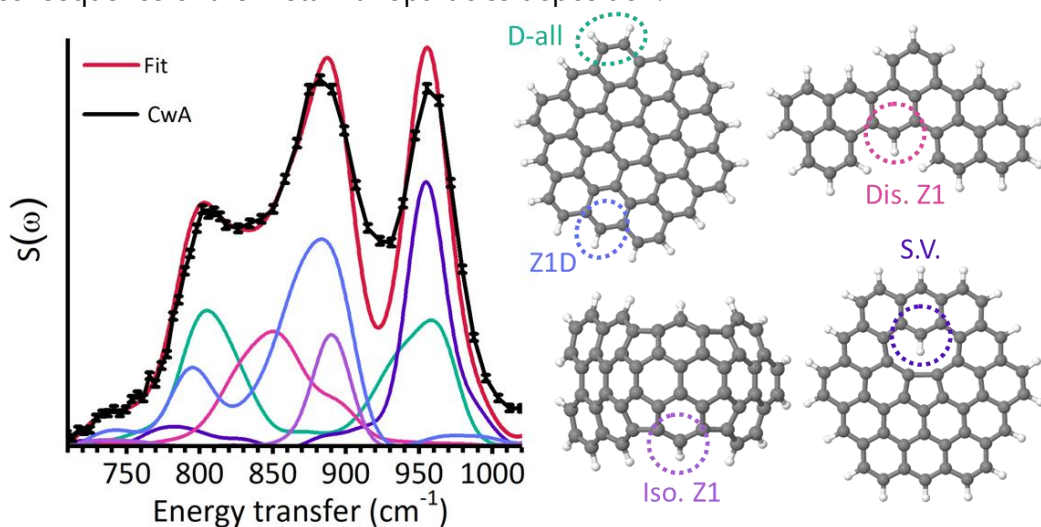


Figure 4. 22: fit of the INS spectrum of CwA using a linear combination of the contribution of regular and defective C-H terminations (Z1D, D-all, Disordered Z1, Isolated Z1 and Single Vacancy). An example of the geometry of each contribution is reported for clarity.

When comparing the results for the supports, it is possible to observe that D-all, Z1D and disordered Z1 are the main contributions for all the samples, while single vacancies and isolated Z1 are present at very low concentrations. The differences among the samples are clear. D-all sites are present at higher concentration in the two carbons of peat origin, and relevant differences are also observed when comparing the two samples of wood origin, which present a significantly different D-all/Z1 ratio (1.5 for CwA and 1.2 for CwB).

Table 4. 1: result of the linear-combination fit analysis on the INS spectra of the steam-activated carbons and related catalysts, comprehending both the contribution from the main regular and defective C-H terminations. The values for the supports are normalised to give 100% as a sum, while the ones of the catalysts are normalised as their parent support. The quality of the fit is evaluated by the RMSE (root mean square error).

	Z1D %	D-all %	Dis. Z1 %	SV %	Iso. Z1 %	TOT	RMSE
CwA	25	38	19	12	5	100	0.001
Pt(R)/CwA	20	36	19	12	5	92	0.001
Pd(NR)/CwA	15	32	17	11	4	78	0.001
Pd(R)/CwA	13	32	19	11	4	79	0.002
CwB	28	33	23	11	5	100	0.001
Pt(R)/CwB	15	29	11	9	4	67	0.001
CpA	24	42	22	10	2	100	0.001
Pt(R)/CpA	16	35	18	9	2	78	0.001
CpB	27	41	20	11	2	100	0.001
Pt(R)/CpB	18	36	19	11	2	86	0.001

As already shown when discussing the experimental spectra in Section 4.2.1, the deposition of the metal nanoparticles causes a reduction of the overall intensity of the spectra. This observation is clearly reflected by the decreasing in the amount of all the C-H terminations calculated by the fit. In addition, this analysis also allowed us to evaluate that, among all the terminations, the greatest variation was observed for Z1D sites. The most modest variation is observed for Pt(R)/CwA, for which the reduction of the Z1D sites corresponds only to the 5%. The deposition of Pd nanoparticles on the same support instead caused a much larger effect, with Z1D sites decreasing of the 10% for Pd(NR)/CwA and of 12% for Pd(R)/CwA. The greatest variation is observed for Pt(R)/CwB, for with the deposition of the Pt nanoparticles resulted in a decrease of the 13% in Z1D sites and of the 12% in disordered Z1 sites. For the two samples of peat origin instead the effect was quite similar, with an observed decrease in Z1D sites of ~ 8-9% and a D-all decrease of ~5-7%. The observation that Z1D sites are more strongly perturbed by the introduction of Pt and Pd nanoparticles suggest that they can play a relevant role in the nanoparticles-support interaction. Similar conclusions were proposed in the work by Poidevin *et al* [14] regarding extended zigzag edges which, according to their simulations, are able to establish covalent bonds with small Pt nanoparticles thanks to the stronger radical character of the molecular orbitals localized at these terminations. On the other hand, their simulations did not predict the same behaviour in the case of models only exhibiting short Z1D edges, which, according to the linear combination fit analysis, would be more representative of our samples.

4.4.2. Qualitative evaluation on the effect of functional groups

Even if the quality of the fit calculated including regular C-H terminations and physical defects is able to give a good description of the INS spectra of steam

activated samples, it still misses some intensity at about 925 cm^{-1} . In addition, the proposed fit is not able to describe the characteristic additional bands of Cchemi and of the oxidised samples at 750 and 910 cm^{-1} . Some of the C-H terminations perturbed by functional groups previously discussed can contribute in these regions, but their introduction into the fit was not feasible as the position of the bands in the simulated spectra of C-H terminations influenced by vicinal functionalities varies too much depending on the model, making it impossible to define a narrow and well-defined function describing the effect of each functional groups. The analysis relative to the effect of the functional groups was thus be purely qualitative.

By comparing the simulated INS spectra of some C-H terminations perturbed by an adjacent carboxylic acid group, and more broadly also carboxylates and carbonyls, with the experimental spectra of CwA-ox and Cchemi-ox a very good matching is observed with the main experimental band at 910 cm^{-1} (Figure 4. 23). This observation is also compatible with the TPD-IR quantification of the functional groups described in Chapter 3, which showed a large concentration of carboxylic acid groups in these samples in comparison with their parent carbons. The best match with the most intense band of these spectra is observed in the case of C-H terminations vibrating alone (i.e. Z1 sites, or C-H which remained alone on a benzene ring after introducing a functional group), while the perturbation of D, T or Q sites would lead to a larger number of bands. In addition, the decrease in the 800 and 950 cm^{-1} bands can be partially explained in terms of a reduction of the contribution arising from unperturbed D-all terminations. This suggests that the majority of C-H groups in the oxidised samples consists in isolated C-H terminations perturbed by a vicinal carboxylic acid group.

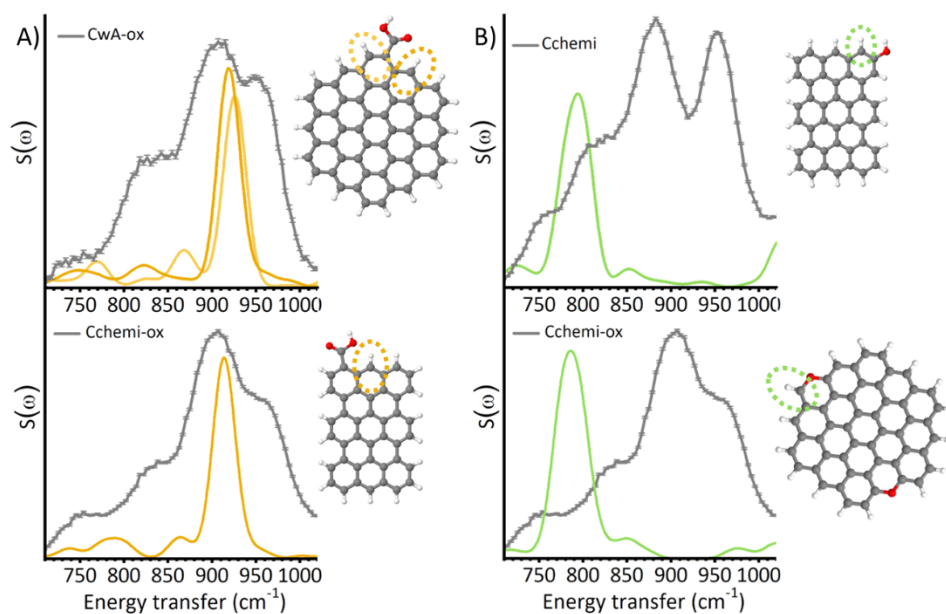


Figure 4. 23: A) Comparison between the simulated INS spectra of C-H terminations adjacent to carboxylic acids groups and the experimental spectra of CwA-ox and Cchemi-ox. B) Comparison between the INS spectra of the C-H group adjacent to phenols (first plot) and ethers (second plot), and the experimental spectra of Cchemi and Cchemi-ox.

From another perspective, this observation can also provide some hints about the position of the functional groups along the borders of the graphenic domains. In fact, if we consider the Z1 and D terminations (both regular and disordered) as the most likely, the position of the functional group that would maximise the number of perturbed C-H terminations vibrating alone would be the D one in Figure 4. 23A, first plot. A functional group in a Z1 position, instead, would result in the perturbation of the adjacent D corners, whose spectra would present a higher number of bands.

The features of the main peak in the spectra of the oxidised samples also appears very similar to the missing component in the linear combination fit used to quantify the terminations in the steam-activated samples (Figure 4. 22). So that the concentration of carboxylic acid groups is expected to be

low in these samples, as discussed in Chapter 3, in this case the role of the perturbation arising from thermo-resistant groups such as carbonyls appears more likely.

Cchemi, Cchemi-ox and, to a lesser extent, CwA-ox, also present a well-defined shoulder at about 750 cm^{-1} . In this case the matching between the experimental spectra and the simulated contributions of C-H terminations perturbed by functional groups are less precise. Among the results of the simulations, the closest results were obtained in the case of C-H terminations vibrating alone and perturbed by an adjacent ether or phenolic group, as shown in Figure 4. 23B. Also in this case, the presence of a sensible amount of this class of functional groups in these samples is confirmed by the results of the TPD-IR quantification discussed in Chapter 3.

4.5. Conclusions

In this chapter, the results of the characterization of the C-H terminations in activated carbons and related catalysts by means of a complementary INS and DFT study were presented and discussed. High resolution INS spectra were collected on four physically activated carbons, six catalysts prepared by depositing on the former supports Pd or Pt nanoparticles, one carbon chemically activated in H_3PO_4 and on two carbons post-oxidised in HNO_3 . The spectra pointed out significant differences among samples obtained from different precursors and/or following different activation routes, but also an important reduction of the intensity of the spectra upon deposition of the metal nanoparticles. In the case of the supported Pt catalysts, the observed decrease in intensity, which was demonstrated to be proportional to a reduction in the hydrogen content in the sample [4], showed a linear trend with the metal nanoparticles dispersion. These observations indicate that the metal nanoparticles are able to interfere with the C-H terminations, and that

the perturbation is stronger for small nanoparticles exposing a higher number of surface sites. It was also possible to observe that the reduction in H content is higher in the case of Pd nanoparticles, albeit their lower dispersion. Very important modifications were also observed following the oxidation of two of the activated carbons, resulting in a drastic decrease of the overall spectral intensity and profile.

In order to interpret the spectra and their differences, a large systematic DFT work on aromatic models featuring regular C-H terminations, defective ones and O-containing functional groups was made. It was possible to observe that the INS spectra of relatively simple aromatic models display analogous features as the experimental spectra of activated carbons, and that the region of the spectra in the 690 – 1020 cm^{-1} range provides a good fingerprint for the local morphology of the C-H terminations. This allowed us to classify a large number of C-H terminations, comprehending regular edges, physical defects and the perturbation arising from functional groups, and associate them with characteristic INS spectra.

In the case of the steam-activated samples and of the related catalysts, which present a low concentration of functional groups, it was possible to quantify the principal C-H terminations by fitting the experimental spectra with a linear combination of regular terminations and physical defects. This analysis pointed out that the most present C-H terminations in these samples are, in the order: 1) C-H at regular armchair borders, at duo corners or at disordered duo terminations (D-all); 2) C-H at regular zigzag borders and vicinal to a duo corner (Z1D); 3) C-H at disordered zigzag borders (disordered Z1); 4) isolated C-H (isolated Z1); and 5) C-H in single vacancies inside the graphenic platelets. It was not possible to obtain a specific fingerprint unambiguously indicating the curvature of the platelets, but some of the contributions resulting from the fit (isolated Z1 and single vacancy) are indeed

not planar, indicating that it is not possible to obtain a good description of the INS spectra of activated carbons by considering flat structures only. Significant differences were observed between the carbons of peat origin and wood origin, with the former exhibiting a larger concentration of D terminations, but also between the two samples of wood origin, with CwB showing a much larger amount of Z1D sites than CwA. Following the metal nanoparticles deposition, the most evident variation in concentration was observed for Z1D sites. Considering also that samples displaying the largest concentration of Z1D sites (Cw samples) also presented the highest metal nanoparticles dispersion, it appears likely that this kind of terminations can play an important role in the interaction between the support and the metal nanoparticles and in favouring a higher dispersion of the metal.

In the case of Cchemi and the two oxidised samples instead, the concentration of functional groups was evidently no more negligible, as also demonstrated by the TPD-IR quantification discussed in Chapter 3. In this case a quantification of the C-H terminations was not possible, but the simulations allowed for some important qualitative observations. First of all, the main band in the spectra of the oxidised samples shows a good match with the simulated spectra of C-H terminations vibrating alone and adjacent to carboxylic acid groups (and, sometimes, carboxylates or carbonyls). This observation, together with the decrease of the signals at 800 and 950 cm^{-1} , that in the case of the steam-activated samples were largely described in terms of D-all terminations, suggests that functional groups are more likely to be present at the D-all terminations than in the Z1 ones. The small shoulder at 750 cm^{-1} in the spectra of Cchemi and of the oxidised samples instead is compatible with the perturbation of ethers and phenols on the adjacent C-H terminations.

The analysis provided a much better understanding of the morphology of the C-H terminations in activated carbons prepared from different precursors and following different activation routes, and also their modification upon the metal nanoparticles deposition and the post-activation oxidation in HNO₃. These insights are very valuable as they allow us to better visualize the nature of these catalysts down to the atomic scale.

References

1. Harris P.J.F., *Fullerene-like models for microporous carbon*. Journal of Materials Science, 2013. **48**(2): p. 565-577.
2. Marsh H. and Rodríguez-Reinoso F., *CHAPTER 2 - Activated Carbon (Origins)*, in *Activated Carbon*, Marsh H. and Rodríguez-Reinoso F., Editors. 2006, Elsevier Science Ltd: Oxford. p. 13-86.
3. Harris P.J.F., Liu Z., and Suenaga K., *Imaging the atomic structure of activated carbon*. Journal of Physics: Condensed Matter, 2008. **20**(36): p. 362201.
4. Albers P.W., Pietsch J., Krauter J., and Parker S.F., *Investigations of activated carbon catalyst supports from different natural sources*. Physical Chemistry Chemical Physics, 2003. **5**(9): p. 1941-1949.
5. Phung T.K. and Garbarino G., *On the use of infrared spectrometer as detector for Temperature Programmed (TP) techniques in catalysts characterization*. Journal of Industrial and Engineering Chemistry, 2017. **47**: p. 288-296.
6. Carosso M., Lazzarini A., Piovano A., Pellegrini R., Morandi S., Manzoli M., Vitillo J.G., Ruiz M.J., Lamberti C., and Groppo E., *Looking for the active hydrogen species in a 5 wt% Pt/C catalyst: a challenge for inelastic neutron scattering*. Faraday Discussions, 2018. **208**(0): p. 227-242.
7. Lazzarini A., Piovano A., Pellegrini R., Leofanti G., Agostini G., Rudić S., Chierotti M.R., Gobetto R., Battiato A., Spoto G., Zecchina A., Lamberti C., and Groppo E., *A comprehensive approach to investigate the structural and surface properties of activated carbons and related Pd-based catalysts*. Catalysis Science & Technology, 2016. **6**(13): p. 4910-4922.
8. Piovano A., Lazzarini A., Pellegrini R., Leofanti G., Agostini G., Rudić S., Bugaev A.L., Lamberti C., and Groppo E., *Progress in the Characterization of the Surface Species in Activated Carbons by means of INS Spectroscopy Coupled with Detailed DFT Calculations*. Advances in Condensed Matter Physics, 2015. **2015**.
9. Cavallari C., Pontiroli D., Jiménez-Ruiz M., Johnson M., Aramini M., Gaboardi M., Parker S.F., Riccò M., and Rols S., *Hydrogen motions in defective graphene: the role of surface defects*. Physical Chemistry Chemical Physics, 2016. **18**(36): p. 24820-24824.
10. Lazzarini A., Pellegrini R., Piovano A., Rudić S., Castan-Guerrero C., Torelli P., Chierotti M.R., Gobetto R., Lamberti C., and Groppo E., *The effect of surface chemistry on the performances of Pd-based catalysts supported on activated carbons*. Catalysis Science & Technology, 2017. **7**(18): p. 4162-4172.

11. Centrone A., Brambilla L., Renouard T., Gherghel L., Mathis C., Müllen K., and Zerbi G., *Structure of new carbonaceous materials: The role of vibrational spectroscopy*. Carbon, 2005. **43**(8): p. 1593-1609.
12. Zander M., *Die Herstellung von Polycyclischen Aromaten*, in *Polycyclische Aromaten: Kohlenwasserstoffe und Fullerene*, Zander M., Editor. 1995, Vieweg+Teubner Verlag: Wiesbaden. p. 158-187.
13. Stone A.J. and Wales D.J., *Theoretical studies of icosahedral C60 and some related species*. Chemical Physics Letters, 1986. **128**(5): p. 501-503.
14. Poidevin C., Paciok P., Heggen M., and Auer A.A., *High resolution transmission electron microscopy and electronic structure theory investigation of platinum nanoparticles on carbon black*. The Journal of Chemical Physics, 2018. **150**(4): p. 041705.

CHAPTER 5

Characterization of Pt-H species in γ -Al₂O₃ supported catalysts

5.1. Introduction

Platinum nanoparticles on transition alumina supports are largely employed as heterogeneous catalysts for many industrially relevant processes, such as the catalytical reforming of gasoline [1, 2], the hydrogenation and dehydrogenation of organic substrates [3, 4], or the oxidation of hydrocarbons and CO [5, 6]. Among the research activities of our group during the last few years, large focus was given to the study of this kind of catalysts, in particular in the frame of the PhD project of Dr. Michele Carosso [7, 8]. The Pt(NR)/Alu sample and its modifications under hydrogenation conditions were extensively characterized by means of FT-IR, INS, XAS and volumetric measurements, and the main results obtained will be summarized in the following. Many of the experimental observations were interpreted on the base of the computational simulations performed at IFPEN, France, demonstrated the H₂ and temperature driven reconstruction of Pt₁₃ nanoparticles supported on γ -Al₂O₃ [9, 10].

The simulation of the vibrational spectra corresponding to the models optimized at IFPEN would allow for a direct comparison of these experimental and computational results, providing a relevant added value to both the researches. A collaboration between the two research groups was thus established, aimed to the simulation of the INS spectra corresponding to the models simulated by the IFPEN group and to their direct comparison with the experimental data collected in the last years by our research group. A large part of my PhD activities were dedicated to this work, whose results will be discussed later in this chapter.

5.2. State-of-the-art

5.2.1. Previous experiments on the Pt(NR)/Alu catalyst

The Pt(NR)/Alu sample was one of the main focuses in the research activities of our group in the last years. The very high dispersion and narrow particle size distribution of the Pt nanoparticles (between 1 and 2 nm [8]) made it the most suited candidate for the spectroscopic characterization of the surface Pt-H species formed upon H₂ exposure. The sample has been widely studied by means of FT-IR, INS and XAS spectroscopies and volumetric measurements. The extensive discussion of these results can be found in reference [7], while a brief summary of the main spectroscopic results will be summarised in the following.

FT-IR and XAS spectroscopies. The results of a combined DRIFT, MS and XAS experiment performed at the ESRF will be here briefly summarised. This experiment focused on the characterization of the Pt-H species formed at the surface of the Pt(NR)/Alu catalyst at 120°C in a 10% H₂/He gas flow and of their evolution upon the progressive reduction of the H₂ concentration. The surface and structural modifications underwent by the system as a function of the hydrogen concentration were simultaneously monitored by means of

DRIFT (Figure 5. 1b and c) and XAS (Figure 5. 2) spectroscopies, while the composition of the gas flux was followed by on-line mass spectrometry (Figure 5. 1a). Analogous FT-IR results in transmission mode were obtained in our laboratory.

When treating the Pt(NR)/Alu sample in a gas flux of H₂/He at 120°C, four bands centred at ca 2115, 2040, 1990 and 1740 cm⁻¹ rapidly appear in the DRIFT spectrum (labels I, II, III, IV in Figure 5. 1c, first spectrum). All these bands were assigned to different linearly adsorbed Pt-H species on the base of the previous literature [11-16], while the bands related to the multi-coordinated Pt-H species are expected at lower frequencies and are hidden by the strong absorption of the support below 1200 cm⁻¹.

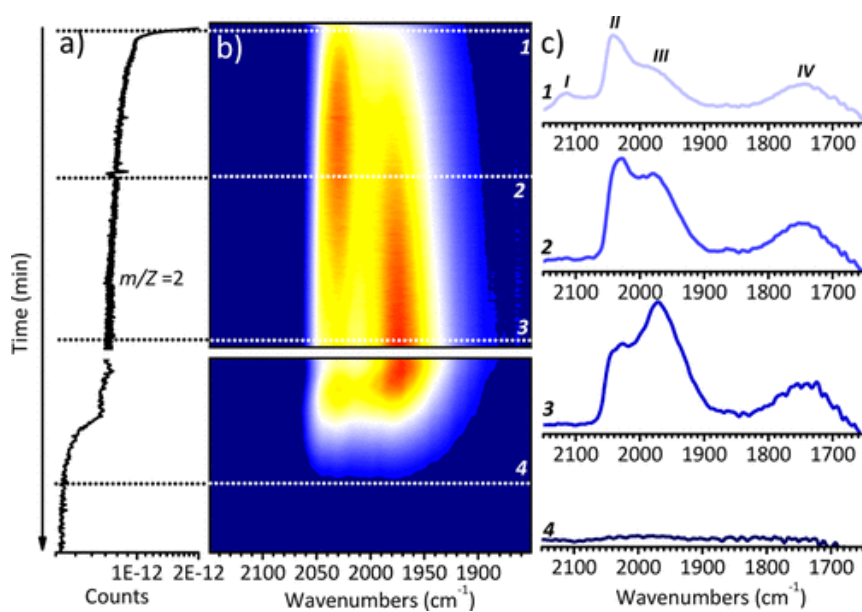


Figure 5. 1: a) evolution of the MS signal corresponding to the H₂ concentration ($m/Z = 2$) as a function of the time. b) 2D spectrum showing the evolution of the intensity of the DRIFT spectra when reducing the concentration of H₂ at 120°C. Blue corresponds to low signals, red to intense signal. c) detail over the DRIFT spectra in correspondence with four different times indicated in part b. From reference [8].

The possible assignment of the bands to Pt-CO species, possible since CO is a common contaminant of H₂ gas, was previously excluded by measuring the FT-IR spectrum of Pt(NR)/Alu in D₂ and observing the expected isotopic shift in the frequencies [8].

The gas feed was then turned to pure He to follow the evolution of the Pt-H species upon their desorption. A rapid decrease of all the four bands was expected, but this behaviour was observed only for band I. Oppositely, band II and III exhibited at first a slow increase in intensity, and started decreasing, i.e. lower H₂ concentration, only after very long times (spectrum 2 and 3 in Figure 5. 1c). Band IV instead remained relatively stable all over the experiment. At the end of the experiment all the Pt-H signals disappeared (spectrum 4 in Figure 5. 1c).

These results were counterintuitive at a first sight, since the increase in intensity of the signal of the linear Pt-H species was observed while reducing the partial pressure of H₂, thus under conditions in which the removal of the adsorbed hydride species was expected. However, comparable results were obtained in the frame of other FT-IR experiments in transmission mode, in both static and *operando* conditions, in the gas phase as well as in the liquid one [7]. This behaviour was explained in terms of Pt nanoparticles reconstruction in function of the H₂ partial pressure, considering the conversion of multi-coordinated Pt-H species (invisible to FT-IR) to linear Pt-H species as the H coverage of the nanoparticles decreased.

This interpretation is also in agreement with the simultaneously measured XAS spectra (Figure 5. 2). The Pt L₃-edge XANES spectra of the catalyst at decreasing hydrogen coverages are reported in Figure 5. 2a (from spectrum 1 to spectrum 4): an evident shift in the edge position and sharpening of the profile was observed upon decreasing the H coverage, and it was interpreted as a progressive modification of the electronic properties

of the Pt nanoparticles. Figure 5. 2b and c instead report the main results of the EXAFS analysis, which indicated a decrease in the Pt-Pt distance and in the Pt coordination number compatible with a reconstruction of the Pt nanoparticles upon dehydrogenation.

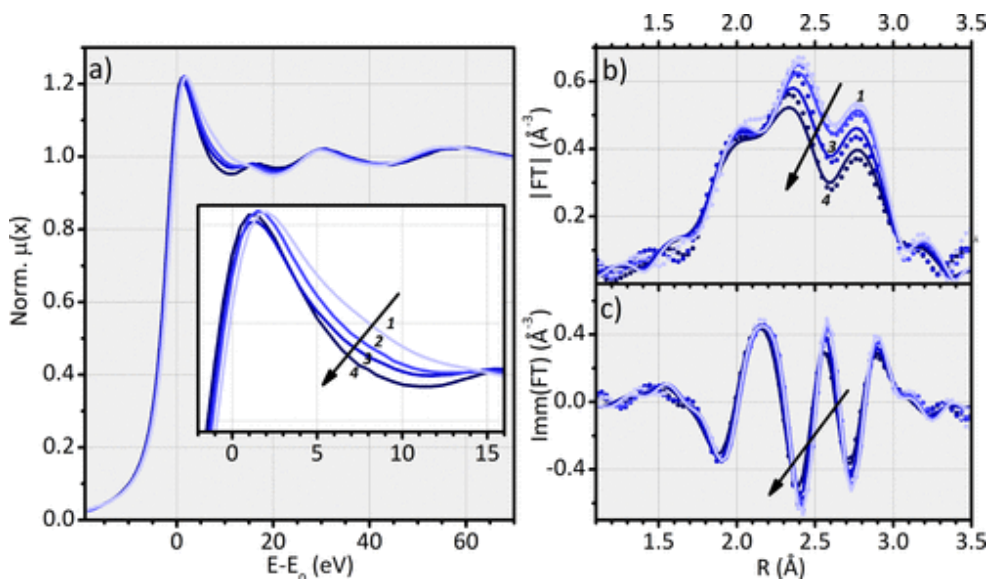


Figure 5. 2: a) Evolution of the normalized Pt L_{3} -edge XANES spectra of the Pt(NR)/Alu catalyst upon progressive dehydrogenation (from spectrum 1 to spectrum 4). The magnification over the white-line region is shown in the inset b) Modulus of the Fourier-transform of the k^2 -weighted EXAFS signals. c) the same as part b, for the imaginary part of the Fourier transform. From reference [8].

INS measurements. The INS spectra of Pt(NR)/Alu as such and in the presence of 420 mbar H_2 where measured on the LAGRANGE spectrometer at the ILL, Grenoble [17]. The spectra obtained are reported in Figure 5. 3a: in both cases, the signal is dominated by an intense and broad band centred at 905 cm^{-1} , which is attributed to the deformation modes of the hydroxyl groups at the alumina surface. By subtracting the INS spectrum of Pt(NR)/Alu as such to the one measured in the presence of H_2 it is possible to obtain the spectral fingerprint of the Pt-H species generated, as shown in Figure 5. 3b.

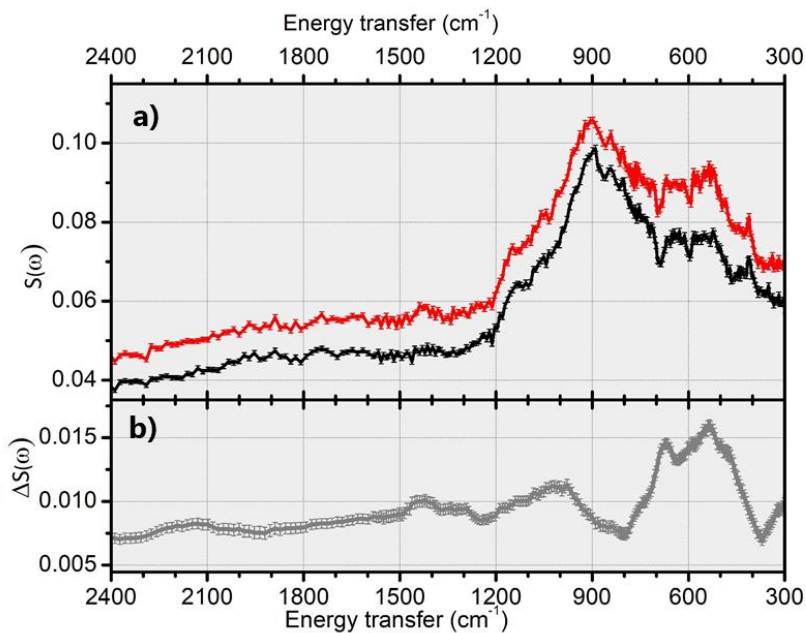


Figure 5. 3: a) INS spectrum of Pt(NR)/Alu as such (black line) and in the presence of 420 mbar of H₂ (red line). b) difference between the two spectra shown in part a, containing the fingerprint of the formed Pt-H species. Adapted from reference [8].

This spectrum presents a main broad signal in the 400–800 cm⁻¹ energy transfer range, and weaker signals between 800 and 1500 cm⁻¹.

These bands were attributed on the base of the previous literature, and in particular following the assignments proposed by Albers and Parker on the base of their INS experiments on high metal loading catalysts (20-60 wt %) [18-20]. Their latter assignment, based on the comparison with other vibrational spectroscopies such as HREELS or FT-IR on Pt extended surfaces, attributed the signals at 520, 950 and 1300 cm⁻¹ to the multi-coordinated Pt-H at the Pt(111) surface, the ones at 640 and 550 cm⁻¹ to the multi-coordinated Pt-H species at the Pt(100) surface, and the ones at 470 and 2080 cm⁻¹ (very weak) to the bending and the stretching mode of the linear Pt-H species, respectively [20]. On this basis, the observed signals at energy transfer lower than 2000 cm⁻¹ in the spectrum in Figure 5. 3b were assigned

to vibrational modes of multi-fold coordinated hydrides, while the weak and broad signal at about 2150 cm^{-1} corresponds to the $\nu(\text{Pt-H})$ of linear species previously discussed for the FT-IR spectra. It worth noticing the complementarity of the two vibrational spectroscopy employed, as INS results more sensible to the low frequency modes of the multi-coordinated Pt-H species, while FT-IR can only access to the stretching modes of the linear ones.

Recently, the research group of Parker and Albers proposed a new assignment, based on the simulation of the INS spectrum of a $\text{Pt}_{44}\text{H}_{80}$ particle with a diameter of 1.1 nm [21], whose results are summarised in Figure 5. 4. Overall this simulation confirmed the previous assignments of the INS signals to the bending of linear Pt-H species and to the vibrational modes of the multi-coordinated Pt-H sites, but it also shows that the signals are much broader than what the early assignment proposed, because of collective vibrational modes involving multiple Pt-H species at once.

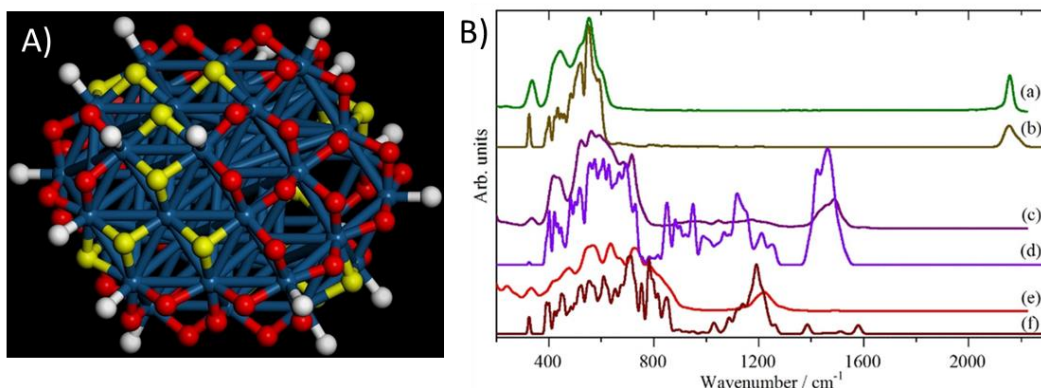


Figure 5. 4: A) $\text{Pt}_{44}\text{H}_{80}$ model simulated in reference [21]. Top Pt-H species are indicated in white, 2-fold coordinated hydrides in red and 3-fold coordinated hydrides in yellow. B) simulated INS spectra of top, 2-fold and 3-fold hydrides calculated by means of AIMD calculation (a, c and e) or lattice dynamics (b, d and f). Only the first order transition is plotted. From reference [21].

5.2.2. Computational evidences for the H₂-induced reconstruction of γ -Al₂O₃ supported Pt nanoparticles

Pt nanoparticles supported on transition alumina are intrinsically complex systems, and the computational simulation of their interaction with H₂ and other adsorbates and reactants is not trivial. The closest models proposed in the literature to our Pt(NR)/Alu sample are the ones described in the works published by the IFPEN group, which mostly focus on Pt₁₃ nanoparticles supported on γ -Al₂O₃ and their modification under interaction with adsorbates [9, 22, 23]. Also extended Pt surfaces [9] and larger supported nanoparticles were considered.

The models. Both the models used for the support and for the nanoparticles are the result of long-lasting research works. For the γ -Al₂O₃ support, which present a high degree of intrinsic disorder, they established that its structure could be simulated considering a fcc lattice of O²⁻ in which the 25% of Al³⁺ cations occupy tetrahedral interstices and the 75% octahedral ones and where both spinel and non-spinel sites can be occupied [24]. The expected crystalline habit of γ -Al₂O₃ is the one represented in Figure 5. 5, according to which the most extended exposed surface is the (110), followed by the (100) one and finally by the (111) one [25]. Hydroxyl groups are generally formed at these surfaces when exposing the material to air, but can be removed by increasing the temperature and reducing the H₂O partial pressure. The thermodynamic stability of the hydroxyl species on the two most extended surfaces was also object of study, and this analysis indicated that under catalytically relevant conditions (T > 600 K and very low H₂O partial pressures) the (100) surface is completely dehydroxylated, while the (110) is still partially covered by -OH groups [26, 27].

These two surfaces were then used as supports for Pt₁₃ clusters (diameter of about 1 nm), where the dimension of the nanoparticles was chosen to have the smallest number of Pt atoms to keep a cubooctahedral geometry, while being representative of real catalysts with a very high metal dispersion [22, 28]. The most stable structures for the Pt₁₃ nanoparticle deposited over the (100) and (110) surfaces of γ -Al₂O₃ were explored by means of molecular dynamics (MD) simulations, indicating that the nanoparticle-support interaction is stronger for the dehydroxylated (100) surface than for the hydroxylated (110) one [22]. This also resulted in a different morphology of the particles, as shown in Figure 5. 5: in fact, in the former case the contact area between the nanoparticle and the support was larger, resulting in a biplanar structure, while in the second case the nanoparticle is weakly bonded to the surface -OH groups and exhibits a more complex 3D geometry. In the latter case, the migration of few H atoms from the support to the Pt₁₃ nanoparticle was also observed.

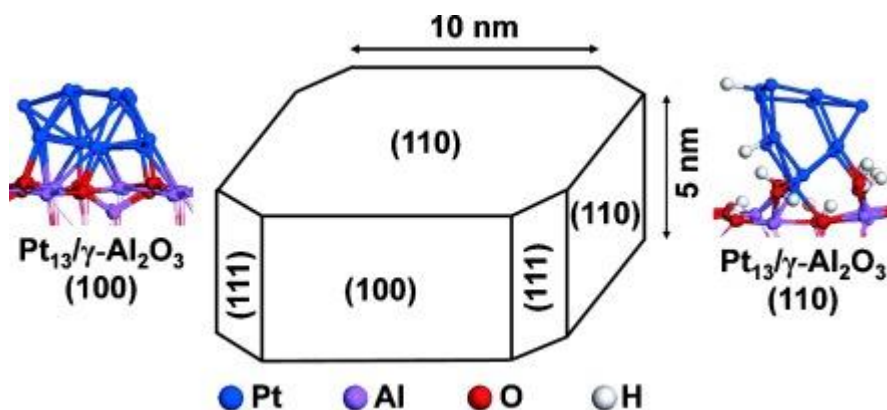


Figure 5. 5: schematic representation of the most common crystal habit for γ -Al₂O₃, and of the optimised structures of the Pt₁₃ nanoparticles located at the γ -Al₂O₃ (100) and (110) surfaces. In the latter case the surface contains -OH groups, and the migration of two H atoms from the support to the nanoparticle is observed. From reference [10].

Interaction with H₂. The IFPEN group also explored the interaction of H₂ with the supported Pt nanoparticles and of extended Pt surfaces. The most stable morphologies for the Pt₁₃ nanoparticles at increasing H coverages were computed by means of molecular dynamics, and the thermodynamic diagram reporting the most stable coverage as a function of the temperature and H₂ partial pressure was calculated. The results obtained for the Pt₁₃ model at the γ -Al₂O₃ (100) surface are described in ref [9], while the one for the Pt₁₃ models at the γ -Al₂O₃ (110) surface are reported in the supporting information of ref [10].

Figure 5. 6 shows the thermodynamic diagram obtained for the Pt₁₃ nanoparticle at the γ -Al₂O₃ (100) surface. We can observe that, upon hydrogenation conditions, the Pt₁₃ nanoparticle is not just increasing its H coverage, but that a complete reconstruction of the cluster to a new geometry occurs. At low H₂ partial pressure and/or high temperature, the biplanar geometry in strong interaction with the support was calculated to be the most stable, while at high H₂ partial pressure and/or low temperature the nanoparticle reconstructed into a high-symmetry cuboctahedric geometry completely solvated by H atoms, with a coverage up to 3 H for each exposed Pt. The transition between the two geometries was calculated to occur at an H coverage between 18 and 20 H atoms.

A more detailed analysis of the structural modifications underwent by the Pt₁₃ nanoparticle is summarised in Figure 5. 7. The transition from a biplanar to a cuboctahedric morphology of the Pt₁₃ cluster clearly corresponded with an increase in the distance with the support (Pt-O and Pt-Al distances) and a loss of the direct bonding between the Pt atoms and the O and Al sites of γ -Al₂O₃ (Figure 5. 7a and b).

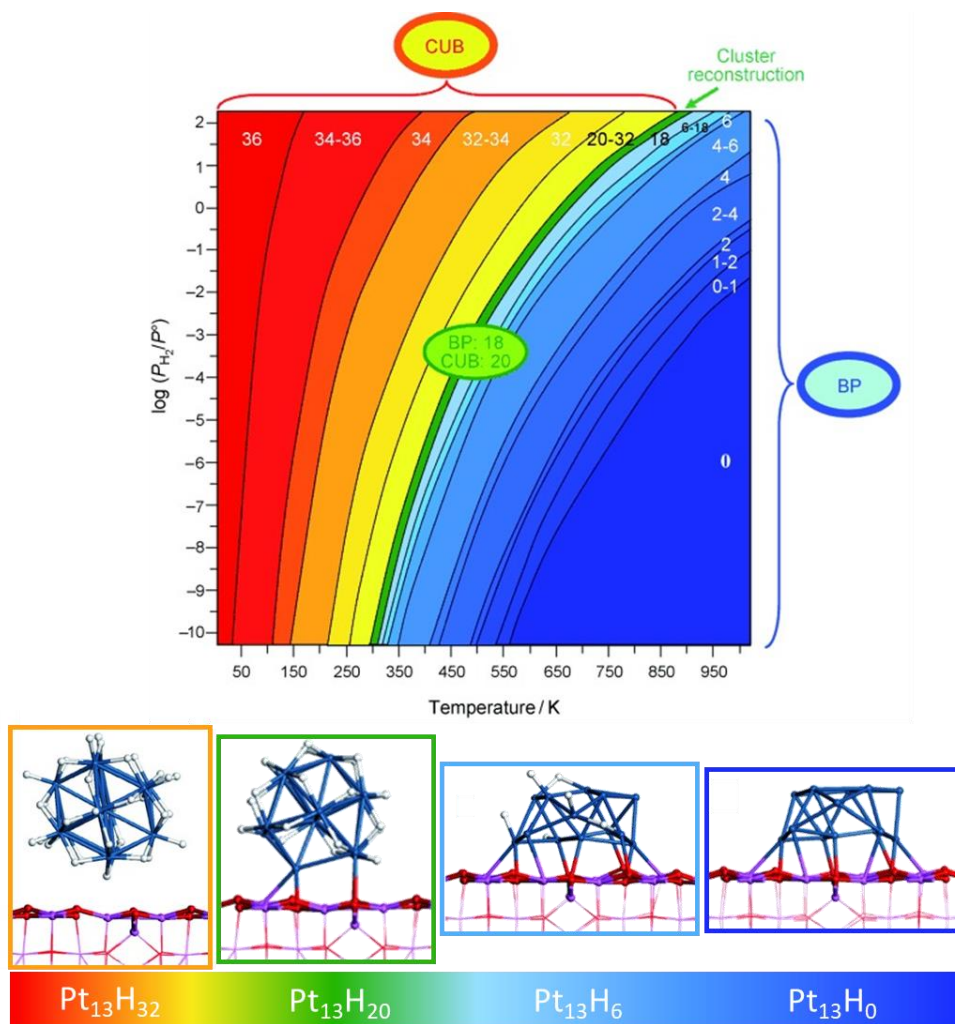


Figure 5. 6: thermodynamic diagram displaying the most stable H coverage of the Pt_{13} nanoparticles supported at the $\gamma-Al_2O_3$ (100) surface as a function of the temperature and of the H_2 partial pressure. The models corresponding to the bare nanoparticle (blue), to a coverage of 6 H (light blue), of 20 H (green) and of 32 H (orange) are shown. At a coverage of 18-20 H, a transition from a biplanar structure in strong interaction with the support to a cuboctahedron in weak interaction with the support occurs. Adapted from reference [9].

In addition, the geometric reconstruction was also associated with a conversion of linear to bridged Pt-H species, as similar numbers of top and bridged sites were observed at coverages lower than 18, while bridged sites

were by far the most favoured at coverages higher than 20 (Figure 5. 7c). A single hollow Pt-H species instead was only observed in the Pt₁₃H₁₈ model. The same kind of analysis on the Pt₁₃ nanoparticles at the hydroxylated γ -Al₂O₃(110) surface also showed similar reconstruction patterns, albeit the low-coverage models systematically exhibited less regular structures [10].

Other computational studies on the interaction of H₂ with supported Pt nanoparticles showed compatible results, such as that of Koningsberger *et al* [29] and Wang *et al* [30].

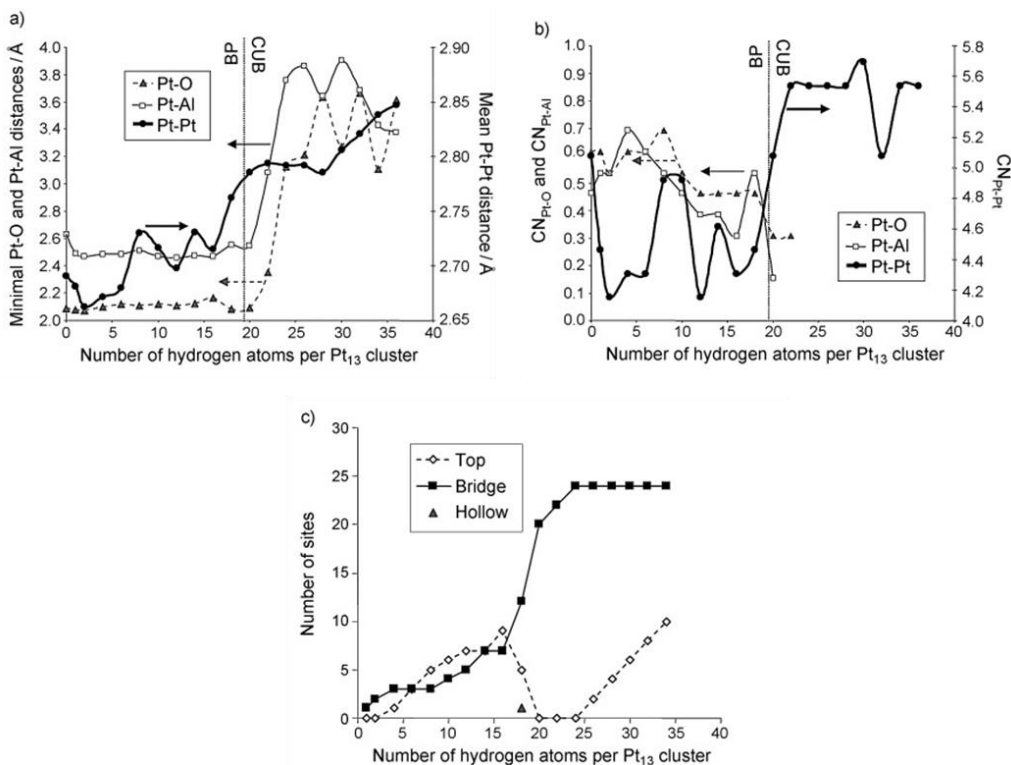


Figure 5. 7: summary of the modification of the main geometrical parameters in the Pt₁₃H_x nanoparticles supported at the γ -Al₂O₃ (100) surface as a function of the H coverage. a) mean Pt-Pt distance and minimal Pt-O and Pt-Al distances between the nanoparticle and the support; b) average Pt coordination number, c) number of Pt-H in top, bridge and hollow position. From reference [9].

The results of these simulations are in good agreement with the experimental observations of others] [31-33] and of our group. In particular, the fact that the maximum number of top Pt-H is observed at a relatively low H coverage of 16 matches with our previous FT-IR results, in which an increase in the signal of the linear Pt-H species was always observed upon H removal, and also by the reconstruction observed by XAS.

5.3. Results and discussion

5.3.1. Pt₁₃H_x nanoparticles supported at the γ -Al₂O₃ (100) surface: simulation of the INS spectra

The INS spectra of four representative models of Pt₁₃H_x nanoparticles deposited on the γ -Al₂O₃ (100) surface I have simulated are shown in Figure 5. 8. The INS spectra of the other models at intermediate hydrogen coverages are reported in Appendix D instead. All the spectra are compared with the experimental difference INS spectrum between the sample Pt(NR)/Alu in presence of 420 mbar of H₂ at room temperature and of the catalyst as such, which contains the fingerprint of the Pt-H species formed on the catalyst under those conditions of H₂ partial pressure and temperature.

Low coverage models with a biplanar structure, such as Pt₁₃H₆ or Pt₁₃H₁₆ (Figure 5. 8A and B), generally contain comparable amounts of top and bridged Pt-H species, while in Pt₁₃H₁₈ one hollow site was also present. Their bridge and hollow sites often present asymmetric Pt-H bond lengths. The vibrational bands at energy transfer higher than ca 2100 cm⁻¹ correspond to the ν (Pt-H) mode of the top species, while the ν_s mode of the bridged Pt-H spans in the 1600-1200 cm⁻¹ region, with the highest frequencies being observed for the most asymmetric species. Following, the corresponding ν_{as} modes falls in the 1200-800 cm⁻¹ range.

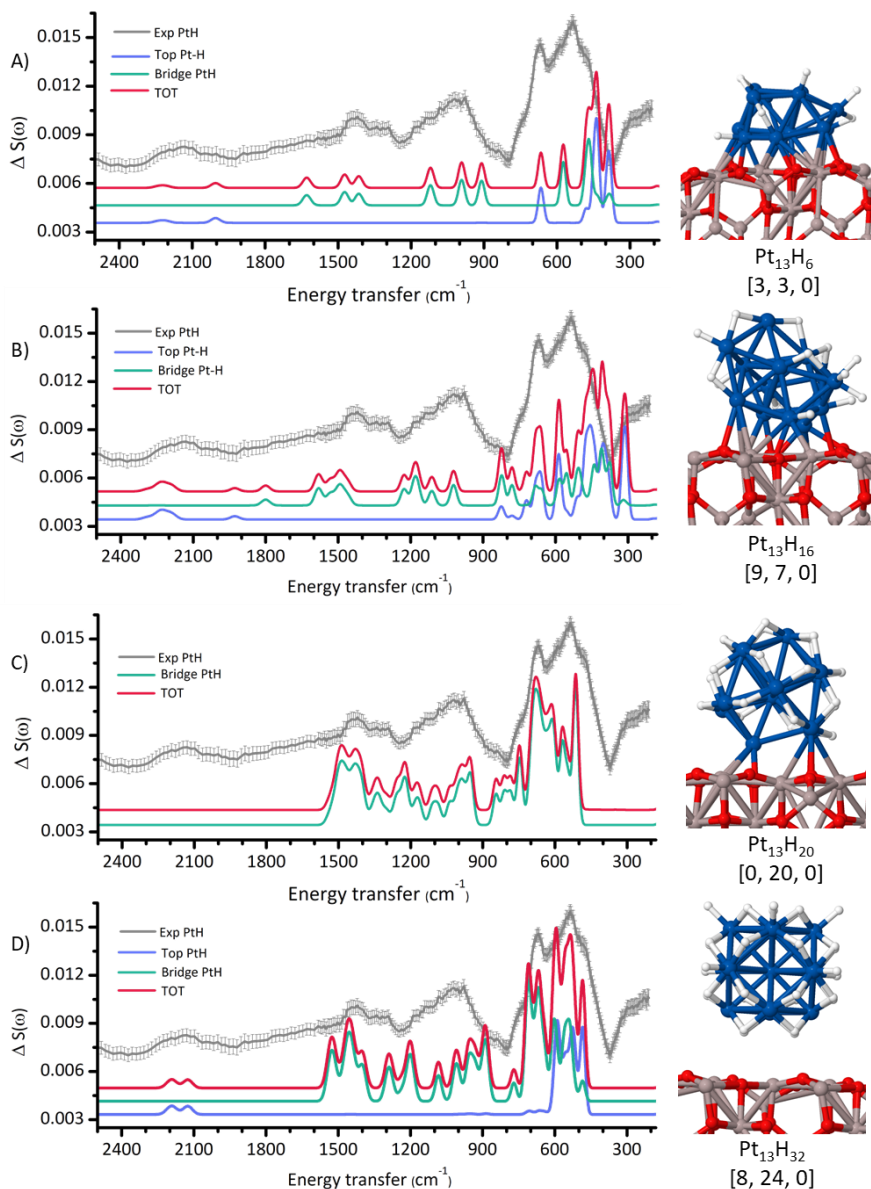


Figure 5. 8: comparison between the experimental difference INS spectrum containing the fingerprints of the Pt-H species (grey) with the simulated spectra of Pt_{13}H_6 (A), $\text{Pt}_{13}\text{H}_{16}$ (B), $\text{Pt}_{13}\text{H}_{20}$ (C) and $\text{Pt}_{13}\text{H}_{32}$ (D) at the $\gamma\text{-Al}_2\text{O}_3$ (100) surface. The contributions arising from top Pt-H (blue), from the bridge ones (green) and the total simulated INS spectra (red) are reported in stacked position. The geometry of each model is shown next to their corresponding spectra, together with a label indicating the formula of the Pt_{13}H_x nanoparticle and the number of Pt-H species of each type in the form [top, bridge, hollow].

Some of the models present Pt-H species perturbed by the support providing extra features in the 2000-1800 cm^{-1} range, which will be discussed in Section 5.3.4. The spectral profile becomes particularly complex in the 800-300 cm^{-1} region, where the observed bands are associated with combined δ modes involving all the Pt-H in the model.

The reconstruction from a biplanar to a cuboctahedric structure starts at a H-coverage of 20 and, as the H coverage increases, the interaction with the support progressively weakens in favour of a complete solvation with H atoms (Figure 5. 8C and D). These models mostly feature bridged sites, which are the only ones present in $\text{Pt}_{13}\text{H}_{20}$, and as the H coverage increases additional top Pt-H sites are progressively formed.

For these models, the spectral ranges occupied by top and bridge Pt-H species are overall similar to the ones observed at lower H-coverage, but generally a little narrowed. For these models, the signals at frequencies higher than 2100 cm^{-1} corresponds to the $\nu(\text{Pt-H})$ modes of top sites, the ones in the 1500-1400 cm^{-1} and 1350-800 cm^{-1} to the ν_s and ν_{as} of the bridged sites, respectively, and the 770-400 cm^{-1} region is associated with δ modes involving all the Pt-H terminations (with the bridge Pt-Hs mostly contributing to the 770-600 cm^{-1} interval, and the top ones to the 600-400 cm^{-1} range). It also worth noticing that the spectral features of the high-coverage cuboctahedric models, unlike the low coverage biplanar ones, are very similar among the models, with the greatest differences arising from variations in ratio between top and bridge Pt-H species. This is probably a consequence of the very similar shape exhibited by these models and of the weaker interaction with the support.

As a general comment, all the reported frequency ranges are relatively wide. This is a consequence of the collective nature of the vibrational modes involving all the Pt-H in the model, which results in a larger spread in the

frequency of the vibrational modes, and in complex spectral profiles which is more characteristic of the whole model than of the single Pt-H group. Consequently, I could not perform a precise classification of the Pt-H species on the base of their INS contribution I did for the activated carbon samples in Chapter 4.

5.3.2. Pt₁₃H_x nanoparticles supported at the γ -Al₂O₃ (110) surface: simulation of the INS spectra

The simulated spectra of the models Pt₁₃H₈, Pt₁₃H₁₆, Pt₁₃H₂₀ and Pt₁₃H₃₆ at the hydroxylated γ -Al₂O₃ (110) surface are reported in Figure 5. 9, while those of other Pt₁₃H_x models on the same γ -Al₂O₃ surface are shown in Appendix D. As discussed for previous calculations, the bare Pt₁₃ nanoparticle for these models presents a weaker interaction with the support, resulting in a lower contact area in comparison with the biplanar structure observed for the (100) surface [22]. The calculations performed at IFPEN also predicted that upon interaction with H₂ a reconstruction to a cuboctahedric geometry occurs [10], similar to that previously discussed. The simulations also pointed out a certain mobility of H atoms from and/or to the Pt nanoparticle, and in particular the migration of a few H atoms from the support to the nanoparticle at the lowest H coverages, and from the nanoparticle to the support at the highest ones.

The same assignment to the vibrational modes to top and bridge Pt-H species commented in the previous section remains valid for these models. Analogously ,INS spectra with complex profiles characterize the lower coverage models (Figure 5. 9A and B), which significantly changes with the geometry of the model.

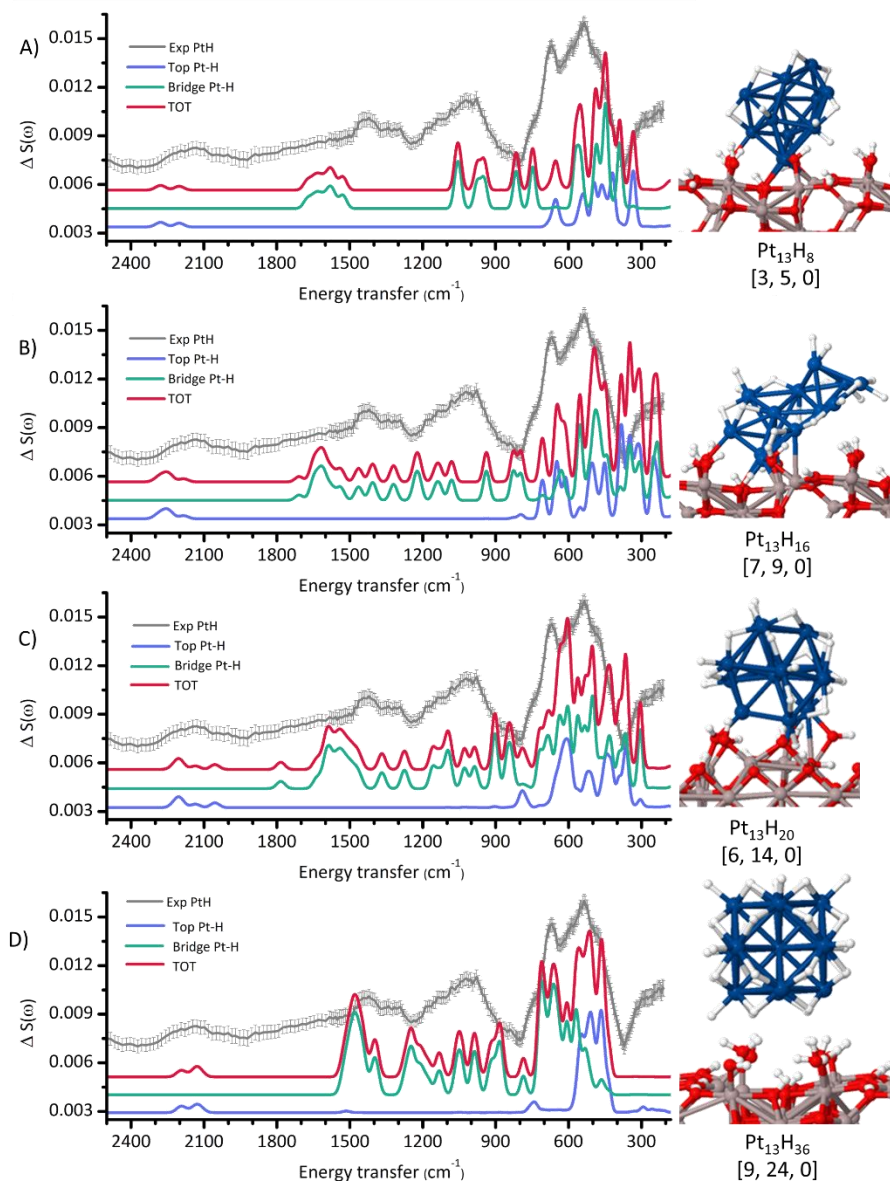


Figure 5. 9: comparison between the experimental difference INS spectrum containing the fingerprints of the Pt-H species (grey) with the simulated spectra of Pt₁₃H₈ (A), Pt₁₃H₁₆ (B), Pt₁₃H₂₀ (C) and Pt₁₃H₃₆ (D) at the γ -Al₂O₃ (110) surface. The geometry of each model is shown next to their corresponding spectra, together with a label indicating the formula of the Pt₁₃H_x nanoparticle and the number of Pt-H species of each type in the form [top, bridge, hollow]. H spillover from the nanoparticle to the support, or vice-versa, were also observed, resulting in a different number of Pt-H species than the expected one.

The reconstruction toward a cuboctahedric geometry (Figure 5. 9C) seems less sharp than in the previous case, resulting in a complex spectrum containing both contributions from top and bridge Pt-H sites, significantly different from its analogous on the γ -Al₂O₃ (100) surface. Finally, both the geometry and the spectral features of the high coverage Pt₁₃H₃₆ model (Figure 5. 9D) strongly resemble the ones of high coverage models previously discussed. This is not surprisingly, considering that these are the models in which the nanoparticle-support interaction is the weakest, and so the influence of the support on the Pt-H species is the lowest.

5.3.3. PtH_x species at larger nanoparticles: simulation of the INS spectra

I also simulated the INS spectra of two larger models, Pt₃₄H₅₄ and Pt₅₅H₄₄ on the (100) surface of γ -Al₂O₃ (Figure 5. 10). The bands assignments to the vibrational modes of top and bridge Pt-H species described in section 5.2.1 remains valid also in this case. In addition, these models include few hollow Pt-H species characterised by very asymmetric bond lengths. Their spectral features are model-dependent, since their vibrational modes are strongly combined with those of top and bridge Pt-H species. They contribute into few stretching bands in the 1500-950 cm⁻¹ range and they also participate to the collective bending modes in the 770-400 cm⁻¹ interval.

5.3.4. Effect of the γ -Al₂O₃ support on the INS spectra

Interfacial Pt-H sites. Up to this point, I neglected the effect of the support. However, I have subsequently performed a more detailed analysis showing that its influence could affect the properties of the Pt-H species in its proximity, with repercussions on the INS spectral features. These effects are relevant mainly for the low coverage models, where the interaction between the hydrogenated nanoparticle and the support is stronger.

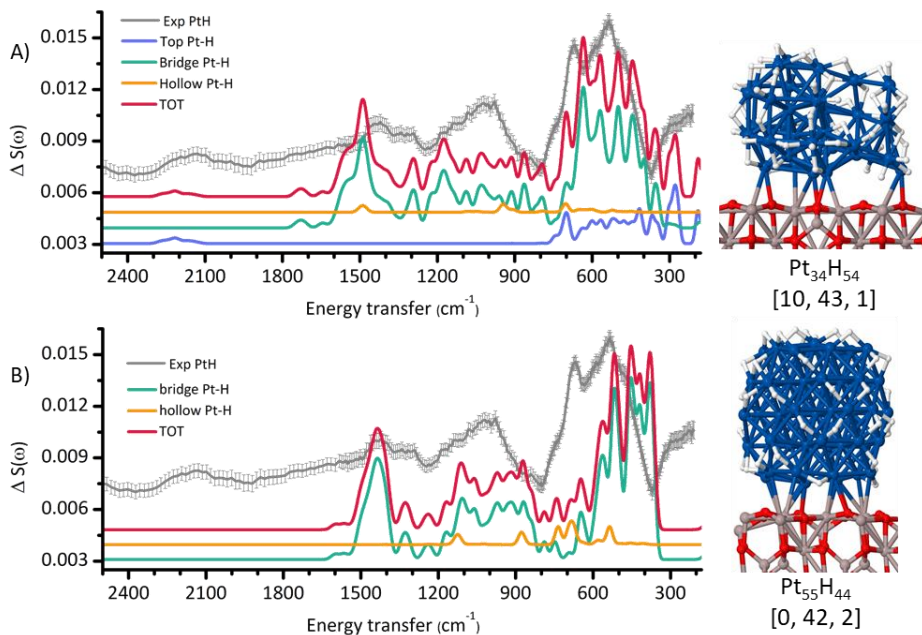


Figure 5. 10: comparison between the experimental difference spectrum containing the fingerprint of the Pt-H species (grey) with the simulated spectra of $\text{Pt}_{34}\text{H}_{54}$ (A) and $\text{Pt}_{55}\text{H}_{44}$ (B), at the $\gamma\text{-Al}_2\text{O}_3$ (100) surface. The geometry of each model is shown next to their corresponding spectra, together with a label indicating the formula of the Pt_xH_y nanoparticle and the number of Pt-H species of each type in the form [top, bridge, hollow].

A first example I present consists in top Pt-H species directly facing the support, in the following defined as interfacial top species (Figure 5. 11A). These linear Pt-H groups are characterized by bond lengths longer than usual, often above 1.60 Å (instead of the typical 1.56 Å), which corresponds to a decrease in the frequency of the $\nu(\text{Pt-H})$ mode with respect to standard linear Pt-H. The position of the bands relative to the $\delta(\text{Pt-H})$ modes, instead, remains in the range 800 to 400 cm^{-1} , as for the other Pt-H species. The most dramatic effect are observed when the H atom is in interaction with a close (~ 2 Å) low-coordination Al^{3+} ion of the support, which are present at the dehydroxylated $\gamma\text{-Al}_2\text{O}_3$ (100) surface but not on the hydroxylated (110) one.

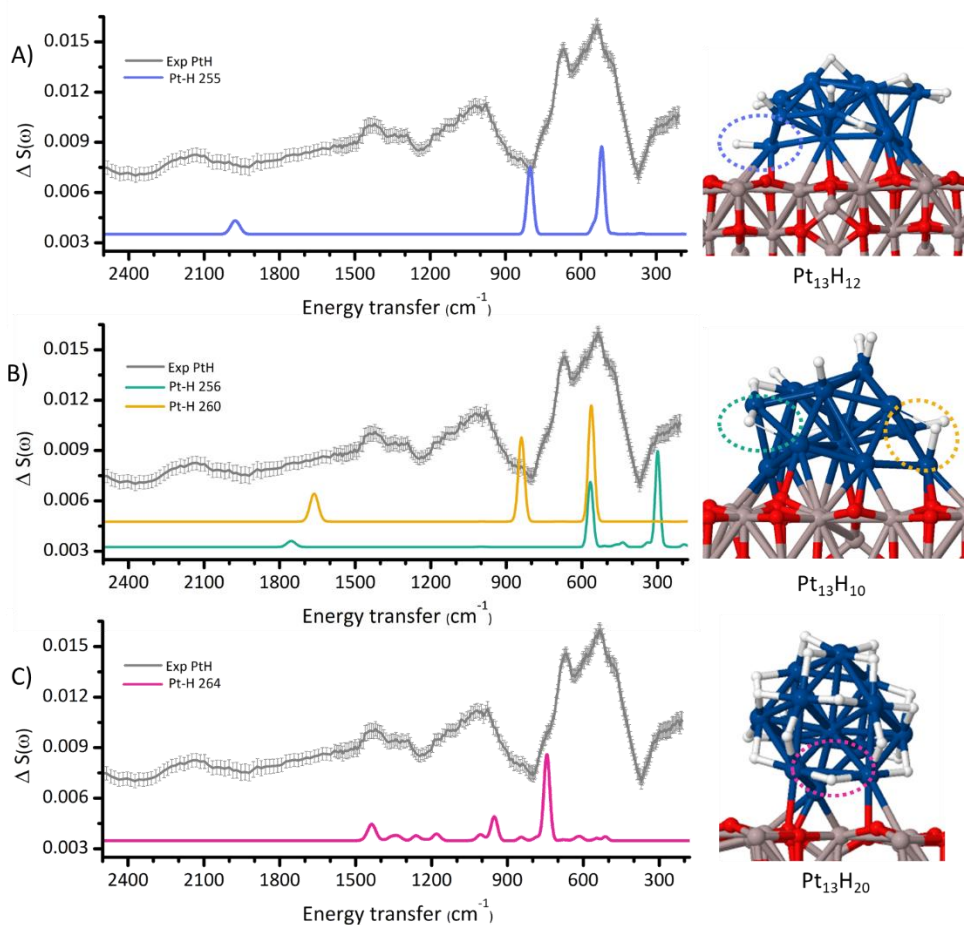


Figure 5. 11: simulated INS spectra of an interfacial top site in the $\text{Pt}_{13}\text{H}_{12}$ model, of two top-bridge sites in $\text{Pt}_{13}\text{H}_{10}$ and of an interfacial bridge species in $\text{Pt}_{13}\text{H}_{20}$. All the models are at the $\gamma\text{-Al}_2\text{O}_3$ (100) surface and are compared with the experimental spectrum.

For this reason, the greatest variations are observed in models at the dehydroxylated (100) surface.

Modifications of top Pt-H species might also occur in the case of the interaction of the H atom with a second Pt atom at a distance of $\sim 2 \text{ \AA}$ (instead of the typical 1.76 \AA), resulting in an intermediate geometry between top and bridge sites and, for this reason, defined in the following as top-bridge sites. These Pt-H species are usually observed when one of the Pt atoms involved

is directly bonded to the support, suggesting that the influence of the support could help to stabilize this kind of geometry. Their simulated INS spectra are reported in Figure 5. 11B: also in this case, the Pt-H bond is evidently elongated and this is reflected by particularly low vibrational frequencies for the $\nu(\text{Pt-H})$ mode, which fall within the $1800\text{-}1600\text{ cm}^{-1}$ range. Their bending mode instead are particularly dispersed in frequency, falling in the $900\text{-}300\text{ cm}^{-1}$ range.

Also bridge Pt-H species may be influenced by the support interaction, as shown in Figure 5. 11C. In this case, the most intense peak in the INS spectrum is observed at 750 cm^{-1} and corresponds to a $\delta(\text{Pt-H})$ vibration.

Surface OH groups. As previously commented, the experimental INS spectrum of the sample Pt(NR)/Alu is dominated by the vibrational modes of the surface hydroxyl groups, which exhibit a broad band in the $1200\text{-}300\text{ cm}^{-1}$ interval. Since the Pt nanoparticles models at the $\gamma\text{-Al}_2\text{O}_3$ (110) surface include surface hydroxyls, I could simulate their contribution to the total INS spectra, as shown in Figure 5. 12A. All the simulated spectra show several bands in the same frequency range as the experimental one, with evident variations in their position and relative intensity depending on the model. It can also be noticed that the intensity profile of the simulated spectra generally does not match well with the experimental, suggesting that these models are not able to fully represent the hydroxyl groups at the surface of the sample. In this regard, a substantial difference between the experimental and the simulated spectra lies in the activation temperature, as the experimental sample was treated at 120°C for removing the adsorbed H_2O and part of the surface -OH [8], while a temperature of $\sim 330^\circ\text{C}$ was considered for the simulations [28]. Thus, some differences in the degree of surface hydroxylation are expected.

The spectral variations among the models is caused by the reorganization of the surface -OH groups upon the reconstruction of the Pt₁₃ nanoparticle in the presence of H₂. The simulations describe a particular complex picture in which in some cases -OH groups can be bonded to the nanoparticle, and in some others the exchange of H atoms between the nanoparticle and the support occurs.

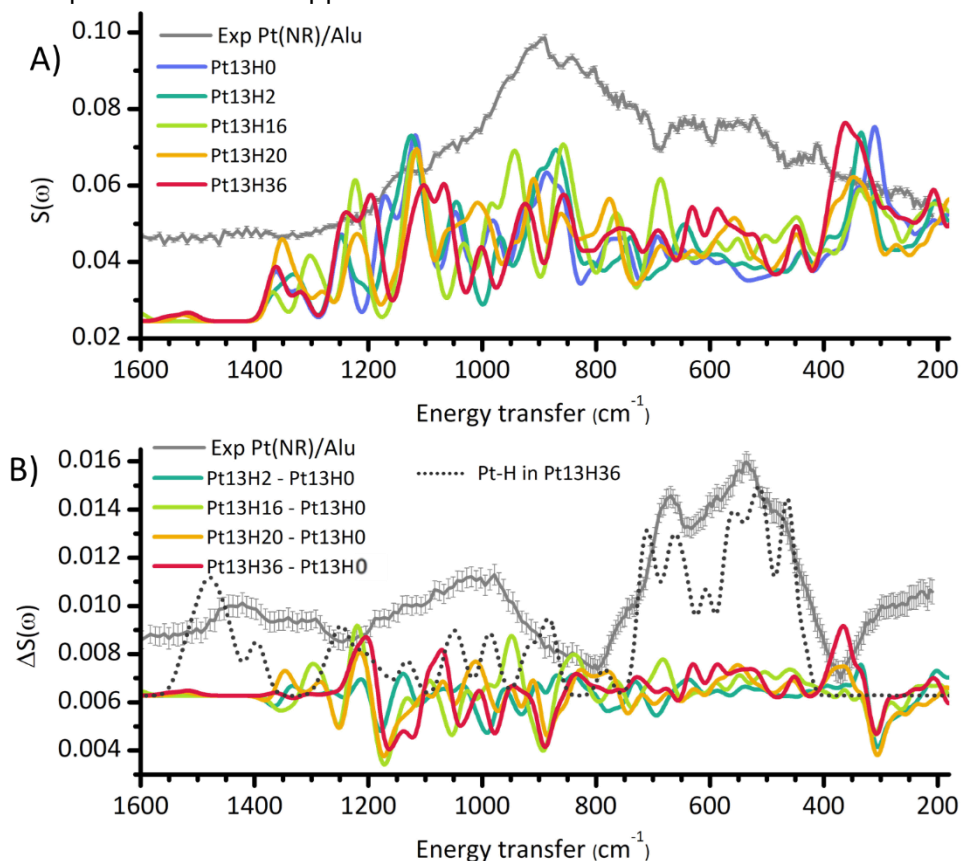


Figure 5. 12: A) experimental INS spectrum of the Pt(NR)/Alu catalyst compared with the contribution of the surface -OH groups in the models at the γ -Al₂O₃ (110) surface. B) Difference experimental spectrum calculated by subtracting the INS spectrum of Pt(NR)/Alu as such to the one collected in a 420 mbar of H₂ atmosphere, compared with the differences between the simulated spectra of the surface -OH groups in the hydrogenated models and Pt₁₃H₀. The simulated spectrum of the Pt-H contributions in Pt₁₃H₃₆ (dotted line) is also reported as a reference for the relative intensities. All the models are related to the hydroxylated γ -Al₂O₃ (110) surface.

In this frame, we can hypothesise that some of the small variations visible in the spectra upon H₂ exposure could arise from the reorganization of the surface hydroxyl groups, and not from the formation of the Pt-H species only. In theory, these differences should also be visible in the difference INS spectrum. To verify whether these contributions are negligible or not in respect with the ones arising from the Pt-H, the difference spectrum between the simulated contributions of the -OH groups in the hydrogenated nanoparticles models and the one of the starting bare Pt₁₃H₀ one were plotted and compared with the experimental difference spectrum, as shown in Figure 5. 11B. In order to compare the intensity of these signals to the ones of Pt-H species, the spectrum of Pt₁₃H₃₆ was also added as a reference. Outside the 1200-800 cm⁻¹ range, the contribution arising from the variations of the surface -OH groups appears negligible in comparison with the formation of Pt-H species.

5.3.5. Extended Pt surfaces: simulation of the INS spectra

For completeness, I have simulated the INS spectra of three typologies of Pt-H species at extended Pt(100) and Pt(111) surfaces, and in all cases both a low coverage of 1 H per unit cell and a high coverage of 4 H per cell were considered. All the simulated spectra are reported in Figure 5. 13. At present, the frequency calculations were limited to the Γ point. Since INS spectroscopy is able to access to the whole Brillouin zone, a phonon dispersion calculation would be needed for a complete simulation of the INS spectra. However, a preliminary test on a 2x2 supercell of the high Pt-H coverage Pt(100) surface, including points away from Γ , showed a limited broadening of the peaks and very small variations in their position, suggesting that the Γ -point simulation could be a good approximation for a first evaluation of the position of these INS signals. This comparison is shown in Appendix D.

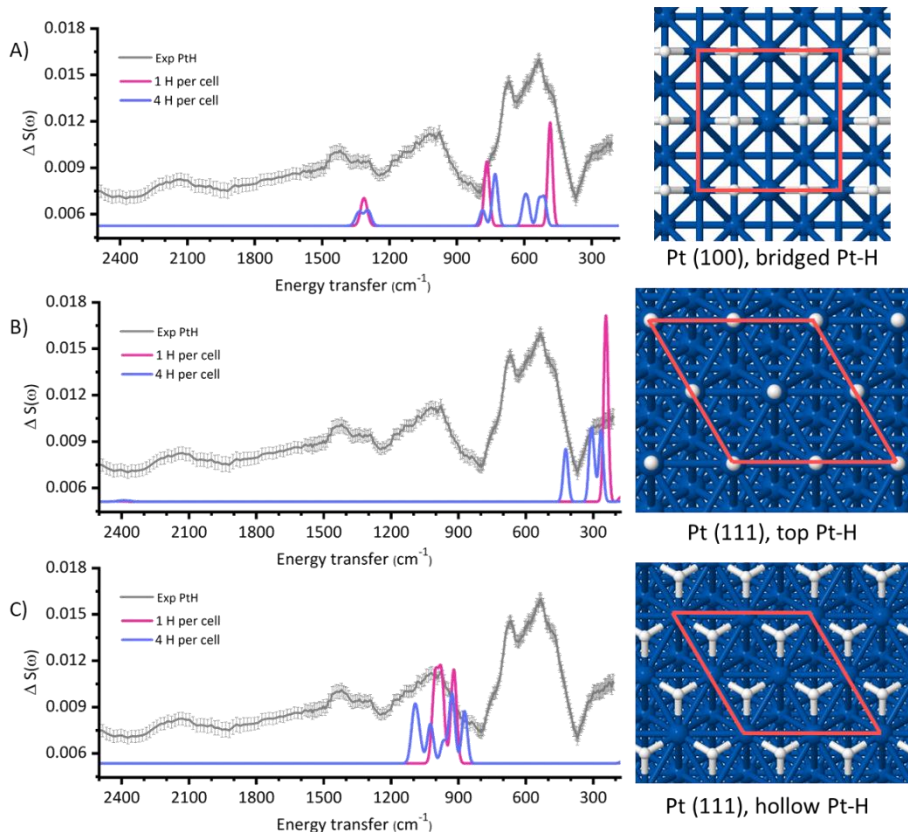


Figure 5. 13: comparison between the experimental difference spectrum containing the fingerprint of the Pt-H species (grey) with the simulated INS spectra of bridged Pt-H species at the extended Pt (100) surface (A), of the top Pt-H at the Pt (111) surface (B) and of the hollow Pt-H at the Pt (111) surface (C). The model corresponding to each spectrum is reported, and the unit cell indicated in red. Two different coverages of 1H and 4 H for unit cell were simulated. All the calculations were run at the Γ point.

The kind of vibrational modes observed are similar to those simulated for the supported nanoparticles systems, but they tend to show much narrower spectral profiles and, sometimes, slight variations in the vibrational frequencies.

- On the Pt(100) surface, Pt-H in bridged position were modelled. Their spectra present, for both the low and high H coverage models, one band at about 1300 cm^{-1} corresponding to the ν_s mode of the bridged Pt-H, a

few bands at about 700 cm^{-1} associated with their ν_{as} mode, and a few bands between 600 and 500 cm^{-1} attributed to the $\delta(\text{Pt-H})$ modes (Figure 5. 13A).

- On the Pt(111) surface instead, both top and hollow Pt-H species were simulated. In the case of the top sites, their INS spectra present a very weak band at about 2400 cm^{-1} associated with the $\nu(\text{Pt-H})$ mode, while the most intense signals correspond to the $\delta(\text{Pt-H})$ modes at frequency lower than 450 cm^{-1} (Figure 5. 13B). The hollow sites instead present a series of peaks in the $1100\text{-}850\text{ cm}^{-1}$ region, associated with different combinations of the Pt-H deformation modes.

5.3.6. Tentative interpretation of the experimental INS spectrum of Pt(NR)/Alu in excess of H_2

Many possible contributions to the experimental INS spectrum of $\text{PtH}_x/\text{Al}_2\text{O}_3$ has been screened. By comparing the experimental spectrum with those simulated for different models it is thus possible to evaluate which species are the ones most likely present in the real sample under the adopted experimental conditions. The contributions of all the simulated INS spectra are summarised in Figure 5. 14.

Considering the Pt_{13} models supported at the two $\gamma\text{-Al}_2\text{O}_3$ surfaces, the best matching with the experimental spectrum is observed for the high H-coverage cuboctahedric models, such as $\text{Pt}_{13}\text{H}_{32}$ at the $\gamma\text{-Al}_2\text{O}_3$ (100) surface (Figure 5. 8D) or $\text{Pt}_{13}\text{H}_{36}$ at the $\gamma\text{-Al}_2\text{O}_3$ (110) surface (Figure 5. 9D). This result appears promising, as under the experimental conditions of the experiment (420 mbar of H_2 sent at room temperature) those are the models that are predicted to be the thermodynamically most stable (Figure 5. 6) [9].

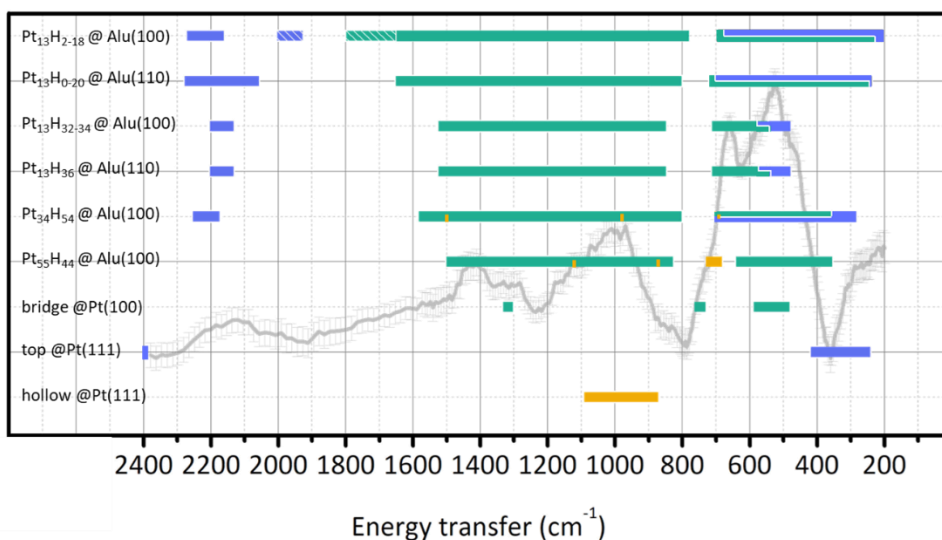


Figure 5. 14: summary of the positions of the spectral contributions of all the simulated INS spectra. Blue bars correspond to the contribution of top species, green to bridge ones and yellow to hollow ones. The lines pattern in the bars indicate the typical features of sites perturbed by the support (interfacial top species and top-bridge ones).

In this respect, most of the bands in the 750 – 400 cm⁻¹ interval are assigned to the bending modes of Pt-H species at reconstructed cuboctahedric nanoparticles (with bridge species mostly accounting for the 750-600 cm⁻¹ range and the top ones for the 600-400 cm⁻¹ interval), the bands in the 1500-800 cm⁻¹ interval comprehend the stretching modes of the bridge Pt-H species, while the weak band centred at about 2150 cm⁻¹ is attributed to the stretching modes of top Pt-H species.

However, it can be observed that the experimental spectrum is not integrally well described by these models alone, as spectral weight is missing in the 1500-900 cm⁻¹ range as well as at ~ 800 and 400 cm⁻¹. One first possible source of this discrepancy is the intrinsic difference between the simulated Pt₁₃ models (nanoparticles diameter ~ 1 nm, including atomic radii) and the Pt particles present in our sample (average dimension 1.5 nm, as evaluated by TEM analysis). In this respect, larger models such as Pt₃₄H₅₄ and Pt₅₅H₄₄ (Figure

5. 10) probably need to be included to provide a closer representation of the real sample under exam. It is possible to observe that, once again, the best match is observed for the model with the highest relative H coverage ($\text{Pt}_{34}\text{H}_{54}$), which presents a less symmetric geometry than the cuboctahedric ones and a more complex spectral profile. Larger nanoparticle, such as the Pt_{34} and Pt_{55} considered in this work, or the Pt_{44} nanoparticle considered in reference [21] also include hollow Pt-H species. Looking at the simulated contributions of these Pt-H species in larger nanoparticles (Figure 5. 10) or at the extended Pt(111) surface (Figure 5. 13C), it appears that the contribution of hollow species could be important to explain the band in the $1200 - 900 \text{ cm}^{-1}$ range of our experimental spectrum, where the contributions of top and bridge Pt-H species alone are not able to fully reproduce the experimental spectral profile. This spectral range is also the one in which the greatest variations in the contributions of the -OH species at the support surface was observed, and consequently it should be considered that part of this band could be ascribed to the hydroxyls groups.

We would also expect our experimental sample to include some interfacial Pt-H species. In this regard, interfacial sites such as interfacial bridge sites (Figure 5. 11C) seem to be able to describe the 800 cm^{-1} signal.

5.4. Outlook and conclusion

In this chapter, the simulation of INS spectra was used to correlate experimental and computational results for the understanding of the interaction of H_2 with Pt nanoparticle catalysts supported on $\gamma\text{-Al}_2\text{O}_3$, in the frame of a collaboration involving the university of Turin, ILL and IFPEN. By comparing the simulated INS spectra with the experimental ones it was possible to conclude that the Pt-H species formed upon hydrogenation at high H_2 pressure at room temperature [8] are in well agreement with the

reconstructed cuboctahedric Pt₁₃ models completely solvated by H atoms [9, 10].

However, the match of the experimental and simulated spectra is still not perfect. From the analysis, it appears that larger nanoparticles, also including interfacial Pt-H species and hollow sites at Pt (111) surfaces, would be required for a better description of the experimental spectra. This observation appears in agreement with the fact that the Pt nanoparticles in Pt(NR)/Alu are slightly larger than the simulated Pt₁₃ clusters, 1.5 nm vs 1 nm. Some differences were also observed regarding the spectral features of the surface -OH groups of the γ -Al₂O₃ support. On this regard, the discrepancy was ascribed to the different temperature of activation of the sample prior to the experimental measurements (120°C) and the one used for calculating the most stable hydroxyls coverage in the models (~ 330°C).

On this regard, extending the study to models closer to the real samples in terms of the metal nanoparticles dimension and the level of hydroxylation of the support surfaces could improve the match between experiment and simulations.

The measurement of new INS spectra measured at low H₂ partial pressure or at variable temperature is planned in the near future (exp nr DIR-177 and 7-05-514 on IN1/Lagrange at the ILL). These measurements would allow to explore experimentally the evolution of the Pt(NR)/Alu catalyst at low H-coverages, further extending this work.

References

1. *Catalytic Naphtha Reforming*. 2nd ed. 2004, Boca Raton: CRC Press
2. Gjervan T., Prestvik R., and Holmen A., *Catalytic reforming*, in *Springer Series in Chemical Physics*. 2004. p. 125-158.
3. Sattler J.J.H.B., Ruiz-Martinez J., Santillan-Jimenez E., and Weckhuysen B.M., *Catalytic Dehydrogenation of Light Alkanes on Metals and Metal Oxides*. *Chemical Reviews*, 2014. **114**(20): p. 10613-10653.
4. Bartók M., *Heterogeneous catalytic enantioselective hydrogenation of activated ketones*. *Current Organic Chemistry*, 2006. **10**(13): p. 1533-1567.
5. Kahlich M.J., Gasteiger H.A., and Behm R.J., *Kinetics of the Selective CO Oxidation in H₂-Rich Gas on Pt/Al₂O₃*. *Journal of Catalysis*, 1997. **171**(1): p. 93-105.
6. Gélin P. and Primet M., *Complete oxidation of methane at low temperature over noble metal based catalysts: a review*. *Applied Catalysis B: Environmental*, 2002. **39**(1): p. 1-37.
7. Carosso M., *PhD thesis: A multi-technique characterization of reactant-induced phenomena on supported Pt and Pd NPs for catalysis*, 2019, Università di Torino.
8. Carosso M., Vottero E., Lazzarini A., Morandi S., Manzoli M., Lomachenko K.A., Ruiz M.J., Pellegrini R., Lamberti C., Piovano A., and Groppo E., *Dynamics of Reactive Species and Reactant-Induced Reconstruction of Pt Clusters in Pt/Al₂O₃ Catalysts*. *ACS Catalysis*, 2019. **9**(8): p. 7124-7136.
9. Mager-Maury C., Bonnard G., Chizallet C., Sautet P., and Raybaud P., *H₂-Induced Reconstruction of Supported Pt Clusters: Metal-Support Interaction versus Surface Hydride*. *ChemCatChem*, 2011. **3**(1): p. 200-207.
10. Gorczyca A., Moizan V., Chizallet C., Proux O., Net W.D., Lahera E., Jean-Louis H., Raybaud P., and Joly Y., *Monitoring morphology and hydrogen coverage of nanometric Pt/ γ -Al₂O₃ particles by in situ HERFD-XANES and quantum*. *Angewandte Chemie - International Edition*, 2014. **53**(46): p. 12426-12429.
11. Eley D.D., Moran D.M., and Rochester C.H., *Infra-red study of interaction between hydrogen and supported platinum catalysts*. *Transactions of the Faraday Society*, 1968. **64**(0): p. 2168-2180.
12. Pliskin W.A. and Eischens R.P., *Infrared Spectra of Hydrogen and Deuterium Chemisorbed on Platinum*. *Zeitschrift für Physikalische Chemie*, 1960. **24**(1-2): p. 11-23.

13. Candy J.-P., Fouilloux P., and Primet M., *Adsorption d'hydrogène entre 300 et 873 K sur un catalyseur Pt/MgO*. Surface Science, 1978. **72**(1): p. 167-176.
14. Dixon L.T., Barth R., and Gryder J.W., *Infrared active species of hydrogen adsorbed by alumina-supported platinum*. Journal of Catalysis, 1975. **37**(2): p. 368-375.
15. Primet M., Basset J.M., Mathieu M.V., and Prettre M., *Infrared investigation of hydrogen adsorption on alumina-supported platinum*. Journal of Catalysis, 1973. **28**(3): p. 368-375.
16. Szilágyi T., *Fourier-transform infrared study of weak adsorption of hydrogen on Pt/SiO₂*. Journal of Catalysis, 1990. **121**(2): p. 223-227.
17. [dataset] Piovano A., Agostini G., Carosso M., Groppo E., Jimenez Ruiz M., Lamberti C., Lazzarini A., Manzoli M., Morandi S., Pellegrini R., and Vottero E., *Study of the Pt-hydride formation and spillover effect on Pt/Al₂O₃ and Pt/C catalysts DOI:10.5291/ILL-DATA.7-05-466*, 2016.
18. Albers P., Auer E., Ruth K., and Parker S.F., *Inelastic Neutron Scattering Investigation of the Nature of Surface Sites Occupied by Hydrogen on Highly Dispersed Platinum on Commercial Carbon Black Supports*. Journal of Catalysis, 2000. **196**(1): p. 174-179.
19. Albers P.W., Lopez M., Sextl G., Jeske G., and Parker S.F., *Inelastic neutron scattering investigation on the site occupation of atomic hydrogen on platinum particles of different size*. Journal of Catalysis, 2004. **223**(1): p. 44-53.
20. Parker S.F., Frost C.D., Telling M., Albers P., Lopez M., and Seitz K., *Characterisation of the adsorption sites of hydrogen on Pt/C fuel cell catalysts*. Catalysis Today, 2006. **114**(4): p. 418-421.
21. Parker S.F., Mukhopadhyay S., Jiménez-Ruiz M., and Albers P.W., *Adsorbed States of Hydrogen on Platinum: A New Perspective*. Chemistry – A European Journal, 2019. **25**(26): p. 6496-6499.
22. Hu C.H., Chizallet C., Mager-Maury C., Corral-Valero M., Sautet P., Toulhoat H., and Raybaud P., *Modulation of catalyst particle structure upon support hydroxylation: Ab initio insights into Pd₁₃ and Pt₁₃/γ-Al₂O₃*. Journal of Catalysis, 2010. **274**(1): p. 99-110.
23. Zhao W., Chizallet C., Sautet P., and Raybaud P., *Dehydrogenation mechanisms of methyl-cyclohexane on γ-Al₂O₃ supported Pt₁₃: Impact of cluster ductility*. Journal of Catalysis, 2019. **370**: p. 118-129.
24. Krokidis X., Raybaud P., Gobichon A.-E., Rebours B., Euzen P., and Toulhoat H., *Theoretical Study of the Dehydration Process of Boehmite to γ-Alumina*. The Journal of Physical Chemistry B, 2001. **105**(22): p. 5121-5130.

25. Beaufile J.-P. and Barbaux Y., *Détermination, par diffraction différentielle de neutrons, des faces cristallines exposées par des supports de catalyseurs en poudre*. J. Chim. Phys., 1981. **78**: p. 347-352.
26. Digne M., Sautet P., Raybaud P., Euzen P., and Toulhoat H., *Hydroxyl Groups on γ -Alumina Surfaces: A DFT Study*. Journal of Catalysis, 2002. **211**(1): p. 1-5.
27. Digne M., Sautet P., Raybaud P., Euzen P., and Toulhoat H., *Use of DFT to achieve a rational understanding of acid–basic properties of γ -alumina surfaces*. Journal of Catalysis, 2004. **226**(1): p. 54-68.
28. Hu C.H., Chizallet C., Toulhoat H., and Raybaud P., *Structural, energetic, and electronic trends in low-dimensional late-transition-metal systems*. Physical Review B, 2009. **79**(19): p. 195416.
29. Oudenhuijzen M.K., van Bokhoven J.A., Miller J.T., Ramaker D.E., and Koningsberger D.C., *Three-Site Model for Hydrogen Adsorption on Supported Platinum Particles: Influence of Support Ionicity and Particle Size on the Hydrogen Coverage*. Journal of the American Chemical Society, 2005. **127**(5): p. 1530-1540.
30. Wang L.-L. and Johnson D.D., *Shear Instabilities in Metallic Nanoparticles: Hydrogen-Stabilized Structure of Pt₃₇ on Carbon*. Journal of the American Chemical Society, 2007. **129**(12): p. 3658-3664.
31. Cabié M., Giorgio S., Henry C.R., Axet M.R., Philippot K., and Chaudret B., *Direct Observation of the Reversible Changes of the Morphology of Pt Nanoparticles under Gas Environment*. The Journal of Physical Chemistry C, 2010. **114**(5): p. 2160-2163.
32. Bus E. and van Bokhoven J.A., *Hydrogen chemisorption on supported platinum, gold, and platinum–gold-alloy catalysts*. Physical Chemistry Chemical Physics, 2007. **9**(22): p. 2894-2902.
33. Singh J., Nelson R.C., Vicente B.C., Scott S.L., and van Bokhoven J.A., *Electronic structure of alumina-supported monometallic Pt and bimetallic PtSn catalysts under hydrogen and carbon monoxide environment*. Physical Chemistry Chemical Physics, 2010. **12**(21): p. 5668-5677.

CHAPTER 6

Conclusions and Perspectives

In the frame of this PhD thesis work, the complementary use of experimental and computational methods was applied to the characterization of heterogeneous catalysts constituted by Pt and Pd nanoparticles supported on activated carbons and $\gamma\text{-Al}_2\text{O}_3$. This work is inserted within the long-lasting collaboration among the Chemistry Department of the University of Turin, the Institut Laue-Langevin in Grenoble and the company Chimet S.p.A., which in the last years provided several results of relevant importance in the field of heterogeneous catalysis by systematically employing a multi-technique approach on the characterization of a well-defined set of samples. In the frame of a co-tutorship agreement, the first half of the PhD activities were

based at the University of Turin, while the second half at the ILL. With the present work, three main topics were explored.

Activated Carbon supports

Activated carbons are very complex and heterogeneous materials, and the choice of the precursors, of the activation procedure or of the post-activation treatments can dramatically influence their composition and their properties in terms of texture (i.e. surface area, porosity) and surface chemistry (i.e. type and relative abundance of C-H terminations and of heteroatom-containing functional groups). This work focused on the characterization of the surface chemistry of seven activated carbons employed as catalytic supports by Chimet S.p.A., namely four samples physically activated by steam (two prepared from wood and two from peat), one sample of wood origin chemically activated by H_3PO_4 , and two samples oxidised in a HNO_3 solution. All the samples were studied by means of TPD-IR, used to identify and quantify the heteroatom-containing functionalities, and by INS spectroscopy coupled with DFT simulations, providing the vibrational fingerprint of their C-H terminations.

Together, the two approaches provided an overall picture of the composition of the terminations of the graphenic domains constituting the activated carbons and of the differences arising from their precursors, activation methods and from the post-activation procedure, in terms of both the geometry of the C-H terminations and the amount of functional groups. The four steam-activated samples show a generally low concentration of O-functional groups, exhibiting a different distribution of carboxylic acids, anhydrides, phenols and ethers depending on the precursor. The INS and DFT results also show that most of the C-H groups along their terminations are unperturbed by the effect of vicinal functional groups, indicating that these

functionalities are rare along the aromatic platelets' borders. The main contributions were instead C-H groups arising from benzene rings exposing one or two hydrogen atoms either along regular or disordered borders, or defects such as small holes saturated by H atoms, which were both identified and quantified by a linear combination fit analysis.

The chemically activated sample instead showed a higher concentration of functional groups, in particular phenols and ethers, and also a residual non-graphitic fraction which gave rise to the evolution of CH₄ during the TPD-IR runs. The higher abundance of functional groups in the aromatic platelets was confirmed also by the INS spectrum which, in comparison with the spectra of the previously discussed physically activated samples, presented some new features compatible with C-H terminations perturbed by vicinal O-containing functional groups.

Finally, the oxidative treatment in HNO₃ was confirmed to be very effective in introducing O-containing functionalities by both the TPD-IR and the INS approaches. In fact, the concentration of functional groups measured by TPD-IR (in particular carboxylic acids, lactones and anhydrides) increased sensibly in respect with the untreated samples, and also INS confirmed an higher abundance of functionalities along the borders, as the main spectral feature observed corresponded to a single C-H termination perturbed by a vicinal functional groups. In addition, TPD-IR also managed to individuate (and partially quantify) the introduction of N-containing functional groups in these two samples, which was never possible with the techniques used before.

Regarding the characterization of the platelets terminations in activated carbons, the main improvement concerns the upgrade of the TPD-IR setup, which could allow to exceed the temperature of 700°C and thus to access the quantification of carbonyls.

Effect of the metal nanoparticles deposition

Six different catalysts obtained by depositing Pt and Pd nanoparticles on the four steam-activated samples were also object of the INS and DFT analysis, providing new information about the perturbation introduced by the metal nanoparticles on the C-H terminations. The experimental spectra exhibited a systematic decrease in intensity upon nanoparticles deposition. The decrease in the integrated area, which is proportional to the amount of C-H terminations lost, displayed an evident linear trend with the nanoparticles dispersion in the case of Pt nanoparticles, indicating that the metal nanoparticles may sit at the C-H terminations of the platelets, and also that the smaller the nanoparticle, the stronger is the perturbation. In addition, not all the bands in the spectra decreased at the same extent, indicating that some C-H terminations were more affected by this interaction. It was possible to interpret this observation thanks to the DFT simulations and the linear combination fit analysis, which clarified that the most affected C-H terminations by the introduction of the metal nanoparticles consist in benzene rings exposing a single C-H group in a regular region of the border, and that this phenomenon is systematically observed for all the samples.

Interaction of H₂ with supported Pt nanoparticles

The phenomena related to the interaction between H₂ and a Pt/ γ -Al₂O₃ catalyst were investigated, in collaboration with the IFPEN group. Also in this case, the complementary use of INS spectroscopy and DFT simulations was fundamental. By simulating the INS spectra corresponding to the models of Pt nanoparticles supported on γ -Al₂O₃ and the ones of extended Pt surfaces at various H coverages and comparing them with the experimental one, it was possible to find a further confirmation of occurrence of a H₂-induced reconstruction of the supported Pt nanoparticles to form highly symmetric

cuboctahedric particles completely solvated by H and in weak interaction with the support.

Several possible routes are possible for the continuation of this topic. Experimentally, the measurement of the INS spectra of the catalyst under different conditions is planned. In particular, experiments at different H₂ partial pressures and temperatures are already planned in the near future (experiments DIR-177 and 7-05-514 accepted on the instrument IN1/Lagrange at the ILL), which would allow to measure the spectra of Pt nanoparticles at lower H coverage. On the computational front instead, it might be useful to explore larger nanoparticles systems as well as different levels of hydroxylation of the support surfaces, in order to have models closer to the experimental sample. The simulation of the IR spectra would also be desirable, as it would be a fundamental step for extending the interpretation of a large number of experimental data collected within our group in the last years.

Acknowledgements

These three last years have been a very eventful part of my life, which contributed to my growth as a researcher, but also as a person.

The PhD position I covered was unique under many aspects, thanks to the co-tutorship agreement between UniTO and the ILL, which allowed me to work in two different countries, and to the collaboration with Chimet S.p.A., which provided an insight on both the academic and industrial world.

I thus want to thank all the involved institutions for having collaborated on this project, which gave me the chance to travel, meet new people and learn as I never did before. I have a very positive opinion of the last three years, and I genuinely hope that other students may be given the opportunity to work on similar projects in the future.

An even greater thank goes to the people I worked with, and in particular to my supervisors Prof. Elena Groppo and Dr. Andrea Piovano. I am very grateful for your constant support all over my PhD, both for the very fruitful scientific discussions and also on the personal and human side. A special thanks also goes to Dr. Riccardo Pellegrini and all the other people involved in the collaboration with Chimet. In any occurrence involving the

Chimet group, I always had a great time both on the scientific side and on the personal one.

I also want to thank Dr. Céline Chizallet and Dr. Pascal Raybaud from IFPEN for the great opportunities opened by this recent, but not less important, collaboration. Even if the situation did not allow us to meet in person, I think that this collaboration is providing very interesting results, and many others may be possible in the future.

In these last three years I had the opportunity to work and interact with many other people, too many for listing them all. I think to have learnt something from the all of you, and I am very grateful for this, as well as for all the help, support and encouragements I received during these years.

APPENDIX A

Input files and scripts

A.1 Crystal17 input files

Geometry optimization

```
_TITLE_LINE_  
MOLECULE  
##_Geometry_of_the_model  
OPTGEOM  
END  
END  
13  
0 0 3 1 1  
18.7311370      0.03349460  
2.8253937      0.23472695  
0.6401217      0.81375733  
0 0 1 0 1  
0.1612778      1.00000000  
0 2 1 0 1
```

1.1000000	1.0000000		
6 4			
0 0 6 2 1			
3047.5249000	0.0018347		
457.3695100	0.0140373		
103.9486900	0.0688426		
29.2101550	0.2321844		
9.2866630	0.4679413		
3.1639270	0.3623120		
0 1 3 4 1			
7.8682724	-0.1193324	0.0689991	
1.8812885	-0.1608542	0.3164240	
0.5442493	1.1434564	0.7443083	
0 1 1 0 1			
0.1687144	1.0000000	1.0000000	
0 3 1 0 1			
0.8000000	1.0000000		
7 4			
0 0 6 2 1			
4173.5110000	0.0018348		
627.4579000	0.0139950		
142.9021000	0.0685870		
40.2343300	0.2322410		
12.8202100	0.4690700		
4.3904370	0.3604550		
0 1 3 5 1			
11.6263580	-0.1149610	0.0675800	
2.7162800	-0.1691180	0.3239070	
0.7722180	1.1458520	0.7408950	
0 1 1 0 1			
0.2120313	1.0000000	1.0000000	
0 3 1 0 1			
0.8000000	1.0000000		
8 4			
0 0 6 2 1			
5484.6717000	0.0018311		
825.2349500	0.0139501		
188.0469600	0.0684451		

52.9645000	0.2327143	
16.8975700	0.4701930	
5.7996353	0.3585209	
0 1 3 6 1		
15.5396160	-0.1107775	0.0708743
3.5999336	-0.1480263	0.3397528
1.0137618	1.1307670	0.7271586
0 1 1 0 1		
0.2700058	1.0000000	1.0000000
0 3 1 0 1		
0.8000000	1.0000000	
99 0		
END		
DFT		
B3LYP		
XLGRID		
END		
MAXCYCLE		
400		
TOLINTEG		
8 8 8 25 50		
TOLDEE		
8		
FMIXING		
60		
PPAN		
DIIS		
HISTDIIS		
50		
THREDIIS		
0.1		
END		

In case of open shell systems, add to the geometry input section:
 SPINLOCK
 1 5

ATOMSPIN
Nr_atoms
1st_atom_label spin 2nd_atom spin

In case of open shell systems, add to the final input section:

DFT
SPIN
B3LYP

Frequency calculation

```
_TITLE_LINE_  
EXTERNAL  
FREQCALC  
PREOPTGEOM  
END  
INTENS  
INTCPHF  
END  
END  
END  
1 3  
0 0 3 1 1  
18.7311370      0.03349460  
2.8253937      0.23472695  
0.6401217      0.81375733  
0 0 1 0 1  
0.1612778      1.0000000  
0 2 1 0 1  
1.1000000      1.0000000  
6 4  
0 0 6 2 1  
3047.5249000    0.0018347  
457.3695100    0.0140373  
103.9486900    0.0688426  
29.2101550     0.2321844  
9.2866630      0.4679413  
3.1639270      0.3623120
```

0 1 3 4 1		
7.8682724	-0.1193324	0.0689991
1.8812885	-0.1608542	0.3164240
0.5442493	1.1434564	0.7443083
0 1 1 0 1		
0.1687144	1.0000000	1.0000000
0 3 1 0 1		
0.8000000	1.0000000	
7 4		
0 0 6 2 1		
4173.5110000	0.0018348	
627.4579000	0.0139950	
142.9021000	0.0685870	
40.2343300	0.2322410	
12.8202100	0.4690700	
4.3904370	0.3604550	
0 1 3 5 1		
11.6263580	-0.1149610	0.0675800
2.7162800	-0.1691180	0.3239070
0.7722180	1.1458520	0.7408950
0 1 1 0 1		
0.2120313	1.0000000	1.0000000
0 3 1 0 1		
0.8000000	1.0000000	
8 4		
0 0 6 2 1		
5484.6717000	0.0018311	
825.2349500	0.0139501	
188.0469600	0.0684451	
52.9645000	0.2327143	
16.8975700	0.4701930	
5.7996353	0.3585209	
0 1 3 6 1		
15.5396160	-0.1107775	0.0708743
3.5999336	-0.1480263	0.3397528
1.0137618	1.1307670	0.7271586
0 1 1 0 1		
0.2700058	1.0000000	1.0000000

```
0 3 1 0 1
  0.8000000      1.0000000
99 0
END
DFT
B3LYP
XLGRID
END
GUESSP
MAXCYCLE
400
TOLINTEG
8 8 8 25 50
TOLDEE
10
FMIXING
60
DIIS
HISTDIIS
50
THREDIIS
0.1
PPAN
END
```

A.2. Linear combination analysis Mathematica script

The script used for the linear combination fit analysis contains two main typologies of sections: the ones for reading the input files corresponding to the contributions to be included into the linear combination fit, followed by the sections containing the linear combination fit for each experimental INS spectrum. One example of section of each type will be provided in the following:

Reading of the input

```
testlist = Import["C:\\Users\\_FILE_PATH_"];  
plotOriginale = ListPlot[testlist, Frame -> True];
```

```
modelD = Interpolation[testlist];
```

```
x1 = 705;  
x2 = 1000;  
y1 = modelD[x] /. x -> x1;  
y2 = modelD[x] /. x -> x2;
```

"Subtraction of the baseline to the spectrum"

```
FunzioneD = modelD[x*s1] - ((x - x1)/(x2 - x1)*(y2 - y1) + y1) ;  
Function_1 = FunzioneD /. s1 -> 1;
```

```
plotmodel2 =
```

```
Plot[{Function_1}, {x, 691, 1019}, Frame -> True, PlotRange -> Full, PlotStyle  
-> {Directive[Red, Thick]}, GridLines -> Automatic];
```

```
Show[plotmodel2]
```

Calculation of the linear combination fit export of the results

```
testlist1 = Import["C:\\Users\\_PATH_EXP_SPECTRUM_ ", "Table"];
testlist = testlist1[[All, {1, 2}]];
error = testlist1[[All, 3]];
datisperimentali = Flatten[Table[ testlist[[i]][[2]], {i, 1, Dimensions[testlist][[1]]}];
plotOriginale = ListPlot[testlist, Frame -> True];
assex = Table[testlist[[i]][[1]], {i, 1, Dimensions[testlist][[1]]};
```

(*Building the function to be fitted to the experimental spectrum*)

```
FunzioneTot = a1*FunzioneD + a2*FunzioneZ1D + a9*FunzionePs +
a14*FunzioneSV + a15*FunzionePls;
```

(*Optimizing the fit *)

```
ricercafit = NonlinearModelFit[ testlist, {FunzioneTot, a1 > 0, a2 > 0, a9 > 0, a14
> 0, a15 > 0, (0.99 < s1 < 1.01), (0.99 < s2 < 1.01), (0.99 < s9 < 1.01), (0.99 < s14
< 1.01), (0.99 < s15 < 1.01), (a2 > (a15 + a9))}, {{a1, 1}, {a2, 1}, {a9, 1}, {a14, 1}, {a15,
a1}, {s1, 1}, {s2, 1}, {s9, 1}, {s14, 1}, {s15, 1}}, x, MaxIterations -> 5000, Weights ->
(10^-6*error^-2), ConfidenceLevel -> 0.99, StepMonitor :> Print["RSS= ",
Sum[(testlist[[i, 2]] - (FunzioneTot /. x -> (testlist[[i, 1]]))^2, {i, 1,
Length[testlist]}]]];
```

(*Results plotting*)

```
ricercafit["ParameterTable"]
```

```

paramfit = ricercafit["BestFitParameters"];
residui = ricercafit["FitResiduals"];
residuiDaPlottare = Transpose@{assex, residui};
Print ["Estimated Variance= ", ricercafit["EstimatedVariance"]]
varianza = ricercafit["EstimatedVariance"];
Rfactor = Sum[Abs[residui[[i]]], {i, 1, Length[residui]}/Sum[datisperimentali[[i]],
{i, 1, Length[residui]}}*100;

Print["RMSE= ", Sqrt[Total[residui^2]/Length[residui]]]
RMSE = Sqrt[Total[residui^2]/Length[residui]];

fit = FunzioneTot /. paramfit;
m1 = a1*{FunzioneD} /. paramfit;
m2 = a2*{FunzioneZ1D} /. paramfit;
m15 = a15*{FunzionePls} /. paramfit;
m9 = a9*{FunzionePs} /. paramfit;
m14 = a14*{FunzioneSV} /. paramfit;

plotmodel = Plot[{fit, m1, m2, m9, m14, m15}, {x, 650, 1050}, Frame -> True,
PlotRange -> Full, PlotStyle -> {Directive[Red, Thick], Directive[Green, Thick],
Directive[Blue, Thick], Directive[Orange, Thick], Directive[Pink, Thick],
Directive[Yellow, Thick], Directive[Magenta, Thick], Directive[Purple, Thick],
Directive[Cyan, Thick], Directive[Gray, Thick], Directive[Black, Thick] };
Show[plotOriginale, plotmodel]
ListPlot[residuiDaPlottare]

```

```
DenominatoreCpB = (a1 + a2 + a9 + a14 + a15) /. paramfit;
```

```
perc1 = a1*100/DenominatoreCpB /. paramfit;
```

```
perc2 = a2*100/DenominatoreCpB /. paramfit;
```

```
perc9 = a9*100/DenominatoreCpB /. paramfit;
```

```
perc14 = a14*100/DenominatoreCpB /. paramfit;
```

```
perc15 = a15*100/DenominatoreCpB /. paramfit;
```

```
SOMMA = perc1 + perc2 + perc9 + perc14 + perc15;
```

```
Percentuali = {perc1, perc2, perc9, perc14, perc15, Rfactor, RMSE, SOMMA};
```

```
Titoli = {"D all", "Z1D", "Z dis", "V sin", "Z iso", "R factor", "RMSE", "SOMMA"};
```

```
Grid[Join[{Titoli}, {Percentuali}], Frame -> All, Spacings -> {2, 1}, ItemStyle ->  
"Text"] // DisplayForm
```

```
(* Export fit results *)
```

```
dataFit = Table[{x, fit}, {x, 700, 1020, 0.5}];
```

```
dataFit = Flatten /@ dataFit;
```

```
Export["C:\\Users\\_EXPORT_PATH_", dataFit, "Table"]
```

```
(*repeat final block for every function you want to export*)
```


A.3 Python 3 script for the OUTCAR/*.aclimax conversion

```
# Read OUTCAR file

Input_name = input("Enter the complete input file name: ")

OUTCAR = open(Input_name, "r")

OUTCAR_List = OUTCAR.readlines()

Lenght = len(OUTCAR_List)

OUTCAR.close()

## reads masses, counts number of elements and take element labels. If you
##use frequently other elements, you would be better to update this
## part with the elements and the masses you need.
## any missing data would be asked in the console

line_app_1 = []
line_app_2 = []
elements_name = []
elements_mass = []
atomic_numbers = []

for line in OUTCAR_List:

    if ' POMASS = ' in line:
        line_app_1 = line.split()

        if line_app_1[2][-1] != ";":
            break

        elements_mass.append(line_app_1[2][-1])

for line in OUTCAR_List:

    if ' TITEL =' in line:
```

```

line_app_2 = line.split( )
elements_name.append(line_app_2[3])

if line_app_2[3] == "Al":
    atomic_numbers.append(13)

elif line_app_2[3] == "O":
    atomic_numbers.append(8)

elif line_app_2[3] == "Pt":
    atomic_numbers.append(78)

elif line_app_2[3] == "H":
    atomic_numbers.append(1)

else:
    atomic_numbers.append(input("Element " + line_app_2[3] + " is not \
listed in the current database. Please enter its atomic number: "))

nr_element_types = len(elements_name)

if nr_element_types == 0:
    print('ERROR, ELEMENT MASSES MISSING')

## Looks for the number of atoms of each type in the OUTCAR file

nro_element = []
tot_atoms = 0

for line in OUTCAR_List:
    if 'ions per type =' in line:
        element_numbers_line = line.split( )
        for i in range (0, nr_element_types):
            nro_element.append(int(element_numbers_line[i+4]))
            tot_atoms = tot_atoms + nro_element[i]
        break

```

```

if len(nro_element)==0:
    print('ERROR, NUMBER OF ATOMS PER ELEMENT MISSING')

## Looks for the initial cartesian coordinates of the atoms

Coordinates_list=[]
line_app = []

for i in range (Lenght):
    if 'position of ions in cartesian coordinates (Angst):' in OUTCAR_List[i]:
        for j in range (1,tot_atoms+1):
            line_app = OUTCAR_List[i+j].split()
            Coordinates_list.append(line_app)
            break

if len(Coordinates_list)==0:
    print('ERROR, CARTESIAN COORDINATES DATA MISSING')

### Look for eigenvalues and eigenvectors in the output

frequencies = []
eigenvectors = []
app = ""
app_2 = []
nro_freq_imm = 0
imm_frequencies = []

for i in range (Lenght):
    if ' f =' in OUTCAR_List[i] :
        app = OUTCAR_List[i].split()
        frequencies.append(float(app[7]))
        for j in range (0,tot_atoms):
            app_2 = OUTCAR_List[i+j+2].split()
            eigenvectors.append(app_2[3:6])

```

```

elif 'f/i= ' in OUTCAR_List[i]:
    app = OUTCAR_List[i].split()
    frequencies.append(-(float(app[6])))
    nro_freq_imm = nro_freq_imm + 1
    imm_frequencies.append(float(app[6]))
    for j in range (0,tot_atoms):
        app_2 = OUTCAR_List[i+j+2].split()
        eigenvectors.append(app_2[3:6])

if len(frequencies) == 0 or len(eigenvectors) == 0:
    print('ERROR, FREQUENCIES OR EIGENVECTORS MISSING')

if nro_freq_imm != 0:
    print("\n ATTENTION, there are some imaginary frequencies! If they are few\
and very small in module you \n" \
        + "can probably ignore them, but you are better to give them a look:\
\n")
    for v in range (0,nro_freq_imm):
        print(str(imm_frequencies[v]) + " i cm-1" )
    print("\n these frequency are going to be reported as negative frequencies\
in the current file")

### Generate output file

Output_name = input("Enter the complete output name, with the *.aclimax\
extension: ")

Aclimax = open(Output_name,"w")

## atomic positions section

Aclimax.write("!# Type Number Mass Coord Coord Coord\
Sigma"+ "\nBEGIN ATOMS")

k = 0

for i in range (0, nr_element_types):

```

```

for j in range(0, nro_element[i]):
    k = k+1
    line = ("\n"+str(k)+ "      " +elements_name[i] + "      " + \
str(atomic_numbers[i])+ "      " + str(elements_mass[i])+ "      " + \
Coordinates_list[k-1][0]+"      " +Coordinates_list[k-1][1]+\
      "      " +Coordinates_list[k-1][2])
    Aclimax.write(line)

```

```
Aclimax.write("\nEND ATOMS\n\n")
```

```
### frequencies and eigenvectors section
```

```
Aclimax.write("BEGIN FREQUENCIES\n\n")
```

```
k1 = 0
```

```
k2 = 0
```

```
for i in range (0, len(frequencies)):
```

```
    Aclimax.write(str(i+1)+ "      " + str(frequencies[i])+"\n\n")
```

```
    for l in range (0, nr_element_types):
```

```
        for j in range(0, nro_element[l]):
```

```
            k1=k1+1
```

```
            k2=k2+1
```

```
            Aclimax.write(str(k1)+ "      " + elements_name[l] + "      " + \
str(atomic_numbers[l])+ "      " +eigenvectors[k2-1][0]+ "      " +eigenvectors[k2-\
1][1]+ "      " +eigenvectors[k2-1][2]+"\n")
```

```
            k1=0
```

```
            Aclimax.write("\n")
```

```
Aclimax.write("END FREQUENCIES")
```

```
Aclimax.close()
```


APPENDIX B

Regular aromatic platelets models

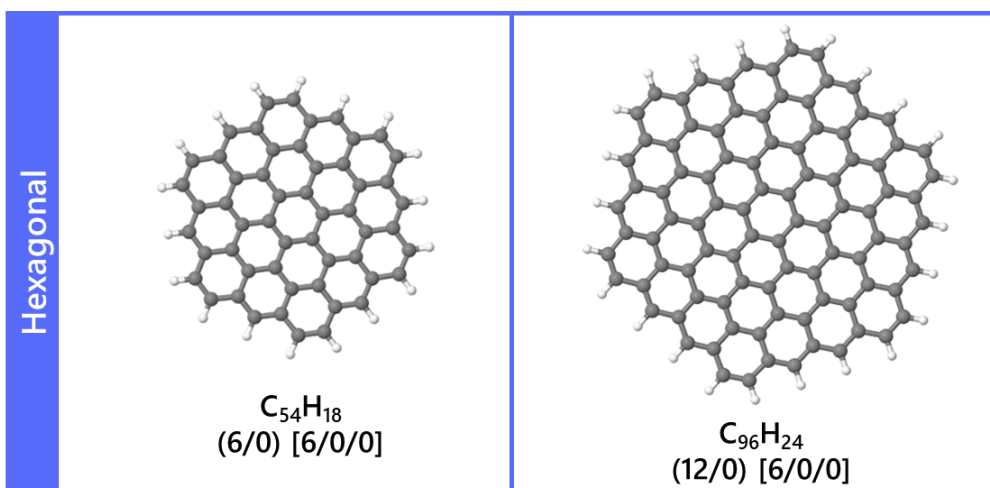


Figure B. 1: regular hexagonal models. Their formula and the number of terminations of each type is summarised following the notation: (Z/A) for the regular borders and [D/T/Q] for the corners.

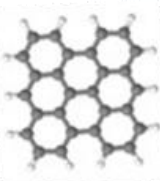
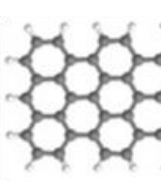
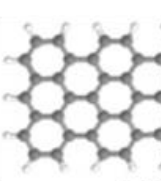
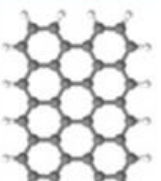
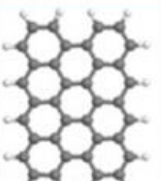
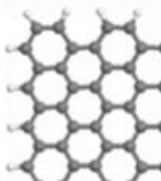
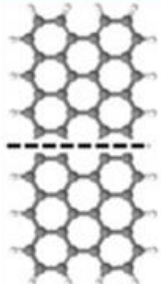
Rectangular	 $C_{28}H_{14}$ $(2/0) [0/4/0]$	 $C_{42}H_{18}$ $(2/2) [0/4/0]$	 $C_{56}H_{22}$ $(2/4) [0/4/0]$
	 $C_{36}H_{16}$ $(4/0) [0/4/0]$		
	 $C_{44}H_{18}$ $(6/0) [0/4/0]$	 $C_{66}H_{22}$ $(6/2) [0/4/0]$	
	 $\dots C_{76}H_{26}$ $(\dots 14/0) [0/4/0]$		

Figure B. 2: regular rectangular models. Their formula and the number of terminations of each type is summarised following the notation: (Z/A) for the regular borders and [D/T/Q] for the corners.

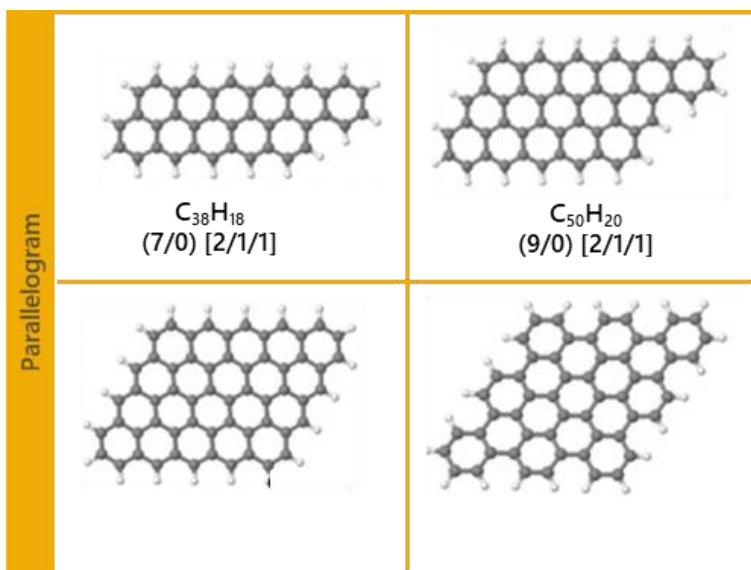


Figure B. 3: regular model with a parallelogram shape. Their formula and the number of terminations of each type is summarised following the notation: (Z/A) for the regular borders and [D/T/Q] for the corners.

APPENDIX C

Linear combination fits

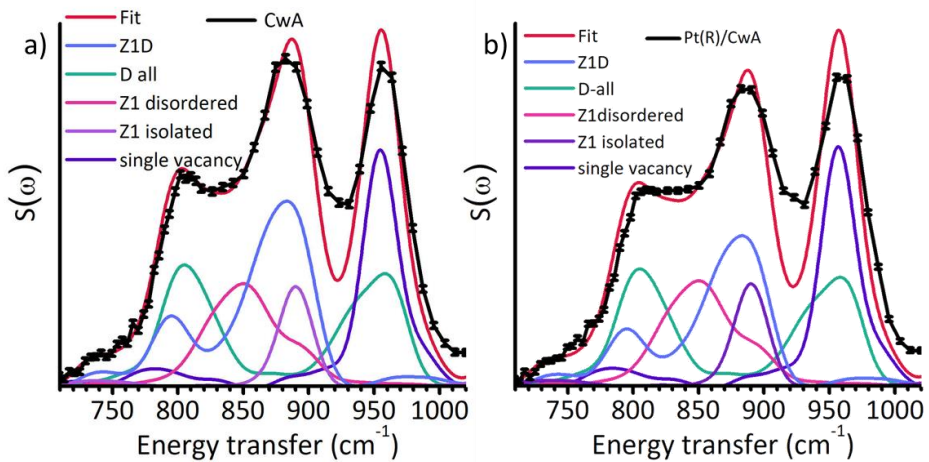


Figure C 1: results of the linear combination fits for the quantification of the C-H terminations in CwA (a) and Pt(R)/CwA (b).

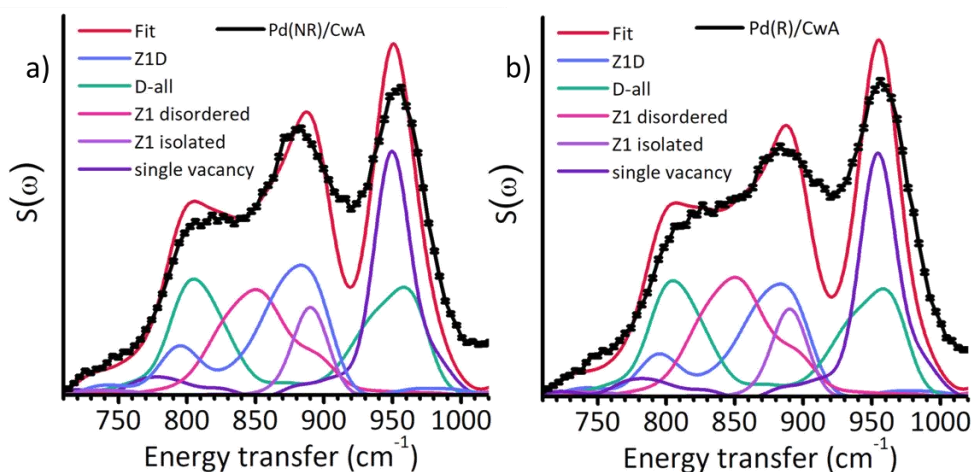


Figure C 2: results of the linear combination fits for the quantification of the C-H terminations in Pd(NR)/CwA (a) and Pd(R)/CwA (b).

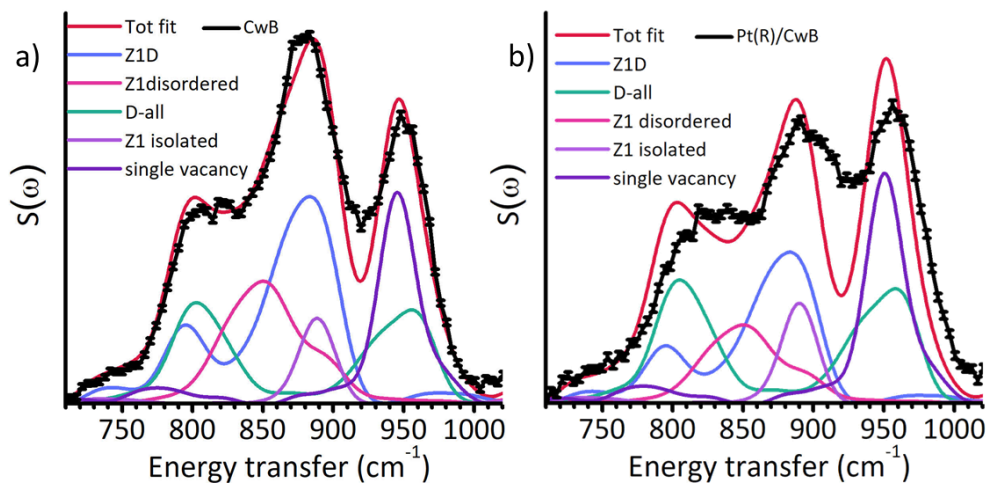


Figure C 3: results of the linear combination fits for the quantification of the C-H terminations in CwB (a) and Pt(R)/CwB (b).

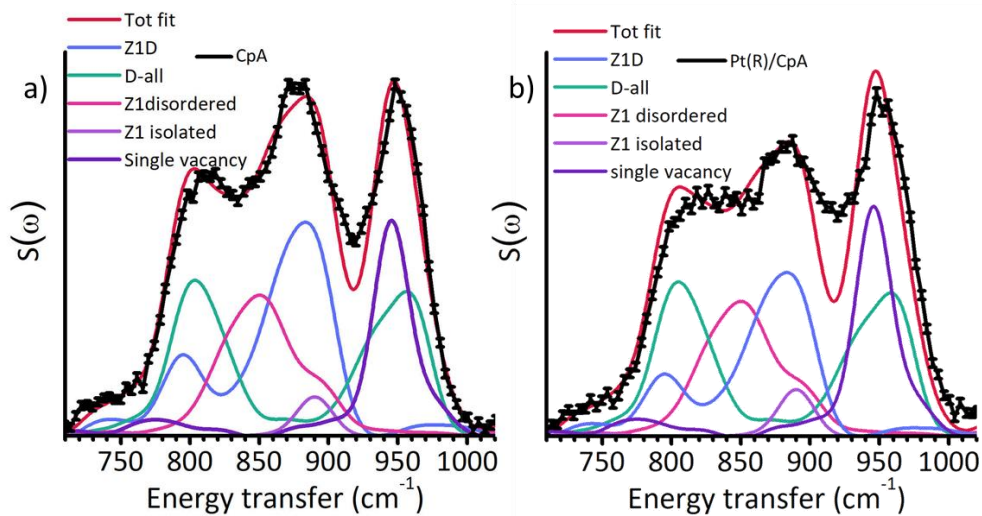


Figure C 4: results of the linear combination fits for the quantification of the C-H terminations in CpA (a) and Pt(R)/CpA (b).

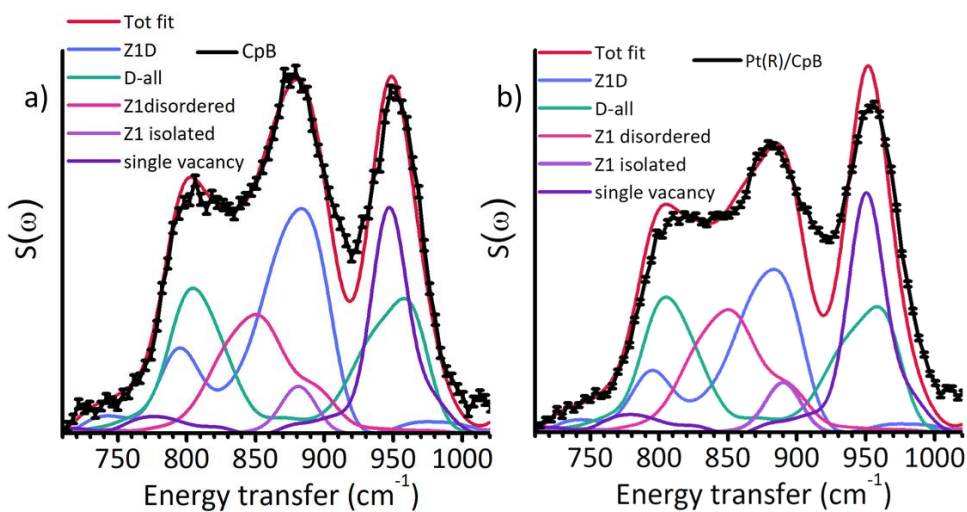


Figure C 5: results of the linear combination fits for the quantification of the C-H terminations in CpB (a) and Pt(R)/CpB (b).

APPENDIX D

Simulated INS spectra of $\gamma\text{-Al}_2\text{O}_3/\text{Pt}_{13}\text{H}_x$

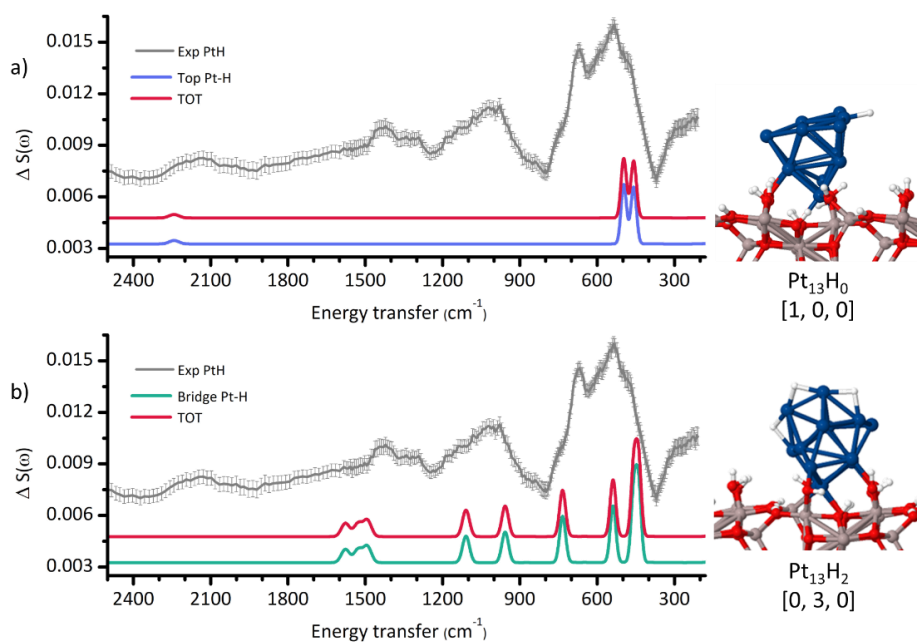


Figure D. 1: simulated INS spectra of Pt_{13}H_0 (a) and Pt_{13}H_2 (b) at the $\gamma\text{-Al}_2\text{O}_3$ (110) surface and their decomposition into the contribution of top and bridge Pt-H species. In both case the migration of one H from the support to the nanoparticle is observed.

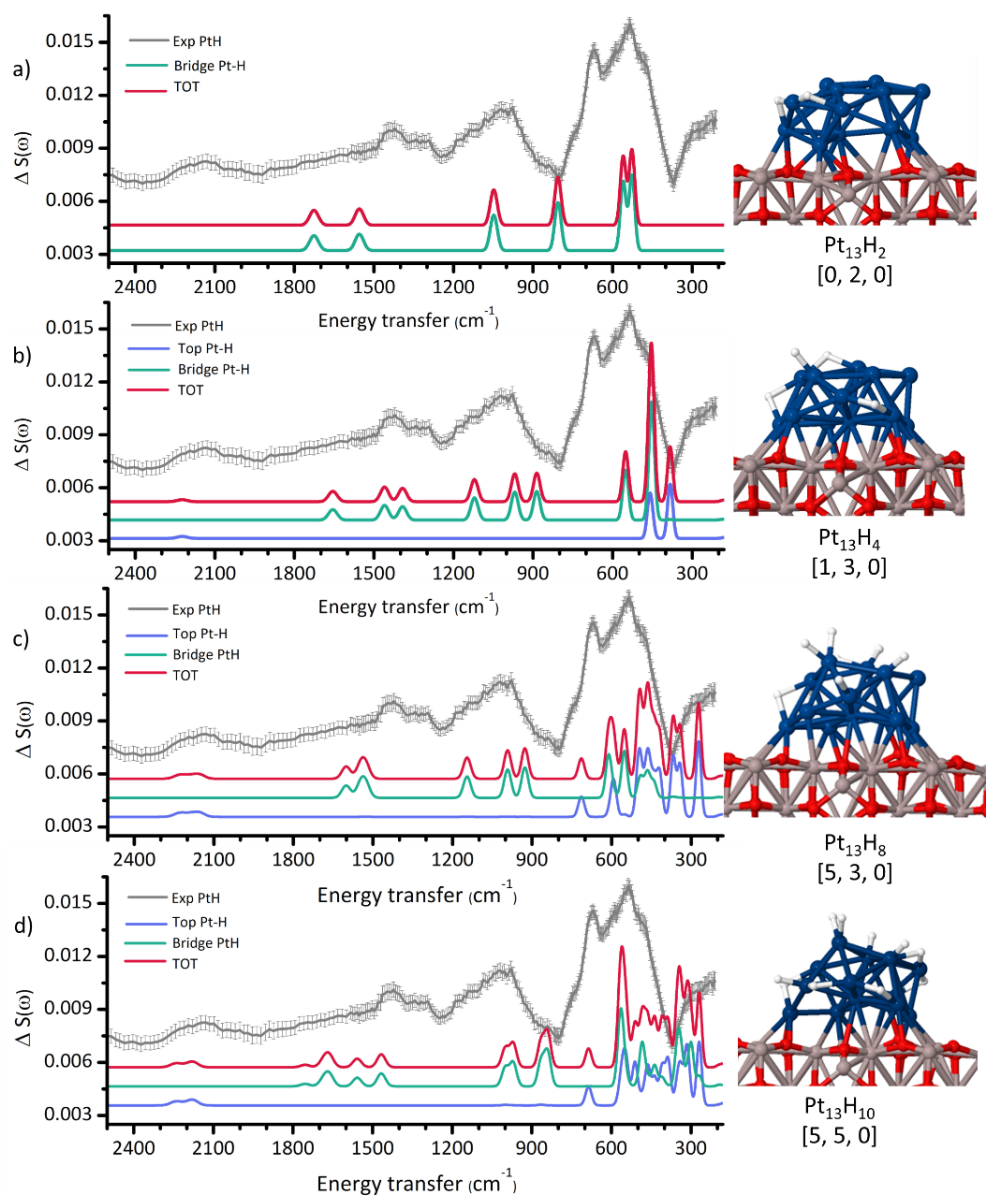


Figure D. 2: simulated INS spectra of Pt_{13}H_2 (a), Pt_{13}H_4 (b), Pt_{13}H_8 (c) and $\text{Pt}_{13}\text{H}_{10}$ (d) at the $\gamma\text{-Al}_2\text{O}_3$ (100) surface and their decomposition into the contribution of top and bridge Pt-H species.

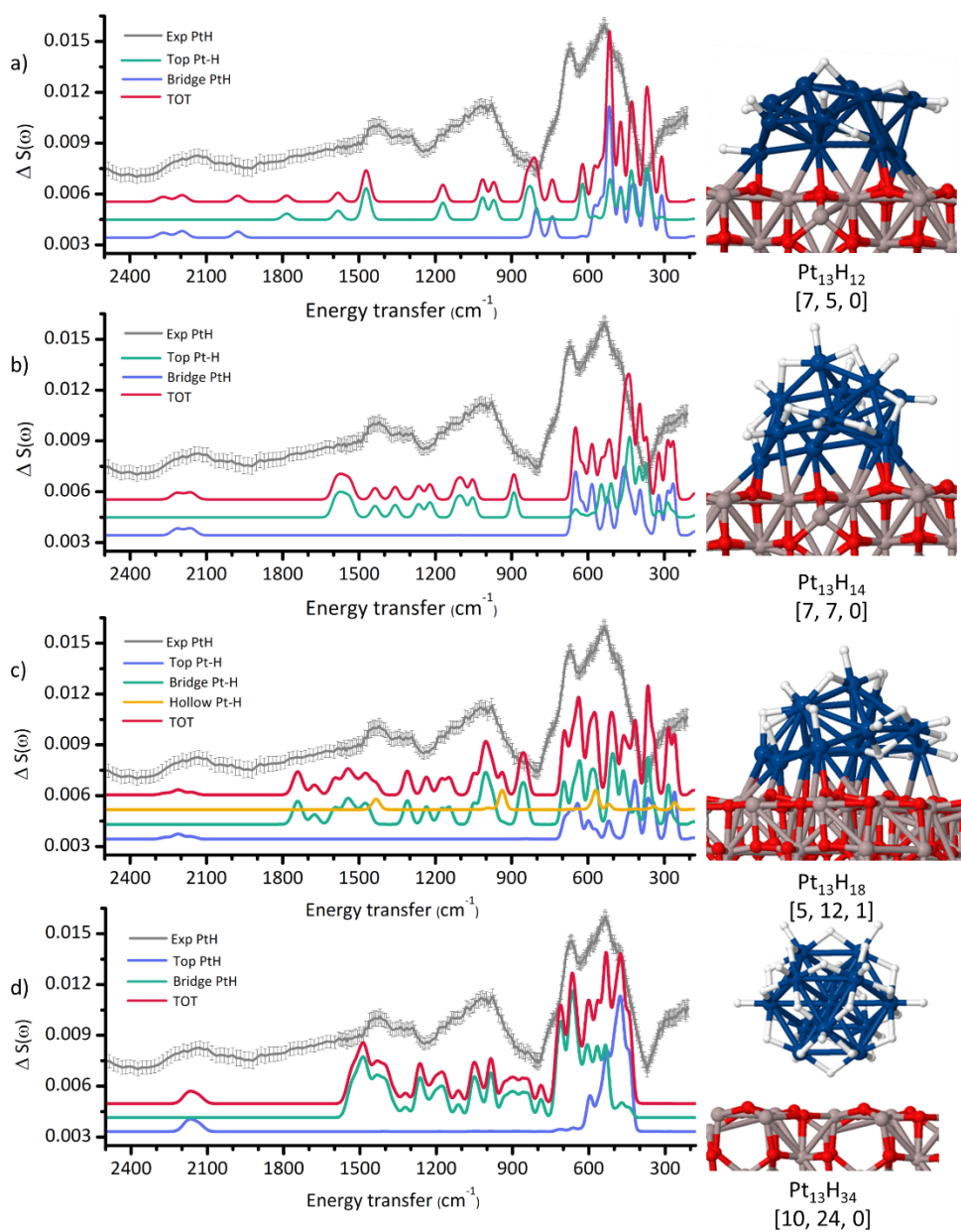


Figure D. 3: simulated INS spectra of Pt₁₃H₁₂ (a), Pt₁₃H₁₄ (b), Pt₁₃H₁₈ (c) and Pt₁₃H₃₄ (d) at the γ -Al₂O₃ (100) surface and their decomposition into the contribution of top and bridge Pt-H species.

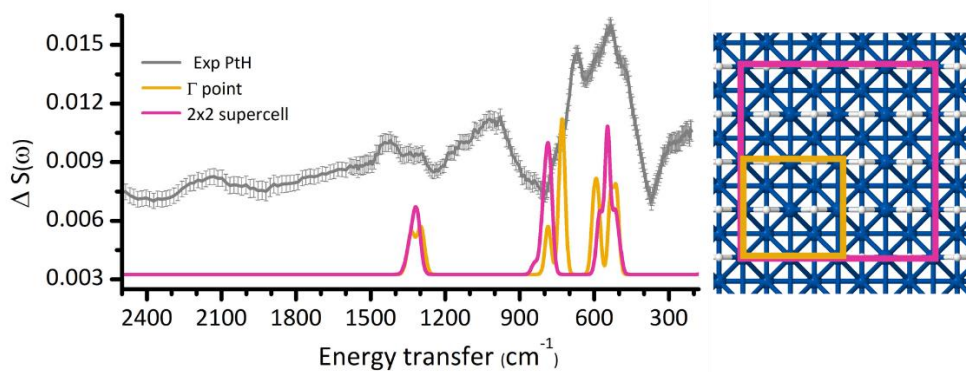
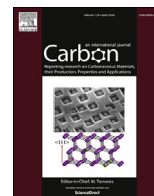


Figure D. 4: comparison of the simulated INS spectra of the high H-coverage (100) surface calculated at the Γ point only and on a 2x2 supercell. The two models are indicated for clarity.

APPENDIX E

Publications



How do the graphenic domains terminate in activated carbons and carbon-supported metal catalysts?

Eleonora Vottero ^{a, b}, Michele Carosso ^a, Mónica Jiménez-Ruiz ^b, Riccardo Pellegrini ^c,
Elena Groppo ^a, Andrea Piovano ^{b, *}

^a Department of Chemistry, NIS Centre and INSTM, University of Turin, Via G. Quarello 15/A, Turin, I-10135, Italy

^b Institut Laue-Langevin (ILL), 71 Avenue des Martyrs, 38042, Grenoble, France

^c Chimet SpA—Catalyst Division, Via di Pesciola 74, Vicomaggio Arezzo, I-52041, Italy

ARTICLE INFO

Article history:

Received 14 April 2020

Received in revised form

10 July 2020

Accepted 13 July 2020

ABSTRACT

This work is focused on the determination of the most likely border morphologies in the H-terminated graphenic domains that constitute activated carbons, focusing on four different carbons and six supported-metal catalysts. Among the available characterization techniques, Inelastic Neutron Scattering spectroscopy provides detailed vibrational spectra containing the fingerprint of the terminal C-H groups of carbon materials. From the experimental spectra, we observed clear differences among carbons having different origin, and a systematic decrease in the integrated area upon metal deposition that linearly scales with the nanoparticles dispersion. Density Functional Theory simulations are fundamental to assign the experimental bands to specific species. Thus, an extended simulation work on both regular and defective aromatic models was carried out, providing the inelastic neutron scattering fingerprint of a large number of different C-H terminations. By fitting the experimental spectra with a linear combination of the simulated spectra, it was possible to quantify the concentration of each terminal C-H geometry in the samples, and to identify the species most affected by the metal nanoparticles deposition. Specific benzene rings exposing a single C-H group appear to have a decisive role in the interaction with the metal nanoparticles and their deposition procedure.

© 2020 Elsevier Ltd. All rights reserved.

1. Introduction

Activated carbons are large surface area carbonaceous materials obtained from the pyrolysis and subsequent activation of several natural bio-polymeric precursors (such as wood, peat or coconut shells) [1]. They are widely employed as adsorbent or storage materials [2,3], as supports in heterogeneous catalysis [4] or as catalysts on their own [5–9], and also for innovative applications such as lithium batteries [10]. From a micro-structural point of view, activated carbons are constituted by small and heterogeneously sized and shaped graphenic domains mainly terminated by C-H groups, which also exhibit variable amounts of functional groups containing heteroatoms (such as oxygen or nitrogen) and a certain degree of defectivity. All these properties, as well as the surface area and porosity, are largely affected by the nature of the starting precursor and by the activation procedure [11,12]. Altogether, the

textural, morphological and surface properties of activated carbons have dramatic effects on their catalytic performances. As an example, we recently demonstrated that, for Pd-based catalysts supported on activated carbons, oxygen-containing functional groups at the carbon surface favour the hydrogenation of polar substrates, while they are detrimental to the hydrogenation of nonpolar substrates [13].

It emerges that a detailed understanding of the microscopic structure of activated carbons is essential to optimize their performance for a specific application, in particular for catalysis. Among the numerous techniques that can be employed for their characterization [14], Inelastic Neutron Scattering (INS) spectroscopy stands up as one of the most powerful methods to determine the nature of the C-H terminations of the graphenic domains. INS is a vibrational spectroscopy that exploits neutrons to excite molecular and/or atomic vibrations inside materials, and the intensity of the signal is proportional to the neutron scattering cross section of the atoms involved in the vibrational mode and to their displacement with respect to their equilibrium position. Since hydrogen

* Corresponding author.

E-mail address: piovano@ill.fr (A. Piovano).

displays both the largest neutron scattering cross section and large displacements due to its lightweight, this technique is particularly sensitive to the hydrogen-containing species in a material. This is the reason why INS spectroscopy has been successfully employed in the study of several carbon-based materials including activated carbons [15–18], carbon blacks [16,19], coals [16,20], glassy carbon [16,21] or reduced graphene oxides [22,23]. Despite the huge variety of properties displayed by these materials, their structure down to the atomic scale is to some extent similar, and so are their main spectral features.

Nevertheless, the bands assignment in an INS spectrum can be tricky. The reason is that this technique has formally no selection rules allowing, at least in principle, the detection of all the vibrational modes. Therefore, INS spectra of complex and heterogeneous samples containing high amounts of hydrogenous species usually show a large number of bands, whose assignment becomes challenging. The employment of computational methods to simulate the INS spectra can be extremely helpful and, among the available computational chemistry approaches, DFT simulations demonstrated to provide reliable results at reasonable computational costs. Albers et al. were the first authors who adopted a combined INS and computational approach to study activated carbons [15]. Their analysis showed that the fingerprint region of the C-H out-of-plane bending modes ($800\text{--}1000\text{ cm}^{-1}$) is the one mostly affected by differences in the microstructure of activated carbons. More recently, some of the authors revisited the interpretation of INS spectral features in the fingerprint region of activated carbons [24]. In particular, a more precise assignment of the contributions from different C-H terminations of the graphenic domains (including zigzag and armchair edges, as well as corners) was proposed. Still, so far the interpretation of the C-H vibrational features in activated carbons was limited to the comparison of experimental data of mediocre quality with simple theoretical models consisting of a few aromatic rings completely terminated by C-H groups, which are not representative of the real complexity of activated carbons.

Thanks to recent advances in INS instrumentations, the spectra collected on modern neutron spectrometers on well-prepared samples show an unprecedented signal-to-noise ratio, allowing for a more precise interpretation of the spectral features and for a higher reliability for the spectral differences. As an example, Cavallari et al. were recently able to collect high quality INS spectra of regular and defective hydrogenated graphene samples [23]. Combining the experimental spectra and DFT simulations, they identified the INS fingerprints of C-H groups at the periphery of the graphenic planes as well as inside holes. They quantified the two species abundance and they were able to monitor the migration of H atoms to adjacent vacant sites as a function of the temperature. Similarly, in our recent work we investigated a 5 wt% Pt catalyst supported on an activated carbon in the presence of different amounts of H_2 [18]. The collected INS data allowed for a detailed difference analysis between the spectrum of the catalyst and that of the carbon support, as well as between the spectrum of the catalyst in the absence and in the presence of H_2 . With this approach, we were able to assess more specifically the location of the Pt nanoparticles on the carbon support and to highlight the occurrence of hydrogen spillover from the Pt nanoparticles to the support. Despite the low Pt loading, we were also able to detect surface Pt-hydride species forming and modifying upon increasing the H_2 concentration. These examples demonstrate that nowadays we can rely on the fact that differences in the INS spectra of carbon-based samples under different conditions can be interpreted as clear structural modifications. At the same time, differences between measured and computed INS spectra can be considered as the result of a lack of specific features in the theoretical model.

In this work, we propose a systematic DFT simulation study of a

large number of graphenic model systems, aimed at providing the INS fingerprints of a wide range of different C-H termination geometries, as well as at understanding how they are affected by the presence of defects. The theoretical results are used for interpreting the experimental INS spectra of four physically activated carbons, deriving from wood and peat, and of a series of carbon-supported Pd- and Pt-based catalysts employed for hydrogenation reactions of industrial relevance. In principle, the same methodology can be easily extended to other classes of carbon-based materials. In this respect, we wish that this paper might become a guide for researchers who want to adopt similar approaches in material science.

2. Experimental

2.1. Activated carbon samples

The four activated carbons investigated in this work were commercially available carbons and were provided by the Catalyst Division of Chimet S.p.A. All of them were physically activated with steam, but they derive from different raw materials, wood (hereafter labelled as CwA and CwB) and peat (labelled as CpA and CpB). The ash content of the four carbons was determined by calcination and is below 2 wt% in the two carbons of wood origin, and of about 3 wt% for CpA and 5.5 wt% for CpB. Table 1 summarizes the specific surface area (SSA_{BET}) and micropore volume (V_{micro}) of the four carbons, as determined by N_2 physisorption measurements. The adsorption isotherms for the four supports are reported in the supporting information, Fig. S1. The catalysts supports are activated carbons derived from natural sources and, as such, they are characterized by a certain degree of heterogeneity in terms of carbon structure, morphology and porosity intrinsic of the natural source. Representative SEM images of the four activated carbons at two different magnifications are reported in Fig. S2 in Supporting Information to show the structural inhomogeneity at the μm scale.

2.2. Catalysts preparation

All the catalysts were prepared in the Chimet S.p.A. laboratories. Two Pd-based catalysts (5 wt% Pd loading) were prepared using CwA as a support, following the deposition–precipitation method as reported elsewhere [25,26]. Na_2PdCl_4 was used as the metal precursor and Na_2CO_3 as the basic agent. The two Pd/CwA catalysts differ in the reduction step: in one case, after the deposition of palladium as hydroxide, a pre-reduction was carried out by means of HCOONa at $55\text{ }^\circ\text{C}$ for 1 h, followed by water washing in order to remove residual chlorine and drying at $120\text{ }^\circ\text{C}$ overnight. In the other case, no pre-reduction was performed and the Pd deposition step was directly followed by washing and drying. The two catalysts are labelled as Pd(R)/CwA and Pd(NR)/CwA, where (R) and (NR) stand for reduced and not-reduced, respectively.

A series of Pt-based catalysts (5 wt% Pt loading) were prepared using the four activated carbons as supports, following a

Table 1
Properties of the activated carbons investigated in this work: raw material, activation method, specific surface area (SSA) as determined by N_2 physisorption measurements by applying the BET method and the corresponding volume of the micropores (V_{micro}).

Sample	Origin	Activation	SSA_{BET} (m^2g^{-1})	V_{micro} (cm^3g^{-1})
CwA	wood	steam	1018	0.63
CwB	wood	steam	1325	0.65
CpA	peat	steam	903	0.49
CpB	peat	steam	882	0.52

deposition-precipitation method similar to the one reported by Kaprielova et al. [27]. A pre-reduction was carried out also in this case by means of HCOONa at 80 °C for 1 h, followed by water washing and drying at 120 °C overnight. These catalysts are labelled with Pt(R), followed by the name of the carbon employed as support. The main characteristics of all the considered catalysts are summarized in Table 2. In all the cases, the metal dispersion was evaluated by means of CO chemisorption. The measurements were performed at 50 °C using a dynamic pulse method on samples pre-reduced in H₂ at 120 °C [28]. In a typical experiment, the catalyst (200 mg) is loaded inside the U-tube, heated in He up to 120 °C (heating rate of 10 °C min⁻¹), reduced in H₂ for 30 min, and finally cooled to 50 °C in He (cooling rate of 10 °C min⁻¹). A CO/metal average stoichiometry of 1 was assumed to calculate the metal dispersion for both the metals, as widely documented [29]. The discussed heterogeneity of the support does not point to a poor quality of the commercial catalysts. To verify that the supported metal nanoparticles are homogeneous in terms of morphology (spherical-like particles) and display a narrow particle size distribution, we recorded TEM micrographs on Pd/CwA and Pt/CwA catalysts (see Fig. S3 in Supporting information for representative images).

2.3. INS measurements

The INS measurements were performed on the LAGRANGE spectrometer at ILL in Grenoble (France) [30–32]. The INS spectra were collected in the 24–1020 cm⁻¹ range, with a resolution of $\Delta E/E$ of about 2%. The spectra were recorded at 20 K to reduce the thermal effects that broaden the spectral features. The raw data were opportunely reduced to the scattering function $S(\omega)$ and plotted versus energy transfer (in units of cm⁻¹). In order to ensure an easy comparison of each catalyst with its respective support, we renormalized the intensity of the former to match the same background intensity of the latter at 1020 cm⁻¹. The analysis, described in section 3.1, confirmed that contributions other than the background are negligible in this region.

Prior to the measure, all the samples were outgassed at 120 °C in dynamic vacuum (equilibrium pressure below 10⁻⁴ mbar) in order to remove the physisorbed water, and any further manipulation was performed within an Ar-filled glovebox in order to avoid any contamination with air moisture. A weighted amount of each sample (in the order of about 2–3 g) was inserted in a cylindrical Al-cell (4 cm high, 16 mm diameter) sealed with In-wire and then measured.

3. Theoretical methods

3.1. DFT simulations of the INS spectra

The DFT simulations of the INS spectra were performed employing the CRYSTAL17 software [33] in combination with the

aClimax software [34]. A good compromise between results reliability and computational cost was found in the combination between the B3LYP hybrid functional [35,36] and the 6-31G** basis set, as also proposed in the literature for similar systems [37,38]. Some models presented an open shell electronic configuration, for which the UB3LYP method was chosen. The general models employed for simulating the structure of activated carbons consist in polycyclic aromatic systems displaying different geometries and extensions, with hydrogen atoms used to saturate dangling bonds at edges and corners. Similar models have been already adopted in the literature to simulate the vibrational properties of the graphenic domains in carbon-based materials [15,24,38]. A total of 16 regular and 6 defective H-terminated different structures are reported in this work (see Figs. 3 and 8), while a greater number of them have been effectively simulated. The geometry of all the models was fully optimised, and successively a calculation of the vibrational modes was performed. All the structures were categorized as true energy minima by the absence of imaginary frequencies. The condition for the SCF convergence was set to 10⁻⁸ and 10⁻¹⁰ hartrees during geometry optimization and frequency calculations, respectively. In order to ensure the best accuracy, very high values (8 8 8 25 50) have been set for the five CRYSTAL17 integrals screening tolerance.

The output of the frequency calculation was used to simulate the INS spectra by employing the aClimax software [34]. Simulations of higher order transitions and phonon wings contributions were also performed, but not included into the final simulated spectra because they generated features that were not experimentally observed. The contribution of specific border fragments to the overall INS spectrum was simulated by manually setting the scattering cross section of all the atoms not included within the interested fragment to 0 barns. For a better comparison with the experimental spectra, the calculated frequencies have been scaled: the employed scaling function was obtained through a least squares linear regression of the experimental and calculated frequencies for the benzene molecule, as proposed in Ref. [39], resulting in the scaling function $\nu_{\text{scaled}} = 22.1 + 0.9543\nu_{\text{calculated}}$.

3.2. Linear combination analysis

To evaluate the weight of each simulated C-H terminal geometry in the experimental spectra, a linear combination fit analysis was performed. Each theoretical C-H contribution was normalised to the intensity of a single C-H group, averaged over similar models and then multiplied for a weight coefficient, whose final value in the best-fit solution is proportional to the concentration of that species in the sample. To compare among the values obtained for different samples, the optimised values of the sum of these coefficients were normalised to 1 for each support, while the catalysts were normalised respect to the corresponding support. A small multiplicative scaling factor s ($0.99 < s < 1.01$) was introduced on the frequency to adjust for small shifts along the horizontal axis.

4. Results and discussion

4.1. Experimental INS spectra

In the analysis of the experimental INS spectra, we decided to focus our attention on the 690–1020 cm⁻¹ range, characteristic of the out-of-plane C-H bending vibrations [15–18,24]. This is the region of the spectra that exhibits the greatest variations among the samples, and thus can be considered as the INS fingerprint of C-H terminations in the activated carbon samples. The spectra in the extended range 200–1020 cm⁻¹ are reported in Figs. S4, S5, S6 and S7 in the supporting information, while an overall assignment of all

Table 2

Properties of the catalysts studied in the current work: the activated carbon support type, the deposited metal, the eventual presence of a pre-reduction step and the metal nanoparticles dispersion (evaluated by means CO chemisorption).

Sample	Support	Metal	Pre-Reduced	Dispersion (%)
Pd(NR)/CwA	CwA	Pd	No	24
Pd(R)/CwA	CwA	Pd	Yes	24
Pt(R)/CwA	CwA	Pt	Yes	72
Pt(R)/CwB	CwB	Pt	Yes	77
Pt(R)/CpA	CpA	Pt	Yes	71
Pt(R)/CpB	CpB	Pt	Yes	69

the observed bands is described elsewhere [17]. Fig. 1 shows the INS spectra of the four activated carbons and of the corresponding Pd- and Pt-based catalysts in the 690–1020 cm^{-1} range. All the spectra are characterized by three main bands centred at similar positions (ca. 800, 880 and 955 cm^{-1} , with a tail extending at 750 cm^{-1}). Differences in the relative intensity of the three bands are observed between carbons derived from different raw materials (Fig. 1a–d), but also between carbons having the same origin (e.g. for CwB, Fig. 1b, the band at ca. 880 cm^{-1} is distinctively more intense than for CwA, Fig. 1a). These variations are expected to be caused by changes in the relative concentration of different C-H terminal geometries of the graphenic domains within the investigated samples.

Variations are also observed when comparing the INS spectra of the Pd and Pt catalysts (red, orange and yellow spectra in Fig. 1a–d) with those of the parent carbons (black spectra). The observed changes are very similar irrespective of the carbon type, of the metal and of the metal deposition method. A decrease in intensity of all the three bands is observed, more pronounced for the one centred at 880 cm^{-1} than for the others. This behaviour could be the result of the interaction of Pt and Pd nanoparticles with the C-H terminations of graphenic domains in the carbon support, and it

highlights that some types of C-H terminations are more affected than others. Similar variations were recently reported for the Pt(R)/CwA catalyst compared to the bare carbon support, and interpreted as an evidence that the Pt nanoparticles can be located at the edges of the sp^2 graphenic domains [18].

The absolute intensity of INS spectra is directly proportional to the hydrogen concentration within each sample [15,17]. In this respect, CwA is the activated carbon displaying the highest hydrogen concentration, closely followed by CwB and CpA, while CpB shows a much lower amount of hydrogen in respect to the others. Albers et al. [15] demonstrated that the integrated area of the spectra in the C-H bending region linearly scales with the H concentration in the sample. We have thus decided to use the integrated area of the spectra in the out-of-plane bending region (690–1020 cm^{-1}) to evaluate the H concentration within each of the samples. The variation in the integrated area of the spectra of all the catalysts with respect to the bare carbon support was calculated and plotted against the metal nanoparticles dispersion, as shown in Fig. 2. For the Pt catalysts, the decrease in the integrated area (i.e. in the H concentration) is directly proportional to the dispersion of the metal nanoparticles, as shown in Fig. 2b. This observation suggests that smaller the nanoparticles, higher is their interaction

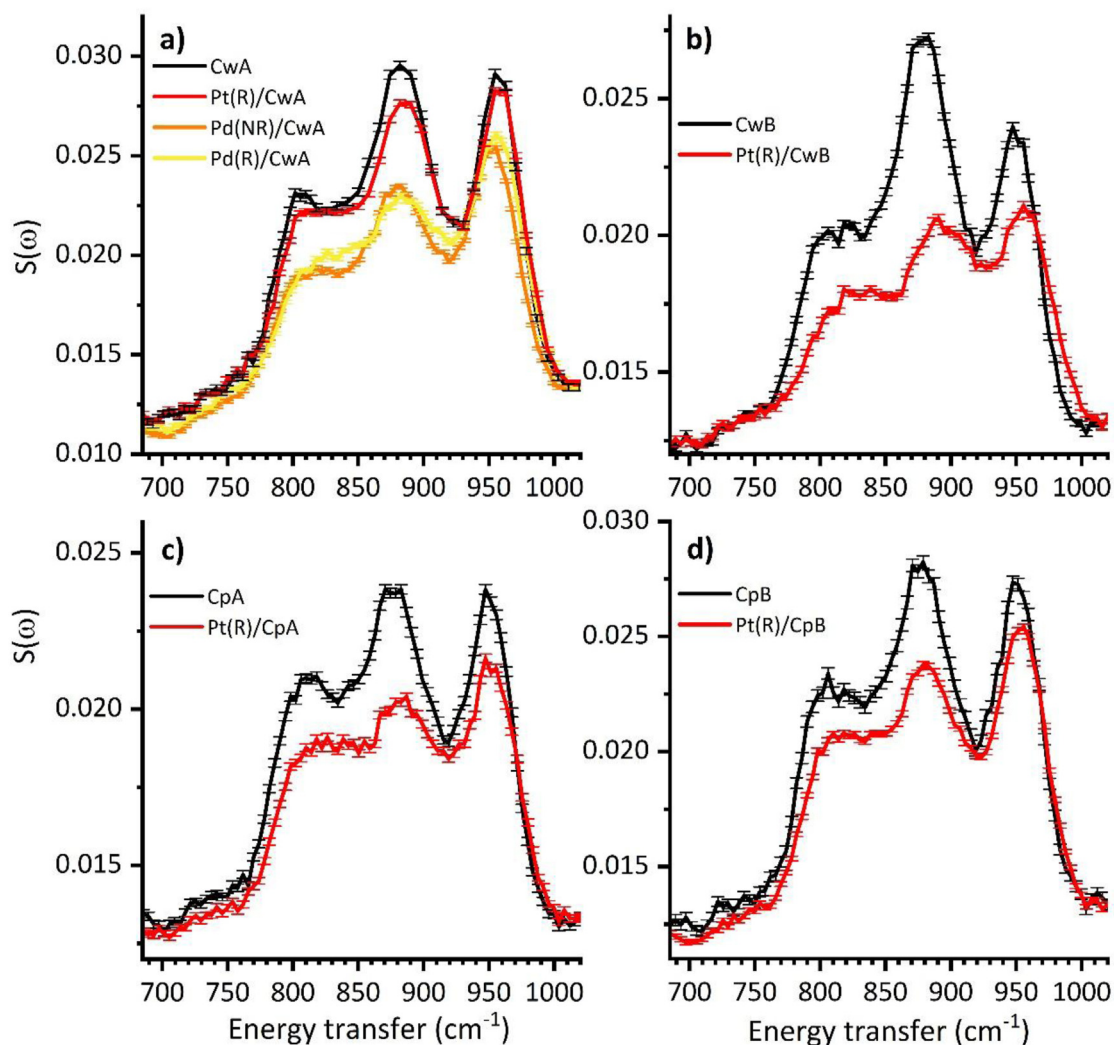


Fig. 1. Experimental INS spectra of the four activated carbons (black) and of the corresponding Pd- and Pt-based catalysts, as measured at the LAGRANGE spectrometer at ILL. The spectra are shown in the 690–1020 cm^{-1} range, characteristic of the out-of-plane C-H bending vibrations. The intensity of the catalysts' spectra is normalised to the one of the support to the value of the background. (A colour version of this figure can be viewed online.)

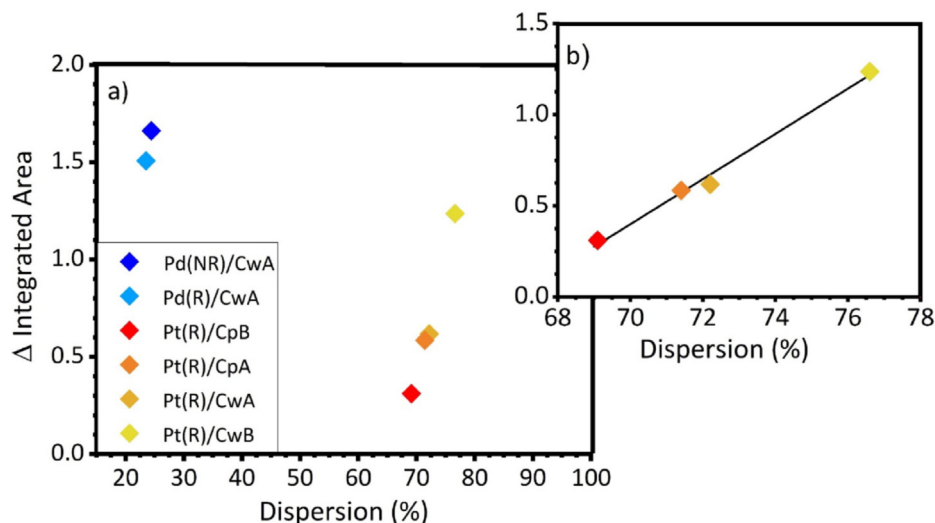


Fig. 2. a) Difference in the integrated area of the INS spectra in the out-of-plane bending region ($690\text{--}1020\text{ cm}^{-1}$) between the bare carbon support and the corresponding catalysts versus the metal dispersion. b) Magnification of the Pt catalysts points: a linear trend can be observed. (A colour version of this figure can be viewed online.)

with the borders of the graphenic platelets. The two Pd catalysts instead exhibit large variations in H content albeit their low dispersion, as shown in Fig. 2a, suggesting that Pd nanoparticles interact more with the C-H terminations than the Pt ones.

4.2. DFT simulations of the INS spectra for regular C-H terminations

The three bands observed in the experimental spectra shown in the previous paragraph are attributed to vibrations of specific C-H terminal geometries. The observed changes in relative intensity thus reflect a change in their concentration. A qualitative bands assignment was done previously on the basis of DFT calculations performed on very simple aromatic models [24], that cannot account for the heterogeneity of real samples. For this reason, we underwent a large and systematic theoretical study aimed at exploring a much wider range of possible sizes, border geometries and terminations, with the aim to perform a quantitative analysis of the experimental spectra.

The models initially employed for the new DFT simulation of the INS spectra consist in regular aromatic structures where all the carbon atoms are sp^2 hybridized and all the terminations are saturated by H atoms. Their geometry can be described in terms of extended regular borders and corners. Extended regular borders can show a regular sequence of benzene rings exposing a single C-H group named zigzag edge (Z), or an alternation of benzene rings exposing two adjacent C-H groups named armchair edge (A). The intersection of two regular borders generates a corner site that can present two, three or four adjacent C-H groups and will be labelled as *duo* (D), *trio* (T) or *quatro* (Q), respectively, following the nomenclature proposed by Zander for substituted benzenes [40,41].

The models have been categorized in Fig. 3 as a function of their shape, i.e. the relative extension of Z and A edges. Fig. 3a summarizes the models having a rectangular shape, which is defined by two zigzag and two armchair edges and by four T corners. Moving in the horizontal direction, the Z edge increases in length while keeping constant the dimension of the A edge; moving in the vertical direction, the A edge increases, instead. Fig. 3b displays models having a parallelogram shape, which is defined by a single type of edge, either Z ($C_{38}H_{18}$, $C_{58}H_{20}$, $C_{50}H_{20}$), or A ($C_{54}H_{22}$). For the $C_{38}H_{18}$ and $C_{50}H_{20}$ models, an aromatic ring was added in order to

break the symmetry, resulting in the addition of a corner of Q type. In this category, the typologies of corners are more varied, resulting in an alternation of D and T corners in the models featuring Z edges and of T and Q corners for the model featuring A edges. Finally, Fig. 3c shows two hexagonal models, the latter being also the largest model adopted in this work, showing only Z edges alternating with D corners. The relative abundance of Z and A edges, as well as of D, T, and Q corners is reported in Fig. 3 for all the models in parenthesis, following the notation (Z/A) for the edges, and [D/T/Q] for the corners.

Fig. 4a shows three representative simulated INS spectra for three models having different size and shape, in comparison with the experimental spectrum of CwA, taken in the following as a reference. As expected, all the models contribute with some bands in the $690\text{--}1020\text{ cm}^{-1}$ range. However, different models clearly show distinct bands in terms of number, position and relative intensity. The simulated INS spectrum of $C_{54}H_{18}$ is the closest to the experimental one in terms of both bands positions and relative intensity, while the INS spectra of $C_{66}H_{22}$ and $C_{38}H_{18}$ evidently show bands not present in the experimental one. This demonstrated that the model geometry has a dramatic effect on the result.

In order to better analyse the characteristic spectral features of each C-H termination portion in the models, their contributions to the overall simulated spectra were separated and analysed individually. For example, model $C_{54}H_{18}$ includes two distinct terminal C-H geometries (Z edges and D corners), whose spectral contributions are reported in Fig. 4b. It is evident that the two C-H terminations display significantly different spectral features: the D corners are responsible for the appearance of the two bands at 800 and 955 cm^{-1} , while the C-H at the Z edges are mainly responsible for the band at 880 cm^{-1} . However, D corners belonging to two different models are characterized by very similar spectral features as shown in Fig. 4c. Analogous considerations apply for the other models and terminations, making it clear that the INS spectra of each C-H termination in the $690\text{--}1020\text{ cm}^{-1}$ range mostly depend on local geometry and are only marginally affected by the general structure of the model. This does not hold for the rest of the spectral range, where the vibrational modes often display collective features, resulting in spectra reflecting the geometry of the whole model more than the single C-H terminations [24].

On these bases, we systematically investigated the INS

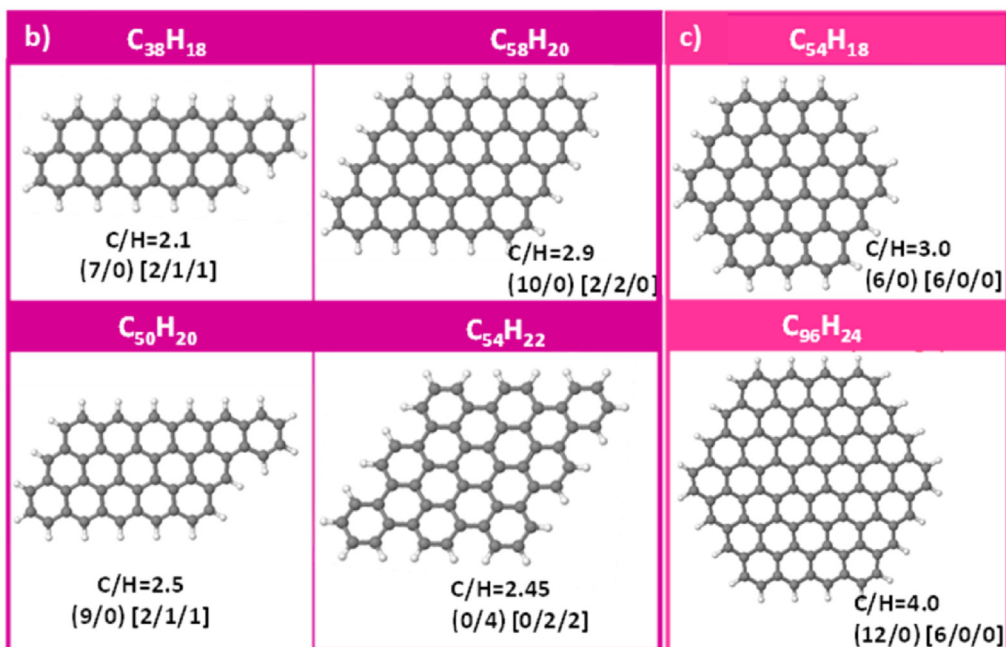
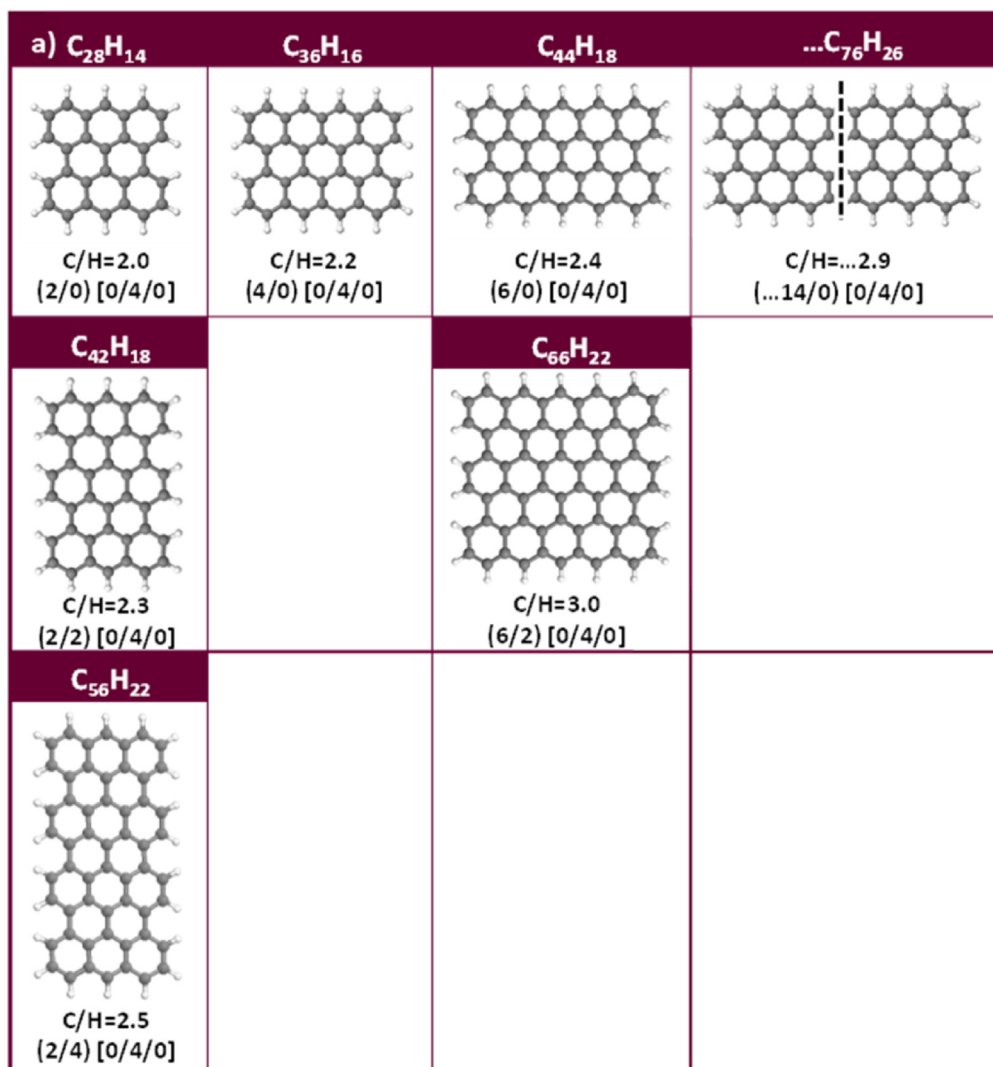


Fig. 3. Overview of the models simulated in this work, categorized in terms of their shape. For all the models, the C/H ratio is indicated, as well as the relative abundance of zigzag and armchair edges (Z/A), and of *duo*, *trio* and *quatro* corners [D/T/Q]. (A colour version of this figure can be viewed online.)

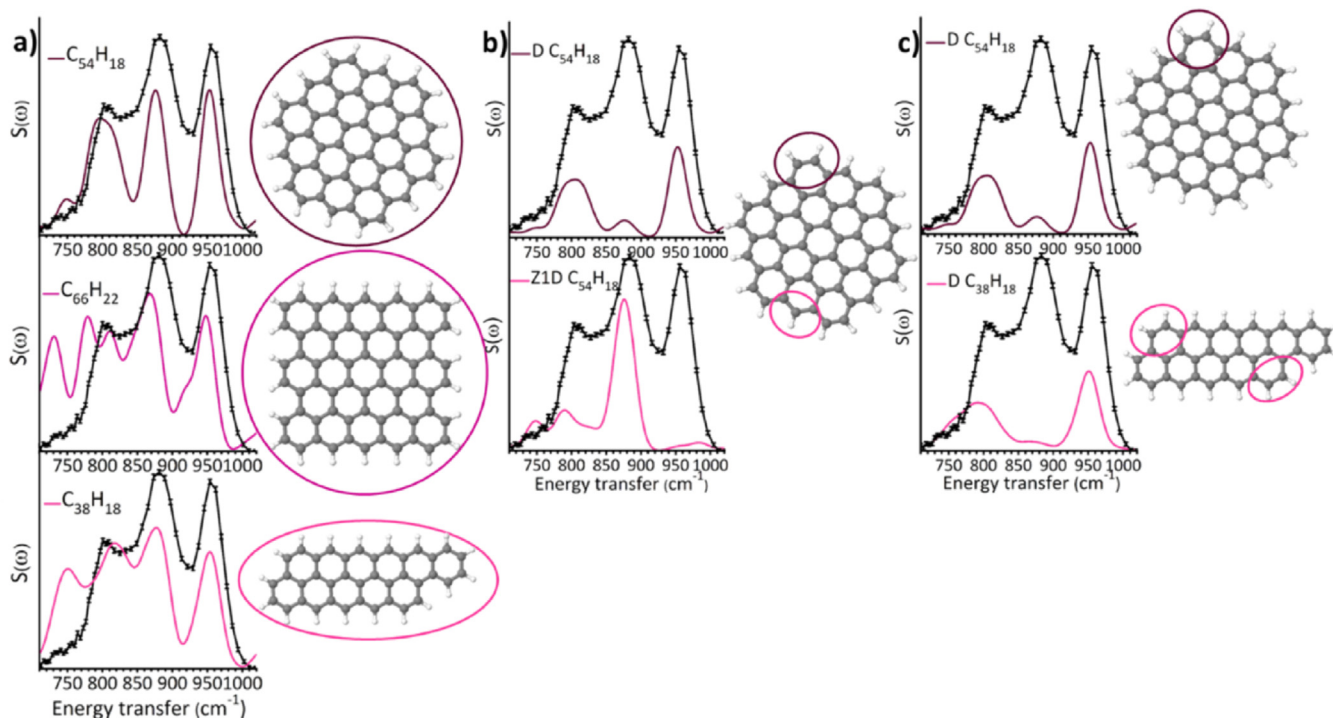


Fig. 4. Part a): Comparison between the simulated INS spectra of three models having different shape and the experimental spectrum of CwA (black). Different model geometries result in different simulated spectra. Part b): The partial contribution of the two types of C-H termination characterizing the C₅₄H₁₈ model in comparison to the experimental spectrum of CwA (black). Part c): Simulated spectral contribution of two D corners belonging to two different models, compared to the experimental spectrum of CwA (black). (A colour version of this figure can be viewed online.)

contributions of specific C-H terminal geometries in the 690–1020 cm⁻¹ range. Five different classes of C-H terminations were identified, and their partial INS spectra were simulated and compared.

Extended zigzag borders give rise to a couple of INS signals centred at ca. 800 cm⁻¹ and 880 cm⁻¹, which are attributed to the out-of-plane bending mode, δ (C-H), in which adjacent C-H sites vibrate out-of-phase and in-phase, respectively. Being a correlated mode, the exact position of these two bands and their relative intensity depend on the extension of the border or, in other words, on

the distance of the C-H groups from the corners. For the sites located at the extremities, it also depends on the geometry of adjacent corner sites. Fig. 5a and b show some representative spectra of zig-zag borders belonging to different models, whereby each C-H group has been labelled as Z, followed by a number indicating the distance from the corner (e.g. Z2 is the second C-H belonging to the regular zigzag border starting counting from the corner). For Z1 sites (i.e. those adjacent to a corner) another letter is added to describe the adjacent corner (D = duo, T = trio). Trying to generalize, the spectra of Z sites far from the corners tend to

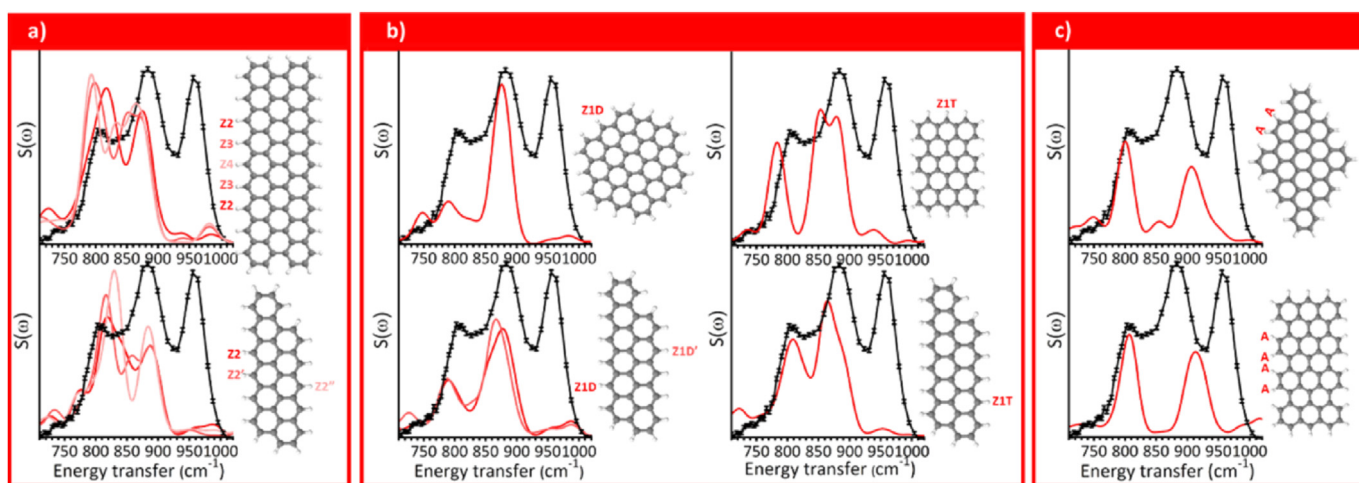


Fig. 5. Part a): Representative contributions of different types of C-H terminations at zig-zag borders (Z sites) far from the corners and belonging to different models. Part b): representative contributions of Z1 C-H terminations differing in the type of adjacent corner (D = duo, T = trio) and belonging to different models. Part c): Representative contributions of different C-H terminations at armchair borders (A sites). (A colour version of this figure can be viewed online.)

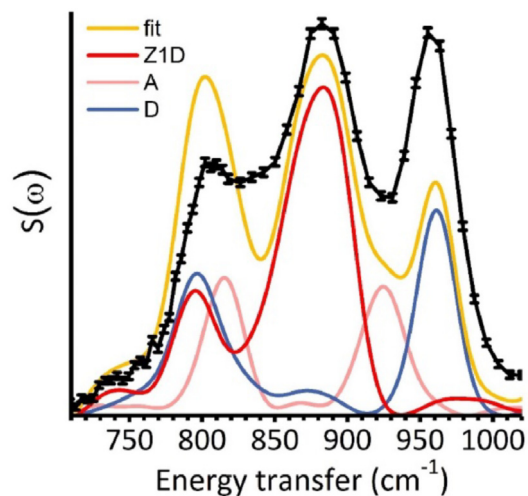
converge, as shown in Fig. 5a (e.g. the spectra of Z3 and Z4 sites in $C_{76}H_{26}$ are very similar). In these cases, usually the band at ca. 800 cm^{-1} is more intense than that at 880 cm^{-1} . Z2 sites tend to show the same two $\delta(\text{C-H})$ bands, shifted at higher energy transfer. The spectra of Z1 sites are more scattered depending on the model (Fig. 5b), and mainly depend on the type of the adjacent corner. For the Z1D sites (i.e. Z1 sites close to a *duo* corner) the band at ca. 800 cm^{-1} is largely reduced in intensity and the spectra are dominated by the band at 880 cm^{-1} . In the spectra of Z1T sites the band at ca. 870 cm^{-1} is usually split in two components and more intense than that at ca. 800 cm^{-1} .

The spectra of **extended armchair borders** (Fig. 5c) are generally characterized by two bands centred at ca. 810 cm^{-1} and 920 cm^{-1} , corresponding to the out-of-plane $\delta(\text{C-H})$ modes of the two adjacent C-H sites that vibrate in-phase and out-of-phase, respectively. In this case, the final spectrum is almost the same irrespective of the length of the border and the geometry of the platelet.

A **duo corner** (Fig. 6a) consists in a benzene ring at a corner position exposing two adjacent C-H groups. The INS spectra of *duo* corners are all characterized by two bands centred at ca. 795 and 960 cm^{-1} , corresponding to the out-of-plane $\delta(\text{C-H})$ modes of the two adjacent C-H groups that vibrate in-phase and out-of-phase, similarly to the extended armchair border case. However, the spectra of D and A sites can be easily distinguished on the bases of the position of the two bands, evidently more spaced for D corners than for A edges. A **trio corner** (Fig. 6b) consists in a benzene ring exposing three adjacent C-H groups. The vibrational modes of the three C-H groups are strongly correlated, and usually four bands are observed, the first two at ca. 750 and 800 cm^{-1} (in some cases the 800 cm^{-1} band appears as a shoulder of the former), the third at 850 and the fourth at 950 cm^{-1} . The relative intensities of the bands appear to be affected by the typology of adjacent extended borders (either Z or A). Finally, a **quatro corner** (Fig. 6c) consists in a benzene ring exposing four adjacent C-H sites. The spectra of Q corners display four bands centred at about 740 , 840 , 930 and 960 cm^{-1} and are almost invariant with the model.

4.3. Linear combination fit with regular C-H components

To quantify, at least in relative terms, the abundance of the different C-H terminal geometries in a certain sample, we fitted the experimental INS spectra shown in Fig. 1 with a linear combination



Z1D	A	D	RMSE
37%	36%	27%	0.003

Fig. 7. Result of the linear combination fit for the experimental spectrum of CwA (black) obtained by including the simulated functions of Z1D, A and D terminations. The best fit solution is reported in yellow, and the percentages of each component of the fit in the final result are reported in table form. The goodness of fit is evaluated by the RMSE. (A colour version of this figure can be viewed online.)

of the simulated spectra discussed in section 4.2. Due to the limited number of experimental points compared to the number of possible C-H contributions from models, we had to limit the number of included functions. Consequently: 1) all the simulated spectra belonging to the same C-H termination category were averaged, reducing the number of possible contributions to eight cases; 2) T and Q corner sites were excluded from the fit analysis because they display too strong contributions in the $730\text{--}800\text{ cm}^{-1}$ region, where the experimental spectra are very weak; 3) the contributions of extended zigzag borders (Z1T, Z2 and Z3–4) always resulted in negligible values (much lower than 1%) when performing preliminary linear combination fit tests, and were thus excluded. Therefore, the experimental spectra were fitted with a linear combination of the simulated functions for Z1D, A and D

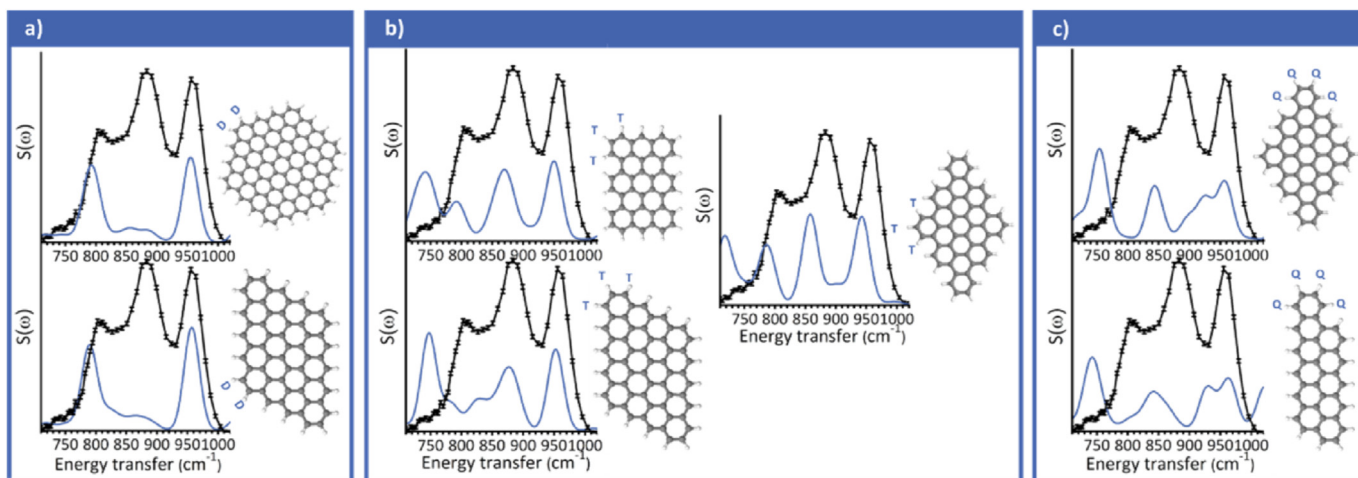


Fig. 6. Representative contributions of different types of C-H corners, belonging to different models: duo (part a), trio (part b) and quatro (part c). (A colour version of this figure can be viewed online.)

terminations. The intensities of the spectra introduced in the linear combination were then normalised to account for a single C-H group.

Fig. 7 shows the best fit (yellow) for the experimental spectrum of CwA (black) and the three different C-H contributions, complemented by a table summarising the resulting relative abundance of the C-H sites. Its Root Mean Square Error (RMSE) expresses the goodness of the fit. Although the three main bands characterizing the experimental spectrum are well reproduced in terms of position, they are not reproduced in terms of relative intensities. In particular, if we renormalize the fitted and experimental spectra to the intensity of the band at 800 cm^{-1} , the bands at 850 and 955 cm^{-1} are missing some intensity as well as additional contributions around 830 and 930 cm^{-1} (i.e. where the experimental spectrum shows two minima) are not accounted for. Analogous results were obtained for all the other samples. Hence, it becomes clear that the fingerprint region of the INS experimental spectrum of a physically activated carbon cannot be fully reproduced by considering only regular C-H terminations.

4.4. DFT simulations of the INS spectra for physical defects

Since activated carbons are by definition disordered and defective materials, the missing components in the fit reported in Fig. 7 might be associated with defects. Defects may arise either because of the presence of heteroatoms (i.e. functional groups), or because of ruptures of the regularity in the aromatic domains (physical defects). Since physically activated carbons display a very low concentration of functional groups [17,42], we focused on the latter class of defects. Although the number of possible physical defects is extremely high, we decided to focus on those containing C-H groups and hence detectable by INS.

First, the aromatic models can simply include some disordered C-H terminations, hardly classifiable as any of the regular borders and corners classes described in section 4.2. For these disordered C-H terminations, the greatest variations in the INS spectra are observed for single zigzag sites, for which some examples are reported in Fig. 8a, first plot. These terminations give a quite broad band centred at ca 830 cm^{-1} , in correspondence with one of the minima of the experimental spectra. Disordered *duo* terminations instead (second plot in Fig. 8a) give two main bands, similarly to the spectra of D and A terminations (Figs. 5c and 6a), but in this case the two bands fall at ca. 800 and 935 cm^{-1} , about midway between the A and D regular cases. Generalizing, we can conclude that the INS fingerprint of terminations consisting in two C-H exposed at the same benzene ring fall within a continuum of cases, of which D and A sites correspond to the two extremes. Finally, T and Q corners are always inserted in peripheral positions in these models and hence they are not affected by disorder and/or defectivity of the model.

We also considered holes within the aromatic platelets and saturated by H atoms, since they have been recently demonstrated to occur in defective graphene [23]. Due to the limited size of the platelets in the activated carbons under investigation [17], only small holes can be imagined. Thus, we have focused on holes created by removing a single C atom from the model forming a five-member ring and a C-H group (Fig. 8b), which we labelled as a single vacancy. A distinct band in the fingerprint region at 950 cm^{-1} , characterizes the simulated INS spectrum of this termination inside the hole.

A third kind of possible irregular termination consists in a single C-H site completely isolated from other C-H groups on adjacent benzene rings (Fig. 8c). In this case, the considered C-H groups are isolated from their neighbours by the presence of four pentagonal rings. In this case, the out-of-plane bending mode of the C-H group has a very little tendency to combine with the vibrations of other C-

H groups, resulting in a single and sharp band centred at ca 880 cm^{-1} .

Activated carbons were also proposed to feature topological defects that introduce local curvature and sphericity within the graphenic planes [43]. We thus decided to simulate two additional models featuring the same kind of C-H terminations as model $\text{C}_{54}\text{H}_{18}$ but with different curvatures, designed by introducing either a five or a seven-member ring at the centre of the model. The analysis of their simulated spectra, shown in Fig. S8 in the supporting information, immediately shows that the spectral features are almost undistinguishable from the corresponding flat model. This indicates that this region of the INS spectra is mostly sensible to the local geometry of the C-H terminations, and much less on defects not directly involving H atoms.

Three further simulations were run on models in which the source of the curvature (i.e. introduction of a five-member ring) is located closer to the borders of the model, and so where it can directly affect the nearby C-H terminations. The characteristic INS spectral features of the three models are reported in Fig. S9 in supporting information. The first two models were built starting from the hexagonal $\text{C}_{54}\text{H}_{18}$ model, by adding five-member rings at two distinct positions close to the border. For these models (Figs. S9A and B), the Z1 and D terminations in close proximity with the five-member rings show bands in the same frequency ranges and with similar intensities as the previously introduced disordered Z1 and D terminations on flat models of Fig. 8a. Consequently, these curved models contribute to the disordered terminations similarly to the flat ones and we cannot distinguish in between them. The third model contains a five-member ring exposing one C-H termination. Its characteristic INS spectrum (Fig. S9C) shows the most intense features in the $600\text{--}750\text{ cm}^{-1}$ range, in correspondence with one of the minima of the experimental spectra. This observation makes us conclude that this specific termination is not expected to be significantly present in our samples.

4.5. Introduction of physical defects in the fit

With the simulations of the physical defects in the hands, we came back to the linear combination analysis and added these new contributions to improve the fit result. To ensure the reliability of the result we limited again as much as possible the number of functions included in the fit, and thus the number of parameters to be optimised. At first, we decided to describe the D, A and disordered D terminations with a single function (D-all), obtained by averaging their characteristic spectra. Then, three new functions were added to the fit, accounting for disordered Z1, isolated Z1 and single vacancy defects, obtained by averaging all the spectra belonging to the same category of C-H terminations.

The new linear combination fit was therefore performed by including five functions Z1D, D-all, disordered Z1, isolated Z1 and single vacancy, and imposing the following constraints: 1) the concentration of regular terminations should be higher than that of irregular and defective sites; 2) for the catalysts, the values of the coefficients in the fit should be equal or lower than those obtained in the fit of the parent carbon. These choices were justified by the observation that the three main peaks in the experimental spectra show a better matching with the spectra of regular terminations, and that the intensity of the INS spectra for the catalysts is always less intense than for the parent carbons. The result of this fit for CwA is shown in Fig. 9. The same procedure was followed for all the other activated carbons and catalysts, resulting in the final values reported in Table 3. For the four activated carbons, all the coefficients obtained from the fit were normalised so that their sum gives 100%, while all the results of the catalysts were normalised

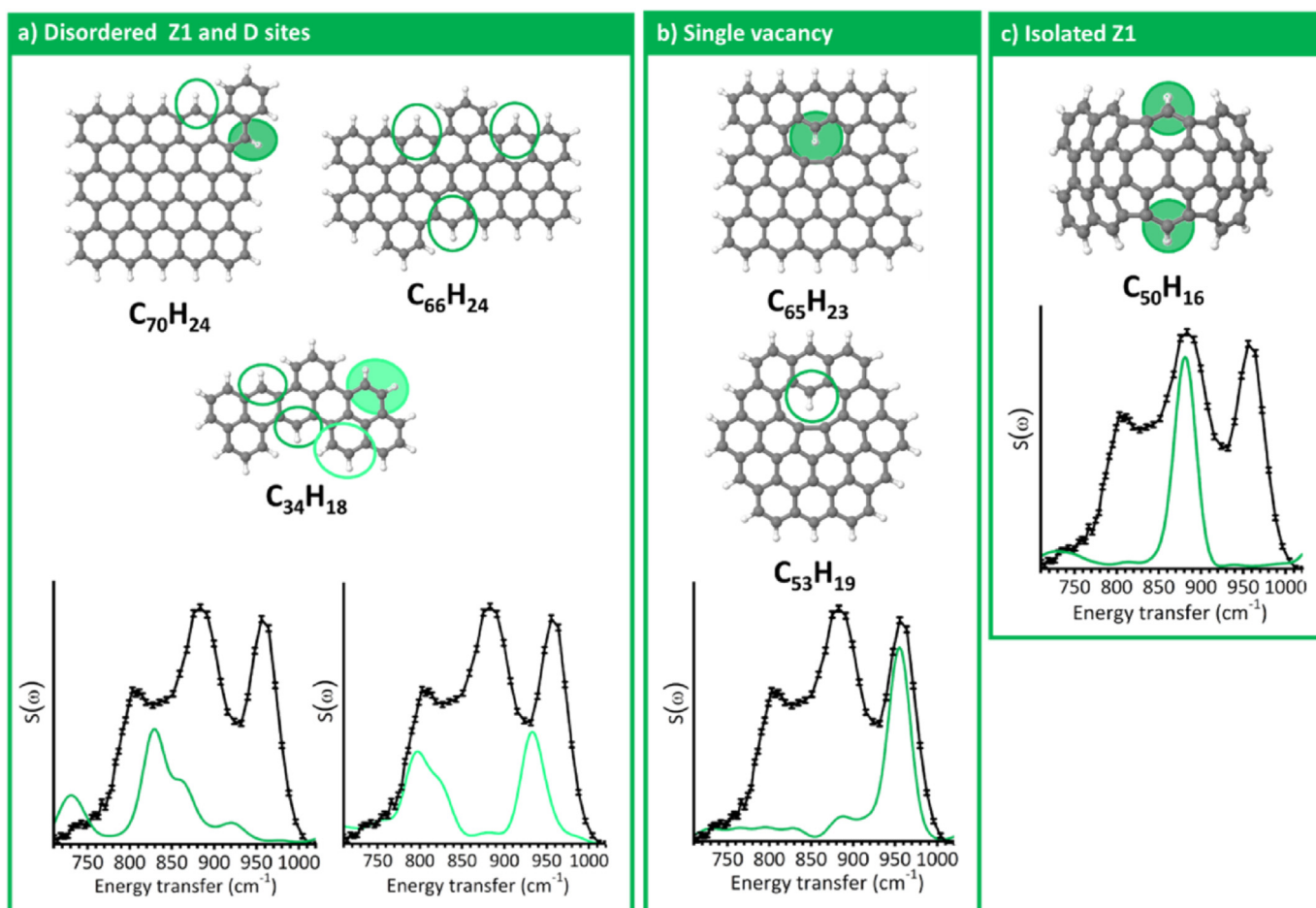


Fig. 8. Disordered and defective models considered in this work and the characteristic contributions to the INS spectra of their defective C-H terminations. The sites that behave differently than the regular ones are indicated by a circle. The reported simulated INS spectra refer to the species highlighted with a full green circle. Part a): Models containing disordered terminations, where disordered Z1 sites are circled in dark green and disordered D sites in light green. A representative spectrum for both disordered Z1 and D sites is reported. Part b): Models containing a Single Vacancy defect saturated by one H atom, and a representative spectrum of their INS contribution. Part c): Model containing an isolated Z1 site, obtained by introducing four five-member rings and curvature in the model, and characteristic INS spectrum of this site. (A colour version of this figure can be viewed online.)

with respect to the parent support, in order to allow a direct evaluation of the loss of hydrogen at the graphenic terminations as a consequence of the metal deposition. The plots showing the results of the linear combination fit analysis for the other samples are reported in Figs. S10, S11, S12 and S13 in the supporting information.

As far as the bare carbons are concerned, the main C-H contributions are relatively similar for all the considered samples. In all the cases the experimental spectra are well reproduced by using mostly Z1D, D-all and disordered Z1 sites, followed by lower amounts of single vacancies, while the contribution of isolated Z1 sites is almost negligible. For all the four carbons, the main contribution is given by D-all sites, followed by Z1D and disordered Z1. The D-all sites are much more frequent in the activated carbons of peat origin than in those of wood origin. Among carbons with the same origin, the greatest difference is observed between CwA and CwB, and it is mostly reflected by the different D-all/Z1D ratio (1.5 and 1.2, respectively).

The deposition of Pd or Pt nanoparticles causes a small decrease in the total intensity of the spectra, as already observed in our previous experiment [5]. The result of the linear combination fit analysis allows us to evaluate which are the most affected C-H species: in fact, albeit the amount of all C-H sites decreases with

respect to the parent carbon, the greatest variation is always observed for Z1D sites. For CwA, the perturbation caused by the deposition of Pt nanoparticles (sample Pt(R)/CwA) is relatively modest, with the greatest change observed for Z1D sites which decreased by about 5%. The deposition of Pd nanoparticles, instead, causes a much larger reduction of the regular C-H terminations, mostly evident for Z1D sites which decrease by about 10% in Pd(NR)/CwA, and by 12% for Pd(R)/CwA. These data also clearly indicate that the cause of the observed H loss in the catalysts is the deposition of the metal, and not the successive pre-reduction step. The most significant change was observed when depositing Pt nanoparticles on the CwB support, which resulted in a decrease of about 13% for Z1D sites and of about 12% for disordered Z1 sites. The effect of the Pt deposition is instead quite similar for the two carbons of peat origin, where the Z1D sites decreased of ca. 8–9% and the D-all decrease by about 5–7%.

Even if the matching between the fitted solution and the experimental spectra improved significantly with the introduction of physical defects, it is evident for all the samples that the fits are still missing some contribution at about 920 cm^{-1} , in correspondence with one of the minima of the experimental spectra. None of the defective models that we have simulated so far seems able to cover that region. Further simulations and experiments in this

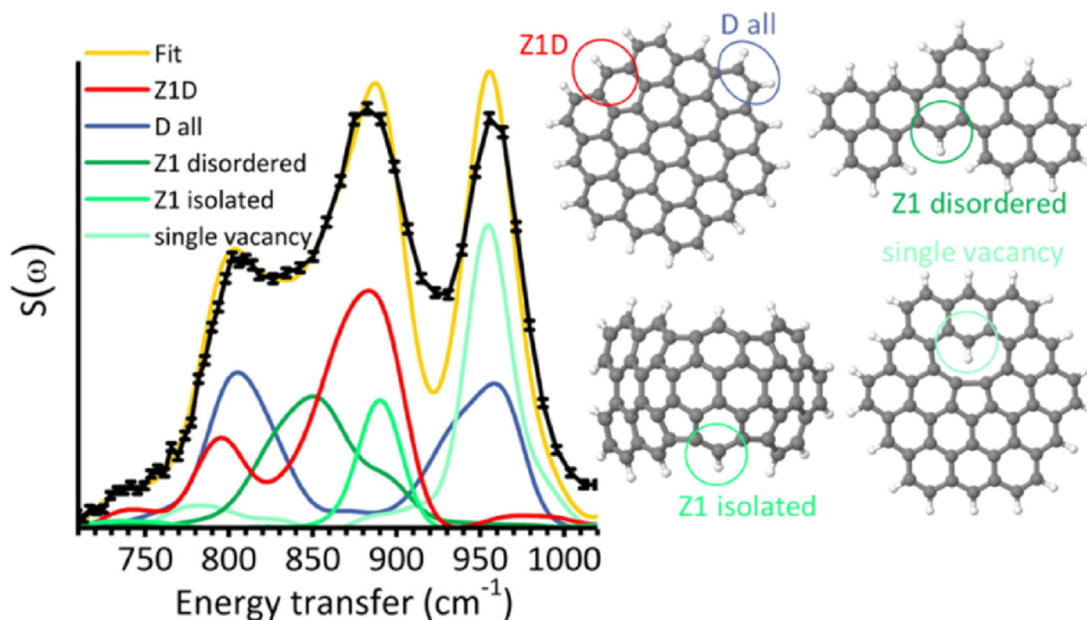


Fig. 9. Result of the linear combination fit for the sample CwA. The best result was obtained by introducing in the linear combination the functions for Z1D, D-all, disordered Z1, isolated Z1 and single vacancy sites. An example of a C-H termination for each function in the fit is reported for clarity. (A colour version of this figure can be viewed online.)

Table 3

Summary of the results of the linear combination fit on the experimental INS spectra of all the activated carbons and catalysts. The values for the activated carbon supports are normalised so that their sum gives 100%, while those of the catalysts were normalised with respect to the parent support. The goodness of the fit is evaluated by the RMSE.

	Z1D %	D-all %	Disordered Z1%	Single vacancy %	Isolated Z1%	TOT	RMSE
CwA	25	38	19	12	5	100	0.001
Pt(R)/CwA	20	36	19	12	5	92	0.001
Pd(NR)/CwA	15	32	17	11	4	78	0.001
Pd(R)/CwA	13	32	19	11	4	79	0.002
CwB	28	33	23	11	5	100	0.001
Pt(R)/CwB	15	29	11	9	4	67	0.001
CpA	24	42	22	10	2	100	0.001
Pt(R)/CpA	16	35	18	9	2	78	0.001
CpB	27	41	20	11	2	100	0.001
Pt(R)/CpB	18	36	19	11	2	86	0.001

direction are planned.

5. Conclusions

In this work, we present the high-resolution INS spectra of four different activated carbons and of six industrial catalysts obtained by depositing Pd or Pt nanoparticles on the same carbons. The INS spectra contain information on the type and amount of the C-H terminations at the graphenic domains constituting the carbon. Albeit the investigated carbon supports show a certain degree of structural, porous and morphological heterogeneity, the unprecedented high signal-to-noise ratio of our spectra in comparison with past measurements [17] allowed us to highlight tiny differences among carbons having different origins, and between the catalysts and the corresponding carbon supports. In particular, we observed that the deposition of the metal nanoparticles causes a general decrease of the C-H signals, which for Pt scales linearly with the metal dispersion: smaller the metal nanoparticles, larger is the amount of C-H affected by the metal deposition.

In order to interpret the differences observed in the

experimental spectra, an extensive DFT study was performed. At first, we simulated the INS spectra of several aromatic models characterized by regular C-H terminations and/or by the presence of some physical defects. Successively, we determined the characteristic INS fingerprint of different C-H terminations. The experimental INS spectra were systematically fitted with a linear combination of five functions corresponding to: 1) C-H at regular zigzag borders and vicinal to a *duo* corner (Z1D); 2) C-H at regular armchair borders, at *duo* corners or at disordered *duo* terminations (D-all); 3) C-H at disordered zigzag borders (disordered Z1); 4) isolated C-H (isolated Z1); and 5) C-H in single vacancies inside the graphenic platelets. We found out that, although regular aromatic models are already able to reproduce the position of the experimental features, physical defects and disordered C-H species are necessary to obtain a good match between experimental and fitted spectra. We were not able to identify a general spectral fingerprint for the curvature and not planarity of the graphenic domains, but two of the defective contributions identified by linear combination analysis (Isolated Z1 and Single Vacancy) were indeed given by not planar models. Thus, it does not appear possible to describe in full

the platelets structure within activated carbons considering flat geometries only.

The results of the fits indicate that the most frequent C-H terminations in all the activated carbons are D-all, followed by Z1D and disordered Z1, while the other two types of defects are much less frequent. The relative abundance of Z1D terminations is lower for carbons of peat origin (Cp) than for those of wood origin (Cw). Since the metal dispersion for catalysts prepared on Cp carbons is systematically lower than that on Cw carbons, these results suggest that the metal dispersion is improved on carbons having a large percentage of Z1D terminations. The decisive role of Z1D sites is confirmed by the observation that the metal nanoparticles deposition mainly affects this typology of C-H termination. These outcomes are particularly relevant for catalysis, since they offer for the first time an explanation of the relationship between the type of the carbon support and the metal dispersion. On a more general ground, this study demonstrates that high resolution INS spectra complemented by a systematic DFT study are invaluable tools for characterizing carbon-based materials.

CRedit authorship contribution statement

Eleonora Vottero: Methodology, Formal analysis, Investigation, Writing - original draft. **Michele Carosso:** Investigation, Writing - review & editing. **Mónica Jiménez-Ruiz:** Investigation, Writing - review & editing. **Riccardo Pellegrini:** Investigation, Resources, Writing - review & editing. **Elena Groppo:** Conceptualization, Methodology, Writing - review & editing, Supervision, Project administration. **Andrea Piovano:** Conceptualization, Methodology, Investigation, Writing - review & editing, Supervision.

Declaration of competing interest

The authors declare that they have no known competing financial interests or personal relationships that could have appeared to influence the work reported in this paper.

Acknowledgments

This work was strongly encouraged from the beginning by our beloved Carlo Lamberti and Giuseppe Leofanti, to whom we will be infinitely grateful for having guided us with passion and enthusiasm. We are also grateful to ILL for the time we have accounted on the computational cluster.

Appendix A. Supplementary data

Supplementary data to this article can be found online at <https://doi.org/10.1016/j.carbon.2020.07.033>.

References

- [1] F. Rodríguez-Reinoso, Production and applications of activated carbons, *Handb. Porous Solid*. (2002) 1766–1827.
- [2] V. Fierro, V. Torné-Fernández, D. Montané, A. Celzard, Adsorption of phenol onto activated carbons having different textural and surface properties, *Microporous Mesoporous Mater.* 111 (1) (2008) 276–284.
- [3] S. Sircar, T.C. Golden, M.B. Rao, Activated carbon for gas separation and storage, *Carbon* 34 (1) (1996) 1–12.
- [4] E. Auer, A. Freund, J. Pietsch, T. Tacke, Carbons as supports for industrial precious metal catalysts, *Appl. Catal. Gen.* 173 (2) (1998) 259–271.
- [5] J.L. Figueiredo, M.F.R. Pereira, The role of surface chemistry in catalysis with carbons, *Catal. Today* 150 (1) (2010) 2–7.
- [6] N. Wang, T. Li, Y. Song, J. Liu, F. Wang, Metal-free nitrogen-doped porous carbons derived from pomelo peel treated by hypersaline environments for oxygen reduction reaction, *Carbon* 130 (2018) 692–700.
- [7] Y. Qiu, S. Ali, G. Lan, H. Tong, J. Fan, H. Liu, B. Li, W. Han, H. Tang, H. Liu, Y. Li, Defect-rich activated carbons as active and stable metal-free catalyst for acetylene hydrochlorination, *Carbon* 146 (2019) 406–412.
- [8] X. Li, X. Duan, C. Han, X. Fan, Y. Li, F. Zhang, G. Zhang, W. Peng, S. Wang, Chemical activation of nitrogen and sulfur co-doped graphene as defect-rich carbocatalyst for electrochemical water splitting, *Carbon* 148 (2019) 540–549.
- [9] Y. Hao, X. Zhang, Q. Yang, K. Chen, J. Guo, D. Zhou, L. Feng, Z. Slanina, Highly porous defective carbons derived from seaweed biomass as efficient electrocatalysts for oxygen reduction in both alkaline and acidic media, *Carbon* 137 (2018) 93–103.
- [10] Z. Qiu, Y. Lin, H. Xin, P. Han, D. Li, B. Yang, P. Li, S. Ullah, H. Fan, C. Zhu, J. Xu, Ultrahigh level nitrogen/sulfur co-doped carbon as high performance anode materials for lithium-ion batteries, *Carbon* 126 (2018) 85–92.
- [11] B.S. Girgis, S.S. Yunis, A.M. Soliman, Characteristics of activated carbon from peanut hulls in relation to conditions of preparation, *Mater. Lett.* 57 (1) (2002) 164–172.
- [12] L.S. de Lima, S.P. Quinária, F.L. Melquiades, G.E.V. de Biasi, J.R. Garcia, Characterization of activated carbons from different sources and the simultaneous adsorption of Cu, Cr, and Zn from metallurgy effluent, *Separ. Purif. Technol.* 122 (2014) 421–430.
- [13] A. Lazzarini, R. Pellegrini, A. Piovano, S. Rudić, C. Castan-Guerrero, P. Torelli, M.R. Chierotti, R. Gobetto, C. Lamberti, E. Groppo, The effect of surface chemistry on the performances of Pd-based catalysts supported on activated carbons, *Catal. Sci. Technol.* 7 (18) (2017) 4162–4172.
- [14] P. Yan, B. Zhang, K.-H. Wu, D. Su, W. Qi, Surface chemistry of nanocarbon: characterization strategies from the viewpoint of catalysis and energy conversion, *Carbon* 143 (2019) 915–936.
- [15] P.W. Albers, J. Pietsch, J. Krauter, S.F. Parker, Investigations of activated carbon catalyst supports from different natural sources, *Phys. Chem. Chem. Phys.* 5 (9) (2003) 1941–1949.
- [16] P.W. Albers, W. Weber, K. Möbus, S.D. Wieland, S.F. Parker, Neutron scattering study of the terminating protons in the basic structural units of non-graphitising and graphitising carbons, *Carbon* 109 (2016) 239–245.
- [17] A. Lazzarini, A. Piovano, R. Pellegrini, G. Leofanti, G. Agostini, S. Rudić, M.R. Chierotti, R. Gobetto, A. Battiato, G. Spoto, A. Zecchina, C. Lamberti, E. Groppo, A comprehensive approach to investigate the structural and surface properties of activated carbons and related Pd-based catalysts, *Catal. Sci. Technol.* 6 (13) (2016) 4910–4922.
- [18] M. Carosso, A. Lazzarini, A. Piovano, R. Pellegrini, S. Morandi, M. Manzoli, J.G. Vitillo, M.J. Ruiz, C. Lamberti, E. Groppo, Looking for the active hydrogen species in a 5 wt% Pt/C catalyst: a challenge for inelastic neutron scattering, *Faraday Discuss* 208 (2018) 227–242, 0.
- [19] P. Albers, K. Seibold, G. Prescher, B. Freund, S.F. Parker, J. Tomkinson, D.K. Ross, F. Fillaux, Neutron spectroscopic investigations on different grades of modified furnace blacks and gas blacks, *Carbon* 37 (3) (1999) 437–444.
- [20] F. Fillaux, R. Papoula, A. Lautié, J. Tomkinson, Inelastic neutron-scattering study of the proton dynamics in carbons and coals, *Carbon* 32 (7) (1994) 1325–1331.
- [21] S.F. Parker, S. Imberti, S.K. Callear, P.W. Albers, Structural and spectroscopic studies of a commercial glassy carbon, *Chem. Phys.* 427 (2013) 44–48.
- [22] I. Natkaniec, E.F. Sheka, K. Druzicki, K. Hoiderna-Natkaniec, S.P. Gubin, E.Y. Buslaeva, S.V. Tkachev, Computationally supported neutron scattering study of parent and chemically reduced graphene oxide, *J. Phys. Chem. C* 119 (32) (2015) 18650–18662.
- [23] C. Cavallari, D. Pontiroli, M. Jiménez-Ruiz, M. Johnson, M. Aramini, M. Gaboardi, S.F. Parker, M. Riccò, S. Rols, Hydrogen motions in defective graphene: the role of surface defects, *Phys. Chem. Chem. Phys.* 18 (36) (2016) 24820–24824.
- [24] A. Piovano, A. Lazzarini, R. Pellegrini, G. Leofanti, G. Agostini, S. Rudić, A.L. Bugaev, C. Lamberti, E. Groppo, Progress in the characterization of the surface species in activated carbons by means of INS spectroscopy coupled with detailed DFT calculations, *Adv. Condens. Matter Phys.* 2015 (2015).
- [25] R. Pellegrini, G. Leofanti, G. Agostini, E. Groppo, M. Rivallan, C. Lamberti, Pd-supported catalysts: evolution of support porous texture along Pd deposition and alkali-metal doping, *Langmuir* 25 (11) (2009) 6476–6485.
- [26] G. Agostini, E. Groppo, A. Piovano, R. Pellegrini, G. Leofanti, C. Lamberti, Preparation of supported Pd catalysts: from the Pd precursor solution to the deposited Pd²⁺ phase, *Langmuir* 26 (13) (2010) 11204–11211.
- [27] K.M. Kaprielova, O.A. Yakovina, I.I. Ovchinnikov, S.V. Koscheev, A.S. Lisitsyn, Preparation of platinum-on-carbon catalysts via hydrolytic deposition: factors influencing the deposition and catalytic properties, *Appl. Catal. Gen.* 449 (2012) 203–214.
- [28] J.R. Anderson, K.C. Pratt, Introduction to Characterization and Testing of Catalysts, Academic Press, Sydney, Australia, 1986.
- [29] G. Agostini, R. Pellegrini, G. Leofanti, L. Bertinetti, S. Bertarione, E. Groppo, A. Zecchina, C. Lamberti, Determination of the particle size, available surface area, and nature of exposed sites for Silica–Alumina-supported Pd nanoparticles: a multitechnical approach, *J. Phys. Chem. C* 113 (24) (2009) 10485–10492.
- [30] M. Jiménez-Ruiz, A. Ivanov, S. Fuard, Lagrange - the new neutron vibrational spectrometer at the ILL, *J. Phys. Conf.* 549 (2014), 012004.
- [31] A. Piovano, G. Agostini, M. Carosso, E. Groppo, M. Jimenez Ruiz, C. Lamberti, A. Lazzarini, M. Manzoli, S. Morandi, R. Pellegrini, E. Vottero, Study of the Pt-Hydride Formation and Spillover Effect on Pt/Al₂O₃ and Pt/C Catalysts, 2016, <https://doi.org/10.5291/ILL-DATA.7-05-466>.
- [32] E. Vottero, M. Carosso, E. Groppo, M. Jimenez Ruiz, C. Lamberti, R. Pellegrini, A. Piovano, Exploring the Surface Chemistry of Activated Carbons by INS and DFT Calculations, 2018, <https://doi.org/10.5291/ILL-DATA.7-04-162>.

- [33] R. Dovesi, A. Erba, R. Orlando, C.M. Zicovich-Wilson, B. Civalleri, L. Maschio, M. Rérat, S. Casassa, J. Baima, S. Salustro, B. Kirtman, Quantum-mechanical condensed matter simulations with CRYSTAL, *Wiley Interdiscipl. Rev.: Comput. Mol. Sci.* 8 (4) (2018).
- [34] A.J. Ramirez-Cuesta, aCLIMAX 4.0.1, the new version of the software for analyzing and interpreting INS spectra, *Comput. Phys. Commun.* 157 (3) (2004) 226–238.
- [35] A.D. Becke, Density-functional thermochemistry. III. The role of exact exchange, *J. Chem. Phys.* 98 (7) (1993) 5648–5652.
- [36] C. Lee, W. Yang, R.G. Parr, Development of the Colle-Salvetti correlation-energy formula into a functional of the electron density, *Phys. Rev. B* 37 (2) (1988) 785–789.
- [37] L. Maschio, M. Lorenz, D. Pullini, M. Sgroi, B. Civalleri, The unique Raman fingerprint of boron nitride substitution patterns in graphene, *Phys. Chem. Chem. Phys.* 18 (30) (2016) 20270–20275.
- [38] T. Kar, S. Scheiner, U. Adhikari, A.K. Roy, Site preferences of carboxyl groups on the periphery of graphene and their characteristic IR spectra, *J. Phys. Chem. C* 117 (35) (2013) 18206–18215.
- [39] M. Alcolea Palafox, Scaling factors for the prediction of vibrational spectra. I. Benzene molecule, *Int. J. Quant. Chem.* 77 (3) (2000) 661–684.
- [40] A. Centrone, L. Brambilla, T. Renouard, L. Gherghel, C. Mathis, K. Müllen, G. Zerbi, Structure of new carbonaceous materials: the role of vibrational spectroscopy, *Carbon* 43 (8) (2005) 1593–1609.
- [41] M. Zander, Die herstellung von Polycyclischen aromaten, in: M. Zander (Ed.), *Polycyclische Aromaten: Kohlenwasserstoffe und Fullerene*, Vieweg+Teubner Verlag, Wiesbaden, 1995, pp. 158–187.
- [42] J.L. Figueiredo, M.F.R. Pereira, M.M.A. Freitas, J.J.M. Órfão, Modification of the surface chemistry of activated carbons, *Carbon* 37 (9) (1999) 1379–1389.
- [43] P.J.F. Harris, Fullerene-like models for microporous carbon, *J. Mater. Sci.* 48 (2) (2013) 565–577.

In re-submission to Catalysis Science & Technology

Simultaneous identification and quantification of functional groups in activated carbons through an innovative TPD-IR approach

Eleonora Vottero,^{1,2} Michele Carosso,¹ Riccardo Pellegrini,³ Andrea Piovano,² Elena Groppo^{1,*}

1) Department of Chemistry, NIS Centre and INSTM, University of Turin, Via G. Quarello 15/A, Turin, I-10135, Italy;

2) Institut Laue-Langevin (ILL), 71 Avenue des Martyrs, 38042 Grenoble, France;

3) Chimet SpA–Catalyst Division, Via di Pescaiola 74, Viciomaggio Arezzo, I-52041, Italy

Abstract

Activated carbons play a key role in catalytic applications thanks to the possibility to tune their surface chemistry by changing the precursor or the activation treatment. However, the characterization of their surface species is not straightforward. Herein, we present the potentials of a newly developed Temperature Programmed Desorption - Infrared approach for the simultaneous identification and quantification of functional groups in activated carbons. We tested it on seven carbons used in catalysis, differing in precursors, activation routes and post-activation treatments. The novelty of our set-up relies in the possibility to accumulate the gaseous decomposition products, which are univocally detected and quantified by IR spectroscopy. This allows the quantification of gases released at high concentration (CO₂ and CO) and of those produced at trace levels (e.g. CH₄, NO). Moreover, H₂O can be quantified, giving information on the fraction of functional groups close enough to condense. As an example of the potential of this setup, we were able to distinguish significant differences between four steam activated carbons, where the amount of functional groups is very low, and to detect N-containing products from carbons oxidized in HNO₃, which demonstrates the presence of N-containing functional groups not distinguished by any other method.

Keywords: activated carbons; functional groups; TPD-IR

* Corresponding author: tel. +39 011 6708373, E-mail: elena.groppo@unito.it

1. Introduction

Activated carbons are high surface area materials, employed in applications ranging from adsorption, storage, environmental remediation, catalysis and many others¹⁻⁵. They are obtained from different carbonaceous precursors (wood, peat, coconut shells, etc.) following either a physical or a chemical activation route^{4,5}. In the former case, the precursor is carbonized at high temperature in inert atmosphere and then activated by weakly reactive species such as steam or CO₂, while in the latter case the precursor is impregnated by a chemical agent (such as ZnCl₂ or H₃PO₄) prior carbonization. They can be further modified by post-activation treatments⁶⁻⁸, for example by strong oxidizing agents. Both the precursor and the activation route affect the textural properties (e.g. specific surface area and porosity)^{9,10}, as well as the concentration of heteroatoms and the nature and content of the functional groups determining their chemical properties^{11,12}. Identifying and quantifying the functional groups in an activated carbon is particularly important since they play a relevant role in most of their applications. For example, electronegative heteroatoms modify the polarity of the carbon surface, with consequences on its adsorption and reactivity properties^{1,13}. Functional groups can also generate specific interactions with other molecules, which can be favorable or detrimental to specific applications¹⁴.

Many experimental techniques allow, in principle, a direct characterization of the functional groups in activated carbons. For example, the Boehm titration method¹⁵ allows the quantification of the O-containing functional groups displaying acidic or basic properties, but it cannot account for neutral species. X-ray photoelectron spectroscopy (XPS) permits to quantify several heteroatoms-containing functional groups¹⁶, but it is limited to the sample surface. Infrared spectroscopy (mostly performed in DRIFT mode) allows in principle the detection of all the IR active species^{14,17,18}, but the bands assignment is often challenging, and even more so is the quantification of the species. Inelastic neutron scattering spectroscopy is useful to detect H containing species¹⁸⁻²⁰, but is poorly sensible to other elements such as O or N. Raman spectroscopy provides information on the degree of aromaticity and disorder of C-C bonds in the graphitic platelets²¹, but is weakly sensible to peripheral species.

To overcome these limitations, TPD (Temperature Programmed Desorption), which demonstrated to be a solid approach for the identification and quantification of adsorbed species²²⁻²⁵, has been efficiently used to indirectly identify and quantify functional groups in activated carbons^{6,7,26-30}. In such case, the technique exploits the fact that each functional group

decomposes within a specific temperature range, generating a few gaseous molecules that, for O-containing functional groups, usually consist in CO, CO₂ and H₂O. Extended studies in the literature allow estimating the decomposition products and the decomposition temperature for the main O-containing functional groups, as summarized in Figure 1. The characteristic temperature intervals for the decomposition of each functional group span over large ranges because of their intrinsic heterogeneity, but also because of a not complete agreement among different authors in the literature. Nevertheless, some general trends can be readily noticed: 1) the low temperature range ($T < 400^{\circ}\text{C}$) is generally attributed to the decomposition of carboxylic acid groups to CO₂^{26, 27, 31-33}; 2) the intermediate temperature range ($400 < T < 650^{\circ}\text{C}$) is characteristic for the decomposition of carboxylic anhydrides to CO₂ + CO and lactones to CO₂^{26, 27, 31-33}; 3) the high temperature range ($T > 550^{\circ}\text{C}$) is the characteristic region for the decomposition of phenols, ethers and carbonyls to CO^{26, 27, 31, 33}.

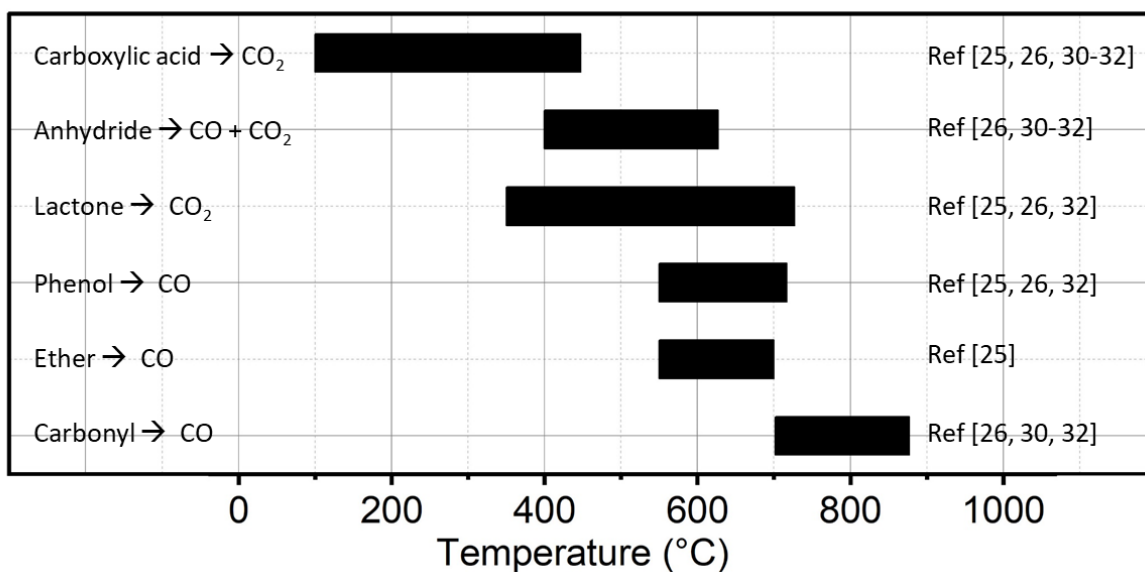


Figure 1: Decomposition temperature intervals for the main oxygen containing functional groups as reported in the literature.

Most of the studies in the literature focus on the formation of CO and CO₂, but the release of H₂O is also observed, although rarely discussed. Weakly adsorbed water gives origin to a large TPD peak at $T < 200^{\circ}\text{C}$ ^{6, 34}, unless this fraction is removed from the samples before the TPD experiment by a treatment in vacuum, in an inert gas flow and/or modest heating ($T < 150^{\circ}\text{C}$). However, some works^{6, 32, 34} pointed out the presence of H₂O peaks in the TPD runs at higher

temperatures, which were attributed either to the desorption of strongly adsorbed water hydrogen-bonded to oxygen-containing functional groups ($T < 400^{\circ}\text{C}$) or to the condensation of two adjacent functional groups with the removal of a H_2O molecule (for example, two carboxylic acids may condense to form an anhydride, or a carboxylic acid and a phenol may condense to form a lactone, or two phenols may condense to give an ether). Finally, the evolution of H_2O at temperature higher than 200°C was also interpreted as due to the direct decomposition of some functional groups. In particular, Li *et al*³⁵ ascribed the simultaneous evolution of CO and H_2O at ca. 240 and 330°C to the decomposition of carboxylic acids groups through an alternative route. Vivo-Vilches *et al*³⁶ reported the contemporary evolution of CO , CO_2 and H_2O at ca. 280°C , attributing these products to the formation and immediate decomposition of an anhydride group from two adjacent carboxylic acid groups. In this perspective, also part of the H_2O released during a TPD run should be accounted for the total O content in an activated carbon.

During a typical TPD experiment on an activated carbon, the sample is heated under an inert gas flow and the decomposition products are detected and quantified on-line by gas chromatography (GC), mass spectrometry (MS) or infrared (FT-IR) spectroscopy³⁷⁻³⁹. The drawback of this approach is that some species may escape on-line detection when the temperature ramp is too fast. In a few cases, and in particular for graphite based samples, the experiments have been conducted under dynamic vacuum or very low pressure values and the measurement of the released gases was performed by MS⁴⁰⁻⁴². However, detection by MS suffers of a difficult calibration and of interpretation issues caused by the overlap of the m/z values of fragments deriving from different gases⁴³.

In this work we developed an experimental set-up to perform a systematic TPD study on several activated carbons, working in static conditions to accumulate the gaseous products in a known volume, and using FT-IR spectroscopy for their detection and quantification. On one hand, the accumulation of the decomposition products as an alternative to a gas flux results in higher concentration of the species in the IR cell, allowing detection and often quantification of minor decomposition products not visible in flux conditions. On the other hand, the identification of the produced gases by FT-IR spectroscopy is straightforward due to the fact that the IR rotovibrational profile of each gas is univocal, while their quantification is possible exploiting the Lambert-Beer law, after a careful calibration. Our system is also flexible regarding the amount of sample, allowing to measure with good resolution the TPD profile of carbons containing either

low or high concentration of functional groups. Our TPD-IR approach was used to characterize seven activated carbons used in catalysis, produced from different precursors and following different activation routes and post-activation treatments. The same samples were already extensively characterized by our research group in the past employing a large variety of techniques^{14, 18-20}, but never performing a systematic identification and quantification of the main functional groups.

2. Experimental

2.1. Samples

All the activated carbons examined in the present work were provided by Chimet S.p.A⁴⁴. Their origin, activation method, post-activation treatment (when present) and the values of specific surface area (SSA_{BET}) and micropore volume (V_{micro}) are summarized in Table 1. The N_2 adsorption isotherms are reported in Figure S1 of the Supporting Information. Four of the carbons were physically activated by steam, two of them originating from wood (CwA and CwB) and two from peat (CpA and CpB). Cchemi was obtained via a chemical activation procedure by means of H_3PO_4 on a wood precursor. Finally, CwA-Ox and Cchemi-Ox were obtained from CwA and Cchemi, respectively, by a post-activation treatment in concentrated HNO_3 (67% w/w) at room temperature for 24 h, followed by washing steps in distilled water until reaching neutral pH.

Table 1: List of the activated carbons analyzed in the present work, specifying the precursor materials, the activation method, the post-activation oxidative treatment (when present), as well as the specific surface area and the micropore volume as determined by N_2 physisorption measurements.

Label	Origin	Activation method	Post-activation	SSA_{BET} (m^2g^{-1})	V_{micro} (cm^3g^{-1})
CwA	Wood	Physical, steam	-	1018	0.63
CwB	Wood	Physical, steam	-	1325	0.65
CpA	Peat	Physical, steam	-	903	0.49
CpB	Peat	Physical, steam	-	882	0.52
Cchemi	Wood	Chemical, H_3PO_4	-	1508	1.11
CwA-Ox	Wood	Physical, steam	CwA + HNO_3	949	0.59
Cchemi-Ox	Wood	Chemical, H_3PO_4	Cchemi + HNO_3	1442	1.13

2.2 TPD-IR set-up and experimental protocol

A simplified scheme of the experimental setup developed in this work for the TPD-IR measurements is reported in Figure 2. It consists of a quartz tube to host the activated carbon (A), an oven (B), an IR cell especially designed for the detection of gases (optical path of 17 cm, C) which is inserted within a FT-IR spectrophotometer (C'), a valve to isolate the system (D) and a vacuum line (E). All the parts are connected through plastic tubes via Swagelok connections. Currently, the thermal resistance of some parts of the set-up does not allow us to exceed the temperature of 700 °C.

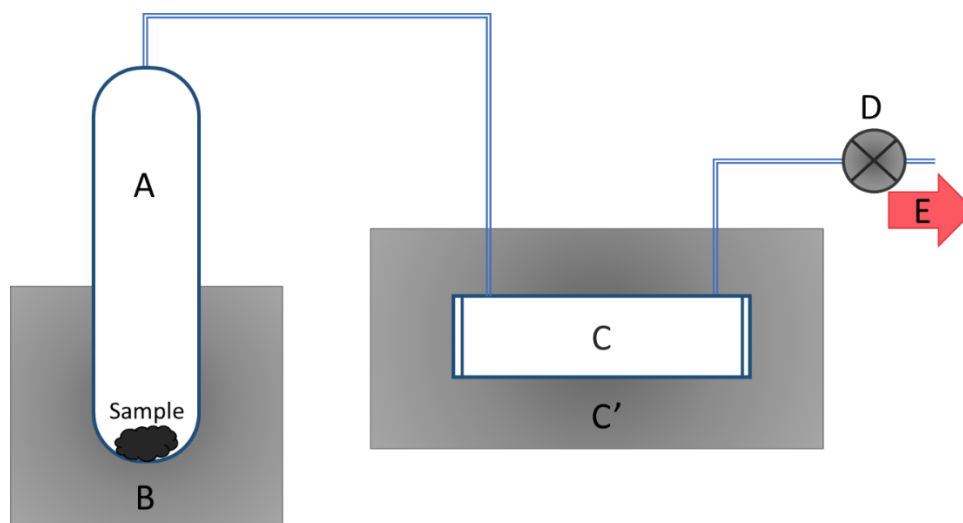


Figure 2: Schematic representation of the experimental set-up developed in this work for the TPD-IR measurements. A) quartz tube; B) oven; C) IR cell for the detection of gases; C') FT-IR spectrophotometer; D) valve; E) vacuum line.

In a standard experiment, the activated carbon is inserted in the quartz tube. The mass varied between ca. 0.2 and 0.8 g, depending on the estimated concentration of functional groups. The tube is connected to the IR cell and the IR cell to the vacuum line, and the whole system is evacuated. Subsequently, the tube is inserted in the oven, a thermocouple is placed closed to the sample, and the activated carbon is heated at 120 °C overnight in dynamic vacuum, in order to remove the weakly physisorbed water. This step allows also for the cleaning from moisture of the whole apparatus. An IR background is then collected, and the TPD run is started. Valve D is closed and the sample is heated at 5 °C/min up to 700 °C, followed by an isotherm at the same temperature for 40 minutes. During the whole TPD run the produced gases are accumulated in the system

volume, and FT-IR spectra are collected every 20 °C (i.e. 4 minutes) during the ramp, and every 5 minutes during the isotherm. The FT-IR spectra were collected with a Nicolet 6700 instrument equipped with a MCT detector, averaging 32 scans, and at a resolution of 0.5 cm⁻¹ in order to resolve the roto-vibrational profile and to identify also gases present in very low concentrations.

The possibility of secondary reactions between the decomposition products and the functional groups in the carbon pores is reported in the literature⁴⁵. These reactions may alter the ratios among the decomposition products and cause erroneous assignment. In order to individuate the possible occurrence of secondary reactions, a series of TPD runs at 15°C/min were also performed, following the indications in the literature^{26,45}. The results were completely comparable with those obtained at 5°C/min, allowing us to exclude relevant alteration of the results arising from secondary reactions.

2.3. TPD-IR data elaboration

Figure 3 summarizes the main steps of the TPD-IR data collection and elaboration. A typical outcome of a TPD-IR run is reported in Figure 3A. Each IR spectrum detects simultaneously all the gases released at a certain temperature. Since the experiment consists in the accumulation of the gases within the IR cell, a progressive increase of the intensity of the overall IR spectra is observed. It is worth noticing that with this set-up we are working in the optimal absorbance range that allowed acquiring high-resolution spectra as those in Figure 3a, most appropriate for a quantitative FT-IR analysis. In order to quantify the partial pressure of a certain gas at each IR spectrum, calibration lines were obtained by measuring the IR spectra of known pressures of the pure gas. Knowing the volume of the whole set-up, the moles of gas in correspondence with each spectrum can be calculated by employing the perfect gas law. Calibration lines for CO, CO₂, H₂O, CH₄ and NO were measured: Figure 3B shows as an example the calibration line for CO, while the others are reported in Figure S2 in the Supporting Information.

Some further corrections accounting for the effects of an uneven temperature distribution among different sections of the set-up were necessary for a correct quantitative analysis. In fact, during some test measurements performed by filling the system with a known amount of a reference gas (CO or CO₂), a progressive increase in the measured absorbance was observed as the temperature ramp proceeded. The entity of this absorbance increase approaches 10% of the initial value when reaching 700°C, and thus could not be ignored. The points measured during

these reference runs were used to find the empirical relation between the increase in absorbance and the temperature. Figure 3C reports the ratio between the absorbance measured at a given temperature T (Abs), and the absorbance measured at room temperature (Abs_0) as a function of the temperature of the ramp. The observed trend was fitted with a third degree polynomial, from which a correction factor Abs/Abs_0 was calculated for each temperature. Then, the absorbance of the measured IR spectra were divided by the Abs/Abs_0 correction factor correspondent to the temperature at which they were collected, obtaining the expected absorbance value at room temperature.

These corrected absorbances were used to calculate the corresponding gas partial pressures, and from the pressures the number of moles present in the IR cell at each temperature (cumulative moles plot, Figure 3D). In order to better visualize the production rate of the gases at each temperature, difference plots were finally obtained, as reported in Figure 3E, where each point represents the number of moles of gas released by the carbon between the collection of two consecutive FT-IR spectra. The points collected during the temperature ramp from 120 to 700°C are shown on white background, while those collected during the 40 min isotherm run at 700°C on grey background.

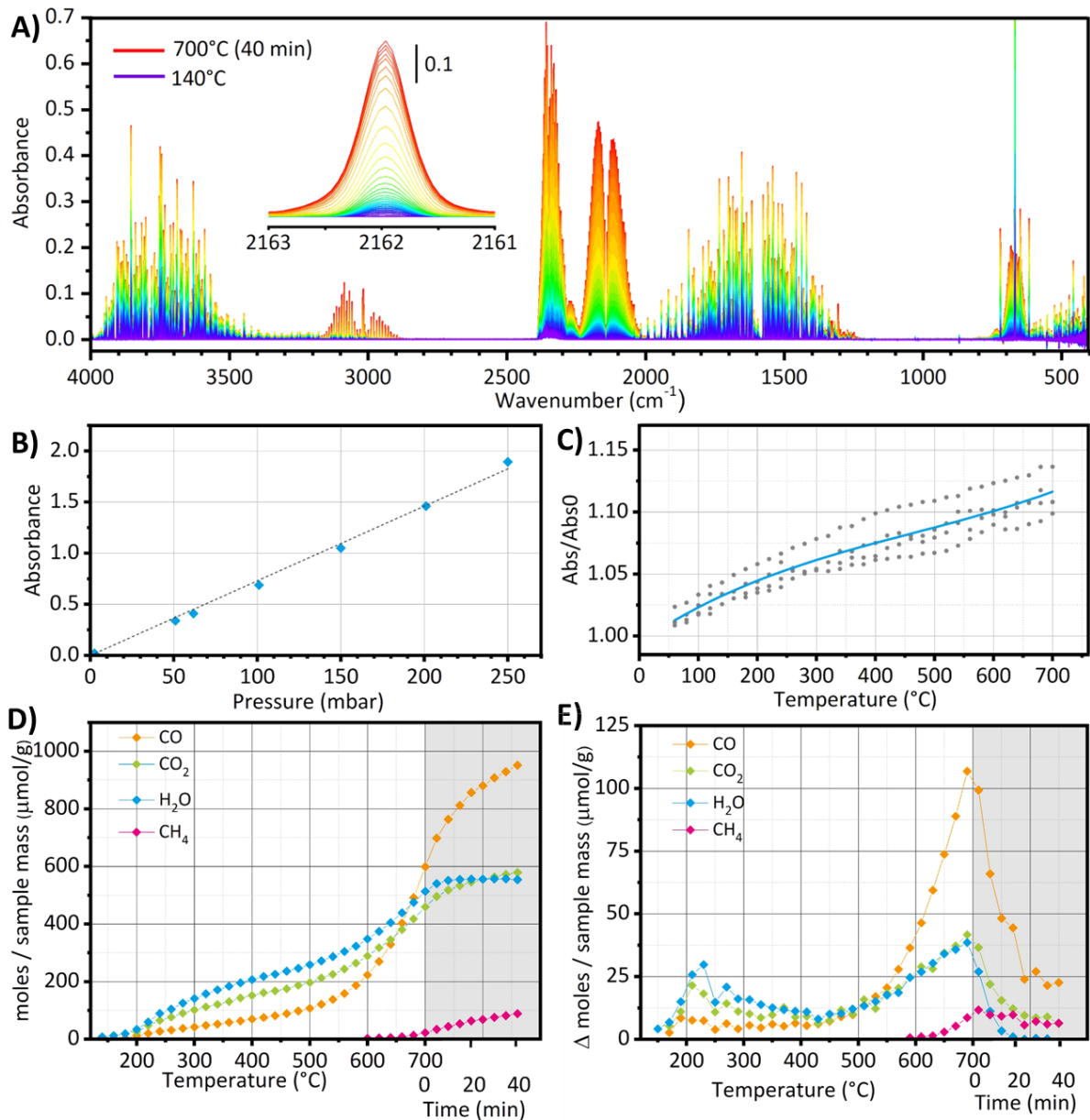


Figure 3: Main steps of the TPD-IR data collection and elaboration. Part A): Example of the raw FT-IR spectra as collected during a TPD run. Part B): calibration line for CO, which correlates the absorbance of the peak at 2162 cm^{-1} to the corresponding equilibrium pressure (in mbar). Part C): Regression curve describing the ratio between the IR absorbance observed at a given temperature (Abs) and the absorbance at room temperature (Abs0) as a function of the temperature. Part D): Cumulative moles plot for CO, as determined from the analysis of the raw IR spectra reported in part A), applying the calibration line shown in part B) after the correction described in part C). Part E): Differential moles plot for CO, where each point is the number of moles of gas released by the carbon between the collection of two consecutive FT-IR spectra. In parts D and E, the temperature ramp range is reported in white background, while the isotherm range in grey background.

3. Results and Discussion

3.3. Gases observed and quantified by FT-IR spectroscopy at the end of the TPD-IR runs

Our TPD-IR approach allowed us to obtain a large number of details about each activated carbon. First of all, a careful inspection of the FT-IR spectra collected during the temperature ramp allowed us identifying all the gaseous products, including those produced in traces, as well as the exact temperature interval in which they are released. The FT-IR spectra collected at the end of each experiment contain the fingerprints of all the gases released by a given carbon during the TPD run, and are reported in Figure 4 (for CwA, CwB, CpA and CpB) and Figure 5 (for Cchemi, CwA-ox and Cchemi-ox), where the absorbance values were also normalized to the sample mass for a better comparison among the samples. In all the cases, the main decomposition products are CO, CO₂ and H₂O, but the analysis of the IR spectra revealed also the presence of other gases. In particular: i) CH₄ is observed in traces for CwA and CpB, while it is quantifiable for Cchemi; ii) SO₂ (bands at 1361, 1150 and 518 cm⁻¹) is clearly observed in the 400-600°C interval for CwB, CpA and CpB, although its quantification is not possible. As for its origin, both woods and peats are known for containing variable amounts of S⁴⁶; iii) a quantifiable amount of NO, and other nitrogen containing molecules (NO₂ 1615 cm⁻¹, N₂O 2223 and 1285 cm⁻¹, and HCN 3310 cm⁻¹) are observed in the IR spectra collected during the TPD run on the two oxidized carbons.

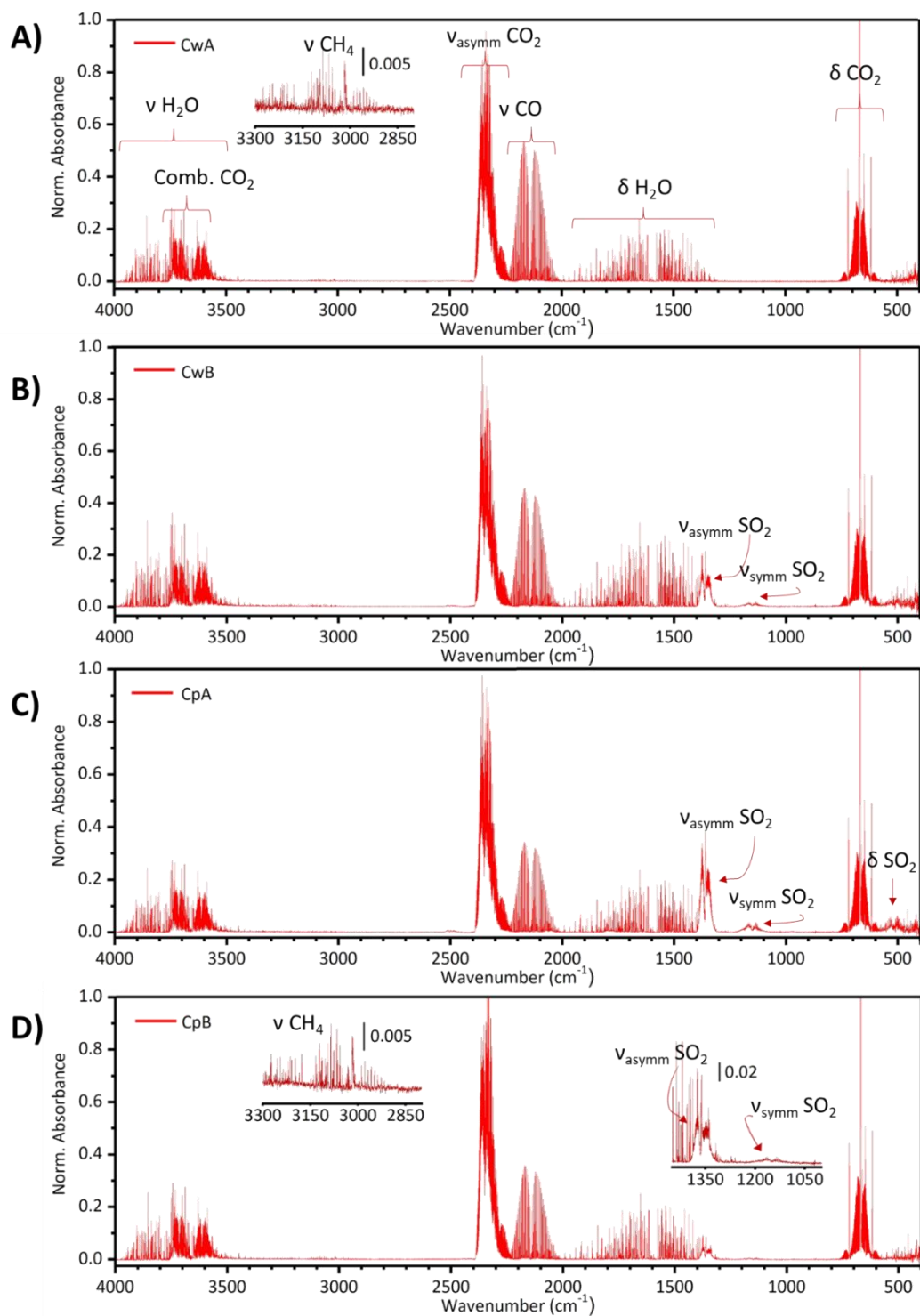


Figure 4: FT-IR spectra collected at the end of the TPD runs on CwA (part A), CwB (part B), CpA (part C) and CpB (part D). The absorbance values are normalized to the sample mass. The fingerprint of CO, CO₂ and H₂O, which are present in all the spectra, are indicated in part A. The fingerprint of the other compounds are indicated in the spectra when present, and in case of weak signals a magnification of that region of the spectra is reported as an inset.

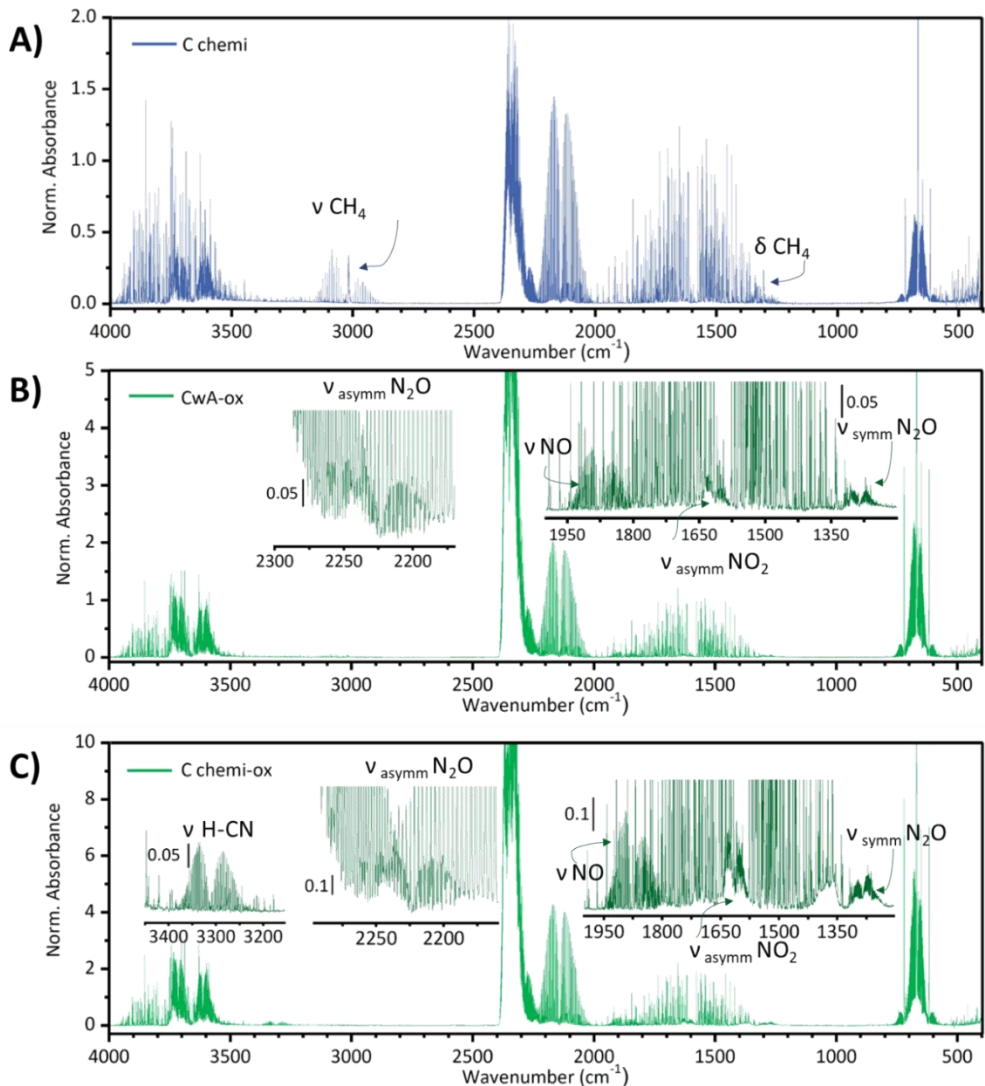


Figure 5: FT-IR spectra collected at the end of the TPD runs on Cchemi (part A), CwA-ox (part B) and Cchemi-ox (part C), normalized to the sample mass. The fingerprints of gases either than CO, CO₂ and H₂O are highlighted.

The FT-IR spectra collected at the end of the TPD runs were used for a quantitative determination of the absolute mass loss (in wt% percentage on the initial mass), and for distributing this mass loss among the quantified products. These data are reported for all the investigated carbons in Table 2. The following comments can be done.

- 1) For all the physically activated carbons the mass loss is less than 10 wt%, except for CpA (12.6 wt%), and the main source of mass loss is the removal of physisorbed water, which seems inversely correlated with the volume of the micropores (smaller V_{micro} , larger the amount of physisorbed water).

- 2) The mass loss for Cchemi is ca. 1.5 times higher than that observed in average for the physically activated carbons, but only half of it is due to physisorbed water, while the absolute amount of CO, CO₂ and H₂O released at the end of the experiment is almost 3 times higher. This is also observable by comparing the intensity of the FT-IR spectrum collected at the end of the TPD-IR run on Cchemi (Figure 5A) with those collected for the physically activated carbons (Figure 4).
- 3) The mass loss is even larger for the two oxidized samples, reaching the relevant value of 41.7 wt% for Cchemi-ox. At the same time, the contribution of physisorbed water to the mass loss gradually decreases (ca. 40-30%), while that of CO, CO₂ and H₂O increases, in agreement with the much larger amount of functional groups expected in the oxidized carbons.

Table 2: Summary of the mass decrease observed during the TPD runs, reported as a wt % on the initial mass. It reports the total mass lost, the fractions explicable with the detected amounts of CO, CO₂, H₂O, CH₄ and NO deriving from the decomposition of functional groups. The “Others” column reports the mass lost derived from not quantified species, and it corresponds mostly to the physisorbed water removed during the activation step at 120 °C overnight.

CARBON	MASS LOST (wt % ON THE INITIAL SAMPLE MASS)						
	total	CO	CO ₂	H ₂ O	CH ₄	NO	Others
CwA	6.0	1.0	1.2	0.3	-	-	3.5
CwB	9.3	0.8	1.3	0.4	-	-	6.8
CpA	12.6	0.6	1.2	0.3	-	-	10.5
CpB	8.9	0.7	1.2	0.3	-	-	6.8
Cchemi	13.6	2.7	2.5	1.7	0.1	-	6.6
CwA-ox	23.2	3.8	7.9	1.4	-	0.3	9.8
Cchemi-ox	41.7	8.2	16.8	2.5	-	1.0	13.2

3.4. Gases production rates as a function of temperature: qualitative description

3.2.1 Physically activated carbons

The difference TPD plots (reporting the number of moles of gas evolved between the collection of two consecutive FT-IR spectra) for the four physically activated carbons are shown in Figure 6.

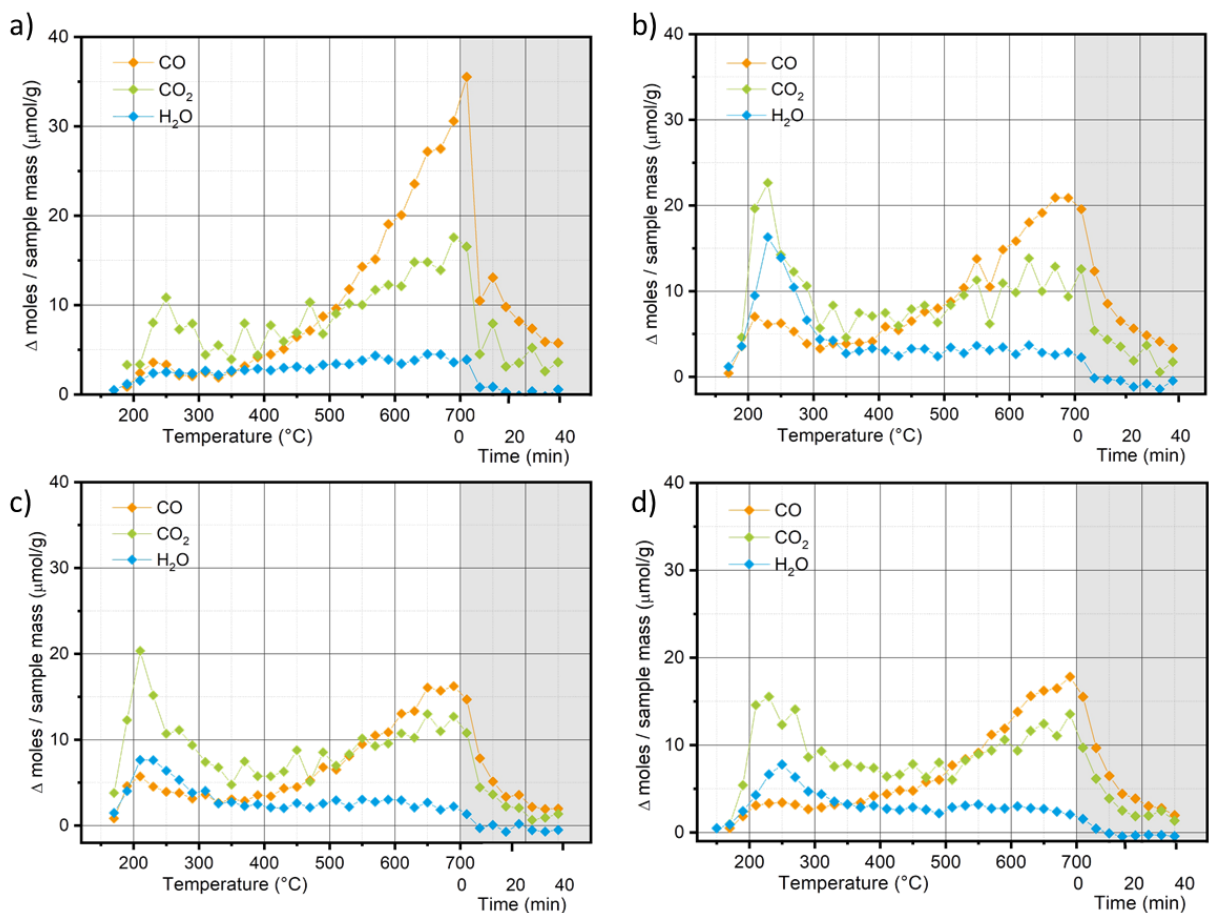


Figure 6: Differential TPD plots of CO, CO₂ and H₂O for the four physically activated carbons: CwA (a), CwB (b), CpA (c) and CpB (d). Each point reports the number of moles of gas evolved by the carbon between the collection of two consecutive IR spectra (i.e. in a temperature interval of 20 °C for the ramp and every 5 min for the isotherm). The data collected during the temperature ramp segment are reported on a white background, while those collected during the isotherm segment are shown on a grey background.

In the low temperature range ($T < 400^{\circ}\text{C}$), the main decomposition product is CO₂, which gives a peak around 250 °C. The CO₂ produced below 400 °C is generally attributed to the decomposition of carboxylic acid groups^{26, 27, 31-33}, and the relative narrowness of this peak suggests that the involved functional groups are energetically very similar. At a closer look, we can notice that all the samples also present a CO and a H₂O peak in correspondence with the CO₂ one, although in lower amounts. The formation of CO at low temperature and in concomitance with the signals of CO₂ was already observed in the past^{6, 33, 47}, while the evolution of H₂O in this temperature range was often attributed to the desorption of strongly adsorbed water (for example,

hydrogen bonded with the O-containing functional groups) or to the condensation of adjacent functional groups^{6, 32, 34}. Nevertheless, our observation of a contemporary evolution of CO₂, CO and also H₂O is actually very similar to what observed by Li *et al*³⁵ and by Vivo-Vilches *et al*³⁶. In the former article an equal amount of CO and H₂O was observed in this temperature interval and assigned to an alternative decomposition route for carboxylic acids. The latter study instead explained the observation considering the condensation of two vicinal carboxylic groups and their immediate decomposition to CO₂ + CO + H₂O. Our results do not fully support either of these reaction stoichiometries, and might be interpreted as a combination of multiple processes occurring simultaneously.

After reaching a minimum around 400 °C, the release of both CO and CO₂ increases steadily above 400 °C for all the carbons. However, for the Cw samples the amount of released CO is clearly higher than CO₂, particularly for CwA where the evolution rate for CO is approximatively the double than CO₂ at 700°C. While for the Cp samples, albeit CO is still the main product, its amount is comparable to that of CO₂. In this temperature range the decomposition of anhydrides, lactones and, later on, also phenols and ethers is expected^{26, 27, 31-33}, and the described differences in the TPD plots for the four samples clearly point to a different distribution of these functional groups, as described in more details in section 3.3. The signal of H₂O, instead, remains stable and low all over the high temperature range for all the four samples. We attribute it to the condensation of vicinal functional groups, likely phenols, and the generally low values suggest a low probability of adjacent functional groups.

The experimental points associated with the isotherm at 700 °C (grey background in Figure 6) provide further details about the kinetics of the decomposition reactions. As expected, the formation rate of all the products progressively decreases. More interestingly, the formation rate for CO and CO₂ does not drop suddenly to zero, but instead it needs more than 20 min before reaching stable values, suggesting that the thermal decomposition of the functional groups is kinetically slow and requires additional time before reaching the thermodynamic equilibrium. In contrast, the signal of H₂O drops to zero almost immediately after the beginning of the isotherm segment, suggesting that the condensation of two adjacent phenolic groups is a kinetically faster process.

3.2.2 Chemically activated carbon

The differential TPD curves for Cchemi are reported in Figure 7. The general trend is similar to those observed for the physically activated carbons (in particular for CwA), except for the higher intensity. Also in this case the largest release of decomposition products is observed at high temperature, but their amount is sensibly higher than in the previous cases indicating a greater concentration of functional groups. This, in turn, could also explain the relatively greater amount of H₂O released, as it corresponds to greater chances of vicinal functional groups, and consequently to more likely condensation processes.

As anticipated above, CH₄ was observed and quantified among the decomposition products of Cchemi. Its signal appears at about 600 °C and continues to consistently increase all over the final part of the experiment. Cchemi was activated at lower temperature than physically activated carbons, and thus the formation of CH₄ in the TPD indicates that we have surpassed the primitive activation temperature and triggered a further carbonization of the sample²⁹. This last process also appears to be kinetically slow, as the production rate of CH₄ does not slow down sensibly during the isotherm segment of the experiment.

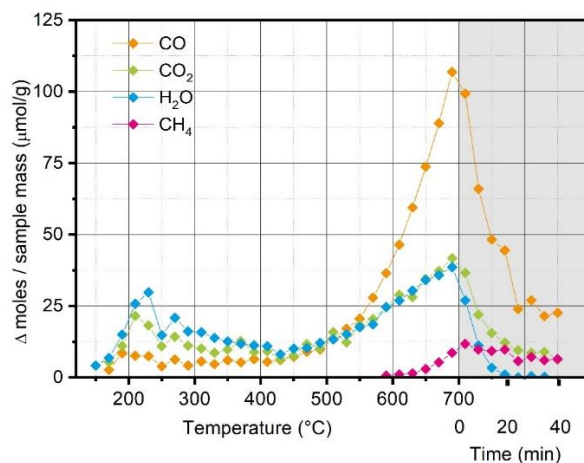


Figure 7: Differential TPD plots of CO, CO₂, H₂O and CH₄ for Cchemi. Each point reports the number of moles of gas evolved by the carbon between the collection of two consecutive IR spectra (i.e. in a temperature interval of 20 °C for the ramp and every 5 min for the isotherm). The data collected during the temperature ramp segment are reported on a white background, while those collected during the isotherm segment are shown on a grey background.

3.2.3 Oxidized activated carbons

The differential TPD curves for CwA-ox and Cchemi-ox are reported in Figure 8. A much larger amount of gases is released during the TPD runs with respect to the previous cases. This is expected, since it is known that oxidation by HNO_3 introduces a large amount of O-containing functional groups in carbons^{6, 7, 27, 32}.

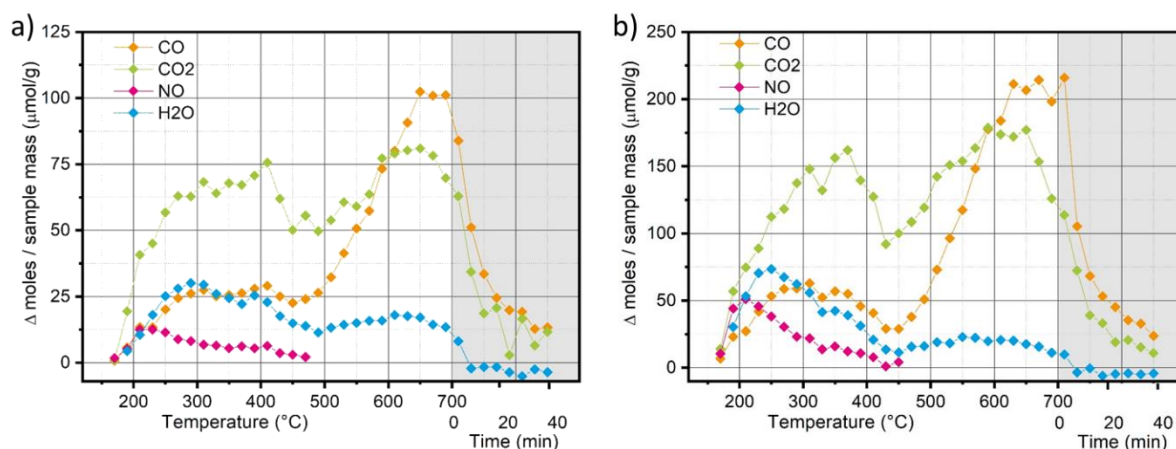


Figure 8: Differential TPD plots of CO, CO₂, H₂O and NO for CwA-Ox (a) and Cchemi-Ox (b). Each point reports the number of moles of gas evolved by the carbon between the collection of two consecutive IR spectra (i.e. in a temperature interval of 20 °C for the ramp and every 5 min for the isotherm). The data collected during the temperature ramp segment are reported on a white background, while those collected during the isotherm segment are shown on a grey background.

As commonly observed for carbons treated by wet oxidation routes^{6, 7, 27}, very large amounts of CO₂, CO and H₂O are released in the low temperature interval. As discussed above, the formation of CO₂ below 400 °C is attributed to the decomposition of carboxylic acid groups. It is worth noticing that the CO₂ peak is much broader than in the previous cases, suggesting a wider distribution of carboxylic acid groups in comparison with the non-oxidized carbons. Also for CwA-ox and Cchemi-ox, CO and H₂O are released simultaneously to CO₂. Here, the moles of CO and H₂O produced over this interval are very similar, supporting the alternative decomposition mechanism of carboxylic acid groups proposed by Li *et al*³⁵, or the decomposition of two vicinal COOH groups proposed by Vivo-Vilches *et al*³⁶.

In addition to CO, CO₂ and H₂O, nitrogen oxides are released at low temperature. In particular, NO was identified and quantified for both samples, but the IR spectra identified also

NO₂ (1615 cm⁻¹), N₂O (2223 and 1285 cm⁻¹) and HCN (3310 cm⁻¹). The presence of these gases clearly indicates the introduction of N-containing functional groups as a consequence of the oxidation treatment in HNO₃.

For both carbons, the release rates of all products reach a minimum at about 450°C, and then quickly rise again as the decomposition of the more thermostable functional groups starts. With respect to the parent carbons (CwA and Cchemi), a significant increase of the amounts of released CO and CO₂ is observed. In contrast, CH₄ is not observed at all in any of the oxidized samples. CH₄ is expected to be formed by carbonization processes of residual aliphatic fractions within the carbon sample. Its absence confirm the fact that the aliphatic fraction is the most vulnerable to the action of oxidative agents, such as HNO₃⁴⁸.

3.5. Quantitative evaluation of the functional groups concentration

The data reported in the differential TPD plots discussed above were used to quantify the amount of gases (in μmol/g) released by a given carbon during three temperature intervals characteristic for the decomposition of different classes of functional groups, as reported in Table 3.

Table 3: Summary of the amounts of CO, CO₂, H₂O, NO and CH₄ released by each carbon during the TPD run. The values are divided into the T < 400°C, 400°C < T < 560°C and T > 560°C intervals.

AMOUNT OF DECOMPOSITION PRODUCTS (μmol/g)												
	T < 400°C				400°C < T < 560°C				T > 560°C			
	CO	CO ₂	H ₂ O	NO	CO	CO ₂	H ₂ O	NO	CO	CO ₂	H ₂ O	CH ₄
CwA	29	68	28	-	68	67	26	-	259	144	35	-
CwB	52	116	80	-	66	65	24	-	185	107	19	-
CpA	43	117	53	-	48	60	20	-	136	103	16	-
CpB	35	111	53	-	51	58	22	-	151	108	18	-
Cchemi	70	152	207	-	89	92	98	-	793	335	249	89
CwA-ox	238	630	246	92	252	467	123	15	864	703	100	-
Cchemi-ox	546	1345	581	321	474	994	138	13	1920	1469	110	-

These data were used to obtain a reasonable estimation of the concentration of different functional groups in the activated carbons, on the basis of the available literature^{26, 27, 31-33, 35, 36} and of the following assumptions. Carboxylic acids decompose at temperatures lower than 400°C, mainly releasing CO₂, but also alternative decomposition routes involving the contemporary formation of CO and H₂O³⁵ or CO, CO₂ and H₂O³⁶ were proposed and appeared compatible with

the TPD plots discussed in section 3.2. Keeping this in mind, we evaluated the concentration of carboxylic acids by summing the $\mu\text{mol/g}$ of CO_2 and CO released in the $T < 400^\circ\text{C}$ interval. An amount of H_2O equal to the released CO is expected to be associated with the decomposition of carboxylic groups as well, while the remaining part is attributed to condensation reactions among vicinal groups or to strongly adsorbed H_2O . Finally, NO is fully attributed to the decomposition of N-containing functional groups such as, for example, nitro groups.

Anhydrides and lactones are the only species expected to decompose in the $400 - 560^\circ\text{C}$ interval. The former decomposes to $\text{CO}_2 + \text{CO}$, while the latter to CO_2 only. Thus, the $\mu\text{mol/g}$ of CO released in this interval can only be attributed to the decomposition of anhydrides, while the concentration of lactones is estimated by subtracting the concentration of anhydrides to the total amount of CO_2 evolved in this interval. All the water observed in this range is attributed to the condensation of vicinal functional groups, most likely phenols.

In the high temperature range ($560 - 700^\circ\text{C}$) the situation is more complex. In fact, the decomposition of anhydrides and lactones continues for the most of the interval, but in addition also the decomposition of phenols and ethers to CO becomes possible. The exact solution of this calculation is not possible, and so in order to proceed we need to introduce some reasonable approximations. First of all, we decided to evaluate together the concentration of phenols and ethers, as it appeared impossible to separate the two variables. Then, we analysed the concentrations of anhydrides and lactones evaluated at $T < 560^\circ\text{C}$: for the physically activated carbons (CwA, CwB, CpA and CpB) and for Cchemi, the concentration of lactones is almost negligible in comparison to anhydrides, while for the oxidised samples (CwA-ox and Cchemi-ox) the concentrations of anhydrides and lactones are very similar. We then assumed that the observed trends between the concentrations of anhydrides and lactones are valid also at $T > 560^\circ\text{C}$. This led to the following approximation in the calculation: the concentration of lactones released in the $560-700^\circ\text{C}$ range is set to zero for CwA, CwB, CpA, CpB and Cchemi, and equal to the concentration of anhydrides for CwA-ox and Cchemi-ox. Within this approximation, it is possible to evaluate the concentration of anhydrides as equal to the $\mu\text{mol/g}$ of CO_2 released in this temperature interval in the first case, or to set the concentration of both anhydrides and lactones as equal to the half of the CO_2 released in the second case. To obtain the total concentration of anhydrides and lactones, it is then necessary to sum these values with the ones obtained in the previous temperature range. The concentration of phenols and ethers, instead, corresponds to the

difference between the $\mu\text{mol/g}$ of CO and the concentration of the anhydrides. Finally, the water released in this interval is also attributed to the condensation of adjacent functional groups, while the CH_4 released by Cchemi is associated with the high carbonization of the non-graphitic portion of the sample.

Since the experiment is stopped at $700\text{ }^\circ\text{C}$, we are not able to provide information about the most thermo-resistant groups, as ketones and quinones.

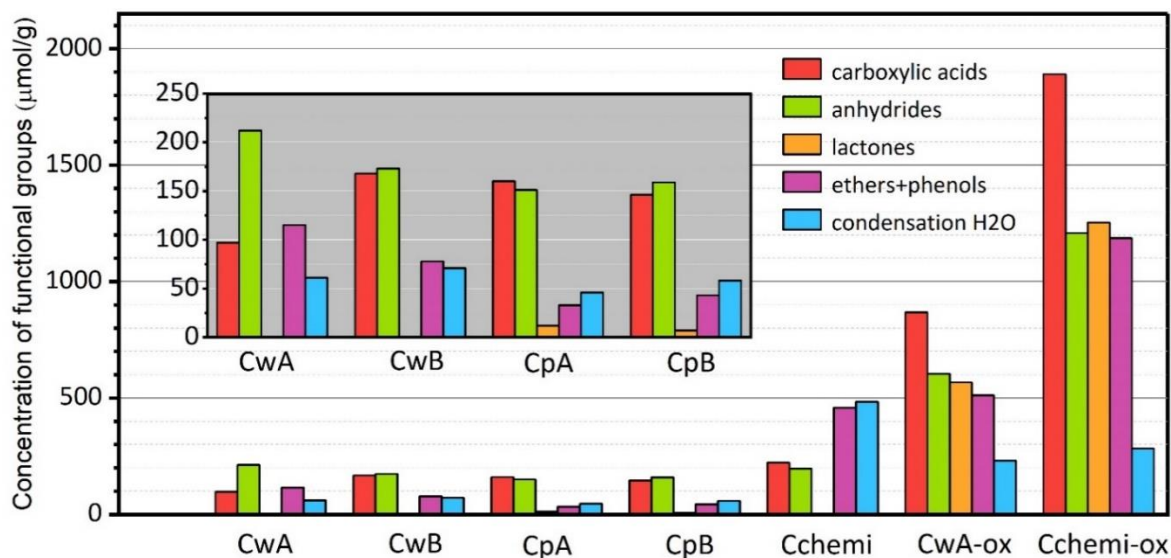


Figure 9: Concentration of functional groups in the seven activated carbons, as evaluated from the measured amounts of released gases in the TPD-IR experiments. A detail over the values calculated for the physically activated carbons is shown in the inset.

The concentration values obtained by this evaluation are reported in Figure 9. For the physically activated carbons (inset in Figure 9), albeit the low concentration of functional groups, we are able to point out analogies and differences among the four samples. The two carbons of wood origin (CwA and CwB) display a different distribution of the functional groups: anhydrides are the most abundant functional groups in CwA, followed by phenols plus ethers and then carboxylic acids, while for CwB anhydrides and carboxylic acids exhibit similar concentrations, and phenols + ethers are less abundant. In both cases, the concentration of lactones is close to zero. The two carbons of peat origin (CpA and CpB) are more similar each others. The concentration of carboxylic acids and anhydrides is similar to CwB, while they contain less phenols and ethers, and a small amount of lactones. Finally, the amount of water attributed to condensation reactions

among vicinal functional groups is very low in all the four carbons, in particular for the Cp samples, and thus the amount of anhydrides, lactones or ethers formed as a consequence of a condensation reaction during the TPD run is expected to be low.

For Cchemi the concentration of functional groups is roughly the double of that estimated for the physically activated samples. According to previous measurements, Cchemi is characterized, on average, by smaller graphitic domains than CwA¹⁸, which means a larger availability of terminations where functional groups can be formed. This hypothesis is strengthened by the observation that the ratio between the total concentrations of functional groups for the corresponding oxidised samples (CwA-ox and Cchemi-ox) remains similar (*vide infra*). On top of this, also the relative distribution of the functional groups in Cchemi is different with respect to the physically activated carbons: phenols and ethers are the most abundant, followed by carboxylic acids and anhydrides at similar values. Also in this case lactones are almost absent. Cchemi also provided the highest amount of released water, suggesting that the condensation of vicinal functional groups is the most likely for this sample.

For the samples oxidised in HNO₃ (CwA-ox and Cchemi-ox), the overall concentration of functional groups increases with respect to the parent carbons. Cchemi-ox has roughly the double of functional groups than CwA-ox (similarly to their parent carbons), but their relative amounts are similar. In both cases, the highest concentration is observed for carboxylic acid groups, closely followed by anhydrides, lactones and phenols + ethers at similar values. The amount of released water is small in comparison with that of any of the observed functional groups, suggesting that the amount of functional groups formed by the condensation of vicinal groups during the TPD run can be considered almost negligible for these samples.

4. Conclusions

Activated carbons play a key role in many catalytic applications. The possibility of tuning their surface chemistry by changing the carbonaceous precursor and/or the activation treatment is the origin of much industrial and fundamental research carried out over the last decade. However, due to their intrinsic structural heterogeneity, the characterization of the nature and amount of surface groups in activated carbons is not straightforward. In this work, we presented the potentials of a newly developed TPD-IR setup and related experimental approach for identifying and quantifying the functional groups in activated carbons. Our setup allowed for the measurement of high-

resolution IR spectra, and demonstrated to be fully suitable for the identification of the IR-active gases released at high concentration as well as of those produced at traces levels, and for the precise quantification of the main products.

The quantified amounts of gaseous products were used for estimating the concentration of the main functional groups in seven carbons characterized by different precursors (wood or peat), activation procedure (physical activation by steam or chemical activation with H_3PO_4) and post-activation treatments (oxidation in HNO_3). For the four steam activated carbons (CwA, CwB, CpA and CpB), the estimated concentration of functional groups is generally low, but significant differences in their relative amount are observed. For most of them, anhydrides and carboxylic acids are present in similar amount, except for CwA where anhydrides are more abundant. Phenols + ethers are more abundant in carbons of peat origin, while lactones are almost negligible in all of them. Apart from the typical TPD products (CO , CO_2 and H_2O), traces of CH_4 are observed in some cases (CwA and CpB), and SO_2 is released from all of them except CwA. The chemically activated carbon exhibits a higher concentration of functional groups than the physically activated ones. This can be due in part to the smaller size of the graphitic domains, but the higher degree of condensation among vicinal functional groups suggests a higher occupancy of the platelets borders by functional groups. The types of functional groups are also significantly different with respect to the physically activated carbons, since in this case the most abundant groups are phenols + ethers. A quantifiable amount of CH_4 is also released above $600\text{ }^\circ\text{C}$. The observation of this signal, together with its absence in the corresponding oxidized sample, suggest that the chemically activated carbon contains a larger fraction of aliphatic groups than the steam activated carbons. Finally, the two carbons oxidized in HNO_3 contain a much larger amount of O-containing functional groups of all types, but in particular carboxylic acids and lactones. The identification of several N-containing gaseous products (NO , NO_2 , N_2O and HCN) and the quantification of NO demonstrate that the oxidation treatment in HNO_3 introduces small amounts of N-containing functional groups.

Overall, the developed TPD-IR approach appears as a promising route to identify and quantify the surface functional groups on different carbons and, coupled with other spectroscopic techniques^{18,19}, may help in shedding light onto the microscopic origin of the catalytic properties of different carbons.

References

1. V. Fierro, V. Torné-Fernández, D. Montané and A. Celzard, *Microporous and Mesoporous Materials*, 2008, **111**, 276-284.
2. S. Sircar, T. C. Golden and M. B. Rao, *Carbon*, 1996, **34**, 1-12.
3. E. Auer, A. Freund, J. Pietsch and T. Tacke, *Applied Catalysis A: General*, 1998, **173**, 259-271.
4. F. Rodríguez-Reinoso, *Handbook of Porous Solids*, 2002, DOI: doi:10.1002/9783527618286.ch24a
10.1002/9783527618286.ch24a, 1766-1827.
5. P. González-García, *Renewable and Sustainable Energy Reviews*, 2018, **82**, 1393-1414.
6. C. Moreno-Castilla, F. Carrasco-Marín and A. Mueden, *Carbon*, 1997, **35**, 1619-1626.
7. A. M. T. Silva, B. F. Machado, J. L. Figueiredo and J. L. Faria, *Carbon*, 2009, **47**, 1670-1679.
8. A. Bhatnagar, W. Hogland, M. Marques and M. Sillanpää, *Chemical Engineering Journal*, 2013, **219**, 499-511.
9. B. S. Girgis, S. S. Yunis and A. M. Soliman, *Materials Letters*, 2002, **57**, 164-172.
10. G. S. Miguel, G. D. Fowler, M. Dall'Orso and C. J. Sollars, *Journal of Chemical Technology & Biotechnology*, 2002, **77**, 1-8.
11. S. Biniak, G. Szymański, J. Siedlewski and A. Świątkoski, *Carbon*, 1997, **35**, 1799-1810.
12. J. Jaramillo, P. M. Álvarez and V. Gómez-Serrano, *Fuel Processing Technology*, 2010, **91**, 1768-1775.
13. J. L. Figueiredo and M. F. R. Pereira, *Catalysis Today*, 2010, **150**, 2-7.
14. A. Lazzarini, R. Pellegrini, A. Piovano, S. Rudić, C. Castan-Guerrero, P. Torelli, M. R. Chierotti, R. Gobetto, C. Lamberti and E. Groppo, *Catalysis Science & Technology*, 2017, **7**, 4162-4172.
15. H. P. Boehm, *Carbon*, 1994, **32**, 759-769.
16. M. Smith, L. Scudiero, J. Espinal, J.-S. McEwen and M. Garcia-Perez, *Carbon*, 2016, **110**, 155-171.
17. A. Dandekar, R. T. K. Baker and M. A. Vannice, *Carbon*, 1998, **36**, 1821-1831.
18. A. Lazzarini, A. Piovano, R. Pellegrini, G. Leofanti, G. Agostini, S. Rudić, M. R. Chierotti, R. Gobetto, A. Battiato, G. Spoto, A. Zecchina, C. Lamberti and E. Groppo, *Catalysis Science & Technology*, 2016, **6**, 4910-4922.
19. E. Vottero, M. Carosso, M. Jiménez-Ruiz, R. Pellegrini, E. Groppo and A. Piovano, *Carbon*, 2020, DOI: <https://doi.org/10.1016/j.carbon.2020.07.033>.
20. M. Carosso, A. Lazzarini, A. Piovano, R. Pellegrini, S. Morandi, M. Manzoli, J. G. Vitillo, M. J. Ruiz, C. Lamberti and E. Groppo, *Faraday Discussions*, 2018, **208**, 227-242.
21. A. C. Ferrari and J. Robertson, *Physical Review B*, 2000, **61**, 14095-14107.
22. F. Lónyi and J. Valyon, *Microporous and Mesoporous Materials*, 2001, **47**, 293-301.
23. S. Boujana, D. Demri, J. Cressely, A. Kiennemann and J. P. Hindermann, *Catalysis Letters*, 1990, **7**, 359-366.
24. J. P. Joly, F. Gaillard, E. Peillex and M. Romand, *Vacuum*, 2000, **59**, 854-867.
25. T. K. Phung and G. Garbarino, *Journal of Industrial and Engineering Chemistry*, 2017, **47**, 288-296.
26. G. de la Puente, J. J. Pis, J. A. Menéndez and P. Grange, *Journal of Analytical and Applied Pyrolysis*, 1997, **43**, 125-138.
27. J. L. Figueiredo, M. F. R. Pereira, M. M. A. Freitas and J. J. M. Órfão, *Carbon*, 1999, **37**, 1379-1389.
28. V. E. Diyuk, R. T. Mariychuk and V. V. Lisnyak, *Journal of Thermal Analysis and Calorimetry*, 2016, **124**, 1119-1130.
29. G. Hotová, V. Slovák, O. S. G. P. Soares, J. L. Figueiredo and M. F. R. Pereira, *Carbon*, 2018, **134**, 255-263.
30. T. Ishii and J. I. Ozaki, *Carbon*, 2020, **161**, 343-349.
31. C. Moreno-Castilla, F. Carrasco-Marín, F. J. Maldonado-Hódar and J. Rivera-Utrilla, *Carbon*, 1998, **36**, 145-151.

32. Y. Otake and R. G. Jenkins, *Carbon*, 1993, **31**, 109-121.
33. J. L. Figueiredo, M. F. R. Pereira, M. M. A. Freitas and J. J. M. Órfão, *Industrial & Engineering Chemistry Research*, 2007, **46**, 4110-4115.
34. S. Haydar, C. Moreno-Castilla, M. A. Ferro-García, F. Carrasco-Marín, J. Rivera-Utrilla, A. Perrard and J. P. Joly, *Carbon*, 2000, **38**, 1297-1308.
35. N. Li, X. Ma, Q. Zha, K. Kim, Y. Chen and C. Song, *Carbon*, 2011, **49**, 5002-5013.
36. J. F. Vivo-Vilches, E. Bailón-García, A. F. Pérez-Cadenas, F. Carrasco-Marín and F. J. Maldonado-Hódar, *Carbon*, 2014, **68**, 520-530.
37. T. Ishii, S. Kashihara, Y. Hoshikawa, J.-i. Ozaki, N. Kannari, K. Takai, T. Enoki and T. Kyotani, *Carbon*, 2014, **80**, 135-145.
38. U. Zielke, K. J. Hüttinger and W. P. Hoffman, *Carbon*, 1996, **34**, 983-998.
39. L. H. Zhang and J. M. Calo, *Colloids and Surfaces A: Physicochemical and Engineering Aspects*, 2001, **187-188**, 207-218.
40. B. Marchon, W. T. Tysoe, J. Carrazza, H. Heinemann and G. A. Somorjai, *The Journal of Physical Chemistry*, 1988, **92**, 5744-5749.
41. S. Haydar and J. P. Joly, *Journal of Thermal Analysis and Calorimetry*, 1998, **52**, 345-353.
42. I. Jung, D. A. Field, N. J. Clark, Y. Zhu, D. Yang, R. D. Piner, S. Stankovich, D. A. Dikin, H. Geisler, C. A. Ventrice and R. S. Ruoff, *The Journal of Physical Chemistry C*, 2009, **113**, 18480-18486.
43. G. Hotová and V. Slovák, *Thermochimica Acta*, 2016, **632**, 23-28.
44. <https://www.chimet.com> Accessed in date 14/08/20).
45. P. J. Hall and J. M. Calo, *Energy & Fuels*, 1989, **3**, 370-376.
46. A. Nordin, *Biomass and Bioenergy*, 1994, **6**, 339-347.
47. S. Kohl, A. Drochner and H. Vogel, *Catalysis Today*, 2010, **150**, 67-70.
48. F. Haghseresht, G. Q. Lu and A. K. Whittaker, *Carbon*, 1999, **37**, 1491-1497.

Dynamics of Reactive Species and Reactant-Induced Reconstruction of Pt Clusters in Pt/Al₂O₃ Catalysts

Michele Carosso,[†] Eleonora Vottero,^{†,‡} Andrea Lazzarini,^{†,§} Sara Morandi,[†] Maela Manzoli,^{||} Kirill A. Lomachenko,[⊥] Monica Jimenez Ruiz,[‡] Riccardo Pellegrini,[#] Carlo Lamberti,[¶] Andrea Piovano,[‡] and Elena Groppo^{*,†}

[†]Department of Chemistry, INSTM and NIS Centre, University of Torino, via Quareello 15, I-10135 Torino, Italy

[‡]Institut Laue-Langevin (ILL), 71 avenue des Martyrs, 38000 Grenoble, France

[§]Centre for Materials Science and Nanotechnology, Department of Chemistry, University of Oslo, Sem Saelands vei 26, N-0315 Oslo, Norway

^{||}Department of Drug Science and Technology, INSTM and NIS Centre, University of Torino, Via Pietro Giuria 9, I-10125 Torino, Italy

[⊥]European Synchrotron Radiation Facility, 71 Avenue des Martyrs, CS 40220, 38043 Grenoble Cedex 9, France

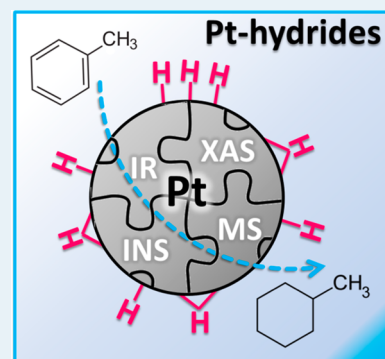
[#]Chimet SpA - Catalyst Division, Via di Pesciola 74, I-52041, Vicinaggio Arezzo, Italy

[¶]Department of Physics and CrisDi Interdepartmental Centre, University of Torino, via Pietro Giuria 1, I-10125 Torino, Italy

^{*}The Smart Materials Research Institute, Southern Federal University, Sladkova Street 178/24, Rostov-on-Don 344090, Russia

ABSTRACT: We report a complete experimental characterization of the surface Pt-hydride species on an industrial 5 wt % Pt/Al₂O₃ catalyst (average particle size of 1.4 ± 0.4 nm) under different hydrogenation/dehydrogenation conditions. By combining inelastic neutron scattering, FT-IR spectroscopy, and synchronous DRIFT/XAS/MS, we identified *n*-fold coordinated Pt-hydrides and four different types of linear Pt-hydrides characterized by different adsorption strength, whose relative proportion depends on the experimental conditions. In particular, we observed that the *n*-fold coordinated hydrides convert into linear ones upon decreasing hydrogen coverage, and vice versa, and we traced this phenomenon to a morphological and electronic reconstruction of the Pt nanoparticles. Although only a fraction of the surface Pt-hydrides are directly involved in the hydrogenation of toluene, all the others play an indirect but fundamental role, maintaining the Pt nanoparticles electronically and morphologically stable during the reaction and hence avoiding the occurrence of deactivation processes. Our results, which are in good agreement with the theoretical predictions reported in the literature, offer a comprehensive picture of the dynamics of Pt nanoparticles in hydrogenation conditions. This always involves a change in the relative proportion of the Pt-hydride species, and only in some cases an electronic and morphological reconstruction of the Pt particles.

KEYWORDS: Pt hydrides, reconstruction, DRIFT spectroscopy, XAS, INS



1. INTRODUCTION

Pt-based heterogeneous catalysts are systems of pivotal industrial relevance, since they are employed in a wide range of industrial processes involving hydrogen, ensuring high selectivity and conversion at relatively mild operating conditions.^{1–4} The key step of the process is the homolytic dissociation of molecular hydrogen at the Pt surface, with the consequent formation of different Pt-hydride species. These atomic hydrogen species are directly involved in the hydrogenation (or hydrogenolysis) of a wide range of organic substrates. Hence, establishing a realistic adsorption model for hydrogen on nanosized Pt particles as a function of the reaction conditions is of crucial importance to design higher-performing catalysts and/or to correctly choose the operating conditions. Although the first experimental evidence of

hydrogen splitting over Pt dates back to the early 1800s,^{5,6} and despite the intense research activity by means of both experimental and theoretical approaches, the nature of the Pt-hydrides (i.e., involved Pt adsorption sites) and their relative concentration under different operating conditions are still a matter of discussion.^{7,8}

Part of the difficulty is associated with the intrinsic complexity of nanosized noble metal clusters.^{9–17} In the last decades a large amount of experimental evidence demonstrated that the Pt clusters undergo electronic and morphological reconstruction as a function of the support, of the adsorbate, and of the reaction temperature.^{15,18–26} Pt L₃-edge XAS

Received: May 20, 2019

Published: June 18, 2019

spectroscopy (in both XANES and EXAFS regions) has been one of the main techniques employed to investigate the structural and electronic changes experienced by nanometric Pt particles supported on different materials in the presence of hydrogen. As far as the XANES region is concerned, it has been observed that H₂ adsorption on small Pt particles causes dramatic changes in the spectra: the “white line” intensity decreases and the spectra broaden to higher energy as hydrogen is added.^{15,20–24,27–35} There have been many efforts to interpret these effects, which are due to both electronic and geometric phenomena.^{22,27–42} Most of the analyses are based on subtracting the Pt L₃-edge spectrum of the catalyst in the absence of adsorbed hydrogen ($\mu(\text{Pt})$) from those in the presence of adsorbed hydrogen ($\mu(\text{Pt-H})$), also known as the ΔXANES approach.⁴³ The resulting difference spectra $\Delta\mu = \mu(\text{Pt-H}) - \mu(\text{Pt})$ contain several features that have been ascribed to specific geometry of the adsorption site on the basis of DFT calculations, although bridged (twofold coordinated) and hollow (threefold coordinated) sites cannot be distinguished.^{18,32,35} On the basis of the ΔXANES approach, Koningsberger’s group proposed a three-site model for hydrogen adsorption on small Pt particles (coordination number $N_{\text{Pt-Pt}} < 6.5$).³⁵ The model suggests the presence of three types of hydrides, whose relative concentrations depend on the hydrogen coverage. At very low coverages, hydrogen strongly adsorbs forming linear hydrides, called “atop”. At intermediate coverages, due to lateral interactions, the strong “atop” hydrides migrate to *n*-fold coordinated sites (bridged or hollow). If the coverage is increased further, the previously freed “atop” sites are refilled, but this time the interaction is much weaker, giving rise to linear hydrides labeled as “on-top”.

As far as the effect of hydrogen adsorption on the Pt L₃-edge EXAFS region is concerned, an elongation of the Pt–Pt first shell distance and a small, but noticeable, increase in the Pt–Pt coordination number upon increasing the amount of hydrogen have been highlighted in many works.^{11,20,22,29,30} The former observation was explained by taking into account the electron withdrawing properties of hydrogen, which induces a weakening of the Pt–Pt bond. The increase in the Pt–Pt coordination number was explained in terms of a change of the cluster morphology toward a more spherical shape.

The three-site model was largely improved some years later, by the group of Raybaud and Sautet.¹⁹ The authors simulated, by means of DFT and molecular dynamic calculations, the morphology of a Pt₁₃ cluster on $\gamma\text{-Al}_2\text{O}_3$ at increasing hydrogen coverages. In the absence of hydrogen, the Pt cluster is strongly anchored to the $\gamma\text{-Al}_2\text{O}_3$ support with a biplanar morphology. Increasing the hydrogen coverage, linear and *n*-fold coordinated Pt-hydrides are formed, that gradually solvate the Pt₁₃ cluster. At the saturation coverage (Pt₁₃H₃₄), the cluster assumes a cuboctahedral morphology, largely detached from the support due to the presence of atomic hydrogen at the particle–support interface. Linear and bridge sites are the most favored adsorption modes, and their relative amount is a function of the hydrogen coverage. Similar conclusions were made by Wang and Johnson,¹⁸ on the basis of DFT calculations performed on a carbon-supported Pt₃₇ nanoparticle with and without hydrogen passivation. The authors found that a hydrogen atmosphere stabilizes a truncated cuboctahedral morphology, with three (111) and three (100) facets. H atoms prefer to adsorb on bridge sites on the (100) faces and on hollow sites on the (111) ones. When all the bridge and hollow sites are occupied (46 H atoms adsorbed for

Pt₃₇ clusters), the energy reduction arising from the addition of a further H atom strongly decreases, giving rise to weakly adsorbed linear (on-top) hydrides, in good agreement with the three-site model proposed by Koningsberger.³⁵ As for the Pt₁₃H_{*n*} cluster on $\gamma\text{-Al}_2\text{O}_3$ discussed above, also in this case the Pt-support interaction is reduced significantly with the H passivation, due to the appearance of hydrogen at the interface between the Pt₃₇ cluster and the carbon. Both models have the potential to explain most of the experimental evidence reported in the literature.

In such a scenario, a relevant missing detail is the capability of discriminating among several Pt hydrides belonging to the same type. Indeed, there are many reasons to believe that, in a nanometric Pt cluster, the linear Pt-hydrides are not all the same, as well as the bridged or hollow sites differing depending on the environment. For example, up to six different features have been observed in hydrogen TPD curves for polycrystalline Pt,^{44–46} suggesting the presence of at least six different adsorption sites characterized by different Pt–H bonding energies. Vibrational spectroscopies might have the capability to discern between different Pt–H species, since the Pt–H vibration is sensitive to even small changes in the coordination geometry. Although some relevant works adopted the IR spectroscopy to investigate the behavior of Pt-supported catalysts in the presence of hydrogen since the early 1960s,^{47–52} the use of FT-IR spectroscopy for the direct characterization of the Pt–H species has been largely overlooked, especially in comparison to the huge amount of work based on XAS. This is primarily due to the relatively low dipole moment involved in the Pt–H bond, that reflects into extremely weak $\nu(\text{Pt-H})$ absorption bands. The second reason is that in practice only linear Pt–H species can be detected by FT-IR spectroscopy, since the vibrational features of bridged and hollow Pt–H species fall in the region usually obscured by the framework modes of the most employed support materials.^{47–50} Incoherent inelastic neutron scattering (INS) might be a powerful alternative, since it is extremely sensitive to hydrogenous species. Indeed, the INS signal is proportional to the neutron cross section of the probed element and to its displacement with respect to the equilibrium position.⁵³ Hydrogen has the largest incoherent cross section among all the elements and also the largest amplitude of motion because of its lightweight.⁵³ The use of INS in this field has been limited so far,^{54–57} due to the difficulty in having access to the neutron sources, the time required for collecting high-quality data (especially in comparison with X-ray based techniques that in the last decades have seen the rapid development of ultrafast methods), and the large amount of sample necessary for the measurements. Only in recent years the neutron instruments have progressed enough, in terms of neutron flux on the sample and efficiency in the neutron detection, to allow an easier investigation of samples of interest in catalysis.⁵⁸

In this work, we discuss some recent results obtained by coupling INS, FT-IR, and XAS spectroscopies to investigate the dynamic behavior of a highly dispersed Pt/Al₂O₃ catalyst in the presence of hydrogen. At first, we will show that INS and FT-IR spectroscopies may offer a complementary insight into the type and relative abundance of the Pt-hydride species, since INS detects more efficiently *n*-fold coordinated Pt-hydrides while FT-IR spectroscopy discriminates between at least four types of linear Pt–H species, whose relative amount is a function of the hydrogen coverage. In light of this experience,

we successively designed a series of DRIFT/XAS/MS experiments aimed at correlating the dynamic behavior of the Pt-hydrides in different reaction conditions with the electronic and structural changes occurring at the Pt nanoparticles. To the best of our knowledge, such an approach was never applied to the study of H₂-induced phenomena occurring on supported Pt nanoparticles.

2. EXPERIMENTAL SECTION

2.1. Catalyst Synthesis and Reduction Procedures.

The 5 wt % Pt/Al₂O₃ catalyst was prepared in the Chimet S.p.A. laboratories employing a high-surface-area activated transitional alumina as a support (SSA = 116 m² g⁻¹; pore volume = 0.41 cm³ g⁻¹), and following a deposition–precipitation method similar to the one reported by Kaprielova et al.⁵⁹ After preparation, the sample was carefully water washed and dried at 120 °C overnight.

For the INS experiment, Pt/Al₂O₃ (ca. 6.0 g) was activated in dynamic vacuum (final equilibrium pressure $P_{\text{eq}} = 10^{-4}$ mbar) at 120 °C and successively reduced in a H₂ atmosphere (two absorption/desorption cycles in hydrogen, absorption pressure: ca. 800 mbar, desorption pressure: dynamic vacuum), at the same temperature for about 1 h, followed by a prolonged evacuation at the same temperature.

For all the *operando* experiments, the catalyst activation and reduction were accomplished following two subsequent steps: (1) the catalyst was heated up to 120 °C (heating rate 5 °C/min) under an inert flow (N₂ or He) and left at this temperature for ca. 30 min, in order to eliminate most of the physisorbed water; (2) the catalyst was treated at 120 °C in a H₂/inert flow for ca. 15 min. During this step, the platinum oxide phase is reduced forming water as a reduction byproduct, followed by formation of Pt-hydrides. We conducted several experiments by changing the total flow rate (in the range 10–50 mL/min) and the H₂ concentration in the gas feed (2, 5, 10 mol %). We found that these two variables do not change the phenomena occurring on the catalyst, but only the involved kinetics (see below).

2.2. Methods. **2.2.1. High Resolution-Transmission Electron Microscopy (HR-TEM).** HR-TEM analysis was performed by means of a JEOL 3010-UHR TEM microscope operating at 300 kV, equipped with a LaB₆ filament, with a 2k × 2k pixels Gatan US1000 CCD camera and with an OXFORD INCA EDS instrument for atomic recognition via energy dispersive spectroscopy. The sample was quickly deposited (in the dry form, i.e., without using any solvent) on a copper grid covered with a lacey carbon film. Histogram of the Pt particle size distribution was obtained by considering a statistical representative number of particles on the HR-TEM images (more than 700), and the mean particle diameter (d_m) was calculated as $\langle d_m \rangle = \frac{\sum d_i n_i}{\sum n_i}$, where n_i is the number of particles of diameter d_i .¹⁶

2.2.2. Inelastic Neutron Scattering (INS). The INS measurements were performed on the LAGRANGE spectrometer at the ILL facility in Grenoble (France).⁶⁰ LAGRANGE is a high resolution filter spectrometer facing an hot moderator allowing the collection of spectra in the 5–525 meV (40–4234 cm⁻¹) energy transfer range with a resolution of $\Delta E/E$ of about 2%. The INS spectra were recorded at 20 K to reduce thermal effects that broaden the spectral features. The raw data are opportunely reduced to the scattering function $S(Q,\omega)$ plotted versus energy transfer (in

units of cm⁻¹). The INS spectra were collected in the whole available range, by properly merging the ranges acquired with three different monochromators: Si(111) for the 7.5–20.0 meV range, Si(311) for the 16.0–30.7 meV range, and Cu(220) for the 26.0–525.0 meV range. The integral of the counts of the three data collections in the two overlapped regions has been used to obtain a unified properly normalized spectrum in the whole range.

After activation, a weighed amount of the sample in the powder form was inserted in a volume-calibrated cylindrical-shaped Al cell (4 cm high, 16 mm diameter) within an Ar-filled glovebox to avoid exposure to air. The cell was sealed with an indium-wire, connected to a gas injection stick, and inserted into a CCR cryostat. The Ar contained in the cell was evacuated and the sample was cooled down to 20 K and a first spectrum of the bare activated sample in vacuum was recorded. Successively, the stick was removed from the cryostat and warmed up to room temperature. Hydrogen was dosed at room temperature by means of a Hiden Isochema gas volumetric device, at an equilibrium pressure of 420 mbar. The sample was cooled again at 20 K, and the INS spectrum in the presence of hydrogen was collected.

2.2.3. Operando FT-IR Spectroscopy. For the *operando* FT-IR measurements, ca. 10 mg of the undiluted Pt/Al₂O₃ catalyst were pressed into a self-supported pellet and placed inside a commercial FT-IR reactor cell (AABSPEC, no. 2000-A multimode), which allows recording the FT-IR spectra under controlled temperature and gas atmosphere. The FT-IR spectra were recorded every 60 s during the reduction step, and every 5 min during the successive treatment in N₂ flow. The FT-IR spectra were recorded in transmission mode, at a resolution of 2 cm⁻¹, on a PerkinElmer System 2000 spectrophotometer equipped with a MCT detector.

2.2.4. DRIFT/XAS/MS. *Operando* DRIFT/XAS/MS experiments were carried out at the BM23 beamline⁶¹ of the European Synchrotron Radiation Facility (ESRF, Grenoble, France). Combined diffuse reflectance infrared fourier transform spectroscopy (DRIFT), X-ray absorption spectroscopy (XAS), and mass spectrometry (MS) experiments were performed using a low-volume cell developed at BM23/ID24 for transient experiments.⁶² The cell was coupled to a Varian 680 FT-IR spectrophotometer equipped with a high-sensitivity MCT detector.

The Pt/Al₂O₃ catalyst (ca. 5 mg) was loaded in the powder form into a cylindrical channel in the sample holder ca. 1 mm in diameter, with two thin glassy carbon windows to ensure the X-ray beam passing through the sample. The dimension of the channel holder was selected to maximize the quality of the XAS spectra. The sample holder was then placed inside the cell, that was sealed on top with a CaF₂ IR-transparent window. The cell was resistively heated, monitoring the sample temperature by a thermocouple inserted in the cell body. The loaded cell was then mounted into a dedicated infrared optical system designed for DRIFT measurements and connected to the gas line. The outlet was connected to a Balzers Prisma MS via a stainless steel capillary kept at a temperature of 423 K, allowing the detection of a number of pertinent masses at each experiment.

The DRIFT spectra were collected continuously during the XAS measurements, from 900 to 4000 cm⁻¹, at 4 cm⁻¹ resolution. Each spectrum (128 scans) required 160 s to be recorded. The spectra were collected in reflectance mode and successively converted into $F(R)$ (Kubelka–Munk). The

background was acquired in the same configuration using powdered KBr as a reference.

For Pt L_3 -edge XAS, the white beam was monochromatized using a double-crystal Si(111) monochromator, and harmonic rejection was performed using two flat Si mirrors (grazing angle of 2 mrad). The spectra were acquired in transmission using ion chambers for the detection of the reference (I_0) and transmitted (I_t) X-rays. A third ionization chamber recorded a Pt foil reference for energy calibration. The XAS spectra were recorded at the Pt- L_3 edge (11 564 eV) with a beam size of ca. $800 \times 100 \mu\text{m}$ ($H \times V$) through the cell. The energy range was scanned from 11 400 to 12 500 eV, with an energy step of 5 eV and an integration time of 1 s/point in the pre-edge region, 0.5 eV step and 3 s/point in the XANES region, while the step in the EXAFS region was chosen to obtain a 0.04 \AA^{-1} step in the k -space with the acquisition time increasing quadratically with k from 3 to 8 s/point. Each spectrum required an acquisition time of about 18 min as a compromise between fast acquisition and quality of the spectra.

2.2.5. XAS Data Analysis. The XANES spectra were aligned and normalized with the Athena software,^{63,64} by means of standard procedures. EXAFS data analysis was performed using the Artemis software.^{63,64} The $k^2\chi(k)$ functions were Fourier transformed (FT) in the $\Delta k = 2.6\text{--}13.0 \text{ \AA}^{-1}$ interval. The first-shell fits were performed in the R space ($\Delta R = 1.0\text{--}3.5 \text{ \AA}$), resulting in a number of independent parameters $n_{\text{ind}} = 2\Delta k\Delta R/\pi$ larger than 16, a value that gives good confidence for a single shell fit.

A preliminary fitting analysis was performed by varying the following parameters: the coordination number (N), the Pt–Pt interatomic distance (R), the correction to the threshold energy (ΔE_0), and the Debye–Waller factor (σ^2). The third-order cumulant, which takes into account the anharmonic correction to the interatomic pair potential, was also included in the analysis, following the indication of previous works.^{22,23} The passive electron amplitude reduction factor (S_0^2) was fixed to 0.80(4), as obtained by analyzing the Pt reference foil. The coordination numbers (N) have been obtained by multiplying the amplitude determined by the fit for the first-shell coordination number in platinum bulk (12), and dividing it for the S_0^2 value. Phase and amplitudes were calculated with the FEFF6.0 code⁶⁵ using as input the structure of Pt bulk. In order to limit the number of variables, the fit was performed simultaneously on four spectra collected under different H_2 coverage at the same reaction temperature (120 °C). Multiple-scattering paths were not included, since the data analysis was limited to the first coordination shell, and the first-neighbor single-scattering path is well isolated from single- and multiple-scattering paths at longer distance. On the basis of this first analysis, a second series of fits were performed, where the σ^2 was fixed to increasing values from 0.007 to 0.011 \AA^2 , while a single ΔE_0 value was fit across the four H_2 coverages. Advantages and disadvantages of the two fitting strategies are described in more detail in the main text.

3. RESULTS AND DISCUSSION

3.1. Preliminary Characterization of the Pt/ Al_2O_3 Catalyst. Figure 1 shows a representative HR-TEM micrograph of Pt/ Al_2O_3 . Very small Pt nanoparticles, homogeneously distributed on the support, and with an almost spherical shape and a regular size are observed. Most of them have a diameter smaller than 2 nm. The particle size distribution and the average particle size were determined by

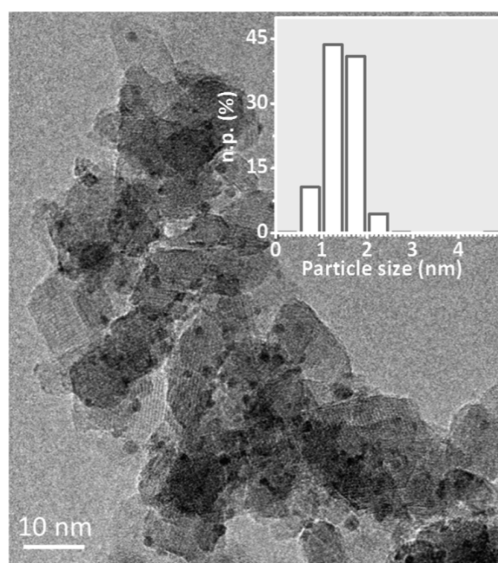


Figure 1. Representative HR-TEM micrograph of Pt/ Al_2O_3 and corresponding particle size distribution (inset). Instrumental magnification 200 000 \times .

analyzing more than 700 particles. The estimated average particle size is $1.4 \pm 0.4 \text{ nm}$, which is in fair agreement with the nominal dispersion $D = 63\%$, as determined by means of a H_2/O_2 titration method.⁶⁶ Such particle size distribution has been demonstrated to be narrow enough to ensure that EXAFS characterization is representative of the whole distribution of particles.^{25,26}

3.2. n -Fold Coordinated Pt-Hydrides as Detected by Inelastic Neutron Scattering (INS). The Pt/ Al_2O_3 system in the presence of H_2 was investigated with the incoherent inelastic neutron scattering (INS) technique. Figure 2a shows the INS spectrum of reduced Pt/ Al_2O_3 in the absence (black)

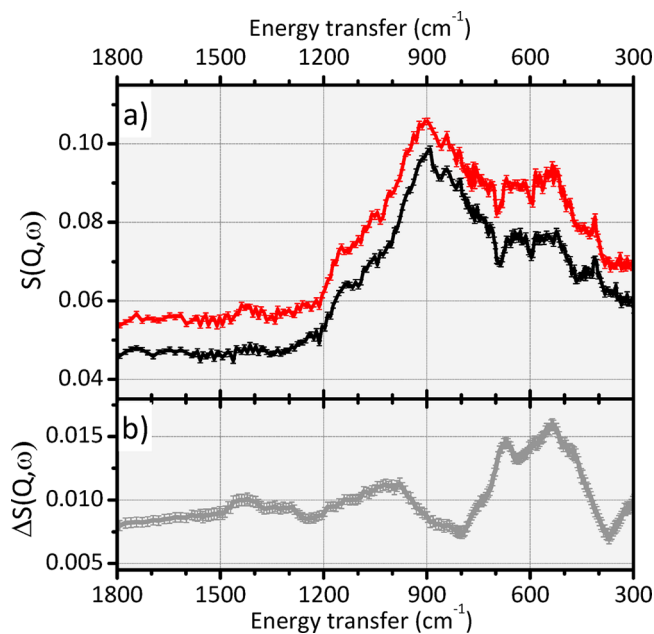


Figure 2. Part (a): INS spectra of the reduced Pt/ Al_2O_3 catalyst in the absence (black) and in the presence (red) of 420 mbar of H_2 . Part (b): Difference between the two spectra reported in part (a).

and in the presence (red) of H_2 (P_{H_2} e.p. = 420 mbar). Both spectra have been collected at 20 K. The two spectra are dominated by an intense peak centered around 905 cm^{-1} (with a shoulder at 760 cm^{-1}) and by a series of overlapping bands at ca. 640 and 550 cm^{-1} , which are all assigned to deformation modes of hydroxyl groups at the alumina surface.⁶⁷ Figure 2b shows the difference between the two spectra, $\Delta S(Q,\omega)$, that is the INS spectrum of hydrogen chemisorbed on the catalyst. Indeed, the absence of relevant porosity in the alumina support prevents the observation of physisorbed hydrogen, as reported, for example, for Pt/C catalysts at comparable H_2 equilibrium pressure.⁵⁸ The $\Delta S(Q,\omega)$ spectrum is characterized by two series of bands having a broad envelope: (1) the most intense signals are in the range $400\text{--}800\text{ cm}^{-1}$ (maxima at 470 , 535 , 590 , 670 , 750 cm^{-1}); (2) a second group of bands having medium intensity is observed in the range $800\text{--}1200\text{ cm}^{-1}$. According to the literature,^{54,56,57,68,69} all these bands are due to Pt–H vibrations of n -fold coordinated (bridged, hollow, and 4-fold coordinated) Pt–H species. Bands in similar positions were previously reported for platinum hydrides on Pt single-crystals,⁶⁹ on 40 wt % Pt/C catalysts,^{54,56,57} and very recently by some of the authors on a very low loaded, industrially relevant, 5 wt % Pt/C catalyst having a particle size comparable with our Pt/ Al_2O_3 .⁵⁸ The exact assignment of these bands is challenging and would require an accurate modeling of the Pt nanoparticles in the presence of hydrogen, which will be the subject of a successive report. The important message to retain here is that INS clearly reveals the presence of variable n -fold coordinated platinum hydrides even in low loaded catalysts.

3.3. Formation of Linear Pt-Hydrides and Their Evolution upon Dehydrogenation, as Monitored by *operando* FT-IR Spectroscopy.

A series of preliminary FT-IR measurements during hydrogen adsorption/desorption cycles on Pt/ Al_2O_3 were performed using the FT-IR *operando* setup described in the Experimental Section. Figure 3a shows the FT-IR spectra of the catalyst before (black) and after (red) the reduction step. The two spectra are dominated by an intense and very broad absorption band centered at ca. 3500 cm^{-1} , which is due to the $\nu(\text{OH})$ of the hydroxyl groups at the alumina surface. Due to the relatively low activation temperature ($120\text{ }^\circ\text{C}$), the fraction of the surface OH species is large, and they interact with each other via hydrogen-bonding. The spectra are cut below 1000 cm^{-1} , where the intense vibrational modes of the alumina framework saturate the detector. For this reason, the absorption bands ascribed to n -fold coordinated Pt–H species (detected by INS) cannot be detected by means of FT-IR spectroscopy. The spectrum collected at the end of the reduction step (red) shows a small amount of physisorbed H_2O ($\nu(\text{OH})$ at ca. 3500 cm^{-1} and $\delta(\text{HOH})$ at ca. 1630 cm^{-1}), which derives from the reduction of the supported PtO_x phase, and a series of very weak bands in the $2200\text{--}1700\text{ cm}^{-1}$ range. This spectral region is magnified in Figure 3b, that shows the spectra collected during the reduction of the Pt/ Al_2O_3 sample after subtraction of the spectrum prior to H_2 dosage. Four absorption bands (labeled I, II, III, and IV) are clearly observable at 2115 , 2041 , ca. 1990 , and ca. 1740 cm^{-1} , respectively. All these bands gradually grow in intensity during the reduction step, and then reach a steady state situation. According to the literature,^{47,48,50,51,70} the 2115 cm^{-1} band is attributed to a weak linearly adsorbed hydride, whereas the two bands at 2041 and 1990 cm^{-1} are related to strongly adsorbed linear hydride species. The difference between these two

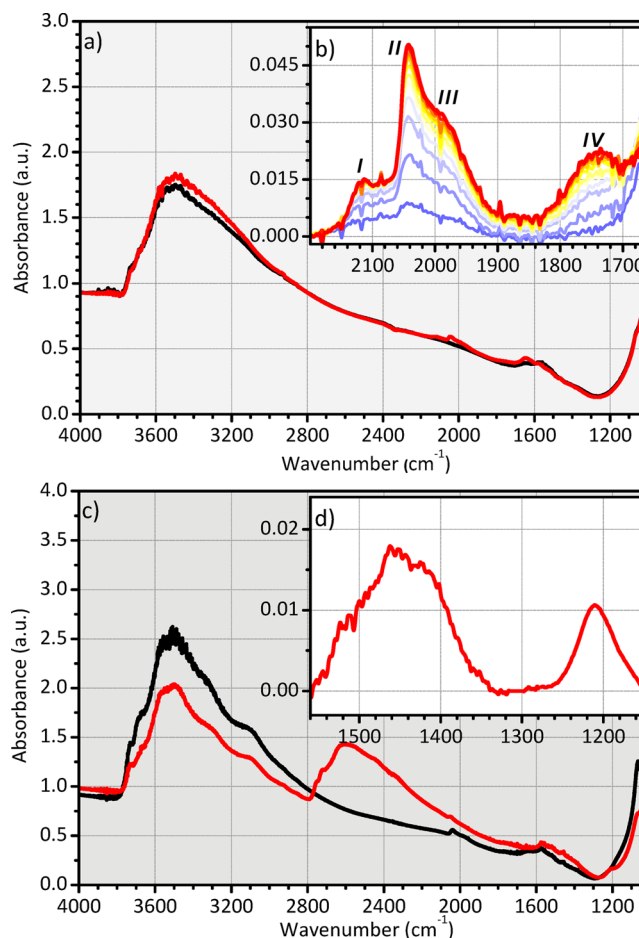


Figure 3. Part (a): FT-IR spectra of the Pt/ Al_2O_3 catalyst before (black) and after (red) the reduction step, accomplished in a H_2/N_2 flow (10% H_2 , 20 mL/min). Part (b): magnification of the $2200\text{--}1700\text{ cm}^{-1}$ range, where linear Pt-hydrides contribute to the spectra. The spectra in part (b) are reported after subtraction of the spectrum prior reduction (black curve in part a). Part (c) FT-IR spectra of the Pt/ Al_2O_3 catalyst after the reduction step (black), and the effect of dosing D_2 (red). The spectrum in part (d) is the difference between the two.

strongly adsorbed species was never clarified in the literature, but it might be related to the type of environment around the hydride. A linear hydride strongly adsorbed nearby another hydride (either linear or n -fold coordinated) might indeed vibrate differently than an isolated linear one. Finally, the band at ca. 1740 cm^{-1} was never discussed in the literature. We anticipate that it might be assigned to linear platinum hydrides in interaction with the Lewis acid sites exposed at the alumina surface. Hence, this band is strictly correlated with the interface between the platinum nanoparticle and the support.

It is worth noticing that as expected these bands are very weak, because of the rather weak dipole moment associated with the stretching mode of linear Pt–H species. This is the reason why the observation of Pt–H by FT-IR spectroscopy has been limited so far, and often questioned.^{49,52} In particular, one of the most frequent criticisms is that the observed bands might be due to chemisorbed CO eventually present as an impurity in the H_2 feed. To be sure that the observed bands are really related to hydride species and not to chemisorbed CO as reported in some cases in the literature,⁷⁰ a further experiment was performed by dosing deuterium after the reduction step in

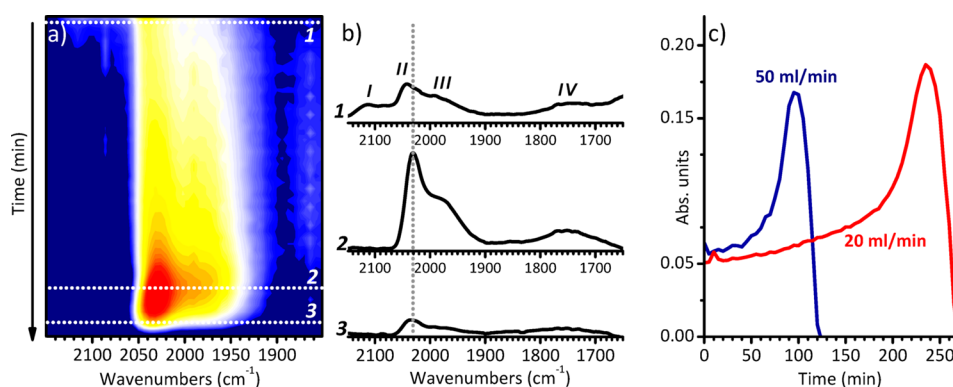


Figure 4. Part (a): 2D map showing the evolution of the FT-IR spectra as a function of time for the Pt/Al₂O₃ catalyst during dehydrogenation in N₂ flow (20 mL/min) at 120 °C. The previous reduction step was accomplished in the presence of 10 mol % H₂ in N₂. The intensity increases from blue to red. Part (b): Three FT-IR spectra selected at specific times (1, 2, and 3 in the 2D map shown in part (a)). The four bands are labeled as *I*, *II*, *III*, and *IV* (see main text for further discussion). The spectra are shown after subtraction of the spectrum of the catalyst at 120 °C before reduction, in the 2150–1850 cm⁻¹ range. Part (c): Evolution of the intensity of the band at 2041 cm⁻¹ (species *II*, dotted vertical line in part b) as a function of time, for the spectra shown in part (a) (20 mL/min, red curve), and for a similar experiment performed with a higher flux (50 mL/min, blue curve).

H₂ (Figure 3c). The FT-IR spectrum of Pt/Al₂O₃ drastically changes, because about half of the surface OH groups undergo exchange with deuterium; hence, the $\nu(\text{OH})$ absorption band at ca. 3500 cm⁻¹ shifts to 2600 and the $\delta(\text{OH})$ band at ca. 1070 cm⁻¹ downward shifts to the spectral region dominated by the alumina framework modes. On top of this, four bands are observed at 1515, 1465, 1422, and 1220 cm⁻¹ (Figure 3d), corresponding to bands *I*, *II*, *III*, and *IV* in Figure 3b. The four bands are isotopically shifted by a factor of ca. 1.39, confirming the assignment to hydride species.⁴⁸ The relative intensity of the four bands is slightly different, but this can be due to the change of the profile of the overall spectrum. The Pt–H bands in the 2150–1750 cm⁻¹ region do not disappear completely in the presence of D₂, suggesting that the H–D exchange is subjected to a complex equilibrium.

After the reduction step, the gas feed composition was switched to pure N₂ at the constant temperature of 120 °C. Figure 4a shows the evolution of the FT-IR spectra collected in these conditions as a function of time in the form of a 2D map (the intensity increases from blue to red), while Figure 4b shows three selected spectra in the map. The band at 2115 cm⁻¹ (species *I*) immediately disappears, proving that it is associated with a very weakly adsorbed Pt–H species, which is stable only in the presence of a H₂ atmosphere. The other three bands, instead, evolve in a counterintuitive way. In particular, the two bands at 2041 and 1990 cm⁻¹ (species *II* and *III*) slowly increase reaching approximately twice their original intensity in about 235 min, while the band at ca. 1740 cm⁻¹ (species *IV*) remains almost unchanged. After reaching the maximum, all the three bands rapidly disappear. Similar experiments were performed by changing the H₂ concentration during the reduction step and/or the total flow rate. The FT-IR spectra evolve in the same way, although with a different velocity. In general, a higher H₂ concentration in the flow caused longer dynamics, while a higher total flow rate was responsible for a shortening. As an example, Figure 4c shows the evolution of the intensity of the band at 2041 cm⁻¹ (species *II*) as a function of time for two experiments performed at the same H₂ concentration (10 mol %) but at a different total flow rate (50 mL/min and 20 mL/min). It is evident that the evolution has the same character, but occurs much faster at 50 mL/min. The reason for these differences

has to be ascribed to the experimental setup. Indeed, our *operando* FT-IR cell is characterized by a large dead volume that, once filled with hydrogen during the reduction step, requires time before being completely cleaned by N₂. In other words, our experimental setup allowed a serendipitous decrease of the hydrogen partial pressure in the cell at a very slow speed, thus permitting us to follow the dynamic of the platinum hydrides as a function of the hydrogen coverage.

The evolution of our FT-IR spectra is in very good agreement with the theoretical model proposed by Raybaud and Sautet,¹⁹ according to which a decrease in the hydrogen partial pressure is responsible for a reconstruction of the Pt particles from a cuboctahedral morphology prevalently solvated by *n*-fold coordinated (bridged and hollow) hydrides, to a biplanar morphology mostly covered by linear hydrides. The model predicts that during the reconstruction of the Pt particles, the relative concentration of the linearly adsorbed hydrides (visible by FT-IR spectroscopy) should increase at the expenses of the *n*-fold adsorbed hydrides (which are invisible by FT-IR spectroscopy, but clearly detected by INS, Figure 2). The theoretical model also predicts the existence, in a large range of hydrogen coverages, of hydrogen at the interface between the Pt cluster and the support, corroborating our assignment of the absorption band at ca. 1740 cm⁻¹ to platinum hydrides in interaction with alumina. Our FT-IR data fit very well with the simpler three-site model proposed earlier by Koningsberger.³⁵ At the maximum hydrogen coverage, the Pt particles are covered by adsorbed “on-top” hydrides (species *I*) and *n*-fold coordinated hydrides (not visible by IR). Upon decreasing the H₂ coverage, the “on-top” hydrides are easily removed and the *n*-fold coordinated hydrides slowly transform themselves into “atop” species, causing the appearance and the transient increase in the intensity of bands *II* and *III*.

3.4. Simultaneous DRIFT/XAS/MS Experiment.

3.4.1. Experimental Results. In order to validate our interpretation, we designed an *ad hoc* DRIFT/XAS/MS experiment to investigate the evolution of the FT-IR bands ascribed to linear Pt-hydrides and, at the same time, the electronic and structural changes occurring at the Pt particles upon decreasing the hydrogen coverage. The main difficulty in coupling DRIFT and XAS spectroscopies in this particular case resides in the unequal time requested for the collection of a

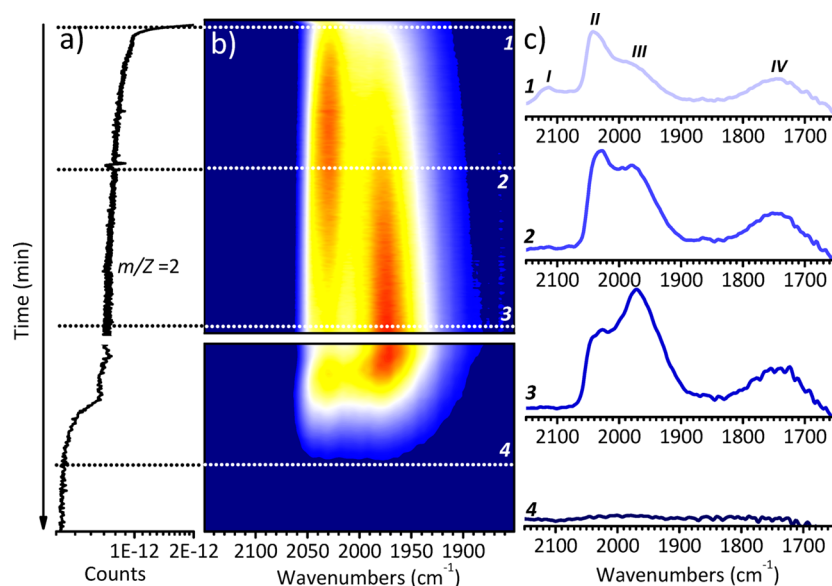


Figure 5. Part (a): Evolution of the signal corresponding to H₂ ($m/Z = 2$) as detected by the mass spectrometer placed at the outlet of the reaction cell. Part (b): 2D map showing the evolution of the DRIFT spectra as a function of time for the Pt/Al₂O₃ catalyst during dehydrogenation in He flow (20 mL/min) at 120 °C, for the operando DRIFT/XAS/MS experiment. The reduction step preceding the dehydrogenation was accomplished in the presence of 10 mol % H₂ in He. The intensity increases from blue to red. Part (c): Four FT-IR spectra selected at specific times (1, 2, 3, and 4 in the 2D map shown in part b). The spectra are shown after subtraction of the spectrum of the catalyst before reduction, in the 2150–1850 cm⁻¹ range.

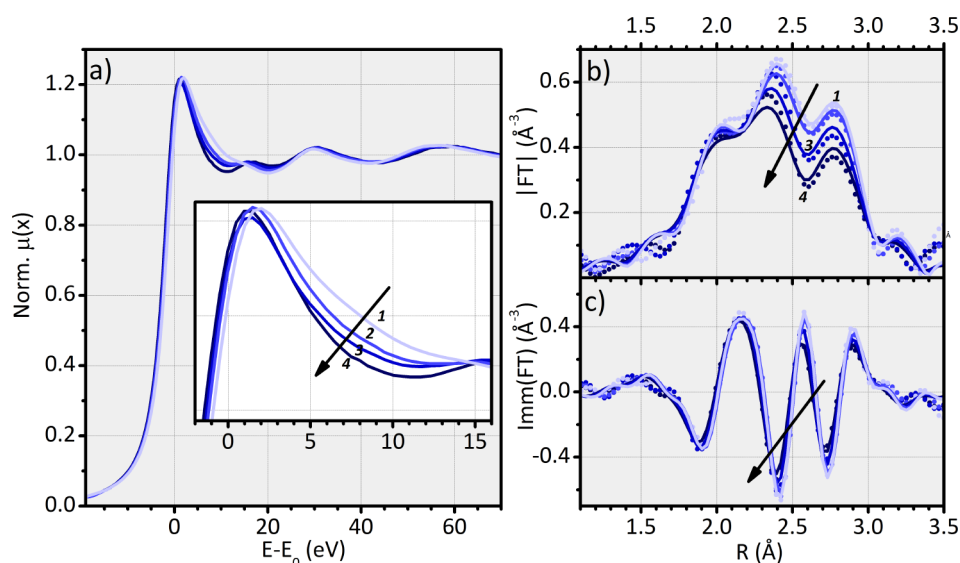


Figure 6. Part (a): Evolution of the normalized Pt L₃-edge XANES spectra of the Pt/Al₂O₃ catalyst during dehydrogenation in He flow (20 mL/min) at 120 °C, collected during the operando DRIFT/XAS/MS experiment ($E_0 = 11\,564$ eV). The inset shows a magnification of the white-line region. Part (b): Modulus of the Fourier-transforms of the k^2 -weighted EXAFS signals collected along with the XANES spectra reported in the part a. The experimental signals (dotted) are overlapped to the first shell fits (full line). Part (c): the same as part b, for the imaginary part of the Fourier transforms. Spectra 1–4 closely correspond to the DRIFT spectra 1–4 in Figure 5.

single spectrum: the collection of a good DRIFT spectrum requires around 2 min, while that of a high-quality XAS spectrum in both XANES and EXAFS regions requires 18 min. Thus, it was of pivotal importance to prolong the duration of the hydrogen removal step in order to collect a significant number of good-quality XAS spectra during the Pt particle reconstruction. This problem was overcome by adding to the setup, prior to the measurement cell and tangential to the flow, a dead volume filled with the same hydrogen concentration adopted during the hydride formation step (10 mol %). The dead volume was left open during the dehydrogenation

treatment under He flow at 120 °C, so that a tiny and gradually decreasing amount of H₂ was constantly stripped by He. The result was that, after a first sudden drop, the H₂ concentration in the feed decreased very slowly, as detected also by MS at the outlet of the cell (Figure 5a). Only after closure of the dead volume, the H₂ concentration in the feed rapidly fell down to zero (and the $m/Z = 2$ mass detected by MS reached the end of scale value).

Figure 5b shows the evolution of the DRIFT spectra, in the form of a 2D map, for the Pt/Al₂O₃ catalyst during the dehydrogenation step, whereas Figure 5c shows four selected

spectra in the map. The evolution of the absorption bands attributed to linear Pt–H species is even more complex than that observed during the *operando* FT-IR experiments in transmission mode (Figure 4a), likely as a consequence of the longer dynamics. However, the general behavior is the same. Band I rapidly disappears, while bands II and III slowly increase up to double their original intensity, although at a different rate. A change in the relative intensity of bands II and III is observed with time, with band III prevailing at longer dehydrogenation times (i.e., at lower hydrogen concentration). After closing the dead volume, bands II and III reach the maximum, and then rapidly disappear. Band IV is the least affected by the whole dehydrogenation process, and remains almost unchanged in intensity until the end when it disappears swiftly as bands II and III.

Figure 6 shows the XAS spectra collected simultaneously to the DRIFT and MS spectra previously discussed. The dehydrogenation induces relevant changes in the Pt L₃-edge XANES spectrum of the catalyst (Figure 6a). Both the shape and the intensity of the white line are affected. Specifically, the white line is shifted to lower energy upon decreasing the hydrogen coverage, and becomes sharper (inset in Figure 6a). This is a typical phenomenon that is well-known in the literature, which has been explained mainly in terms of an electronic effect of the adsorbate.^{18,22,24,27–30,34–42} Spectrum 4

is collected at the end of the dehydrogenation step and can be considered representative of bare platinum nanoparticles. As far as the EXAFS part of the spectra (Figure 6b,c) is concerned, the dehydrogenation process induces a small but visible decrease in the intensity of the first shell contribution to the FT, and a shift toward shorter distances, which is more visible by looking at the imaginary part of the FT (Figure 6c).

3.4.2. EXAFS Data Analysis. As widely documented in the literature, the EXAFS data analysis of nanometric and subnanometric Pt particles in the presence of adsorbates should be done with caution, since it is difficult to discriminate among the effects of temperature, particle size, and disorder, based on the magnitude of the FT alone.^{25,26}

As a first attempt, the fit was performed simultaneously on the four spectra collected under different H₂ coverages at the same temperature (Figure 6b,c), by varying ΔE_0 , N , R , σ^2 , and the third cumulant. The results are summarized in the first part of Table 1. Without chemisorbed hydrogen (spectrum 4), the Pt–Pt interatomic distance R is 2.70(2) Å. Thus, the Pt–Pt bond is contracted by 0.074 Å compared to bulk Pt ($R_{\text{eff}} = 2.774$ Å), corresponding to $\Delta R = -2.7\%$. Contraction values up to 0.10 Å have been reported for particles having similar size.^{22,23,71} The mean Pt–Pt bond relaxes in the presence of chemisorbed hydrogen reaching the value $R = 2.74(1)$ Å ($\Delta R = -1.2\%$) for spectrum 1. This is also well documented in the literature and is explained in terms of the electron-withdrawing properties of chemisorbed hydrogen, that leads to a reduced electron density among the platinum atoms.²² The interpretation of the coordination number N and of the Debye–Waller factor σ^2 is more delicate. Without chemisorbed hydrogen (spectrum 4), the Pt nanoparticles are characterized by $N = 8.0(8)$ and $\sigma^2 = 0.0105(9)$ Å². Although these values look reasonable, the trend across the spectral series does not. Indeed, N does not vary within the experimental error and the experimentally observed increase in the amplitude of the FT is all accounted for by σ^2 , that drops from 0.0105(9) for spectrum 4 to 0.0085(5) Å² for spectrum 1 (i.e., $\Delta\sigma^2 = -19\%$). These results are doubtful because the change in σ^2 values

Table 1. Results of the First Shell EXAFS Data Analysis for Spectra 1–4 Reported in Figure 6^a

First Fitting Approach – $R_{\text{factor}} = 0.012$					
Spectrum	ΔE_0 (eV)	N	R (Å)	σ^2 (Å ²)	$\sigma^3 10^{-4}$ (Å ³)
1	5.7(6)	8.0(5)	2.738(9)	0.0085(5)	0(1)
2	5.6(5)	7.7(5)	2.717(8)	0.0086(4)	0(1)
3	5.9(9)	8.0(7)	2.71(1)	0.0094(8)	2(2)
4	5.7(9)	8.0(8)	2.70(2)	0.0105(9)	2(2)
Second Fitting Approach – $R_{\text{factor}} = 0.015$					
Spectrum	ΔE_0 (eV)	N	R (Å)	σ^2 (Å ²)	$\sigma^3 10^{-4}$ (Å ³)
1	5.7(3)	8.4(3)	2.737(7)	0.009	0(1)
2		8.1(2)	2.722(6)		0(1)
3		7.7(4)	2.711(9)		1(1)
4		7.0(4)	2.702(9)		1(2)

^aThe fits were performed simultaneously in the R space ($\Delta R = 1.0$ – 3.5 Å, $\Delta k = 2.6$ – 13.0 Å⁻¹, resulting in $2\Delta k\Delta R/\pi = 16.55$), following two approaches. At first, we varied the correction to the threshold energy (ΔE_0), the first shell Pt–Pt coordination number (N), the Pt–Pt interatomic distance (R), the Debye–Waller factor (σ^2), and the third cumulant (σ^3). In a second moment, we fit a single ΔE_0 common to the four spectra, and we fixed σ^2 to increasing values in the 0.007–0.011 Å² range. We report here the results of the best fit, obtained for $\sigma^2 = 0.009$ Å². The results of the other fits are summarized in Figure 7.

looks much larger than expected. In this respect, it is useful to recall that σ^2 contains a static (σ_s^2) and a dynamic (σ_d^2) part, $\sigma^2 = \sigma_s^2 + \sigma_d^2$. As demonstrated by Sanchez et al.,²⁶ the static part σ_s^2 depends on both particle size and type of adsorbate. For example, for 1.1 nm Pt nanoparticles (similar to 1.4 nm particles in the current work), σ_s^2 was reported to be 0.0045(2) Å² in He and 0.0037(2) Å² in H₂ atmosphere (extrapolated close to 0 K from $\sigma^2(T)$ curve), indicating that H-passivation induces a strong ordering in the Pt nanoparticles. On the other hand, the dynamic part of the Debye–Waller factor, σ_d^2 , depends on both temperature and adsorbate. In particular, it was demonstrated that σ_d^2 increases with temperature more rapidly in H₂ than in He.²⁶ The consequence for Pt nanoparticles is that, although σ_s^2 measured in H₂ is lower than that measured in He, for temperatures above a certain threshold the total σ^2 measured in H₂ starts to exceed that measured in He. This threshold is very close to 120 °C for 1.1 nm Pt nanoparticles, meaning that at this temperature the total σ^2 of hydrogenated and bare particles should be very similar to each other. Indeed, from the data of Sanchez et al. the expected difference between the two σ^2 is less than 10^{-4} Å², which is well below our fitting error.²⁶

The consideration above, and the observation of a very strong correlation between N and σ^2 in our fit, induced us to use another, more conservative, approach in analyzing the EXAFS data, starting from the assumption that for 1.4 nm Pt nanoparticles measured at 120 °C we do not expect σ^2 to vary with any statistical significance with the H₂ concentration. On this basis, we performed a series of fit by varying ΔE_0 , N , R , and the third cumulant, and fixing σ^2 at different values in the 0.007–0.011 Å² range. The main results are summarized in Figure 7, that shows the behavior of N and R as a function of the H₂ coverage (decreasing from spectrum 1 to spectrum 4), and the R -factor of all the fits. It is evident that the behavior of N and R across the spectral series is the same irrespective of σ^2 : N decreases of ca. 20% during the dehydrogenation (from spectrum 1 to spectrum 4), and R decreases of ca. 1.3%.

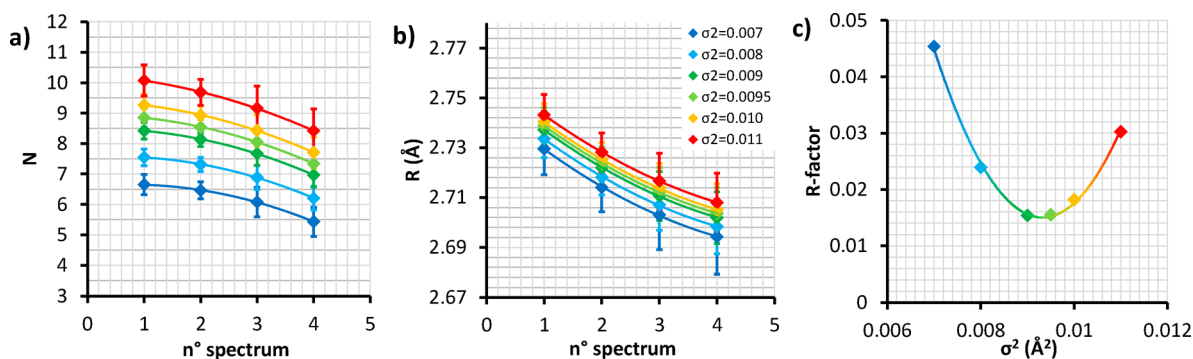


Figure 7. Summary of the results of the EXAFS data analysis on spectra 1–4 reported in Figure 6b,c, performed by varying ΔE_0 , N , R , and the third cumulant, and fixing σ^2 at different values in the 0.007–0.011 \AA^2 range. Parts (a) and (b) show the behavior of N and R across the spectral series, whereas part (c) reports the quality of the fits (R_{factor}) as a function of σ^2 .

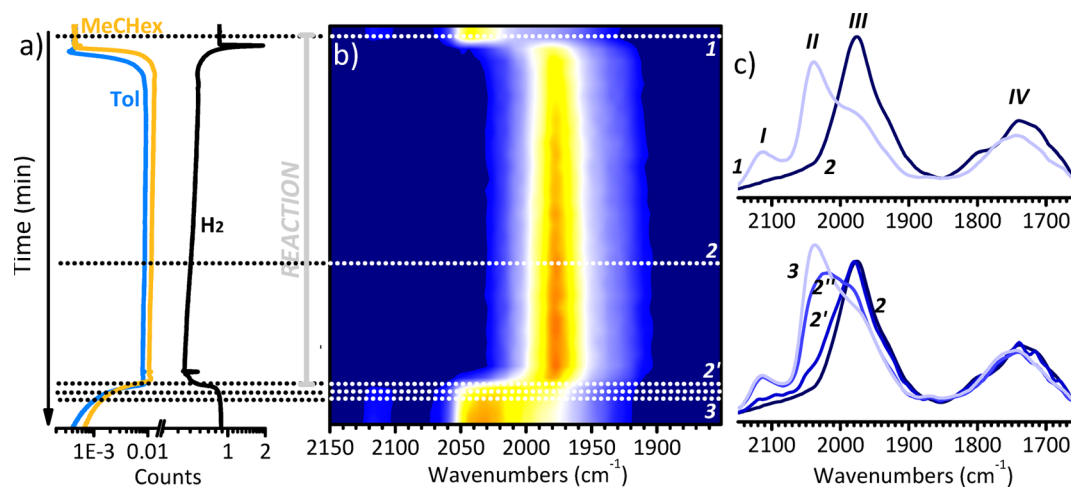


Figure 8. Part (a): Evolution of the signals corresponding to H₂ ($m/Z = 2$), toluene ($m/Z = 91$), and methylcyclohexane ($m/Z = 55$), as detected by the mass spectrometer placed at the outlet of the reaction cell. Part (b): 2D map showing the evolution of the DRIFT spectra as a function of time for the Pt/Al₂O₃ catalyst during hydrogenation of toluene to methylcyclohexane at 120 °C. The reduction step preceding the reaction was accomplished in the presence of 10 mol % H₂ in He. The intensity increases from blue to red. Part (c): FT-IR spectra selected at specific times as indicated in the 2D map shown in part (b). The spectra are shown after subtraction of the spectrum of the catalyst before reduction, in the 2150–1850 cm^{-1} range.

Considering the R_{factor} trend, $\sigma^2 = 0.009 \text{ \AA}^2$ is a well-behaved absolute minimum for the fit. The corresponding fitted parameters are reported in the second part of Table 1.

The validity of this approach is testified by the fact that the coordination number N estimated by considering the average particle size as determined by HR-TEM^{72,73} and assuming a truncated cuboctahedral model (which is the shape more similar to that expected for dehydrogenated particles)¹⁹ is 7.6, that is just 8% above the N value determined by EXAFS in the absence of H₂.

Overall, the spectroscopic data discussed so far and the detailed EXAFS data analysis clearly demonstrate that the Pt nanoparticles in our Pt/Al₂O₃ catalyst undergo a slow and progressive reconstruction upon hydrogenation/dehydrogenation, in very good agreement with theoretical predictions.¹⁹ XANES and EXAFS techniques were already largely adopted in the past to demonstrate this effect, and our data reproduce those present in the literature. However, the novelty of our work is the simultaneous observation of what happens at the surface of the Pt nanoparticles. The DRIFT spectra collected synchronously to the XAS ones reveal for the first time which kind of platinum hydrides are present at each moment of the dehydrogenation step. Interestingly, species IV survives for a

prolonged time (i.e., also at low hydrogen coverage), suggesting that the platinum hydrides at the Pt/Al₂O₃ interface are quite stable irrespective of the particle morphology. We will see in the following that the observation of what happens at the surface of the Pt nanoparticles will be particularly relevant during the catalysis.

3.5. Behavior of Pt-Hydrides during the Hydrogenation of Toluene. We also investigated the structural and surface dynamics of the Pt nanoparticles in Pt/Al₂O₃ applying the same DRIFT/XAS/MS approach described above, during the catalytic hydrogenation of toluene to methylcyclohexane. The reaction was selected as a model for catalytic hydrogenation of substituted benzenes, because toluene has a high vapor pressure (i.e., it is easily extracted from the liquid phase by an inert flow also at room temperature) and because the IR absorption bands characteristic of reagents and products are clearly discernible and do not overlap with the $\nu(\text{Pt-H})$ features we want to monitor. After the reduction step, the 10% H₂ in He flow (20 mL/min) was used to strip toluene vapors from a saturator, and DRIFT/XAS/MS data were collected continuously for ca. 1 h. We selected the aforementioned conditions in order to be far enough from the stoichiometric toluene hydrogenation; in this

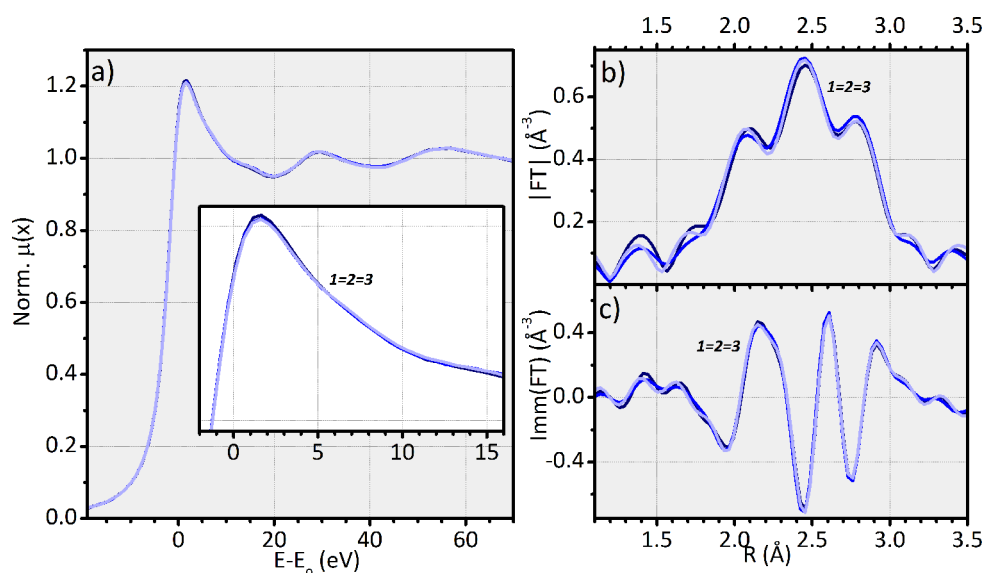


Figure 9. Part (a): Evolution of the normalized Pt L_3 -edge XANES spectra of the Pt/ Al_2O_3 catalyst during hydrogenation of toluene to methylcyclohexane at 120 °C, collected during the operando DRIFT/XAS/MS experiment ($E_0 = 11\,564$ eV). The inset shows a magnification of the white-line region. Part (b): Modulus of the Fourier-transforms of the k^2 -weighted EXAFS signals collected along with the XANES spectra reported in part a. Part (c): the same as part b, for the imaginary part of the Fourier Transforms. Spectra 1–3 closely correspond to the DRIFT spectra 1–3 in Figure 8 (i.e., spectrum 1 is collected before introducing toluene in the reaction feed, spectrum 2 during the toluene hydrogenation reaction, and spectrum 3 after removal of toluene from the reaction feed).

way, we are sure to avoid the total depletion of the Pt-hydride species that we are interested in during the reaction. The DRIFT and MS results are summarized in Figure 8, while the XANES and EXAFS results are shown in Figure 9.

The MS data (Figure 8a) indicate that toluene conversion starts instantaneously and proceeds at a constant rate for the whole investigated time. At the same time, relevant changes are observed in the DRIFT spectra (Figure 8b,c): bands *I* and *II* immediately disappear, while band *III* rapidly increases in intensity. In contrast, band *IV* is almost unaffected. The spectra remain then constant along the whole reaction. The reverse behavior is observed when, after ca. 1 h of reaction, toluene is removed from the reaction feed. Band *III* decreases in intensity, and bands *II* and *I* are restored again. The spectrum collected in these conditions (spectrum 3) is almost equal to that collected before the onset of the reaction (spectrum 1). Interestingly, no changes are observed neither in the XANES spectra (Figure 9a) nor in the EXAFS ones along all the reaction time (Figure 9b,c). This univocally demonstrates that, in the adopted experimental conditions, the Pt nanoparticles are structurally and electronically stable during the whole reaction time.

Taken as a whole, these results indicate that, under the adopted experimental conditions, the changes occurring at the Pt surface during the catalysis are not accompanied by a change in the structure and morphology of the Pt nanoparticles. Moreover, the DRIFT data shown in Figure 8b,c suggest that only a fraction of the platinum hydrides are directly involved in the hydrogenation reaction. Species *I*, which are the weakly adsorbed hydrides (hence more available), are immediately consumed and no longer observed during the reaction, a behavior that indicates their direct participation in the reaction. The destiny of species *II* is less straightforward. Indeed, band *II* also immediately disappears as soon as toluene reaches the sample. However, a careful inspection to the sequence of the spectra suggests that it is

converted into band *III*. Indeed, an isosbestic point is observed at 2006 cm^{-1} . Hence, in the presence of toluene, the strongly adsorbed hydrides of type *II* are converted into hydrides of type *III*. This is the same effect observed during the dehydrogenation, when band *III* increases in intensity at the expense of band *II* (Figure 5b,c). This evidence further corroborates the assignment of bands *II* and *III* to very similar strongly adsorbed “atop” platinum hydrides that differ in terms of the surface environment. Species *III* is more isolated than species *II*, and hence is favored in the presence of toluene, that competes for the adsorbing sites at the platinum surface. Finally, species *IV* seems unaffected by the occurrence of the reaction, as also observed during the dehydrogenation. Even though the majority of the observed linear Pt-hydrides do not participate directly to the hydrogenation reaction (i.e., they are not used to hydrogenate the substrate), they play a fundamental role, maintaining the Pt nanoparticle shape along the reaction.

4. CONCLUSIONS

It is a well-known phenomenon that supported Pt nanoparticles subjected to hydrogenation conditions undergo electronic and morphological reconstructions depending on a range of parameters, among which are the employed support, the adopted temperature and pressure, the atmospheric composition, and the hydrogen coverage. So far, the occurrence of these reconstruction phenomena has been predicted by theoretical calculation on different Pt-based systems,^{18,19,35} which are in good agreement with the structural and electronic information derived from EXAFS and XANES data. However, a complete experimental characterization of all the surface Pt-hydride species and of their dynamic behavior in different reaction conditions was still missing, despite its crucial importance in hydrogenation catalysis. In this work we have tried to fill this gap, by investigating an industrial 5 wt % Pt/ Al_2O_3 catalyst (average particle size of 1.4 ± 0.4 nm) under

different hydrogenation/dehydrogenation conditions with a multitechniques approach, including HR-TEM, INS and FT-IR spectroscopy, and synchronous DRIFT/XAS/MS.

Briefly, we have been able to identify at the Pt surface both n -fold coordinated Pt-hydrides and four different types of linear Pt-hydrides characterized by different adsorption strengths. We have observed experimentally the conversion of the n -fold coordinated hydrides into linear ones upon decreasing the hydrogen coverage, and vice versa, and correlated it to the morphological and electronic reconstruction of the Pt nanoparticles, in fair agreement with the theoretical predictions.¹⁹ Even more important for the catalysis, we have demonstrated that only the weakest adsorbed hydrides (species I) are directly involved in the hydrogenation of toluene (chosen as a model hydrogenation reaction). All the other surface hydrides, however, play an indirect but fundamental role, since they maintain the Pt nanoparticles H-solvated, and hence electronically and morphologically stable during the reaction, avoiding the occurrence of deactivation processes.

From a more general point of view, the data shown in this work clearly reveal how the catalytic phenomena occurring at metal nanoparticles arise from a delicate balance of electronic, geometric, and surface properties. Understanding how to optimize all these features is of extreme importance to design increasingly performing catalysts, but it requires the concerted application of several complementary characterization techniques. In this respect, we wish to emphasize that each technique employed in this work, if taken as a single measurement, cannot lead to a complete picture of the whole problem. For example, XAS spectroscopy is not able to distinguish the surface Pt-hydride species directly involved in catalysis, while FT-IR and INS spectroscopies detect only a fraction of the surface Pt-H species and are unable to determine the structure and morphology of the Pt nanoparticles.

AUTHOR INFORMATION

Corresponding Author

*E-mail: elena.groppo@unito.it.

ORCID

Andrea Lazzarini: 0000-0002-0404-6597

Sara Morandi: 0000-0003-0577-7911

Maela Manzoli: 0000-0002-4427-7939

Kirill A. Lomachenko: 0000-0003-0238-1719

Monica Jimenez Ruiz: 0000-0002-9856-807X

Carlo Lamberti: 0000-0001-8004-2312

Andrea Piovano: 0000-0002-5005-6307

Elena Groppo: 0000-0003-4153-5709

Notes

The authors declare no competing financial interest.

REFERENCES

- (1) Blaser, H.-U.; Schnyder, A.; Steiner, H.; Roessler, F.; Baumeister, P., Selective hydrogenation of functionalized hydrocarbons. In *Handbook of Heterogeneous Catalysis*, 2nd ed., Ertl, G.; Knoezinger, H.; Schuth, F.; Weitkamp, J., Eds.; Wiley-VCH Verlag GmbH & Co. KGaA, 2008; Vol. 1, pp 3284–3308.
- (2) Ertl, G.; Knoezinger, H., Eds. *Handbook of Heterogeneous Catalysis*; Wiley-VCH, 1997; Vol. 5.
- (3) Nishimura, S. *Handbook of Heterogeneous Catalytic Hydrogenation for Organic Synthesis*; Wiley, 2001.

- (4) Rylander, P. *Catalytic Hydrogenation in Organic Syntheses*; Academic Press, 1979.

- (5) Che, M. Nobel Prize in chemistry 1912 to Sabatier: Organic chemistry or catalysis? *Catal. Today* **2013**, 218–219, 162–171.

- (6) Zecchina, A.; Califano, S. Chapter 1 - From the Onset to the First Large-Scale Industrial Processes. In *The Development of Catalysis: A History of Key Processes and Personas in Catalytic Science and Technology*; John Wiley & Sons, 2017; pp 1–57.

- (7) Andrews, L.; Wang, X.; Manceron, L. Infrared spectra and density functional calculations of platinum hydrides. *J. Chem. Phys.* **2001**, 114, 1559–1566.

- (8) Mueller, W. M.; Blackledge, J. P.; Libowitz, G. G. *Metal Hydrides*; Academic, 1968.

- (9) Beale, A. M.; Sankar, G. Following the structural changes in iron phosphate catalysts by in situ combined XRD/QuEXAFS technique. *J. Mater. Chem.* **2002**, 12, 3064–3072.

- (10) Brueckner, A. Simultaneous combination of in situ-EPR/UV-VIS/on line GC: a novel setup for investigating transition metal oxide catalysts under working conditions. *Chem. Commun. (Cambridge, U. K.)* **2001**, 2122–2123.

- (11) Frenkel, A. I.; Small, M. W.; Smith, J. G.; Nuzzo, R. G.; Kvashnina, K. O.; Tromp, M. An in Situ Study of Bond Strains in 1 nm Pt Catalysts and Their Sensitivities to Cluster-Support and Cluster-Adsorbate Interactions. *J. Phys. Chem. C* **2013**, 117, 23286–23294.

- (12) Grunwaldt, J.-D.; Clausen, B. S. Combining XRD and EXAFS with on-Line Catalytic Studies for in situ Characterization of Catalysts. *Top. Catal.* **2002**, 18, 37–43.

- (13) Marinkovic, N. S.; Wang, Q.; Frenkel, A. I. In situ diffuse reflectance IR spectroscopy and X-ray absorption spectroscopy for fast catalytic processes. *J. Synchrotron Radiat.* **2011**, 18, 447–455.

- (14) Newton, M. A.; Jyoti, B.; Dent, A. J.; Fiddy, S. G.; Evans, J. Synchronous, time resolved, diffuse reflectance FT-IR, energy dispersive EXAFS (EDE) and mass spectrometric investigation of the behaviour of Rh catalysts during NO reduction by CO. *Chem. Commun. (Cambridge, U. K.)* **2004**, 2382–2383.

- (15) Small, M. W.; Sanchez, S. I.; Marinkovic, N. S.; Frenkel, A. I.; Nuzzo, R. G. Influence of Adsorbates on the Electronic Structure, Bond Strain, and Thermal Properties of an Alumina-Supported Pt Catalyst. *ACS Nano* **2012**, 6, 5583–5595.

- (16) Agostini, G.; Pellegrini, R.; Leofanti, G.; Bertinetti, L.; Bertarone, S.; Groppo, E.; Zecchina, A.; Lamberti, C. Determination of the Particle Size, Available Surface Area, and Nature of Exposed Sites for Silica-Alumina-Supported Pd Nanoparticles: A Multi-technical Approach. *J. Phys. Chem. C* **2009**, 113, 10485–10492.

- (17) Arrigo, R.; Badmus, K.; Baletto, F.; Boeije, M.; Bowker, M.; Brinkert, K.; Bugaev, A.; Bukhtiyarov, V.; Carosso, M.; Catlow, R.; Chanerika, R.; Davies, P. R.; Dononelli, W.; Freund, H. J.; Friend, C.; Gallarati, S.; Gates, B.; Genest, A.; Gibson, E. K.; Hargreaves, J.; Helveg, S.; Huang, H.; Hutchings, G.; Irvine, N.; Johnston, R.; Lai, S.; Lamberti, C.; Macginley, J.; Marchant, D.; Murayama, T.; Nome, R.; Odarchenko, Y.; Quinson, J.; Rogers, S.; Russell, A.; Said, S.; Sermon, P.; Shah, P.; Simoncelli, S.; Soulantica, K.; Spolaore, F.; Tooze, B.; Torrente-Murciano, L.; Trunschke, A.; Willock, D.; Zhang, J. The challenges of characterising nanoparticulate catalysts: General discussion. *Faraday Discuss.* **2018**, 208, 339–394.

- (18) Wang, L.-L.; Johnson, D. D. Shear Instabilities in Metallic Nanoparticles: Hydrogen-Stabilized Structure of Pt37 on Carbon. *J. Am. Chem. Soc.* **2007**, 129, 3658–3664.

- (19) Mager-Maury, C.; Bonnard, G.; Chizallet, C.; Sautet, P.; Raybaud, P. H₂-induced reconstruction of supported Pt clusters: metal-support interaction versus surface hydride. *ChemCatChem* **2011**, 3, 200–207.

- (20) Alexeev, O. S.; Li, F.; Amiridis, M. D.; Gates, B. C. Effects of Adsorbates on Supported Platinum and Iridium Clusters: Characterization in Reactive Atmospheres and during Alkene Hydrogenation Catalysis by X-ray Absorption Spectroscopy. *J. Phys. Chem. B* **2005**, 109, 2338–2349.

- (21) Kang, J. H.; Menard, L. D.; Nuzzo, R. G.; Frenkel, A. I. Unusual Non-Bulk Properties in Nanoscale Materials: Thermal Metal-Metal Bond Contraction of γ -Alumina-Supported Pt Catalysts. *J. Am. Chem. Soc.* **2006**, *128*, 12068–12069.
- (22) Bus, E.; van Bokhoven, J. A. Hydrogen chemisorption on supported platinum, gold, and platinum-gold-alloy catalysts. *Phys. Chem. Chem. Phys.* **2007**, *9*, 2894–2902.
- (23) Bus, E.; Miller, J. T.; Kropf, A. J.; Prins, R.; van Bokhoven, J. A. Analysis of in situ EXAFS data of supported metal catalysts using the third and fourth cumulant. *Phys. Chem. Chem. Phys.* **2006**, *8*, 3248–3258.
- (24) Bus, E.; Miller, J. T.; van Bokhoven, J. A. Hydrogen chemisorption on Al₂O₃-supported gold catalysts. *J. Phys. Chem. B* **2005**, *109*, 14581–14587.
- (25) Li, L.; Wang, L.-L.; Johnson, D. D.; Zhang, Z.; Sanchez, S. I.; Kang, J. H.; Nuzzo, R. G.; Wang, Q.; Frenkel, A. I.; Li, J.; Ciston, J.; Stach, E. A.; Yang, J. C. Noncrystalline-to-Crystalline Transformations in Pt Nanoparticles. *J. Am. Chem. Soc.* **2013**, *135*, 13062–13072.
- (26) Sanchez, S. I.; Menard, L. D.; Bram, A.; Kang, J. H.; Small, M. W.; Nuzzo, R. G.; Frenkel, A. I. The Emergence of Nonbulk Properties in Supported Metal Clusters: Negative Thermal Expansion and Atomic Disorder in Pt Nanoclusters Supported on γ -Al₂O₃. *J. Am. Chem. Soc.* **2009**, *131*, 7040–7054.
- (27) Lytle, F. W.; Wei, P. S. P.; Gregor, R. B.; Via, G. H.; Sinfelt, J. H. Effect of chemical environment on magnitude of x-ray absorption resonance at LIII edges. Studies on metallic elements, compounds, and catalysts. *J. Chem. Phys.* **1979**, *70*, 4849–4855.
- (28) Vaarkamp, M.; Miller, J. T.; Modica, F. S.; Koningsberger, D. C. On the relation between particle morphology, structure of the metal-support interface, and catalytic properties of Pt/ γ -Al₂O₃. *J. Catal.* **1996**, *163*, 294–305.
- (29) Reifsnnyder, S. N.; Otten, M. M.; Sayers, D. E.; Lamb, H. H. Hydrogen Chemisorption on Silica-Supported Pt Clusters: In Situ X-ray Absorption Spectroscopy. *J. Phys. Chem. B* **1997**, *101*, 4972–4977.
- (30) Ramaker, D. E.; Mojet, B. L.; Garriga Oostenbrink, M. T.; Miller, J. T.; Koningsberger, D. C. Contribution of shape resonance and Pt-H EXAFS in the Pt L_{2,3} X-ray absorption edges of supported Pt particles: Application and consequences for catalyst characterization. *Phys. Chem. Chem. Phys.* **1999**, *1*, 2293–2302.
- (31) Ankudinov, A. L.; Rehr, J. J.; Low, J. J.; Bare, S. R. Theoretical interpretation of XAFS and XANES in Pt clusters. *Top. Catal.* **2002**, *18*, 3–7.
- (32) Ankudinov, A. L.; Rehr, J. J.; Low, J. J.; Bare, S. R. Effect of hydrogen adsorption on the x-ray absorption spectra of small Pt clusters. Reply to Comment. *Phys. Rev. Lett.* **2002**, *89*, 139702–139701.
- (33) Koningsberger, D. C.; Oudenhuijzen, M. K.; De Graaf, J.; Van Bokhoven, J. A.; Ramaker, D. E. In situ X-ray absorption spectroscopy as a unique tool for obtaining information on hydrogen binding sites and electronic structure of supported Pt catalysts: towards an understanding of the compensation relation in alkane hydrogenolysis. *J. Catal.* **2003**, *216*, 178–191.
- (34) Teliska, M.; O'Grady, W. E.; Ramaker, D. E. Determination of H Adsorption Sites on Pt/C Electrodes in HClO₄ from Pt L_{2,3} X-ray Absorption Spectroscopy. *J. Phys. Chem. B* **2004**, *108*, 2333–2344.
- (35) Oudenhuijzen, M. K.; Van Bokhoven, J. A.; Miller, J. T.; Ramaker, D. E.; Koningsberger, D. C. Three-Site Model for Hydrogen Adsorption on Supported Platinum Particles: Influence of Support Ionicity and Particle Size on the Hydrogen Coverage. *J. Am. Chem. Soc.* **2005**, *127*, 1530–1540.
- (36) Asakura, K.; Kubota, T.; Ichikuni, N.; Iwasawa, Y. A new characterization method for adsorbed hydrogen on supported Pt particles. *Stud. Surf. Sci. Catal.* **1996**, *101*, 911–919.
- (37) Ichikuni, N.; Iwasawa, Y. In situ d electron density of platinum particles on supports by XANES. *Catal. Lett.* **1993**, *20*, 87–95.
- (38) Kubota, T.; Asakura, K.; Ichikuni, N.; Iwasawa, Y. A new method for quantitative characterization of adsorbed hydrogen on Pt particles by means of Pt L-edge XANES. *Chem. Phys. Lett.* **1996**, *256*, 445–448.
- (39) Mansour, A. N.; Cook, J. W., Jr.; Sayers, D. E. Quantitative technique for the determination of the number of unoccupied d-electron states in a platinum catalyst using the L_{2,3} x-ray absorption edge spectra. *J. Phys. Chem.* **1984**, *88*, 2330–2334.
- (40) Mojet, B. L.; Miller, J. T.; Ramaker, D. E.; Koningsberger, D. C. A New Model Describing the Metal-Support Interaction in Noble Metal Catalysts. *J. Catal.* **1999**, *186*, 373–386.
- (41) Samant, M. G.; Boudart, M. Support effects on electronic structure of platinum clusters in Y zeolite. *J. Phys. Chem.* **1991**, *95*, 4070–4074.
- (42) Watari, N.; Ohnishi, S. Electronic structure of H adsorbed on Pt₁₃ clusters. *J. Chem. Phys.* **1997**, *106*, 7531–7540.
- (43) Ramaker, D. E., Novel XAS Techniques for Probing Fuel Cells and Batteries. In *X-Ray Absorption and X-Ray Emission Spectroscopy: Theory and Applications*, van Bokhoven, J. A.; Lamberti, C., Eds.; John Wiley & Sons: Chichester (UK), 2016; pp 485–522.
- (44) Tsuchiya, S.; Amenomiya, Y.; Cvetanovic, R. J. Study of metal catalysts by temperature programmed desorption. II. Chemisorption of hydrogen on platinum. *J. Catal.* **1970**, *19*, 245–255.
- (45) Dixon, L. T.; Barth, R.; Kokes, R. J.; Gryder, J. W. Hydrogen adsorption by alumina-supported platinum. *J. Catal.* **1975**, *37*, 376–382.
- (46) Miller, J. T.; Meyers, B. L.; Modica, F. S.; Lane, G. S.; Vaarkamp, M.; Koningsberger, D. C. Hydrogen temperature-programmed desorption (H₂ TPD) of supported platinum catalysts. *J. Catal.* **1993**, *143*, 395–408.
- (47) Pliskin, W. A.; Eischens, R. P. Infrared spectra of hydrogen and deuterium chemisorbed on platinum. *Z. Phys. Chem. (Muenchen, Ger.)* **1960**, *24*, 11–23.
- (48) Eley, D. D.; Moran, D. M.; Rochester, C. H. Infrared study of interaction between hydrogen and supported platinum catalysts. *Trans. Faraday Soc.* **1968**, *64*, 2168–2180.
- (49) Primet, M.; Basset, J. M.; Mathieu, M. V.; Prettre, M. Infrared investigation of hydrogen adsorption on alumina-supported platinum. *J. Catal.* **1973**, *28*, 368–375.
- (50) Dixon, L. T.; Barth, R.; Gryder, J. W. Infrared active species of hydrogen adsorbed by alumina-supported platinum. *J. Catal.* **1975**, *37*, 368–375.
- (51) Candy, J. P.; Fouilloux, P.; Primet, M. Hydrogen adsorption between 300 and 873 K on a platinum/magnesium oxide catalyst. *Surf. Sci.* **1978**, *72*, 167–176.
- (52) Szilagyi, T. Fourier-transform infrared study of weak adsorption of hydrogen on platinum/silica. *J. Catal.* **1990**, *121*, 223–227.
- (53) Mitchell, P. C. H.; Parker, S. F.; Ramirez-Cuesta, A. J.; Tomkinson, J. *Vibrational Spectroscopy With Neutrons, With Applications in Chemistry, Biology, Materials Science and Catalysis*; World Scientific: Singapore, 2005.
- (54) Albers, P.; Auer, E.; Ruth, K.; Parker, S. F. Inelastic Neutron Scattering Investigation of the Nature of Surface Sites Occupied by Hydrogen on Highly Dispersed Platinum on Commercial Carbon Black Supports. *J. Catal.* **2000**, *196*, 174–179.
- (55) Albers, P. W.; Krauter, J. G. E.; Ross, D. K.; Heidenreich, R. G.; Koehler, K.; Parker, S. F. Identification of Surface States on Finely Divided Supported Palladium Catalysts by Means of Inelastic Incoherent Neutron Scattering. *Langmuir* **2004**, *20*, 8254–8260.
- (56) Albers, P. W.; Lopez, M.; SEXTL, G.; Jeske, G.; Parker, S. F. Inelastic neutron scattering investigation on the site occupation of atomic hydrogen on platinum particles of different size. *J. Catal.* **2004**, *223*, 44–53.
- (57) Parker, S. F.; Frost, C. D.; Telling, M.; Albers, P.; Lopez, M.; Seitz, K. Characterisation of the adsorption sites of hydrogen on Pt/C fuel cell catalysts. *Catal. Today* **2006**, *114*, 418–421.
- (58) Carosso, M.; Lazzarini, A.; Piovano, A.; Pellegrini, R.; Morandi, S.; Manzoli, M.; Vitillo, J. G.; Ruiz, M. J.; Lamberti, C.; Groppo, E. Looking for the active hydrogen species in a 5 wt% Pt/C catalyst: a challenge for inelastic neutron scattering. *Faraday Discuss.* **2018**, *208*, 227–242.
- (59) Kaprielova, K. M.; Yakovina, O. A.; Ovchinnikov, I. I.; Koscheev, S. V.; Lisitsyn, A. S. Preparation of platinum-on-carbon

catalysts via hydrolytic deposition: Factors influencing the deposition and catalytic properties. *Appl. Catal., A* **2012**, *449*, 203–214.

(60) Piovano, A.; Agostini, G.; Carosso, M.; Groppo, E.; Jimenez Ruiz, M.; Lamberti, C.; Lazzarini, A.; Manzoli, M.; Morandi, S.; Pellegrini, R.; Vottero, E. *Study of the Pt-hydride formation and spillover effect on Pt/Al₂O₃ and Pt/C catalysts*; 2016; DOI: 10.5291/ILL-DATA.7-05-466.

(61) Mathon, O.; Beteva, A.; Borrel, J.; Bugnazet, D.; Gatla, S.; Hino, R.; Kantor, I.; Mairs, T.; Munoz, M.; Pasternak, S.; Perrin, F.; Pascarelli, S. The time-resolved and extreme conditions XAS (Texas) facility at the European Synchrotron Radiation Facility: The general-purpose EXAFS bending-magnet beamline BM23. *J. Synchrotron Radiat.* **2015**, *22*, 1548–1554.

(62) Agostini, G.; Meira, D.; Monte, M.; Vitoux, H.; Iglesias-Juez, A.; Fernandez-Garcia, M.; Mathon, O.; Meunier, F.; Berruyer, G.; Perrin, F.; Pasternak, S.; Mairs, T.; Pascarelli, S.; Gorges, B. XAS/DRIFTS/MS spectroscopy for time-resolved operando investigations at high temperature. *J. Synchrotron Radiat.* **2018**, *25*, 1745–1752.

(63) Newville, M. IFEFFIT: interactive XAFS analysis and FEFF fitting. *J. Synchrotron Radiat.* **2001**, *8*, 322–324.

(64) Ravel, B.; Newville, M. ATHENA, ARTEMIS, HEPHAESTUS: data analysis for X-ray absorption spectroscopy using IFEFFIT. *J. Synchrotron Radiat.* **2005**, *12*, 537–541.

(65) Zabinsky, S. I.; Rehr, J. J.; Ankudinov, A.; Albers, R. C.; Eller, M. J. Multiple-Scattering Calculations of X-Ray-Absorption Spectra. *Phys. Rev. B: Condens. Matter Mater. Phys.* **1995**, *52*, 2995–3009.

(66) Benson, J. E.; Boudart, M. Hydrogen-oxygen titration method for the measurement of supported platinum surface areas. *J. Catal.* **1965**, *4*, 704–710.

(67) McInroy, A. R.; Lundie, D. T.; Winfield, J. M.; Dudman, C. C.; Jones, P.; Parker, S. F.; Lennon, D. The interaction of alumina with HCl: An infrared spectroscopy, temperature-programmed desorption and inelastic neutron scattering study. *Catal. Today* **2006**, *114*, 403–411.

(68) Kolesnikov, A. I.; Antonov, V. E.; Bashkin, I. O.; Grosse, G.; Moravsky, A. P.; Muzychka, A. Y.; Ponyatovsky, E. G.; Wagner, F. E. Neutron spectroscopy of C60 fullerene hydrogenated under high pressure; evidence for interstitial molecular hydrogen. *J. Phys.: Condens. Matter* **1997**, *9*, 2831–2838.

(69) Renouprez, A. J.; Jobic, H. Neutron scattering study of hydrogen adsorption on platinum catalysts. *J. Catal.* **1988**, *113*, 509–516.

(70) Paleček, D.; Tek, G.; Lan, J.; Iannuzzi, M.; Hamm, P. Characterization of the Platinum–Hydrogen Bond by Surface-Sensitive Time-Resolved Infrared Spectroscopy. *J. Phys. Chem. Lett.* **2018**, *9*, 1254–1259.

(71) Delley, B.; Ellis, D. E.; Freeman, A. J.; Baerends, E. J.; Post, D. Binding energy and electronic structure of small copper particles. *Phys. Rev. B: Condens. Matter Mater. Phys.* **1983**, *27*, 2132–2144.

(72) Agostini, G.; Piovano, A.; Bertinetti, L.; Pellegrini, R.; Leofanti, G.; Groppo, E.; Lamberti, C. Effect of different face centered cubic nanoparticle distributions on particle size and surface area determination: A theoretical study. *J. Phys. Chem. C* **2014**, *118*, 4085–4094.

(73) Montejano-Carrizales, J. M.; Aguilera-Granja, F.; Moran-Lopez, J. L. Direct enumeration of the geometrical characteristics of clusters. *Nanostruct. Mater.* **1997**, *8*, 269–287.

Inelastic Neutron Scattering Investigation of MgCl₂ Nanoparticle-Based Ziegler–Natta Catalysts for Olefin Polymerization

Maddalena D'Amore,* Alessandro Piovano, Eleonora Vottero, Andrea Piovano, Svemir Rudić, Alessandro Erba, Elena Groppo, and Bartolomeo Civalieri



Cite This: <https://dx.doi.org/10.1021/acsanm.0c02296>



Read Online

ACCESS |



Metrics & More



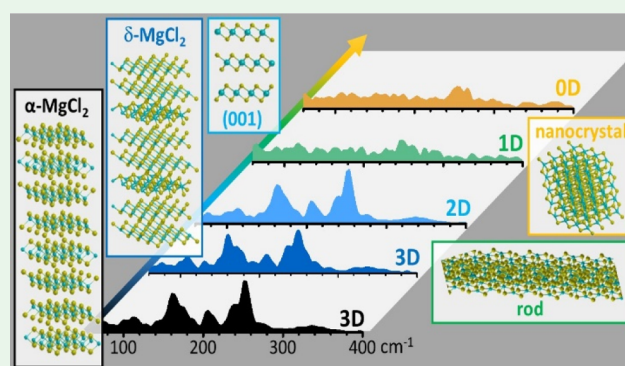
Article Recommendations



Supporting Information

ABSTRACT: The effect of nanosize and structural disorder on the MgCl₂ support of Ziegler–Natta catalysts has been investigated in terms of induced changes to their vibrational spectroscopic fingerprint. In particular, the inelastic neutron scattering (INS) technique was used, which allowed sampling of the whole lattice dynamics of the support. The experimental INS spectra of several ball-milled, polycrystalline, samples of MgCl₂ were collected for the first time and were compared to simulated spectra from quantum-mechanical density functional theory calculations. Theoretical calculations were performed on a variety of MgCl₂ structural models: (i) ordered and disordered bulk (3D); (ii) low-dimensional structures such as surfaces (2D) and nanorods (1D); and nanoclusters (0D). This allowed us to link specific features of the spectra to specific changes in the atomic structure and dynamics of the catalyst support. In particular, the effect of translational symmetry breaking and rotational disorder is discussed. Furthermore, the present data suggest that the ball-milling process mostly leads to the formation of bulk-like crystallites rather than nanoparticles. This work ultimately highlights the combined use of INS measurements and quantum-mechanical simulations as an effective approach for the atomistic characterization of defective (nano)materials.

KEYWORDS: inelastic neutron scattering, phonon dispersion, quantum mechanical simulations, nanostructuring, heterogeneous catalysts, inelastic neutron scattering, phonon dispersion, QM simulations, nanostructuring in catalysis, MgCl₂



1. INTRODUCTION

The loss of long-range order (i.e., periodicity in at least one direction) in extended solids is a key feature that determines not only their intrinsic physical and chemical properties but also their relevance for optical, electronic, magnetic, and catalytic applications.^{1,2} Therefore, there is much interest in finding synthetic procedures that enable full control of the shape—and thus properties—of nano-objects (such as surfaces, rods, nanotubes, and nanocrystals).^{3,4} Despite the great impact that nanoparticles with controlled morphology had in many fields, it is still difficult to control, design, or even predict their shape.^{5–9}

The majority of industrial catalysts are constituted from high-surface-area supports with a nanosized active phase dispersed on top.¹⁰ The effect of the particle size on the performance of the catalyst has motivated extensive studies on the fundamental aspects governing crystal growth. The concept of a thermodynamic “equilibrium shape” of nanocrystals, originally formulated by Wulff,¹¹ has recently been complemented with the analysis of the kinetic growth rate of different facets and the kinetics of transformation of a “growth shape” into the “equilibrium shape” at a given temperature.^{12,13}

Another key factor that should be taken into account when referring to nanocatalysts is the effect of adsorbates, which may influence the relative stability of the catalyst nanoparticle-exposed surfaces and lead, depending on the experimental conditions, to their reconstruction.^{9,14–17} A number of advanced experimental techniques have been developed for the direct (transmission electron microscopy, and scanning tunneling microscopy) and indirect (X-ray-based methods such as small-angle X-ray scattering or X-ray absorption spectroscopy) characterization of the morphology of nanoparticles.^{15,18–21} Such developments progressively increased the resolution toward the atomic scale, thus fostering the development of experimental tools suitable for the characterization of nanocatalysts in the presence of adsorbates. However, in most cases, a full elucidation of the structure—

Received: August 24, 2020

Accepted: October 27, 2020



property relation of these systems requires a complementary quantum-mechanical description.

The nanosizing is not the only means to reduce the crystal periodicity. Disorder can have a similar effect. For example, the stacking faults commonly occur in crystals with close-packed lattices. For a regular cubic close-packed lattice, the stacking sequence of the layers is ABCABCABC. However, the stacking faults can be introduced, disrupting the stacking sequence (e.g., ABCABABC).²² Due to the typical low-energy barriers for the incorporation or removal of these atomic planes, these defects can be easily formed.

Nanosize and disorder are key features of many catalysts and, among others, of MgCl_2 -based Ziegler–Natta catalysts for olefin polymerization.^{22–24} These catalysts represent the industrial evolution of “violet” (α , γ , and δ) TiCl_3 polymorphs²⁵ for the production of isotactic polypropylene. In this context, we have recently performed a systematic study of a series of mechanically and chemically activated MgCl_2 nanosamples, aimed at analyzing their structure, type, and extent of disorder, size, and morphology.^{26,27} Quantum-mechanical simulations suggested that stacking faults in MgCl_2 have a vanishing thermodynamic cost.²⁷ The complementary use of powder X-ray diffraction (PXRD) and pair distribution function (PDF) analyses enabled the determination of the type and the extent of disorder.²⁶ Far-IR spectroscopy coupled with quantum-mechanical simulations and complemented by Fourier transform infrared spectroscopy of CO adsorbed at 100 K gave a comprehensive picture of the morphology of MgCl_2 nanoparticles and their surface properties.²⁷

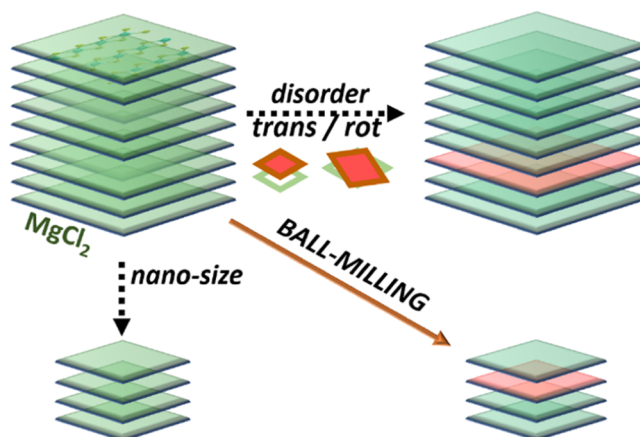
Herein, we extended that investigation by specifically looking at the lattice dynamics of MgCl_2 systems by means of inelastic neutron scattering (INS) spectroscopy, which is a valuable method to probe the motion of atoms within a material and hence understand the structural disorder of nanosized systems.

The system investigated in this work is quite simple in terms of chemical composition (pure MgCl_2) and synthesis method (ball-milling). Nevertheless, we have set up Scheme 1 that should help the reader in understanding the phenomena involved in the ball-milling process.

INS measurements do not limit the sampling to the Brillouin zone center—in contrast with other vibrational spectroscopies such as infrared and Raman—and they are not constrained by symmetry selection rules. This implies that all vibrational modes are allowed and in principle visible in an INS spectrum, provided that the neutron scattering cross-section of the species involved and the amplitude of motion of the atoms in the vibrational mode are sufficiently large. Neutrons deeply penetrate the matter for large distances before being scattered (or absorbed), so they “see” everything, and the spectra are representative of both the bulk and the surface of the materials. As a consequence, the phonon modes of nanocrystalline domains may be different from those of bulk since surface modes may be dominated by surface effects.²⁸

The ability of INS to detect such surface effects resides in the choice of high surface area materials where the ratio of atoms at the surface and in the bulk is large. Although INS has been adopted to investigate a variety of materials,²⁹ it has been often overlooked in the field of catalysis,³⁰ mainly as a consequence of the poor range of sensitivity of the first neutron instruments. Only recently, INS has started to be applied to catalysts in the presence of adsorbates. Examples

Scheme 1. Schematic Representation of the Synthesis Process for the MgCl_2 Investigated in This Work and of the Phenomena Involved^a



^aRed layers indicate the insertion of disorder (either translational or rotational).

include the investigation of Pd- or Pt-based catalysts in the presence of hydrogen,^{30–34} or the study of molecular mobility in zeolites.³⁵

Despite the relatively large total scattering cross-section of chlorine (16.8 b), which makes it a suitable target for INS, the investigation of systems like MgCl_2 with neutron spectroscopy remains scarce.³⁶ Going beyond the target of a simple identification of chemical species through INS, the present study aims to show the potential of INS in the characterization of nanosizing and disorder effects in MgCl_2 -based materials. The analysis of experimental INS data is complemented with a detailed theoretical characterization by means of quantum-mechanical calculations of several nanosized and disordered models, that help provide insights into the origin of the observed changes in the INS spectra.

2. METHODS

2.1. DFT Modeling. All calculations were performed with the help of the periodic quantum-mechanical CRYSTAL17 software.^{37–40} Calculations were performed by using the B3LYP functional⁴¹ augmented with a correction to include dispersion forces according to Grimme’s semiempirical DFT-D2^{42–44} approach with the empirical term refitted for crystalline systems.⁴⁵ TZVP quality basis sets have been employed for Mg atoms⁴⁶ and Cl atoms,⁴⁷ except for the outermost sp and d shells of Cl and Mg,⁴⁸ where the exponents have been adjusted at the values reported in a previous paper by some of us from energy minimization of the cubic packed MgCl_2 α -form unit cell.^{48,49}

Due to the size of the atomistic models investigated in the present work (vide infra), the massively parallel distributed data version of the code (MPPCrystal) has been employed, which features an excellent strong scaling due to the very high degree of parallelization of the code.^{40,50} A reduced required memory per core is also a valuable feature of the present code. Both these features are key for an effective quantum-mechanical investigation of large systems (containing several hundreds or thousands of atoms per cell), with little or no point-symmetry. Calculations were performed at the SuperMUC phase-1 (LRZ, Germany) HPC IBM iDataPlex machine powered by 16 Intel cores per node running at 2.7 GHz, with 2 GB/core and SCARF facilities at Rutherford Appleton Laboratories. The largest calculations were run on 1024 ÷ 2048 cores.

Pack–Monkhorst grids⁵¹ for sampling the reciprocal space were used. These consisted of at least 16 k points in the first Brillouin zone

(FBZ), depending on the examined system (further details are provided later on and in the Supporting Information section for each model system).

The truncation of the Coulomb and exchange infinite lattice series is controlled by five thresholds T_i (see CRYSTAL17 manual for more details), which have been set to 8 (T_1 – T_4) and 16 (T_5). The convergence threshold on energy for the self-consistent field procedure has been set to 10^{-8} Ha for structural optimization and to 10^{-13} Ha for vibration calculations. Full relaxation of internal coordinates and cell parameters has been carried out.

2.2. Vibrational Frequencies and Phonon Modes. Harmonic phonon frequencies ω_p at the Γ point (i.e., the center of the FBZ in the reciprocal space) were obtained from the diagonalization of the mass-weighted Hessian matrix of the second energy derivatives with respect to atomic displacements u by using algorithms implemented in the CRYSTAL program.^{52,53}

Sampling of phonon dispersion inside the FBZ is obtained by building and diagonalizing a set of dynamical matrices for a set of k points in the FBZ. A “direct space” approach^{54–57} is used here, which allows to build such dynamical matrices from a Fourier transform of the elements of direct space Hessian matrices computed within a supercell (SC) of the crystallographic cell. From the diagonalization of dynamical matrices, normal modes and corresponding vibrational frequencies are sampled over the FBZ.

Long-range electrostatic contributions to the force constants are accounted for by means of an approach presented by Wang and collaborators⁵⁸ in combination with Fourier interpolation. This mixed-space approach is implemented in CRYSTAL for 3D periodic systems and has been documented to provide accurate phonon dispersions and phonon density of states (PDOS) for systems of different symmetries.⁵⁸ For low-dimensional periodic systems (<3D), only a direct method has been applied involving the adoption of larger SCs to fully converge the long-range electrostatic terms. Systems under investigation have periodicity ranging from 3D to 0D, and both ordered and disordered 3D systems have been considered. For calculating the force constants in the real space, $3 \times 3 \times 3$, $3 \times 3 \times 4$, and $4 \times 4 \times 2$ SCs have been adopted for the ordered hexagonal cell of α -MgCl₂ and disordered bulk models, as reported by some of us in a previous paper.²⁷ To further check the numerical accuracy of our computational approach, test calculations were performed with different basis sets, Fourier and Wang⁵⁸ interpolation parameters on smaller $2 \times 2 \times 2$ SCs, and Heyd and Peintinger⁵⁹ basis set, along with a customized basis set (see Table S1 in the Supporting Information).

2.3. Simulation of the INS Spectra. Our data include both coherent and incoherent scattering from samples that are both polyatomic and polycrystalline. In the case of scattering from single crystals, the scattering vector Q has a definite orientation with respect to the reciprocal space of the single crystal, while in powder samples, the averaging over the various grains is equivalent to averaging over all orientations of the scattering vector. In the incoherent approximation,⁶⁰ it is proposed that the rotational averaging due to the powder nature of the sample cancels out correlations between distinct atoms. This approximation brings to the following formulation of the neutron scattering function

$$S_{\text{inc}}(Q, \omega) = \exp(-2\bar{W}(Q)) \frac{Q^2}{\hbar\omega} n + \frac{1}{2} \pm \frac{1}{2} \left[\sum_a \frac{\sigma_a^{\text{scatt}}}{2M_a} g_a(\omega) \right]$$

where $g_a(\omega)$ is the atomic partial density of state. With this, much simpler, expression we can transform our (Q, ω) data set into the PDOS, only supplying the mean-squared displacement and atomic composition. The neutron-weighted PDOS is the sum of the partial components of the density of states weighted by the scattering cross-section integrated over all Q . This may not find a complete correspondence with the experimental data obtained on the instrument where Q is limited to specific values, but the approximation generally does not sensibly modify the relative peak intensities and does not affect the difference spectra. The consistent

application of such an approximation to all simulated spectra may keep their quantitative comparison valuable.

A detailed treatment of neutron scattering for single crystal and polycrystalline samples can be found elsewhere.⁶¹

Neutron-weighted PDOS (NWPDOS) are here computed quantum-mechanically from the full phonon dispersion of the different models.^{62,63} The total PDOS is defined by the formula

$$g(\omega) = \frac{1}{V_{\text{BZ}}} \int_{\text{BZ}} \sum_{p=1}^{3N} \delta(\omega_{kp} - \omega) dk$$

where V_{BZ} is the volume of the Brillouin zone and N is the number of atoms per crystallographic cell, so that $\int g(\omega) d\omega = 3N$. This total density of states can be partitioned into atomic contributions: $g = \sum_a g_a(\omega) x_a$. For each atomic species, a present in the system with a fraction x_a , the corresponding contribution is

$$g_a(\omega) = \frac{1}{n_k} \sum_{p,k} |e_{p,k;a}|^2 \delta(\omega_{kp} - \omega)$$

where $e_{p,k;a}$ are the eigenvectors of the dynamical matrices.

A NWPDOS can be defined as⁶²

$$g^{\text{NW}}(\omega) = C \sum_a \frac{\sigma_a}{M_a} g_a(\omega) x_a$$

where C is a normalization factor to satisfy $\int g^{\text{NW}}(\omega) d\omega = 3N$, and where each atomic species is weighted by a factor that is the ratio of the corresponding scattering cross-section and mass.⁶⁴ A thermal correction to the computed NWPDOS is not applied because the comparison is performed with the experimental spectra recorded at 15 K.

Due to the different ratios σ_a/M_a for Mg and Cl of 0.15 and 0.39 b mol/g, respectively, the spectra are dominated by Cl atoms.

The normal modes are analyzed and those largely involving Cl atoms used to characterize the spectral features due to bulk, surfaces, and/or border atoms.

Finally, the energy resolution in the experimental measurements would affect the comparison with computed NWPDOSS shown in Section 3.3, hence similar to what can be done on $S(Q, \omega)$ by Mantid⁶⁵ for indirect-geometry instruments such as TOSCA, the simulated data were convolved with an experimental resolution function $f(\omega)$ of the form

$$f(\omega) = \frac{1}{\sqrt{2\sigma^2(\omega)\pi}} \exp\left(-\frac{1}{2} \frac{\omega^2}{\sigma^2(\omega)}\right)$$

where

$$\sigma(\omega) = A\omega^2 + B\omega + C$$

A , B , C being instrument-dependent constants.

2.4. Experimental Details. Three MgCl₂ samples characterized by increasing surface area were measured. A highly crystalline MgCl₂ sample was donated by Toho Titanium Co., Ltd. [MgCl₂ A, specific surface area (SSA): 9.3 m²/g]. MgCl₂ B and MgCl₂ C were obtained by planetary ball milling the initial highly crystalline MgCl₂ A sample for different times, resulting into SSA of 55 and 73 m² g⁻¹, respectively. The same three samples have been the subject of a detailed characterization in our previous works,^{26,27} ensuring high purity and good reproducibility. In particular, according to the structural analysis in ref 34, the average dimensions of MgCl₂ particles are 55 × 55 × 42 nm³ in A, 16 × 16 × 13 nm³ in B, and 13 × 13 × 8 nm³ in C.

The experimental INS spectra were recorded at 15 K using the TOSCA spectrometer at the ISIS spallation Neutron and Muon Source (Rutherford Appleton Laboratory, UK),^{32,66,67} with a $\Delta E/E$ resolution of 2%. The samples were inserted in a thin aluminum envelope and placed into In-wire sealed Al cells. All manipulations were performed inside a glovebox to prevent contamination by moisture. The cell was then inserted in a duplex CCR cryostat and cooled down. The INS signals from sample scattered neutrons were

recorded by detectors both in forward and in backward directions for about 10 h per sample, then they were extracted and combined using Mantid software.⁶⁵ The neutron beam area at the sample position is 45 mm × 45 mm, ensuring that the whole sample enclosed within aluminum envelope was measured. The spectra were normalized in relation to sample mass (ca. 7 g per sample) and incoming proton current (ca. 2000 μ A per sample) values, in order to allow a quantitative comparison.

3. RESULTS AND DISCUSSION

In the following, we will first discuss the experimental INS spectra of three MgCl₂ samples having a progressively increasing SSA. Then, the *ab initio* simulated INS spectra obtained for different MgCl₂ model systems will be presented, starting from the bulk and ordered α -MgCl₂ model and moving to models that account for disorder effects in the bulk and nanosizing effects (2D, 1D, and 0D models).

3.1. Experimental INS Spectra. Figure 1 shows the experimental INS spectra of MgCl₂ A, MgCl₂ B, and MgCl₂ C.

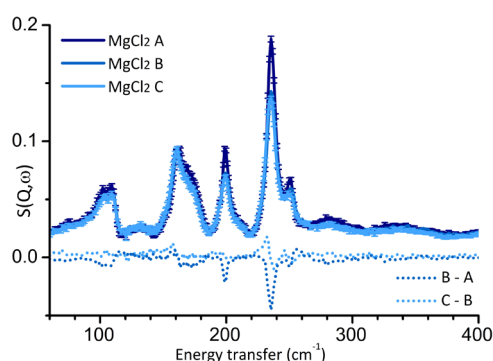


Figure 1. INS spectra of MgCl₂ A, MgCl₂ B, and MgCl₂ C samples and their differences. See the text for further details.

The three spectra have been normalized to the sample mass. In order to highlight the effect of ball milling on the spectral features, Figure 1 reports also the difference spectra [$\Delta S(Q,\omega)$] obtained by subtracting to the spectra of MgCl₂ B and MgCl₂ C by their respective preceding one in the series. The largest part of information in the plot of total $S(Q,\omega)$ versus energy transfer falls in the 60–400 cm^{-1} range, where several well-defined bands are observed at ~ 100 cm^{-1} (doublet), 162 cm^{-1} (with a shoulder at ~ 170 cm^{-1}), 200, 236, and 251 cm^{-1} .

At a first glance, INS spectra appear much richer in details than the corresponding far-IR spectra,²⁷ which are dominated by a very broad band centered at ~ 243 cm^{-1} , with a shoulder at 295 cm^{-1} and two weaker bands at ~ 370 and 410 cm^{-1} . Far-IR spectroscopy turned out to be sensitive to the morphology of the MgCl₂ nanoparticles (i.e., to the relative extent of the exposed surfaces), while quantum-mechanical simulation revealed that it was almost insensitive to the MgCl₂ disorder.²⁷ The unprecedented detail of our INS spectra, together with the newly performed simulations, will now permit to complement and extend our previous work shedding light on the disordering and nanostructuring effects.

All INS bands are sensitive to a different extent to the ball-milling time and either decrease in intensity or slightly shift in position (or both) by moving from MgCl₂ A to MgCl₂ C. The most affected bands are those at 200, 236, and 251 cm^{-1} , which decrease in intensity at longer ball-milling times. It is widely recognized^{22,23,26,68} that increasing the ball-milling time

brings about an increase in MgCl₂ disorder (introducing both stacking and rotational disorder), a decrease in the particle size and a change in the morphology (i.e., in the type and relative extent of the exposed surfaces). In order to understand which one of these three effects mainly affects the INS spectrum of MgCl₂, we carried out a comprehensive quantum-mechanical computational work.

3.2. Simulation of the INS Spectra: Atomistic Models and Approach. We considered various atomistic models of decreasing dimensionality (from 3D and 0D models) that mimic disorder and nanosizing effects. More in detail, by starting from the crystalline structure of α -MgCl₂, two types of disorder were simulated (Figure 2A), as already performed in

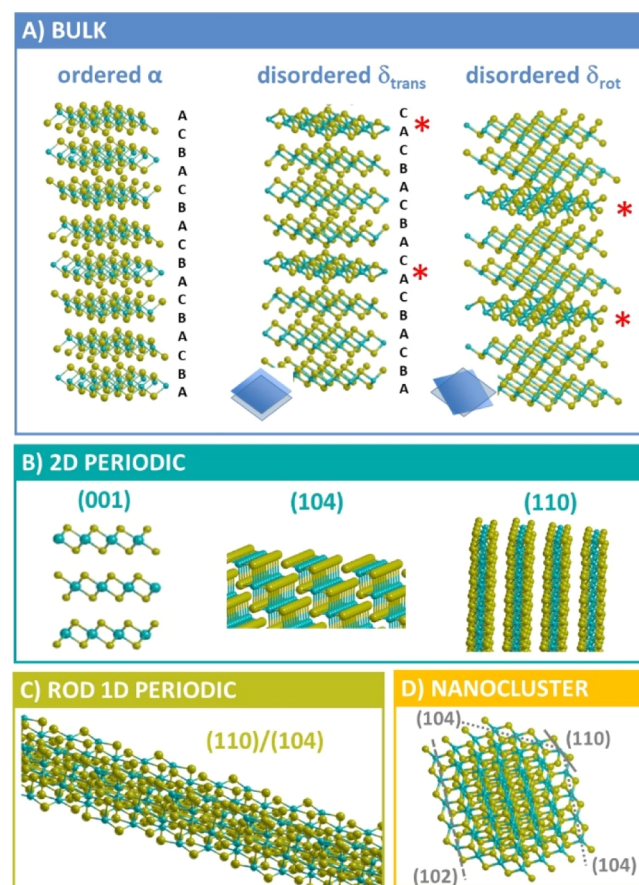


Figure 2. Ordered and disordered 3D models for MgCl₂ [panel (A)] as well as low-dimensionality models ranging from 2D to 0D adopted for simulating the INS spectra. In models of disordered δ forms, the faults have been indicated by red asterisks. Panel (B) reports main surfaces of interest in catalytic processes (110) and (104), together with the basal (001) surfaces, whereas in panel (C), a polymeric model (i.e., 104/110 rod) is reported. The nanocluster in panel (D) is obtained according to the Wulff polar plot, as already reported in reference.²⁷ All structures represent local topologies typical of polycrystalline MgCl₂ adopted in Ziegler–Natta catalysis.

our previous work:²⁷ (a) a translational stacking fault was simulated by alternating layers of α -MgCl₂ (which has a ABCABC sequence) with layers of β -MgCl₂ (having a ABABAB sequence), to create the δ_{trans} form;^{22,24,68} (b) a rotational disorder was simulated from α -MgCl₂ by a simple rotation of one layer of 60° around the *c*-axis, resulting into the δ_{rot} model. 2D systems were modeled as slabs of well-defined thickness, as described in previous papers by some of us.^{9,48,69}

Slab models were built to simulate MgCl_2 surfaces of interest for their role in Ziegler–Natta catalysts, namely the (104) and (110) faces, along with the ubiquitous basal (001) one (Figure 2B).

To model the presence of edges in nanosized catalysts, the (110)/(104) edge was also explored by creating a 1D infinite rod generated by intercepting the two faces (Figure 2C). Finally, a nanocrystal (formed by 240 atoms) having the crystalline structure of MgCl_2 but a finite size was also modeled (Figure 2D). The model was designed by cutting the $\alpha\text{-MgCl}_2$ crystal according to the Wulff polar plot predicted for $\alpha\text{-MgCl}_2$ on the basis of the Gibbs free energy of formation of surfaces (G_s). This nanocrystal represents a model for the most stable thermodynamic morphology at 298 K.³ The polyhedron has been obtained by cutting the crystal along the largest extended families of planes (104), (012), and (001) with further cuts along (110) planes that are supposed to be the theater of catalysis.

All model systems investigated in the present work are expected to be representative of typical local structures occurring in MgCl_2 adopted in Ziegler–Natta catalysis.

3.3. Prediction of INS Spectra for Ordered and Disordered Bulk MgCl_2 . The simulation of an INS spectrum for a crystalline material requires the calculation of the vibrational spectrum in reciprocal space points other than Γ from the Hessian matrix on a SC of the original primitive cell. To achieve well-converged neutron spectra that can be reliably compared to the experimental ones, we have to decide how much dense the reciprocal space sampling need to be. Such a convergence trend is analyzed in this work as a function of the number of k points used for integration in the reciprocal space. The method implies the construction of consistent SCs in each case. For this purpose, for ordered $\alpha\text{-MgCl}_2$ (the most stable polymorph of MgCl_2 at TPS), phonon dispersion calculations have been performed on SCs of increasing size, namely $2 \times 2 \times 2$ (72 atoms), $3 \times 3 \times 3$ (243 atoms), $3 \times 3 \times 4$ (324 atoms), and $4 \times 4 \times 2$ (288 atoms). Computational details are reported in Table S1 in the Supporting Information.

Figure 3 shows the NWPDOS for ordered $\alpha\text{-MgCl}_2$ simulated for different SCs of increasing dimensions, compared to the experimental INS spectrum of MgCl_2 B. With the only exception of the spectrum obtained for the smallest $2 \times 2 \times 2$ SC, which shows a much larger number of bands than the experimental one, the other models consistently describe the experimental scattering function in terms of number of bands

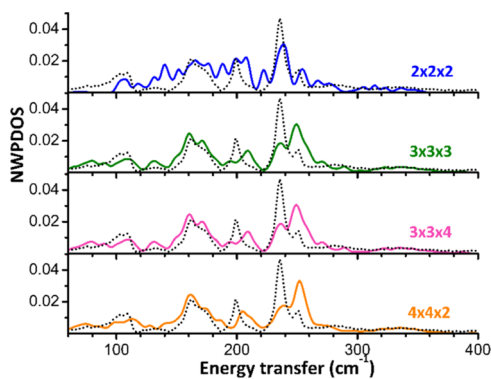


Figure 3. Neutron-weight corrected DOS (full lines) simulated for ordered bulk $\alpha\text{-MgCl}_2$ by means of SCs of increasing size, compared to the experimental INS spectrum of MgCl_2 B (dotted line).

and positions, while there are some discrepancies in terms of their relative intensities. In particular, the intensity of the band at 236 cm^{-1} is underestimated, while that of the band at 251 cm^{-1} is overestimated, resulting in an inversion in the relative intensity of the two bands with respect to the experimental spectrum. Higher order effects, such as contributions from second- and third-overtones, are negligible and do not affect the profile of the INS spectra in this region (see Figures S2–S4 in the Supporting Information). In contrast, the prediction of the stacking can be more relevant than expected, so that motion of the atoms might be influenced by the description of the weak interactions that take place among layers and might also suffer from the underestimation of the c cell parameter due to the adopted computational methodology.

The main bands observed in the experimental INS spectra are ascribed to the vibrational modes sketched in Figure 4, as follows.

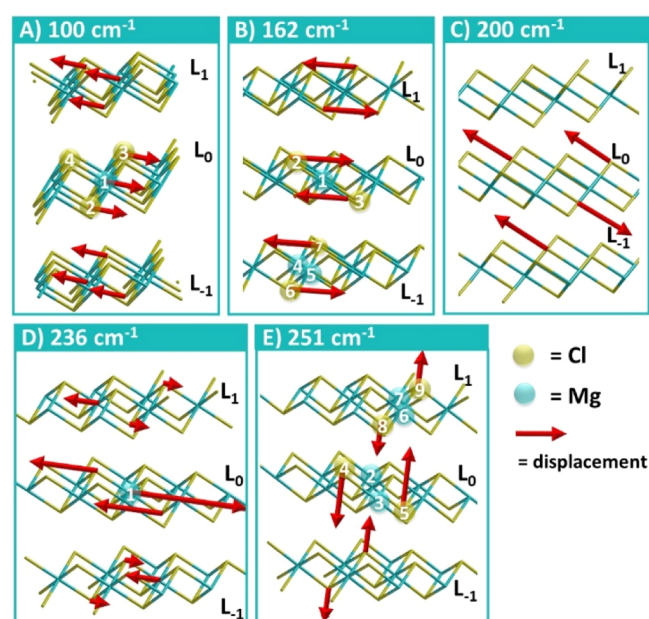


Figure 4. Graphical representation of normal modes associated to main phonon bands of ordered $\alpha\text{-MgCl}_2$. Mg atoms are represented in green, whereas chlorine atoms are shown in yellow; arrows showing direction of the atomic displacements (in red) have been added to help reader in visualizing the vibrational modes. The labels are explained in the text.

The doublet at $\sim 100\text{ cm}^{-1}$ (Figure 4A) is due to the “Raman active” displacement of the magnesium cation (Mg_1) in phase with two chlorine ligands (Cl_2 and Cl_3) along the b direction and to the analogous “IR active” vibrational mode. The atom displacements by breaking the axial $\text{Mg}-\text{Cl}$ bonds (i.e., Mg_1-Cl_4) would leave Mg ions binding four Cl ligands in the plane and would allow the creation of nanoribbons of MgCl_4 . The displacement of atoms in one layer (L_0) is opposite to that of the atoms belonging to adjacent layers (L_{-1} and L_1). The band arises when k points other than the Γ point are considered, and this explains why this band was not discussed in the paper of Brambilla et al., reporting the IR and Raman experimental vibrational frequencies of MgCl_2 .⁷⁰

The band at 162 cm^{-1} (Figure 4B) involves the intralayer deformation of four-membered $\text{Cl}-\text{Mg}-\text{Cl}-\text{Mg}$ rings with a stretching in the ab plane; to elaborate, in layer L_0 , an in-phase

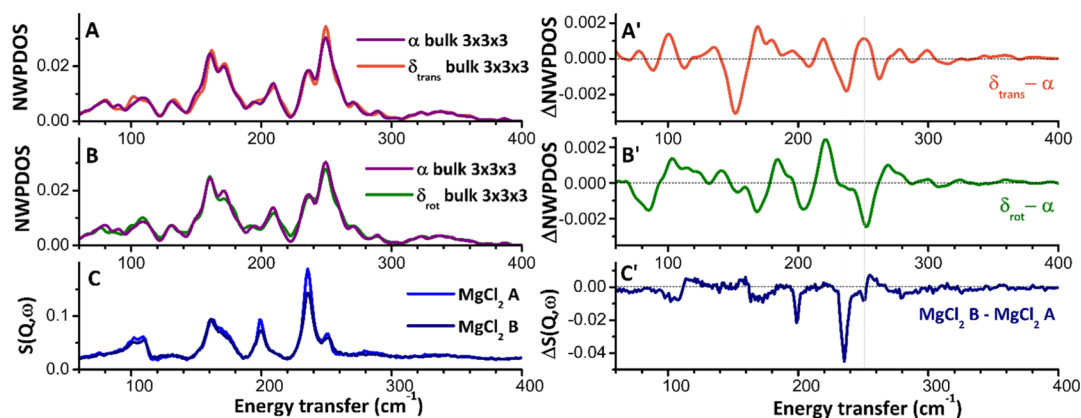


Figure 5. Neutron-weighted PDOS simulated for ordered bulk α -MgCl₂ and disordered δ_{trans} [part (A)] and δ_{rot} [part (B)] forms by means of $3 \times 3 \times 3$ SCs, compared to the experimental INS spectra of MgCl₂ A, MgCl₂ B, and MgCl₂ C [part (C)]. Difference simulated spectra Δ calculated by subtracting the spectrum of ordered bulk α -MgCl₂ to those of δ_{trans} [part (A')] and δ_{rot} [part (B')], compared to the difference experimental spectrum calculated by subtracting that of MgCl₂ A from that of MgCl₂ B and the spectrum of MgCl₂ B from MgCl₂ C [part (C')].

shortening of Mg₁–Cl₂ and Mg₁–Cl₃ bonds produces the rings' deformation, whereas in the adjacent layer L₋₁, a rotation around the Mg₄Mg₅ axis occurs with a deformation of the Cl–Mg–Cl–Mg ring in the *ab* plane. The vibrational modes of layers L₀, L₋₁, and L₁ are coupled together.

The phonon band at 200 cm⁻¹ (Figure 4C) is absent in Γ and arises from calculation of phonon dispersion. The mode is associated to the in-phase elongation of the Mg–Cl bonds in layer L₀ toward the interlayer region, coupled with a single Mg–Cl elongation occurring in the adjacent layer L₋₁.

The band at 236 cm⁻¹ (Figure 4D) is mainly due to the vibrational modes involving MgCl₆ moieties with a bulk hexacoordinated Mg²⁺ cation (i.e., Mg₁). Starting from the frame where magnesium and four chlorine atoms lie in the same plane, a pyramidalization at Mg₁ occurs with a consequent inversion of the MgCl₄ “umbrella” with Mg₁ atom passing again through the planar frame. Also, atoms of adjacent layers are involved albeit at a less significant extent. It turns out that these vibrational modes involve the movement of atoms of the inner layers of the SC model.

Finally, considering the axis formed by the axial chlorine ligands at hexacoordinated Mg atoms, the band at 251 cm⁻¹ (Figure 4E) is mainly due to the rotation of that axis with respect to the *ab* plane (i.e., the axis formed by Cl₄Cl₅ bound to Mg₁ into L₀ layer). A coupling with rotations of opposite chlorine atoms in Mg–Cl–Mg–Cl cycles in upper and lower layers is observed (i.e., a Cl₈Cl₉ axis in L₁ layer with respect to the *ab* plane). The tilting four-membered Mg–Cl–Mg–Cl ring, which is almost a ubiquitous topological “leit motiv” of halides of alkaline earths, is present in the bulk (intralayer) but is also part of the penta-coordinated surfaces. Hence, at a qualitative level, it is worth saying that this band might originate from the atomic vibrations of both inner and surface atoms (see the following section). The displacements here described cause the movement of chlorine atoms along the *c*-axis, that is parallel to the stacking direction.

Experiments reveal that the bands most affected by ball milling are those at 200 and 236 cm⁻¹, which decrease in intensity by about 25% from MgCl₂ A to MgCl₂ B and still slightly more from MgCl₂ B to MgCl₂ C, and the band at 251 cm⁻¹, which gradually reduces in intensity by about 10% at each step. The band at 162 cm⁻¹, instead, slightly shifts downward.

To elucidate the origin of these changes in the experimental INS spectra, the effect of disorder of bulk MgCl₂ was investigated. Figure 5 shows the neutron-weighted DOS simulated for the δ_{trans} (Figure 5A) and δ_{rot} (Figure 5B) models, compared to that of ordered α -MgCl₂. The experimental spectra are also reported as references (Figure 5C). The INS spectra of the disordered models are quite similar to that of the ordered one. To better appreciate the small changes, difference spectra $\delta_{\text{trans}} - \alpha$ and $\delta_{\text{rot}} - \alpha$ are reported in Figure 5A',B', respectively. At a first inspection, it can be observed that the introduction of a stacking fault or of a rotational fault causes a variation in either the position or the intensity (or both) of all of the main bands. As far as the decrease in intensity is concerned, the Δ NWPDOS spectra are of the same order of magnitude of the experimental $\Delta S(Q, \omega)$ spectrum (Figure 5C'), corresponding to a maximum of 10% with respect to the intensity of the spectrum of ordered MgCl₂. Actually, none of the Δ NWPDOS spectra are able to reproduce the experimental $\Delta S(Q, \omega)$ spectrum. However, at a glance, some bands look more sensitive to the translational disorder while some others are more affected by the rotational one. The two bands most influenced by translational disorder are those at 162 cm⁻¹, which shifts upward, and that at 236 cm⁻¹, which decreases in intensity. Both bands are associated with vibrational modes involving atom displacements in the *ab* plane. Rotational disorder, instead, has a larger impact on the bands at 200 and 251 cm⁻¹, which decrease in intensity with respect to the spectrum of the bulk α phase. Both bands are ascribed to vibrational modes involving atom displacements along the *c*-axis.

By analogy, a description of the experimental $\Delta S(Q, \omega)$ spectra in terms of combination of translational and rotational disorder can be attempted. On the one hand, the decrease in intensity of the two bands at 200 and 251 cm⁻¹ that can be observed in both Figure 5C',B' may indicate the occurrence of some rotational disorder. On the other hand, the decrease in intensity of the band at 236 cm⁻¹ and the shift in position of the band at 162 cm⁻¹ suggest that ball milling (see Figure 5A',C') could also induce a certain degree of translational disorder. It is worth noticing that the direction of the shift for the band at 162 cm⁻¹ predicted by our δ_{trans} model is the opposite of that observed experimentally. However, this might be due to the fact that δ_{trans} contains a single stacking fault,

while in the real case, the number of stacking faults can be higher and/or a stacking fault can be adjacent to a rotational fault. Indeed, the mode at 162 cm^{-1} is associated to the displacement of atoms in three adjacent layers. There are some major fluctuations in Figure 5A',B' that cannot be seen in Figure 5C'. Those are likely due to some combination of defects of different types: rotational and translational ones but maybe also to some combination of disorder with surface effects (e.g., steps or edges). Figure 5C' reports the integral effect of both the rotational and translational disorder summed over many possible faults in stacking and combination of them while simulation refers to two possible models. Nevertheless, the global effect consists of a reduction/increase of intensity of some peaks but also the shift and broadening of bands that is the one close to 160 cm^{-1} is to some extent visible in both experimental and simulated difference spectra. The reproduction of the experimental $\Delta S(Q,\omega)$ spectrum would require the simulation of a very large number of models with a different percentage of stacking and rotational faults, which is clearly not possible. Overall, the data displayed in Figure 5 indicate that INS is sensitive to the introduction of both translational and rotational disorder in MgCl_2 bulk.

3.4. Prediction of INS Spectra for MgCl_2 Surfaces. It is worthy to recall that for polar compounds and ionic crystals, the long-range character of Coulomb interaction causes the force constants to remain large, even when the atoms are far away. For this reason, it is impossible to obtain a finer sampling of the reciprocal space just by means of Fourier interpolation, and a computational cheap solution is the Wang correction cited above for 3D systems.

Therefore, due to the ionic nature of MgCl_2 materials, for lower dimensionality systems as 2D and 1D models (surface/rods), where long-range electrostatic contributions to the force constants are accounted for through a direct approach, the slow decay of Coulomb interactions with atomic distances required the adoption of sufficiently large SCs to guarantee reliable (i.e., well-converged) scattering simulations. We checked convergence in results of scattering behavior of bidimensional lattices as a function of SC size, ending in the identification of 4×4 SCs as a provider of valuable prediction of the INS spectra. Accordingly, SCs of different sizes (i.e., 2×2 , 4×4 , 8×4 , and 8×8) have been adopted for phonon dispersion calculations. To provide a measure of the size of the SCs adopted as surface models, the (104) surfaces contain a number of atoms ranging from 192 [4×4] to 768 [8×8]. Further computational details are reported in Table S2 in the Supporting Information. It was found that 4×4 SCs provide reliable predictions of the INS spectra; more extended systems did not show any significant difference in simulated PDOS. It turns out that cell parameters corresponding to values close to the "critical dimension" of 12 \AA are large enough to guarantee converged results that is to obtain a valuable sampling of the reciprocal space and long-range effects.

For 2D models having a 4×4 SC, the simulated INS spectra are reported in Figure 6 and compared to the spectrum simulated for the ordered bulk $\alpha\text{-MgCl}_2$ ($4 \times 4 \times 2$ SC). The INS spectrum of the basal (001) surface almost coincides with that of the bulk. The simulated INS spectra for the (104) and (110) surfaces, instead, are less intense than that of the basal plane and characterized by a series of additional vibrational modes below 200 cm^{-1} . In the $220\text{--}260\text{ cm}^{-1}$ region, the spectrum of the (104) surface displays a band at $\sim 251\text{ cm}^{-1}$, whereas there are no significant contributions to the peak at

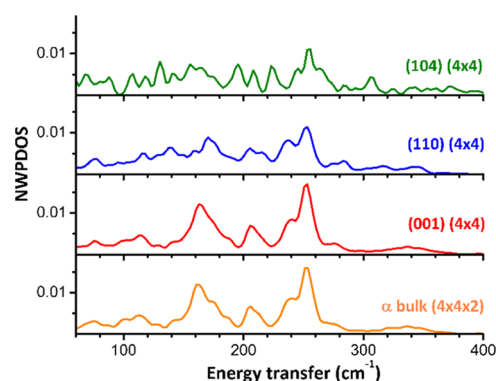


Figure 6. Neutron-weighted corrected DOS simulated for surfaces of $\alpha\text{-MgCl}_2$ of interest in catalysis [i.e. (104) and (110)] and the basal one [i.e. (001)], compared to that simulated for ordered bulk $\alpha\text{-MgCl}_2$.

$\sim 236\text{ cm}^{-1}$. The spectrum of the (110) surface shows both bands at 251 and 236 cm^{-1} , but they show a different relative intensity with respect to those of the (001) basal one.

Overall, according to the data reported in Figure 6, the (104) and (110) surfaces do not contribute to the INS spectrum of MgCl_2 with specific features different from those of the (001) basal one, but eventually only with a poorly defined and weak band in the $100\text{--}200\text{ cm}^{-1}$ region. This means that, for MgCl_2 particles with lateral sizes of approximately $10\text{--}15\text{ nm}$ whose morphology is dominated by the basal plane (like those obtained by ball milling), INS is not expected to provide information on the morphology of the particles (i.e., on the exposed surfaces). The scenario might change for smaller MgCl_2 particles approaching the size of ca. 1 nm , where the relative contribution of surfaces different from the basal one can be higher, especially in the presence of capping agents (as it happens for chemically activated Ziegler–Natta precatalysts).

3.5. Prediction of INS Spectra for 1D Periodic and 0D MgCl_2 Models. The presence of edges in nanosized MgCl_2 has been simulated by the (110)/(104) rod (Figure 2C). The corresponding INS spectrum is shown in Figure 7. The

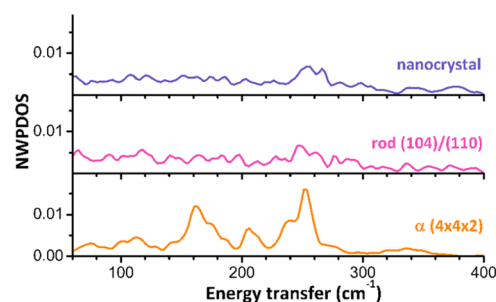


Figure 7. Neutron-weight corrected DOS simulated for $\alpha\text{-MgCl}_2$, a (110/104) rod, and a MgCl_2 nanocrystal.

intensity of the overall spectrum is even lower than that for the (104) and (110) surfaces and it is hard to identify distinctive features. Only two bands at 247 and 260 cm^{-1} slightly emerge from the continuum, which are shifted toward higher frequencies with respect to the two bands at 236 and 251 cm^{-1} dominating the spectrum of bulk MgCl_2 .

Finally, to investigate the effect of nanosizing on the INS spectrum of MgCl_2 , a nanocluster containing 240 atoms and

exposing surfaces according to the Wulff polyhedron predicted for MgCl_2 ^{3,26} has been cut out from the bulk. The simulated INS spectrum is also shown in Figure 7. Its overall intensity is comparable to that of the (104)/(110) rod, and also in this case, only two bands at 252 and 265 cm^{-1} clearly emerge from the continuum.

Overall, the data shown in Figure 7 clearly demonstrate that nanosizing of MgCl_2 (i.e., reduction of the particle size and increasing importance of edges) causes a drastic decrease in intensity of the overall INS spectrum, the disappearance of the features below 200 cm^{-1} characteristic for the bulk, and an upward shift of the features around 250 cm^{-1} . In other words, a key feature of nanosizing is the loss of all INS spectral features characteristic of MgCl_2 bulk and the rise of a couple of weak bands around 260 cm^{-1} , which have no direct relation with the surfaces terminating the crystal, but rather are connected with the vibrational properties of the edges.

4. CONCLUSIONS

The INS spectra of ball-milled MgCl_2 samples have been measured for the first time in order to investigate the disorder and nanosizing effects, which are relevant when MgCl_2 is used as a support for Ziegler–Natta catalysts. Indeed, CI shows a total scattering cross-section that makes it a suitable target for the INS and allows better understanding of atomic motion with respect to typical IR and Raman vibrational spectroscopies.

In order to assign the bands observed in the experimental spectra and deepen the understanding of structural disorder and nanosizing effects in these systems, the INS spectra have been simulated for 3D models containing stacking or rotational disorder and for models of decreasing dimensionality (from 2D to 0D models).

The experimental results have shown that the bands most affected by ball milling are those at 200, 236, and 251 cm^{-1} , which gradually reduce in intensity upon ball milling. These changes can be rationalized in terms of an increase in the structural disorder. In particular, according to the computed results and simulated INS spectra, the decrease in intensity of the bands at 200 and 251 cm^{-1} (which are assigned to the vibrational modes involving atom displacement along the *c*-axis) indicates the occurrence of some rotational disorder, while the decrease in intensity of the band at 236 cm^{-1} (which is assigned to the vibrational modes involving atom displacement in the *ab* plane) suggests that ball milling induces also a certain degree of translational disorder. This is clear evidence that the INS measurements are sensitive to the introduction of disorder in bulk MgCl_2 .

For 2D atomistic models, well-converged simulated PDOS are obtained for cell parameters corresponding to values close to 12 ÷ 15 Å. Notably, the INS spectrum of the basal (001) surface almost coincides with that of the bulk. Because MgCl_2 particles with lateral sizes of about 10–15 nm (like those obtained by ball milling) are dominated by the basal plane, INS is not expected to provide information on the morphology of the particles (i.e., on the exposed surfaces). This picture might change for MgCl_2 particles approaching the size of ca. 1 nm, where the relative contribution of surfaces different from the basal one can be higher, especially in the presence of adsorbates like in Ziegler–Natta precatalysts obtained with chemical activation methods. However, it is important to underline that our calculations performed on 1D and 0D models clearly indicate that a key feature of nanosizing is the

loss of the entire INS spectral features characteristic of MgCl_2 bulk.

In conclusion, our modeling provides a full rationale of the trends observed in the experimental INS spectra of samples of MgCl_2 with different degrees of ball milling. The ball-milling process leads mostly to the formation of bulk-like MgCl_2 crystallites rather than nanoparticles. The weak bonding among MgCl_2 layers allows for an easier cleavage along the stacking direction with the emergence of both rotational and translational disorder, which explains the decrease in intensity of some bands in the INS spectrum, while nanosizing effects are less evident.

We briefly underline some key features of INS spectroscopy as applied to MgCl_2 materials, in comparison to other vibrational spectroscopies and structural methods. Far-IR spectra were found to be sensitive to the morphology of the MgCl_2 nanoparticles, revealing the type and the relative extension of exposed surfaces, but almost insensitive to MgCl_2 disorder. A previous Raman study⁷⁰ did not even assign some peaks (i.e., $\sim 100 \text{ cm}^{-1}$). Beyond the field of spectroscopy, we proved in previous papers that the combination of PXRD, PDF, and relative simulation have the potential to provide information on the dimension and disorder of $\delta\text{-MgCl}_2$ in MgCl_2 -supported Ziegler–Natta catalysts. The results discussed in the present work demonstrate that INS mimics the X-ray ability to reveal different types of disorders, as well as surface/border effects for objects at the nanoscale.

In perspective, besides the interest in the field of Ziegler–Natta catalysis, the present work paves the route to the use of INS as a method for the characterization of materials with a certain degree of defectivity and shows the central role of quantum-mechanical simulations in a correct interpretation and valorization of the experimental INS spectra.

■ ASSOCIATED CONTENT

SI Supporting Information

The Supporting Information is available free of charge at <https://pubs.acs.org/doi/10.1021/acsnm.0c02296>.

Details on the adopted models; information on the adopted computational methodology and basis set effect; influence of overtones and higher-order effects on simulated INS spectrum of MgCl_2 ; neutron-weight-corrected DOS simulated for both α and β polymorph of MgCl_2 at 0 K (PDF)

■ AUTHOR INFORMATION

Corresponding Author

Maddalena D'Amore – Department of Chemistry and NIS Centre, University of Turin, 10125 Torino, Italy; DPI, 5600 AX Eindhoven, The Netherlands; orcid.org/0000-0002-4248-8767; Email: maddalena.damore@unito.it

Authors

Alessandro Piovano – Department of Chemistry and NIS Centre and INSTM, University of Turin, 10125 Torino, Italy; DPI, 5600 AX Eindhoven, The Netherlands; orcid.org/0000-0002-5784-6897

Eleonora Vottero – Department of Chemistry and NIS Centre and INSTM, University of Turin, 10125 Torino, Italy; Institut Laue-Langevin (ILL), 38042 Grenoble, France

Andrea Piovano – Institut Laue-Langevin (ILL), 38042 Grenoble, France; orcid.org/0000-0002-5005-6307

Svemir Rudić – ISIS Facility, Rutherford Appleton Laboratory, Didcot, Oxfordshire OX11 0QX, U.K.

Alessandro Erba – Department of Chemistry and NIS Centre, University of Turin, 10125 Torino, Italy; orcid.org/0000-0002-2986-4254

Elena Groppo – Department of Chemistry and NIS Centre and INSTM, University of Turin, 10125 Torino, Italy; orcid.org/0000-0003-4153-5709

Bartolomeo Civalieri – Department of Chemistry and NIS Centre and INSTM, University of Turin, 10125 Torino, Italy; orcid.org/0000-0003-3198-3161

Complete contact information is available at:
<https://pubs.acs.org/10.1021/acsnm.0c02296>

Author Contributions

The manuscript was written thanks to the contributions of all authors.

Notes

The authors declare no competing financial interest.

ACKNOWLEDGMENTS

We kindly acknowledge PRACE initiative for computing resources (Grant: Project 2016163997). ISIS Rutherford Appleton Laboratory UKRI, NScD Oak Ridge National Laboratory, European Spallation for experiments and SCARF Scientific Computing Department, STFC Rutherford Appleton Laboratory for computer facilities. The work of A.P. and E.G. forms part of the research program of DPI, project #802. Toru Wada, Gentoku Takasao, Ashutosh Thakur, Patchanee Chammingkwan, Minoru Terano, and Toshiaki Taniike are kindly acknowledged for useful discussions on structural disorder effects of investigated systems. We are grateful to Dr. Jeff Armstrong from the Science and Technology Facilities Council for careful reading of the manuscript.

REFERENCES

- (1) Behrens, M.; Studt, F.; Kasatkin, I.; Köhl, S.; Hävecker, M.; Abild-Pedersen, F.; Zander, S.; Girsdiess, F.; Kurr, P.; Knief, B.-L.; Tovar, M.; Fischer, R. W.; Norskov, J. K.; Schlögl, R. The Active Site of Methanol Synthesis over Cu/ZnO/Al₂O₃ Industrial Catalysts. *Science* **2012**, *336*, 893–897.
- (2) Zecchina, A.; Groppo, E.; Bordiga, S. Selective Catalysis and Nanoscience: An Inseparable Pair. *Chem.—Eur. J.* **2007**, *13*, 2440–2460.
- (3) D'Amore, M.; Causà, M. *Extracting NanoRods and NanoCrystals from Bulk*.
- (4) Evarestov, R. A. *Theoretical Modeling of Inorganic Nanostructures: Symmetry and Ab-Initio Calculations of Nanolayers, Nanotubes and Nanowires*; Springer-Verlag: Berlin Heidelberg, 2015.
- (5) *Catalysis and Electrocatalysis at Nanoparticle Surfaces*; Wieckowski, A., Savinova, E., Vayenas, C., Eds.; CRC Press, 2003.
- (6) Pal, M.; García Serrano, J.; Santiago, P.; Pal, U. Size-Controlled Synthesis of Spherical TiO₂ Nanoparticles: Morphology, Crystallization, and Phase Transition. *J. Phys. Chem. C* **2007**, *111*, 96–102.
- (7) Kawasaki, H. Surfactant-Free Solution-Based Synthesis of Metallic Nanoparticles toward Efficient Use of the Nanoparticles' Surfaces and Their Application in Catalysis and Chemo-/Biosensing. *Nanotechnol. Rev.* **2013**, *2*, 5–25.
- (8) Wang, C.; Tian, W.; Ding, Y.; Ma, Y.-q.; Wang, Z. L.; Markovic, N. M.; Stamenkovic, V. R.; Daimon, H.; Sun, S. Rational Synthesis of Heterostructured Nanoparticles with Morphology Control. *J. Am. Chem. Soc.* **2010**, *132*, 6524–6529.
- (9) Thushara, K. S.; D'Amore, M.; Piovano, A.; Bordiga, S.; Groppo, E. The Influence of Alcohols in Driving the Morphology of

Magnesium Chloride Nanocrystals. *ChemCatChem* **2017**, *9*, 1782–1787.

(10) Bell, A. T. The Impact of Nanoscience on Heterogeneous Catalysis. *Science* **2003**, *299*, 1688–1691.

(11) Wulff, G. Zur Frage Der Geschwindigkeit Des Wachstums Under Auflösung Der Krystallflächen. *Z. für Kristallogr. - Cryst. Mater.* **1901**, *34*, 449.

(12) Herring, C. *The Physics of Powder Metallurgy*; Kingston, W. E., Ed.; McGraw-Hill: New York, 1951.

(13) Henry, C. R. Morphology of Supported Nanoparticles. *Prog. Surf. Sci.* **2005**, *80*, 92–116.

(14) Harris, P. J. F. Sulphur-Induced Faceting of Platinum Catalyst Particles. *Nature* **1986**, *323*, 792–794.

(15) Neumaier, M.; Weigend, F.; Hampe, O.; Kappes, M. M. Binding Energy and Preferred Adsorption Sites of CO on Gold and Silver-Gold Cluster Cations: Adsorption Kinetics and Quantum Chemical Calculations. *Faraday Discuss.* **2008**, *138*, 393–406.

(16) Roldan Cuenya, B.; Beharfarid, F. Nanocatalysis: Size- and Shape-Dependent Chemisorption and Catalytic Reactivity. *Surf. Sci. Rep.* **2015**, *70*, 135–187.

(17) Gao, F.; Zhang, Y.; Song, P.; Wang, J.; Yan, B.; Sun, Q.; Li, L.; Zhu, X.; Du, Y. Shape-Control of One-Dimensional PtNi Nanostructures as Efficient Electrocatalysts for Alcohol Electrooxidation. *Nanoscale* **2019**, *11*, 4831–4836.

(18) Combe, N.; Jensen, P.; Pimpinelli, A. Changing Shapes in the Nanoworld. *Phys. Rev. Lett.* **2000**, *85*, 110–113.

(19) Schapotschnikow, P.; Pool, R.; Vlucht, T. J. H. Molecular Simulations of Interacting Nanocrystals. *Nano Lett.* **2008**, *8*, 2930–2934.

(20) Henry, C. R. Surface Studies of Supported Model Catalysts. *Surf. Sci. Rep.* **1998**, *31*, 231–325.

(21) Yacamán, M. J.; Ocaña, T. High-resolution Dark-field Electron Microscopy of Small Metal Particles. *Phys. Status Solidi* **1977**, *42*, 571–577.

(22) Galli, P.; Barbè, P.; Guidetti, G.; Zannetti, R.; Martorana, A.; Marigo, A.; Bergozza, M.; Fichera, A. The Activation of MgCl₂-Supported Ziegler-Natta Catalysts: A Structural Investigation. *Eur. Polym. J.* **1983**, *19*, 19–24.

(23) Zannetti, R.; Marega, C.; Marigo, A.; Martorana, A. Layer-lattices in Ziegler-Natta Catalysts. *J. Polym. Sci., Part B: Polym. Phys.* **1988**, *26*, 2399–2412.

(24) Martorana, A.; Zannetti, R.; Marigo, A.; Ajò, D.; Malta, V. PROVA, a Program for the Calculation of X-Ray Powder Spectra (Ordered and Disordered Structures). *Comput. Phys. Commun.* **1982**, *27*, 49–55.

(25) Sementa, L.; D'Amore, M.; Barone, V.; Busico, V.; Causà, M. A Quantum Mechanical Study of TiCl₃ α , β and γ Crystal Phases: Geometry, Electronic Structure and Magnetism. *Phys. Chem. Chem. Phys.* **2009**, *11*, 11264–11275.

(26) Wada, T.; Takasao, G.; Piovano, A.; D'Amore, M.; Thakur, A.; Chammingkwan, P.; Bruzzese, P. C.; Terano, M.; Civalieri, B.; Bordiga, S.; Groppo, E.; Taniike, T. Revisiting the Identity of δ -MgCl₂: Part I. Structural Disorder Studied by Synchrotron X-Ray Total Scattering. *J. Catal.* **2020**, *385*, 76–86.

(27) Piovano, A.; D'Amore, M.; Wada, T.; Cleto Bruzzese, P.; Takasao, G.; Thakur, A.; Chammingkwan, P.; Terano, M.; Civalieri, B.; Bordiga, S.; Taniike, T.; Groppo, E. Revisiting the Identity of δ -MgCl₂: Part II. Morphology and Exposed Surfaces Studied by Vibrational Spectroscopies and DFT Calculation. *J. Catal.* **2020**, *387*, 1–11.

(28) Bozyigit, D.; Yazdani, N.; Yarema, M.; Yarema, O.; Lin, W. M. M.; Volk, S.; Vuttivorakulchai, K.; Luisier, M.; Juranyi, F.; Wood, V. Soft Surfaces of Nanomaterials Enable Strong Phonon Interactions. *Nature* **2016**, *531*, 618–622.

(29) Mitchell, P. C. H.; Parker, S. F.; Ramirez-Cuesta, A.; Tomkinson, J. *Vibrational Spectroscopy with Neutrons, with Applications in Chemistry, Biology, Materials Science and Catalysis*; World Scientific Publishing Co. Pte. Ltd., 2005.

- (30) Parker, S. F.; Collier, P. Applications of Neutron Scattering in Catalysis. *Johnson Matthey Technol. Rev.* **2016**, *60*, 132–144.
- (31) Pinna, R. S.; Rudić, S.; Parker, S. F.; Armstrong, J.; Zanetti, M.; Škoro, G.; Waller, S. P.; Zacek, D.; Smith, C. A.; Capstick, M. J.; McPhail, D. J.; Pooley, D. E.; Howells, G. D.; Gorini, G.; Fernandez-Alonso, F. The Neutron Guide Upgrade of the TOSCA Spectrometer. *Nucl. Instrum. Methods Phys. Res., Sect. A* **2018**, *896*, 68–74.
- (32) Arrigo, R.; Badmus, K.; Baletto, F.; Boeije, M.; Brinkert, K.; Bugaev, A.; Bukhtiyarov, V.; Carosso, M.; Catlow, R.; Chutia, A.; Davies, P.; De Leeuw, N.; Dononelli, W.; Freund, H.-J.; Friend, C.; Gates, B.; Genest, A.; Hargreaves, J.; Hutchings, G.; Johnston, R.; Lamberti, C.; Marbaix, J.; Miranda, C. R.; Odarchenko, Y.; Richards, N.; Russell, A.; Selvam, P.; Sermon, P.; Shah, P.; Shevlin, S.; Shoji, M.; Skylaris, C.-K.; Soulantica, K.; Torrente-Murciano, L.; Trunschke, A.; Van Santen, R.; Verga, L. G.; Whiston, K.; Willock, D. Theory as a Driving Force to Understand Reactions on Nanoparticles: General Discussion. *Faraday Discuss.* **2018**, *208*, 147–185.
- (33) Bertini, F.; Glatz, M.; Stöger, B.; Peruzzini, M.; Veiros, L. F.; Kirchner, K.; Gonsalvi, L. Carbon Dioxide Reduction to Methanol Catalyzed by Mn(I) PNP Pincer Complexes under Mild Reaction Conditions. *ACS Catal.* **2019**, *9*, 632–639.
- (34) Parker, S. F. Spectroscopy and Bonding in Ternary Metal Hydride Complexes-Potential Hydrogen Storage Media. *Coord. Chem. Rev.* **2010**, *254*, 215–234.
- (35) O'Malley, A. J.; Parker, S. F.; Catlow, C. R. A. Neutron Spectroscopy as a Tool in Catalytic Science. *Chem. Commun.* **2017**, *53*, 12164–12176.
- (36) McGreevy, R. L.; Mitchell, E. W. J. Collective Modes in Molten Alkaline Earth Chlorides: Iii. Inelastic Neutron Scattering from Molten MgCl₂ and CaCl₂. *J. Phys. C: Solid State Phys.* **1985**, *18*, 1163–1178.
- (37) Dovesi, R.; Orlando, R.; Erba, A.; Zicovich-Wilson, C. M.; Civalieri, B.; Casassa, S.; Maschio, L.; Ferrabone, M.; De La Pierre, M.; D'Arco, P.; Noël, Y.; Causà, M.; Rérat, M.; Kirtman, B. CRYSTAL14: A Program for the Ab Initio Investigation of Crystalline Solids. *Int. J. Quantum Chem.* **2014**, *114*, 1287–1317.
- (38) Erba, A.; Baima, J.; Bush, I.; Orlando, R.; Dovesi, R. Large-Scale Condensed Matter DFT Simulations: Performance and Capabilities of the CRYSTAL Code. *J. Chem. Theory Comput.* **2017**, *13*, 5019–5027.
- (39) Dovesi, R.; Erba, A.; Orlando, R.; Zicovich-Wilson, C. M.; Civalieri, B.; Maschio, L.; Rérat, M.; Casassa, S.; Baima, J.; Salustro, S.; Kirtman, B. Quantum-Mechanical Condensed Matter Simulations with CRYSTAL. *Wiley Interdiscip. Rev.: Comput. Mol. Sci.* **2018**, *8*, No. e1360.
- (40) Orlando, R.; Delle Piane, M.; Bush, I. J.; Ugliengo, P.; Ferrabone, M.; Dovesi, R. A New Massively Parallel Version of CRYSTAL for Large Systems on High Performance Computing Architectures. *J. Comput. Chem.* **2012**, *33*, 2276–2284.
- (41) Becke, A. D. Density-functional Thermochemistry. III. The Role of Exact Exchange. *J. Chem. Phys.* **1993**, *98*, 5648–5652.
- (42) Grimme, S. Semiempirical GGA-Type Density Functional Constructed with a Long-Range Dispersion Correction. *J. Comput. Chem.* **2006**, *27*, 1787–1799.
- (43) Grimme, S.; Antony, J.; Ehrlich, S.; Krieg, H. A Consistent and Accurate Ab Initio Parametrization of Density Functional Dispersion Correction (DFT-D) for the 94 Elements H-Pu. *J. Chem. Phys.* **2010**, *132*, 154104.
- (44) Grimme, S. Accurate Description of van Der Waals Complexes by Density Functional Theory Including Empirical Corrections. *J. Comput. Chem.* **2004**, *25*, 1463–1473.
- (45) Civalieri, B.; Zicovich-Wilson, C. M.; Valenzano, L.; Ugliengo, P. B3LYP Augmented with an Empirical Dispersion Term (B3LYP-D*) as Applied to Molecular Crystals. *CrystEngComm* **2008**, *10*, 405–410.
- (46) Valenzano, L.; Noël, Y.; Orlando, R.; Zicovich-Wilson, C. M.; Ferrero, M.; Dovesi, R. Ab Initio Vibrational Spectra and Dielectric Properties of Carbonates: Magnesite, Calcite and Dolomite. *Theor. Chem. Acc.* **2007**, *117*, 991–1000.
- (47) Apra, E.; Causa, M.; Prencipe, M.; Dovesi, R.; Saunders, V. R. On the Structural Properties of NaCl: An Ab Initio Study of the B1-B2 Phase Transition. *J. Phys. Condens. Matter* **1993**, *5*, 2969–2976.
- (48) D'Amore, M.; Credendino, R.; Budzelaar, P. H. M.; Causà, M.; Busico, V. A Periodic Hybrid DFT Approach (Including Dispersion) to MgCl₂-Supported Ziegler-Natta Catalysts - 1: TiCl₄ Adsorption on MgCl₂ Crystal Surfaces. *J. Catal.* **2012**, *286*, 103–110.
- (49) Credendino, R.; Busico, V.; Causà, M.; Barone, V.; Budzelaar, P. H. M.; Zicovich-Wilson, C. Periodic DFT Modeling of Bulk and Surface Properties of MgCl₂. *Phys. Chem. Chem. Phys.* **2009**, *11*, 6525–6532.
- (50) Erba, A.; Baima, J.; Bush, I.; Orlando, R.; Dovesi, R. Large-Scale Condensed Matter DFT Simulations: Performance and Capabilities of the CRYSTAL Code. *J. Chem. Theory Comput.* **2017**, *13*, 5019–5027.
- (51) Monkhorst, H. J.; Pack, J. D. Special Points for Brillouin-Zone Integrations. *Phys. Rev. B* **1976**, *13*, 5188–5192.
- (52) Zicovich-Wilson, C. M.; Pascale, F.; Roetti, C.; Saunders, V. R.; Orlando, R.; Dovesi, R. Calculation of the Vibration Frequencies of α -Quartz: The Effect of Hamiltonian and Basis Set. *J. Comput. Chem.* **2004**, *25*, 1873–1881.
- (53) Pascale, F.; Zicovich-Wilson, C. M.; López Gejo, F.; Civalieri, B.; Orlando, R.; Dovesi, R. The Calculation of the Vibrational Frequencies of Crystalline Compounds and Its Implementation in the CRYSTAL Code. *J. Comput. Chem.* **2004**, *25*, 888–897.
- (54) Parlinski, K.; Li, Z. Q.; Kawazoe, Y. First-Principles Determination of the Soft Mode in Cubic ZrO₂. *Phys. Rev. Lett.* **1997**, *78*, 4063–4066.
- (55) Togo, A.; Oba, F.; Tanaka, I. First-Principles Calculations of the Ferroelastic Transition between Rutile-Type and CaCl₂-Type SiO₂ at High Pressures. *Phys. Rev. B: Condens. Matter Mater. Phys.* **2008**, *78*, 134106.
- (56) Alfè, D. PHON: A Program to Calculate Phonons Using the Small Displacement Method. *Comput. Phys. Commun.* **2009**, *180*, 2622–2633.
- (57) Erba, A.; Ferrabone, M.; Orlando, R.; Dovesi, R. Accurate Dynamical Structure Factors from Ab Initio Lattice Dynamics: The Case of Crystalline Silicon. *J. Comput. Chem.* **2013**, *34*, 346–354.
- (58) Wang, Y.; Wang, J. J.; Wang, W. Y.; Mei, Z. G.; Shang, S. L.; Chen, L. Q.; Liu, Z. K. A Mixed-Space Approach to First-Principles Calculations of Phonon Frequencies for Polar Materials. *J. Phys. Condens. Matter* **2010**, *22*, 202201.
- (59) Peintinger, M. F.; Oliveira, D. V.; Bredow, T. Consistent Gaussian Basis Sets of Triple-Zeta Valence with Polarization Quality for Solid-State Calculations. *J. Comput. Chem.* **2013**, *34*, 451–459.
- (60) Carpenter, J. M.; Price, D. L. Correlated Motions in Glasses Studied by Coherent Inelastic Neutron Scattering. *Phys. Rev. Lett.* **1985**, *54*, 441–443.
- (61) Piovano, A. Inelastic Neutron Scattering Applied to Materials for Energy. *EPJ Web Conf.* **2015**, *104*, 01006.
- (62) Baima, J.; Ferrabone, M.; Orlando, R.; Erba, A.; Dovesi, R. Thermodynamics and Phonon Dispersion of Pyrope and Grossular Silicate Garnets from Ab Initio Simulations. *Phys. Chem. Miner.* **2016**, *43*, 137–149.
- (63) Lucas, M. S.; Kresch, M.; Stevens, R.; Fultz, B. Phonon Partial Densities of States and Entropies of Fe and Cr in Bcc Fe-Cr from Inelastic Neutron Scattering. *Phys. Rev. B: Condens. Matter Mater. Phys.* **2008**, *77*, 184303.
- (64) Osborn, R.; Goremychkin, E. A.; Kolesnikov, A. I.; Hinks, D. G. Phonon Density of States in MgB₂. *Phys. Rev. Lett.* **2001**, *87*, 017005.
- (65) Arnold, O.; Bilheux, J. C.; Borreguero, J. M.; Buts, A.; Campbell, S. I.; Chapon, L.; Doucet, M.; Draper, N.; Ferraz Leal, R.; Gigg, M. A.; Lynch, V. E.; Markvardsen, A.; Mikkelsen, D. J.; Mikkelsen, R. L.; Miller, R.; Palmen, K.; Parker, P.; Passos, G.; Perring, T. G.; Peterson, P. F.; Ren, S.; Reuter, M. A.; Savici, A. T.; Taylor, J. W.; Taylor, R. J.; Tolchenov, R.; Zhou, W.; Zikovsky, J. Mantid - Data Analysis and Visualization Package for Neutron Scattering and μ SR Experiments. *Nucl. Instrum. Methods Phys. Res., Sect. A* **2014**, *764*, 156.

(66) Colognesi, D.; Celli, M.; Cilloco, F.; Newport, R. J.; Parker, S. F.; Rossi-Albertini, V.; Sacchetti, F.; Tomkinson, J.; Zoppi, M. TOSCA Neutron Spectrometer: The Final Configuration. *Appl. Phys. A: Mater. Sci. Process.* **2002**, *74*, s64–s66.

(67) Parker, S. F.; Fernandez-Alonso, F.; Ramirez-Cuesta, A. J.; Tomkinson, J.; Rudic, S.; Pinna, R. S.; Gorini, G.; Fernández Castañón, J. Recent and Future Developments on TOSCA at ISIS. *J. Phys.: Conf. Ser.* **2014**, *554*, 012003.

(68) Giunchi, G.; Allegra, G. Structural Disorder In Microcrystalline MgCl₂. *J. Appl. Crystallogr.* **1983**, *17*, 172–178.

(69) D'Amore, M.; Thushara, K. S.; Piovano, A.; Causà, M.; Bordiga, S.; Groppo, E. Surface Investigation and Morphological Analysis of Structurally Disordered MgCl₂ and MgCl₂/TiCl₄ Ziegler-Natta Catalysts. *ACS Catal.* **2016**, *6*, 5786–5796.

(70) Brambilla, L.; Zerbi, G.; Nascetti, S.; Piemontesi, F.; Morini, G. Experimental and Calculated Vibrational Spectra and Structure of Ziegler-Natta Catalyst Precursor: 50/1 Comilled MgCl₂-TiCl₄. *Macromol. Symp.* **2004**, *213*, 287–302.

Deactivation of industrial Pd/Al₂O₃ catalysts by ethanol: a spectroscopic study

Michele Carosso,^{*[a]} Eleonora Vottero,^[a,b] Sara Morandi,^[a] Maela Manzoli,^[c] Davide Ferri,^[d] Thibault Fovanna,^[d] Riccardo Pellegrini,^[e] Andrea Piovano,^[b] and Elena Groppo^[a]

- [a] Dr. M. Carosso, Mrs. E. Vottero, Dr. S. Morandi, Prof. E. Groppo
Department of Chemistry, INSTM and NIS Centre
University of Torino
via Quarello 15/A, I-10135 Torino, Italy
E-mail: michele.carosso@unito.it
- [b] Mrs. E. Vottero, Dr. A. Piovano
Institut Laue-Langevin (ILL)
71 avenue des Martyrs, F-38000 Grenoble, France
- [c] Prof. M. Manzoli
Department of Drug Science and Technology, INSTM and NIS Centre
University of Torino
via Pietro Giuria 9, I-10125 Torino, Italy
- [d] Dr. D. Ferri, Dr. T. Fovanna
Paul Scherrer Institut
Forschungsstrasse 111, CH-5232 Villigen PSI, Switzerland
- [e] Dr. R. Pellegrini
Chimet SpA - Catalyst Division
via di Pescaiola 74, I-52041, Viciomaggio Arezzo, Italy

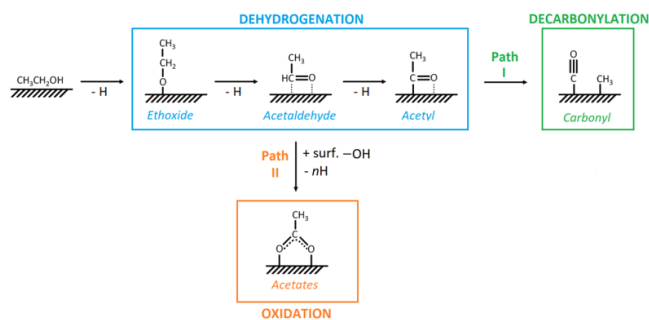
Abstract: The chemical processes involved in the decomposition of ethanol over two industrial Pd/Al₂O₃ catalysts characterized by different Pd dispersions, particles morphology and reducibility of the active metal phase was thoroughly investigated in gas-phase and in liquid-phase by transmission FT-IR and ATR-IR spectroscopies, respectively. In both cases, two main products were detected, arising from two competitive paths: acetates from ethanol oxidation and carbonyls from acetaldehyde decarbonylation. The regularity of the Pd particles greatly affects the relative proportion of the two products, while the initial Pd oxidation state influences the kinetics of the two processes. Ethanol oxidation to acetates is the kinetically favored reaction path both in gas-phase and in liquid-phase. In contrast, the presence of a solvent dampens the decarbonylation process to very low levels, because the solvent competes with ethanol in occupying the available surface sites. Since adsorbed carbonyls are considered as surface poisons of industrial Pd/Al₂O₃ catalysts in processes involving aliphatic as well as aromatic alcohols, the rationalization of the experimental variables affecting alcohols decomposition can help in establishing working protocols and in designing preparation procedures that minimize the unwanted poisoning effects.

Introduction

Heterogeneous catalysts based on supported Group VIII metals are widely employed in industrial processes involving hydrogenation of reducible molecular moieties or formation of C-C and C-N chemical bonds, such as in the synthesis of pharmaceuticals and specialty chemicals.^[1-4] In the industrial practice, these reactions are carried out in a solvent, such as an aliphatic alcohol.^[2-3] However, it has been demonstrated that in some cases alcoholic solvents are not innocuous and lead to a

worsening of the catalytic performances.^[2-3] As an example, Singh *et al.* documented a five-fold suppression in the rate of cyclohexene reduction when Pd/C was aged for 8-20 h in ethanol, as a consequence of surface poisoning. The same effect was reported for debenzoylation reactions and reduction of polar functional groups such as the nitro group.^[5]

The occurrence of anaerobic dehydrogenation of alcohols over these metals is a well-known phenomenon, whose reaction pathway was firstly investigated in a series of seminal surface science works. For primary alcohols interacting at 443 °C with a Pd(111) single-crystal surface, Davis and Barteau proposed a decomposition pathway corresponding to the reverse of alcohols synthesis (Scheme 1):^[6-7] the alcohol chemisorbs on the metal surface as an alkoxide, which experiences the cleavage of the C-H bond in α position leading to a $\eta^2(\text{O,C})$ -aldehyde and, by further dehydrogenation, to a $\eta^2(\text{O,C})$ -acyl species. The adsorbed acyl undergoes decarbonylation, resulting in adsorbed CO, hydrogen and carbonaceous fragments, responsible for the surface poisoning and the subsequent worsening in the catalytic performances. The carbonaceous fragments may react with the adjacent hydrogen species, desorbing as hydrocarbons, or may experience further dehydrogenation leading to an adsorbed carbon phase. Similar findings were reported for Ni(111),^[8] Pt(111)^[9] and Pd(110),^[10] indicating that this mechanism is structure-insensitive. A further confirmation of the involvement of aldehydes and acyl species as intermediates in the anaerobic dehydrogenation of alcohols arises from the observation that when aldehydes are directly contacted with Pd(111) and Pd(110) surfaces, CO, hydrogen and carbonaceous fragments are produced.^[11-12]



Scheme 1. Schematic representation of the possible decomposition routes for ethanol over Pd/Al₂O₃ catalysts. Ethanol is initially dehydrogenated to give ethoxide and acetaldehyde intermediates. Path I (decarbonylation) involves the complete decomposition of the intermediates, to give carbonyls and carbonaceous fragments. Path II (oxidation) involves the oxidation of the intermediates by surface -OH groups, leading to adsorbed acetates. Both reaction paths require the presence of Pd⁰, but the reaction products might be localized also on the alumina support.

Despite their pivotal importance, surface science investigations lack the complexity of real heterogeneous catalysts, where surface chemistry is determined by several parameters such as the morphology and size of the supported metal nanoparticles, the nature of the support and the possible presence of promoters and/or poisons. So far, the reactivity of aliphatic alcohols over Pd-based heterogeneous catalysts was investigated mainly by means of spectroscopic methods. Most of the studies regard methanol and confirm the decomposition pathway proposed on the basis of surface science studies. For example, Solymsi and co-workers reported that gaseous methanol decomposes at room temperature on Pd/SiO₂, giving mostly multi-coordinated carbonyls.^[13] Formation of transient formaldehyde was detected by FT-IR spectroscopy. They also found that doping with K adatoms is beneficial in diminishing the surface poisoning by adsorbed CO, stabilizing the intermediates of methanol decomposition. A similar effect was documented by Cabilla *et al.* on unpromoted and Ca-promoted Pd/SiO₂ catalysts.^[14] Zecchina and co-workers investigated the Pd-mediated methanol decomposition on Pd/MgO, chlorine-doped Pd/MgO and Pd/Al₂O₃ catalysts.^[15] Irrespective of the system, physisorbed methanol and methoxy species chemisorbed at the support were detected, while CO formation was observed at room temperature only on Pd/MgO. Such behaviour was ascribed to the superior basicity of the MgO support.^[16] Interestingly, upon increasing the working temperature, formate species were formed on Pd/MgO, indicating the occurrence of an oxidation reaction. Similar evidences for formation of oxidation products in anaerobic conditions were reported for ethanol interacting with a Pt/CeZrO₂ bifunctional catalyst^[17] and with Pd/CeO₂.^[18] Since in all the cases the metal phase was completely reduced, the observation of oxidation products was ascribed to a reaction of the alkoxy species with the -OH groups at the surface of the support (path II in Scheme 1). All in all, these studies indicate that the reactivity of gaseous aliphatic alcohols with Pd-based heterogeneous catalysts depends not only on the Pd phase, but also on the properties of the support (e.g. hydroxylation degree, basicity/acidity, etc.). Moreover, it is clear that CO is always one of the final products of alcohols decomposition over metal surfaces. It is known that CO, due to

its very strong adsorption ability, is one of the major poisons for Pd-based catalysts, resulting in the blockage of the available reactive sites and in a subsequent worsening of the catalytic performances when alcohols are used as a reaction media. As an example, the presence of adsorbed CO strongly inhibits the alcohols oxidation activity on Pd/Al₂O₃ catalysts.^[19-20]

Similar studies were also conducted on not pre-reduced Pd-based heterogeneous catalysts, i.e. where the active phase is initially PdO or surface oxidized Pd. It has been demonstrated that in anaerobic conditions primary alcohols reduce oxidized Pd surfaces, and that the sample reducibility greatly affects the process under investigation.^[21] Newton *et al.* hypothesized two reaction routes for ethanol interacting with a PdO phase.^[21-22] The alcohol can directly reduce the oxidized metal surface, via an intermediate ethoxide species adsorbed at the PdO phase. The reaction products are Pd⁰, acetaldehyde (that can further dehydrogenate on the reduced surface following the previously discussed pathway) and a water molecule. An alternative route forecasts that the reduction of the PdO phase is assisted by gaseous H₂, generated by recombination of adsorbed hydroxyls groups and atomic hydrogen formed upon oxidation of ethanol into acetaldehyde.

The studies discussed above, dealing with reactions occurring at a solid-gas interface, are still over-simplified with respect to industrial conditions, where reactions are carried out in the presence of a solvent and hence occur at a solid-liquid interface. While the characterization for catalytic solid-gas interfaces by FT-IR spectroscopy has reached a very high degree of sophistication,^[23-25] much less studies are reported in the literature for heterogeneous catalysts working in a liquid environment,^[26] mainly because of technical limitations. Most of the commonly employed organic solvents, as well as water, show absorption bands in spectral regions of interest for elucidating reaction mechanisms, whose intensity can be orders of magnitude stronger than that of the adsorbed surface species. In addition, the large optical path characteristic of transmission cells seriously limits the adoption of FT-IR spectroscopy in transmission for investigating solid-liquid interfaces.^[27] On the other hand, attenuated total reflection infrared (ATR-IR) spectroscopy presents a suitable optical geometry for the study of phenomena occurring at solid surfaces immersed in a liquid.^[28-32] The oxidation of various alcohols over catalysts immersed in a liquid environment has been the subject of extensive spectroscopic investigation.^[33-34] The liquid-phase Pd-mediated dehydrogenation of aliphatic and aromatic alcohols was studied in both anaerobic and aerobic conditions using ATR-IR.^[26, 35-38] In the absence of O₂, benzyl alcohol was shown to dehydrogenate into benzaldehyde, which further experiences decarbonylation leading to a CO adlayer that poisons the catalyst surface. Benzoate species were detected also in anaerobic conditions, as a consequence of benzyl alcohol oxidation by some oxygen source (either in the feed and/or at the catalyst surface). The adoption of aerobic conditions enhances the stability of the benzaldehyde intermediate at the expenses of CO formation and favours oxidation to benzoate. It is worth mentioning that electrochemistry tools were also employed to investigate the surface phenomena occurring at the solid-liquid interface of metal electrodes in alkaline liquid media, which are however conditions far from those of interest in catalysis.^[39-42]

In this work, we provide an extensive spectroscopic characterization of the ethanol anaerobic dehydrogenation over two industrial Pd/Al₂O₃ catalysts produced by Chimet S.p.A. for hydrogenation of functional groups and debenzilation reactions, in the field of the production of active pharmaceutical ingredients and fine chemicals. The two catalysts differ in terms of dispersion and reducibility of the Pd phase. Moreover, both gas-phase and liquid-phase protocols have been adopted, in order to bridge the gap of knowledge between the two approaches. The final aim is to provide insights into the preparation and activation variables which have an influence on the ethanol decomposition process, and hence on the catalysts deactivation due to adsorbed CO. The results are useful to select the best synthesis and activation procedures that minimize the surface poisoning effects. It is worth remembering that one of the main drawbacks in adopting infrared spectroscopy as a characterization tool arises from the absorption of spectator species that could overwhelm the signals of the species of interest: while this is particularly relevant for liquid-phase protocols, due to the presence of a bulk solvent, it is not significant for gas-phase protocols, where ethanol is carried out by an inert carrier.

Results and Discussion

Preliminary characterization of the Pd/Al₂O₃ catalysts

The two Pd/Al₂O₃ catalysts under study were already characterized in a previous work by applying a multi-technique approach (including HR-TEM, TPR, SAXS and FT-IR spectroscopy of adsorbed CO),^[43] which was devoted to correlate the reduction state of Pd/Al₂O₃ catalysts and their catalytic performance. Hereinafter, the two catalysts will be labeled as PdAl(F) (pre-reduced in liquid-phase with sodium formate) and PdAl (not pre-reduced), following the same nomenclature as in Ref.^[44] It was found that in PdAl(F) the surface and sub-surface of the Pd phase was oxidized, but this Pd²⁺ phase is easier to be reduced than the bulk PdO particles present in PdAl. Moreover, the two catalysts displayed a different Pd dispersion, D(%), as evaluated by CO chemisorption, namely D = 24% for PdAl(F) and D = 36% for PdAl. The lower Pd dispersion in PdAl(F) was ascribed to a greater interaction of the Pd nanoparticles with the support and a slightly larger particle size. Once reduced in H₂, the Pd nanoparticles in PdAl(F) exhibited a larger fraction of sites located on extended surfaces, while those in PdAl were more irregular and displayed a larger fraction of edges and corners. Analysis of SAXS data revealed for PdAl an average particle size centered around 1.5 nm. PdAl(F) has a similar value, but its size distribution is characterized by a tail towards greater values, that explains the lower dispersion.^[43]

Reactivity of gaseous ethanol over Al₂O₃ and Pd/Al₂O₃ catalysts: assignment of the main IR absorption bands

Before investigating the interaction of ethanol with the Pd/Al₂O₃ catalysts, we considered its adsorption on the bare Al₂O₃ support. Figure 1a shows the FT-IR spectra of Al₂O₃ (activated at 120 °C in a N₂ stream for 30 min) before (spectrum 1, black) and after ethanol exposure (spectrum 2, blue), while Figure 1c reports the difference between the two spectra (spectrum 2,

blue) compared with that of gaseous ethanol (spectrum 1, grey) in the 2200-1200 cm⁻¹ region. The FT-IR spectrum of Al₂O₃ activated at 120 °C is dominated by the ν(OH) stretching modes of the surface hydroxyl groups showing a different degree of hydrogen-bonding (bands in the 3800-3000 cm⁻¹ range) and by the framework modes of Al₂O₃ (below 1000 cm⁻¹). Upon exposure of Al₂O₃ to ethanol at room temperature, the vibrational features of gaseous and physisorbed ethanol appeared immediately. The most intense bands are observed in the 3000-2800 cm⁻¹ range (ν(CH_x) stretching modes) and at ca. 1050 cm⁻¹ (ν(C-O) stretching mode) (Figure 1a). In the 1500-1200 cm⁻¹ range (Figure 1c) the weak bands at ca. 1490 (δ(CH₂) mode), 1452 (δ_{asym}(CH₃)), 1394 (δ_{sym}(CH₃)) and 1242 cm⁻¹ (δ(OH)) are ascribed to gaseous ethanol (spectrum 1, grey), while those (more intense) at 1485, 1450, 1385 and 1242 cm⁻¹ are assigned to the same vibrational modes of physisorbed ethanol (spectrum 2, blue). At the same time, the broad band due to the hydroxyl groups of the Al₂O₃ surface was affected by the presence of ethanol. In particular, the shoulder of isolated -OH species at ca. 3720 cm⁻¹ was consumed in favor of a more pronounced band at ca. 3500 cm⁻¹, testifying the occurrence of a hydrogen-bonding interaction between the Al₂O₃ surface and physisorbed ethanol. It is worth noticing that the presence of physisorbed ethanol does not allow to discriminate chemisorbed ethoxy species possibly formed upon reaction of ethanol with surface -OH species, as previously documented for Al₂O₃ as well as for other supports.^[13-14]

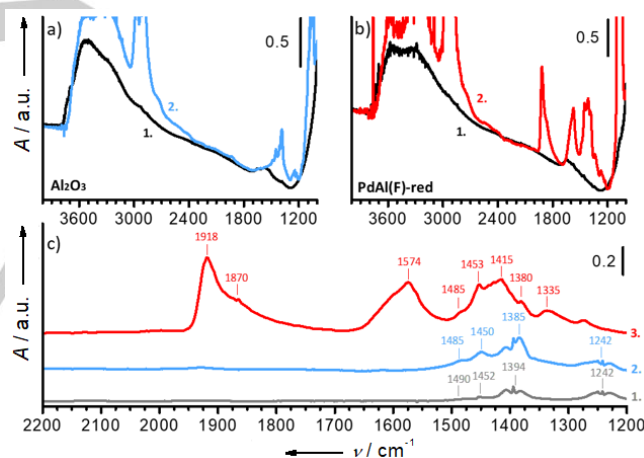


Figure 1. Part a): FT-IR spectra of Al₂O₃ activated at 120 °C (spectrum 1, black) and of the same sample exposed to ethanol at room temperature for 30 min (spectrum 2, blue). Part b): FT-IR spectra of PdAl(F)-red (spectrum 1, black) and of the same sample after a prolonged exposure to ethanol at room temperature (spectrum 2, red). Part c): difference between the two spectra reported in part a) (spectrum 2, blue) and part b) (spectrum 3, red), compared to the spectrum of gaseous ethanol (spectrum 1, grey), in the 2200–1200 cm⁻¹ region.

The same experiment was repeated on the two Pd/Al₂O₃ catalysts activated according to the two protocols described in the experimental section. The reaction products were the same in the four experiments, although their relative amount and the kinetics of their formation were different from case to case, as it will be discussed in the following section. Herein, we start discussing the main reaction products and their spectroscopic features, taking the PdAl(F)-red catalyst as an example. Figure

1b shows the FT-IR spectra of activated PdAl(F)-red before (spectrum 1, black) and after ethanol exposure (spectrum 2, red), while Figure 1c reports the difference between the two spectra (spectrum 3, red). The spectrum of the activated catalyst is almost indistinguishable from that of activated Al_2O_3 (Figure 1a). After interaction with ethanol (up to 100 min), the absorption bands of gaseous and physisorbed ethanol are well visible. Moreover, very intense bands appeared in the $2200\text{--}1200\text{ cm}^{-1}$ region, which were not present in the case of bare Al_2O_3 (compare blue and red spectra in Figure 1c). These bands are assigned to two products of the ethanol reaction with the catalyst.

The bands at 1918 and 1870 cm^{-1} belong to 2-fold bridged carbonyls at Pd(100) and 3-fold carbonyls in hollow sites at Pd(111) surfaces, respectively. Bands in similar position have been reported for CO adsorbed on Pd single crystals,^[45-46] and on Pd nanoparticles,^[16, 47-48] at low CO coverages. The observation of these bands indicates the occurrence of the decarbonylation path on PdAl(F)-red. The bands at 1574 (vs) and 1415 (vs) cm^{-1} are assigned to the $\nu_{\text{as}}(\text{COO})$ and $\nu_{\text{s}}(\text{COO})$ modes of acetate species, respectively, whose $\delta(\text{CH}_3)$ mode is overlapped to those of physisorbed ethanol. The position of the $\nu(\text{COO})$ bands indicates that the acetates are adsorbed in a bridged geometry.^[49] Adsorbed acetates must derive from the oxidation of acetaldehyde, the product of ethanol dehydrogenation.^[15, 17-18, 36, 40-41] Since the Pd phase in the PdAl(F)-red catalyst was completely reduced, the most likely oxidant species are the hydroxyl groups at the Al_2O_3 surface, as suggested previously.^[13-14, 17-18] As far as the location of the acetates is concerned, they might be at the surface of both Al_2O_3 and Pd. However, their absence when ethanol was dosed on bare Al_2O_3 encourages us to conclude that their formation requires the presence of Pd. Hence, our data suggest a close cooperation between the Pd nanoparticles and the Al_2O_3 support in the formation of the acetate species. Pd is necessary to dehydrogenate ethanol into acetaldehyde, while further oxidation is supported by the only available oxidant source, the hydroxyl groups of the support. These hydroxyls located at the metal-support interface are those most likely involved, being the closest to the dehydrogenation product.

Ethanol decomposition over PdAl(F) and PdAl: reaction by-products and their formation kinetics

Figure 2 reports the whole sequences of FT-IR spectra collected during the prolonged treatment in ethanol for the two catalysts activated according to the two different protocols described in the experimental section. As anticipated above, regardless of the sample and of the activation protocol, the same decomposition products were observed (namely, carbonyls and acetates), although the kinetics of their formation and their relative concentration differed from sample to sample.

In all the experiments, except for PdAl-ox, the bands assigned to acetates appeared almost immediately, and reached their maximum intensity within 3 min. This is particularly evident for the $\nu_{\text{as}}(\text{COO})$ mode at 1574 cm^{-1} (as shown in Figure 3, which reports the evolution of the band intensity as a function of time), while the $\nu_{\text{s}}(\text{COO})$ mode at 1415 cm^{-1} overlapped with the bands of physisorbed ethanol that increased constantly along the whole experiment. This observation suggests that the oxidation of ethanol to acetates is kinetically favored, but also that the oxidant species are rapidly consumed. Such

consideration, together with the experimental evidence of the absence of acetate species when ethanol interacts with the bare Al_2O_3 support, confirms that ethanol oxidation is mediated by the Pd phase and that the most likely oxidant species are the $-\text{OH}$ groups located at the metal-support interface. On PdAl-ox (Figure 2d) the bands due to acetates appeared at a much lower rate, and reached their maximum intensity after more than 1 h (Figure 3d). Such behavior is in agreement with previous findings indicating that, despite the role of the $-\text{OH}$ groups at the Al_2O_3 surface as oxidants, Pd^0 is necessary for catalyzing ethanol oxidation through dehydrogenation. In this sample, Pd is initially entirely in the form of PdO, which needs to be reduced to Pd^0 by ethanol (which is oxidized to acetaldehyde) for initiating its catalytic activity, thus explaining the delay in the appearance of the absorption bands of acetates.

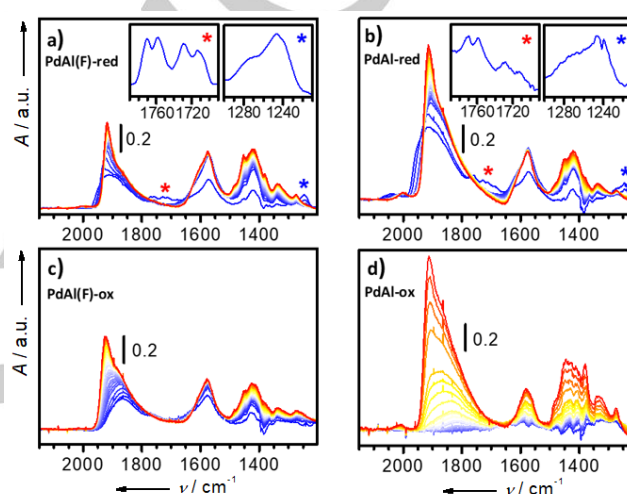


Figure 2. FT-IR spectra collected during the exposure of the PdAl(F) and PdAl catalysts to ethanol at room temperature. All the spectra are shown after subtraction of the spectrum of the catalyst prior the exposure to ethanol. Samples were activated following the two different protocols described in the experimental section (red and ox). Insets in parts a) and b) show a magnification of the signals labelled with an asterisk.

Besides the appearance of the acetate bands, as soon as ethanol reached the reduced catalysts two weak transient bands were observed at ca. 1730 and 1250 cm^{-1} (asterisks in Figure 2a and Figure 2b, magnified in the insets), which disappeared after 5 min. Their transient character suggests an attribution to labile intermediates. More in detail, the broad and weak feature at 1730 cm^{-1} is composed of two pairs of bands centered at 1770 and 1758 cm^{-1} and at 1729 and 1713 cm^{-1} . The latter pair is ascribed to gaseous acetaldehyde ($\nu(\text{C}=\text{O})$), formed as a labile intermediate in ethanol dehydrogenation according to Scheme 1. The pair of bands at 1770 and 1758 cm^{-1} and the band at 1250 cm^{-1} are assigned to ethyl acetate ($\nu(\text{C}=\text{O})$ and $\nu(\text{C}-\text{C}-\text{O})$ respectively).^[50] Ethyl acetate is likely formed through the Al_2O_3 -catalyzed Tishchenko reaction,^[51] which consists in a proton transfer between two adsorbed acetaldehyde molecules. The net result is the formation of an acetate species in the proximity of an ethoxide: the two species quickly react with each other, via esterification. In the experiments performed on the oxidized catalysts these species are not detected, likely because acetaldehyde is rapidly oxidized by PdO before reacting with the Al_2O_3 surface.

The absorption bands of palladium carbonyls increased at different rates in the four experiments and were characterized by different intensities. Figure 3 shows the evolution of the intensity of the bands at 1918 cm^{-1} (2-fold carbonyls at Pd(100), full line) and 1870 cm^{-1} (3-fold carbonyls at Pd(111), dotted line) along the course of the experiments during ethanol exposure. In all the cases, the band at 1870 cm^{-1} saturated first, indicating that the 3-fold hollow sites at the Pd(111) surfaces are more rapidly filled by CO. On the contrary, the band at 1918 cm^{-1} increased initially fast and then slower along the experiment, indicating that the Pd nanoparticles are not saturated by CO and that decarbonylation progresses slowly with time. Regardless of the sample and/or activation protocol, the formation of acetates is kinetically favored over carbonyls, reflecting the ready availability of the oxidant species (the -OH groups at the Al_2O_3 support), as shown in Figure 3 (black line).

The two reduced catalysts (Figure 3a and b) exhibited a similar behavior. However, the spectra of PdAl-red displayed almost a double intensity compared to those of PdAl(F)-red along the whole experiment. On the other hand, comparison of PdAl(F)-red and PdAl(F)-ox (Figure 3a and c) demonstrates different kinetics, carbonyls appearing at a slower rate in the case of PdAl(F)-ox. This is particularly evident for the absorption band at 1918 cm^{-1} that, for the first 20 min, was less intense than that at 1870 cm^{-1} . However, after 100 min of reaction, the intensity of both bands was almost the same in the two experiments. This behavior is enhanced in the case of PdAl-ox (Figure 3d), where the bands at 1918 and 1870 cm^{-1} started to appear only after about 20 min of reaction. However, also in this case, after 100 min the intensity of both bands was almost the same as that observed during the experiment on PdAl-red (Figure 3b). The delay in the appearance of the carbonyls in the experiments performed on the two oxidized catalysts is explained again by considering that Pd^0 is necessary for catalyzing the decarbonylation, and consequently this process can only begin after the reduction of PdO by ethanol. This process is very slow on PdAl-ox because only in this sample the palladium phase was initially entirely in the PdO form. On PdAl(F)-ox instead the activation in air forms an outer layer of PdO, which is quickly reduced by ethanol.

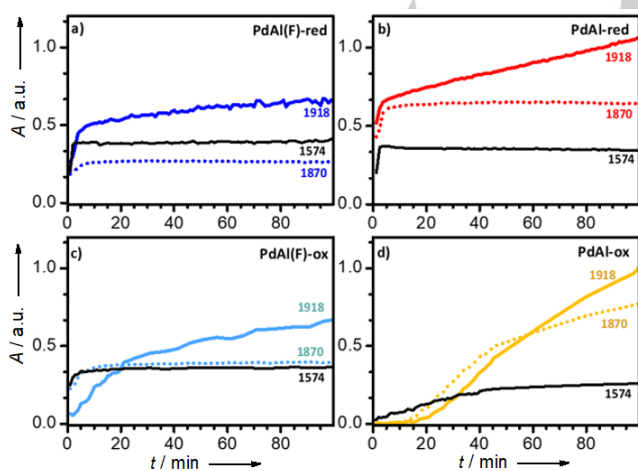


Figure 3. Temporal dependence of the absorption bands at 1918 cm^{-1} (2-fold carbonyls at Pd(100), full line) and 1870 cm^{-1} (3-fold carbonyls at Pd(111), dotted line) ascribed to adsorbed CO, and at 1574 cm^{-1} (black line) ascribed to adsorbed acetates.

Figure 4 compares the $\nu(\text{CO})$ region of the spectra collected after 2 min (Figure 4a) and 100 min (Figure 4b) of exposure of the catalysts to ethanol in the four experiments. The first important observation is the negligible amount of linear carbonyls ($2100\text{--}2000\text{ cm}^{-1}$) observed along the whole reaction with ethanol. This indicates that the CO coverage remains low, as a consequence of the competition with ethanol adsorption on Pd. Indeed, as reported in the literature for supported Pd NPs, linear carbonyls form only at high CO coverages, when the molecules are forced in the top position due to compression effects.^[16]

As already commented above, both at the beginning and at the end of the experiment, the intensity of the carbonyl bands of PdAl-red is almost double compared to that of PdAl(F)-red, indicating that a larger amount of carbonyls is formed on the former. The spectra collected at the beginning of the experiment on PdAl(F)-red and PdAl-red (spectra 1 and 2, Figure 4a) are very similar. They are dominated by a very broad band, which is the result of the overlap of the two components at 1918 and 1870 cm^{-1} with an additional band at ca. 1950 cm^{-1} . The latter band is also ascribed to 2-fold carbonyls coordinated to Pd(100), but for higher CO coverage. This band disappears after a few minutes of reaction, as a result of the competition between CO and ethanol for the occupancy of the same surface sites, which causes a decrease of the overall CO coverage. Moreover, in the spectrum of PdAl-red a weak band is also observed at 2040 cm^{-1} (inset of Figure 4a), which is assigned to a small fraction of linear carbonyls. The low frequency of this band is explained by considering that the linear carbonyls are perturbed by the presence of other adsorbed species nearby (such as physisorbed ethanol, ethoxy, methyl, etc.).

The spectra collected at the end of the experiment (spectra 1 and 2, Figure 4b) are also very similar and are dominated by the band at 1918 cm^{-1} due to 2-fold bridged carbonyls on Pd(100). In both cases, a weak band is observed at ca. 2000 cm^{-1} (inset of Figure 4b) revealing the presence of a few linear carbonyls. It is interesting to note that this band is red-shifted by ca. 40 cm^{-1} with respect to the beginning of the experiment (inset of Figure 4a). We assign this shift to the interaction of adsorbed CO with a larger amount of adsorbed species, which results in a very low net CO coverage where all the adsorbed carbonyls are "isolated".

In the case of PdAl(F)-ox, where the kinetics of carbonyls formation is slightly slower than on PdAl(F)-red, the initial spectrum (spectrum 3, Figure 4a) shows only the band at 1870 cm^{-1} . Hence, the 3-fold hollow sites at the Pd(111) surface are the very first ones to be occupied as soon as CO is formed in the reaction. This view is in accordance with the evidence by Ferri and co-workers that benzyl alcohol decomposition to CO preferentially occurs on hollow sites located at (111) facets, while the preliminary dehydrogenation step (aldehyde formation) occurs on (100) facets.^[35] In marked contrast, the spectrum collected after 100 min of reaction (spectrum 3, Figure 4b) is very similar to that of PdAl(F)-red (spectrum 1, Figure 4b), in terms of both intensity and band position. The main difference is the position of the weak band assigned to linear carbonyls, which is observed at 2015 cm^{-1} for PdAl(F)-ox and at 2000 cm^{-1} for PdAl(F)-red (inset of Figure 4b). Finally, no carbonyls are observed on PdAl-ox after 2 min of exposure to ethanol (spectrum 4, Figure 4a), while at the end of the experiment (spectrum 4, Figure 4b) the spectrum is very similar to that

collected on PdAl-red (spectrum 2, Figure 4b), except for the small shift in the position of the band ascribed to linear carbonyls (inset of Figure 4b).

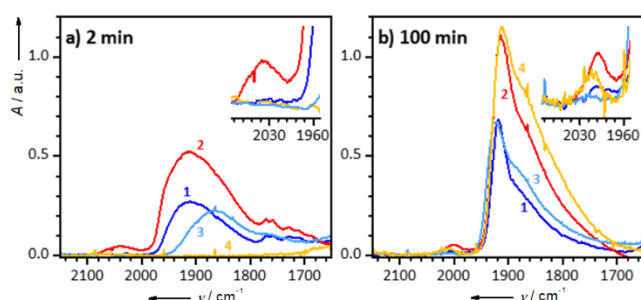


Figure 4. FT-IR spectra, in the $\nu(\text{CO})$ region, collected after 2 min (part a) and 100 min (part b) of catalysts exposure to the $\text{N}_2/\text{ethanol}$ flow. In both parts, the labels are as following: 1 = PdAl(F)-red; 2 = PdAl-red; 3 = PdAl(F)-ox; 4 = PdAl-ox. The insets show a magnification of the 2100–1950 cm^{-1} region. All the spectra are shown after subtraction of the spectrum of the catalyst prior to ethanol exposure.

Altogether, the data reported in Figure 3 and Figure 4 demonstrate that ethanol undergoes decomposition to CO on both PdAl(F) and PdAl catalysts. The oxidation state of the Pd phase (which is tuned through the activation treatment, i.e. reduction vs. oxidation) does not affect the result of exposure to ethanol: after 100 min in the same reaction conditions, the amount and the type of carbonyls are the same on PdAl(F)-red and PdAl(F)-ox as well as on PdAl-red and PdAl-ox. However, the oxidation state of Pd strongly influences the kinetics of the decarbonylation: the more oxidized the Pd phase, the slower the reaction. The size and the surface regularity of the Pd particles, instead, have an effect on the efficiency of the decarbonylation. Irrespective of the kinetics, after 100 min of reaction the amount of carbonyls formed on PdAl is on average twice that observed on PdAl(F). This is not only due to the higher dispersion of PdAl than PdAl(F). According to our previous work,^[43] the ratio between the intensity of bands of CO adsorbed at room temperature on PdAl and PdAl(F) is only 1.4. Hence, we can conclude that carbonyls formation is favored on the small and defective Pd nanoparticles present on PdAl rather than on the large and regular ones observed on PdAl(F).

Effect of the liquid environment on ethanol decomposition

For the industrial applications of the catalysts, their interaction with liquid ethanol should be considered. However, the investigation of the phenomena occurring at a solid-liquid interface is complicated by the presence of the bulk liquid phase. For this reason, it is a common academic practice to dilute the considered solvent molecule in another one, that is innocuous toward the system and whenever possible toward spectroscopy. In the present case, we investigated the decomposition of ethanol on the H_2 -reduced PdAl(F) catalyst using a 10 mM ethanol solution in cyclohexane. The rather low concentration of ethanol was selected in order to allow for a kinetically controlled formation of the surface species arising from ethanol decomposition over the Pd phase. The ethanol/cyclohexane solution can be considered as a model of what the chemistry

that occurs in the presence of pure ethanol, that is the situation more common in industrial applications.

The ATR-IR spectra collected during exposure of the PdAl(F)-red catalyst to the ethanol/cyclohexane solution are reported in Figure 5a. Ideally, the experiment is equivalent to that reported in Figure 2a, except that the H_2 -reduction step is conducted at 70 °C (instead of 120 °C) and the solvent is present. The decomposition products observed during the experiment are essentially the same as in the gas-phase experiments, namely acetates and Pd-carbonyls. However, in the presence of the solvent, a single carbonyl band is observed at 1845 cm^{-1} , which is weak and red-shifted with respect to those observed in the gas-phase experiment. The band is assigned to 3-fold carbonyls adsorbed at hollow sites on Pd(111) facets. Both position and intensity indicate that the CO coverage is much lower when ethanol reaches the catalyst in the presence of the cyclohexane solvent than in the gas-phase. The intensity ratio between acetate and Pd-carbonyl signals is in favor of the former species, while Pd-carbonyls dominate in the gas-phase experiments. While this can be certainly attributed also to the low concentration of ethanol in the ATR-IR experiment compared to the ethanol partial pressure in the gas-phase, we consider as well that the cyclohexane solvent competes for the occupancy of the adsorption sites on the Pd nanoparticles responsible for ethanol decomposition, preventing at least partially the decarbonylation. This effect could even be enhanced by the presence of reduced metal because of a potentially stronger Pd-cyclohexane interaction compared to PdO.

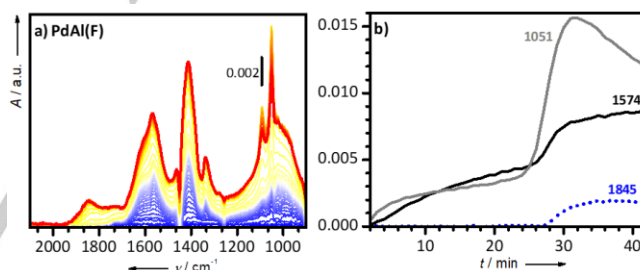


Figure 5. Part a): ATR-IR spectra collected during the exposure of H_2 -reduced PdAl(F) catalyst to a 10 mM ethanol solution in cyclohexane at room temperature. All the spectra were recorded after collecting a background prior to the dosage of the ethanol containing solution. Part b): Temporal dependence of the absorption bands at 1845 cm^{-1} ascribed to adsorbed CO, at 1574 cm^{-1} ascribed to adsorbed acetates, and at 1051 cm^{-1} due to physisorbed ethanol.

Figure 5b shows the evolution of the intensity of the bands at 1574 cm^{-1} ($\nu_{\text{as}}(\text{COO})$ of acetates), 1845 cm^{-1} (3-fold carbonyls at Pd(111), dotted line) and 1051 cm^{-1} ($\nu(\text{C-O})$ of physisorbed ethanol) along the course of the experiment. Comparison with Figure 3 reveals that the kinetics are much slower than in the gas-phase, which can be attributed again to the very low ethanol concentration in the liquid medium (10 mM), at least partly. The three signals experience an intensity jump at about 25 min after introduction of ethanol, but it is clear that ethanol was converted to acetate species before this event. We attribute this behavior to the poor solubility of ethanol in cyclohexane at ambient temperature and hence to its low diffusion within the liquid medium.^[52] The sudden increase in intensity is likely due to the

arrival at the catalyst surface of a “drop” of solvent particularly rich in ethanol, as the following intensity decrease of the signal at 1051 cm^{-1} suggests. This accelerates both ethanol decomposition and oxidation pathways. As observed in the gas-phase, formation of acetates (i.e. the oxidation route) is kinetically favored over decarbonylation. However, the presence of the solvent has the effect of lowering the surface poisoning effects induced by adsorbed CO species, with a pronounced preference towards ethanol oxidation.

Conclusion

In this work we provided a comprehensive characterization of the potentially poisoning phenomena occurring at the surface of two industrial Pd/Al₂O₃ catalysts exhibiting different size and surface regularity of the Pd nanoparticles using *operando* FT-IR and ATR-IR spectroscopy. The two catalysts were activated following two different protocols in order to tune the oxidation state of Pd. We confirmed that ethanol decomposes following two parallel paths: it is rapidly oxidized to acetates and it is slowly dehydrogenated to acetaldehyde (detected as a labile intermediate together with ethyl acetate), which further decarbonylates to give Pd carbonyls.

In gas-phase, oxidation is very fast when the Pd phase is reduced, but it stops as soon as the oxidant species (i.e. the -OH groups at the Al₂O₃ surface) are consumed. When Pd is partially or completely oxidized, the reaction is slower, because ethanol must first reduce PdO to Pd⁰. Ethanol dehydrogenation and subsequent acetaldehyde decarbonylation proceed with slower kinetics than ethanol oxidation. These reactions continue accumulating surface species, thus bearing the potential to poison Pd/Al₂O₃ for prolonged exposure, with the consequent worsening of the catalytic performances. At long reaction times, the extent of decarbonylation does not depend on the oxidation state of Pd, but it is strongly affected by the size and the surface regularity of the Pd particles: in the same experimental conditions, smaller and irregular Pd particles decompose ethanol to a larger extent compared to larger and more regular ones. The oxidation state of Pd, instead, plays a role in the kinetics of ethanol dehydrogenation, the more oxidized the Pd phase, the slower the reaction. Ethanol oxidation to acetates remains the kinetically favored reaction path also in liquid-phase. In contrast, the decarbonylation process is dampened to very low levels, because the solvent competes with ethanol in occupying the available surface sites.

Although most of the spectroscopic data presented in this work have been collected in conditions far from those adopted industrially, they provide important information to rationalize how different variables affect ethanol decomposition on industrial Pd/Al₂O₃ catalysts used in liquid-phase catalyzed reactions, helping in establishing working protocols and in designing preparation procedures that minimize the unwanted poisoning effects. According to our results, when working with ethanol as a solvent, it is preferable to employ catalysts having a lower Pd dispersion and with the Pd phase in the oxidized state. Ethanol decomposition cannot be avoided, but it will be delayed and it will be less efficient than that occurring on catalysts with a higher Pd dispersion and with the Pd phase in the reduced state.

Experimental Section

Catalysts synthesis

Two industrial 5 wt% Pd/Al₂O₃ catalysts (provided by Chimet S.p.A.) were prepared from a commercial high-surface-area transition alumina as the support (specific surface area, $116\text{ m}^2\text{-g}^{-1}$; pore volume, $0.41\text{ cm}^3\text{-g}^{-1}$) following a deposition-precipitation using Na₂PdCl₄ as the metal precursor and Na₂CO₃ as the basic agent as described elsewhere.^[43-44, 53-54] Both catalysts were carefully washed with water until complete removal of chlorine residues and kept in the wet state (ca. 50 wt% water) until the measurements. In one case, after Pd deposition and before Cl⁻ removal, the catalyst was pre-reduced in liquid-phase using sodium formate at 65 °C for 1 h.

Methods

Gas-phase *operando* FT-IR spectroscopy

For the *operando* FT-IR measurements, ca. 10 mg of each catalyst were pressed into self-supported pellets and placed inside a commercial FT-IR reactor cell (AABSPEC, no. 2000-A multimode), which allows recording spectra under controlled temperature and gas atmosphere. The FT-IR spectra were recorded in transmission mode at a resolution of 2 cm^{-1} on a PerkinElmer System 2000 spectrophotometer equipped with a MCT detector.

The samples were activated directly inside the cell. Two activation protocols (for the reduction and the oxidation of the catalyst, respectively) were adopted consisting in three equivalent subsequent steps except for the gas used in step 2. 1) The catalysts were heated to 120 °C (heating rate 2.5 °C/min) under a N₂ flow (50 mL/min) and left at this temperature for 30 min in order to eliminate most of the physisorbed water; then, 2) they were treated in a pure H₂ (or air) flow (50 mL/min) for 30 min; finally, 3) they were quickly cooled to room temperature in flowing N₂ (50 mL/min). The catalyst labels are therefore followed by -red if they have been treated in H₂ or by -ox if they have been treated in air. Hence, four cases are discussed: PdAl(F)-red, PdAl-red, PdAl(F)-ox and PdAl-ox. In the first two cases, the Pd nanoparticles are expected to be completely reduced to Pd⁰.

After activation, a spectrum of the catalyst was collected before ethanol was dosed at room temperature by flowing N₂ (50 mL/min) through an ethanol-filled saturator, and spectra were recorded every minute for the first 10 min, then every 2 min up to 20 min, and finally every 5 min for a total of 100 min of exposure.

Liquid-phase *operando* ATR-IR spectroscopy

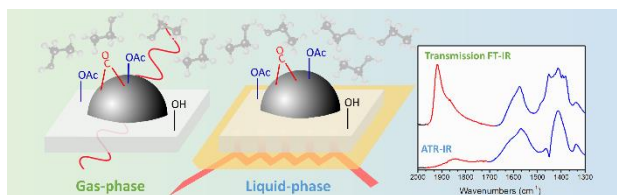
For the *operando* ATR-IR experiments, a slurry of the PdAl(F) powder catalyst (ca. 10 mg) in milli-Q water (1 mL) was dropped on a ZnSe internal reflection element (IRE; 52x20x2 mm) and was dried overnight in a fume hood. The dried catalyst layer was then inserted into a home-made ATR-IR cell working in continuous flow and whose temperature is regulated using a recirculating water bath. Cyclohexane was selected as the solvent, because it does not exhibit absorptions in the spectral region of interest and allows us working at relatively high temperature (70 °C). All the measurements were performed employing a Bruker Vertex70 spectrophotometer equipped with

a MCT detector and a commercial mirror unit. The ATR-IR spectra were collected at 4 cm⁻¹ resolution in the 4000-500 cm⁻¹ range.

H₂-saturated cyclohexane was continuously pumped over the catalyst layer during the activation procedure at 70 °C using a peristaltic pump (Ismatec). In order to compensate for the spectral features of the IRE, of the sample and of cyclohexane, a background was collected immediately prior to the dosage of the ethanol solution. Then, an Ar-saturated ethanol solution (10 mM) in cyclohexane was introduced in the cell at room temperature, and spectra were collected every minute until no spectral changes occurred.

Keywords: Pd/Al₂O₃ catalysts • Alcohol • Poisoning • Gas-phase FT-IR spectroscopy • Liquid-phase ATR-IR spectroscopy

- [1] R. L. Augustine in *Heterogeneous Catalysis for the Synthetic Chemist*, Dekker, New York, **1995**, pp. 640.
- [2] G. M. Loudon in *Organic Chemistry, 2nd Ed*, Benjamin/Cummings Pub. Co., Menlo Park, **1988**, pp. 1259.
- [3] S. Nishimura in *Handbook of Heterogeneous Catalytic Hydrogenation for Organic Synthesis*, Wiley, Chichester, **2001**, pp. 784.
- [4] P. N. Rylander in *Best Synthetic Methods: Hydrogenation Methods*, Academic Press, London, **1985**, pp. 193
- [5] U. K. Singh, S. W. Krska, Y. Sun, *Org. Process Res. Dev.* **2006**, *10*, 1153-1156.
- [6] J. L. Davis, M. A. Barteau, *Surf. Sci.* **1987**, *187*, 387-406.
- [7] J. L. Davis, M. A. Barteau, *Surf. Sci.* **1990**, *235*, 235-248.
- [8] S. M. Gates, J. N. Russell, J. T. Yates, *Surf. Sci.* **1986**, *171*, 111-134.
- [9] B. A. Sexton, K. D. Rendulic, A. E. Hugues, *Surf. Sci.* **1982**, *121*, 181-198.
- [10] R. Shekhar, M. A. Barteau, *Catal. Lett.* **1995**, *31*, 221-237.
- [11] J. L. Davis, M. A. Barteau, *J. Am. Chem. Soc.* **1989**, *111*, 1782-1792.
- [12] R. Shekhar, M. A. Barteau, R. V. Plank, J. M. Vohs, *J. Phys. Chem. B* **1997**, *101*, 7939-7951.
- [13] J. Raskó, J. Bontovics, F. Solymosi, *J. Catal.* **1994**, *146*, 22-33.
- [14] G. C. Cabilla, A. L. Bonivardi, M. A. Baltanás, *J. Catal.* **2001**, *201*, 213-220.
- [15] S. Bertarione, D. Scarano, A. Zecchina, V. Johaneck, J. Hoffmann, S. Schaueremann, J. Libuda, G. Rupprechter, H.-J. Freund, *J. Catal.* **2004**, *223*, 64-73.
- [16] S. Bertarione, D. Scarano, A. Zecchina, V. Johaneck, J. Hoffmann, S. Schaueremann, M. M. Frank, J. Libuda, G. Rupprechter, H.-J. Freund, *J. Phys. Chem. B* **2004**, *108*, 3603-3613.
- [17] S. M. De Lima, A. M. Silva, U. M. Graham, G. Jacobs, B. H. Davis, L. V. Mattos, F. B. Noronha, *Appl. Catal., A* **2009**, *352*, 95-113.
- [18] A. Yee, S. J. Morrison, H. Idriss, *J. Catal.* **1999**, *186*, 279-295.
- [19] J. Wang, G. Aguilar-Rios, R. Wang, *Appl. Surf. Sci.* **1999**, *147*, 44-51
- [20] C. Keresszegi, T. Bürgi, T. Mallat, A. Baiker, *J. Catal.* **2002**, *211*, 244-251
- [21] J. B. Brazier, B. N. Nguyen, L. A. Adrio, E. M. Barreiro, W. P. Leong, M. A. Newton, S. J. A. Figueroa, K. Hellgardt, K. K. M. Hii, *Catal. Today* **2014**, *229*, 95-103.
- [22] M. A. Newton, J. B. Brazier, E. M. Barreiro, S. Parry, H. Emmerich, L. A. Adrio, C. J. Mulligan, K. Hellgardt, K. K. Hii, *Green Chem.* **2016**, *18*, 406-411.
- [23] C. Lamberti, E. Groppo, G. Spoto, S. Bordiga, A. Zecchina, *Adv. Catal.* **2007**, *51*, 1-74
- [24] G. Rupprechter, *Adv. Catal.* **2007**, *51*, 133-263
- [25] N.-Y. Topsøe, *Catal. Today* **2006**, *113*, 58-64.
- [26] D. Ferri, A. Baiker, *Top. Catal.* **2009**, *52*, 1323-1333.
- [27] C. H. Rochester, *Adv. Colloid Interface Sci.* **1980**, *12*, 43-82.
- [28] T. Bürgi, R. Wirz, A. Baiker, *J. Phys. Chem. B* **2003**, *107*, 6774-6781.
- [29] G. M. Hamminga, G. Mul, J. A. Moulijn, *Chem. Eng. Sci.* **2004**, *59*, 5479-5485.
- [30] A. Pintar, R. Malacea, C. Pinel, G. Fogassy, M. Besson, *Appl. Catal., A* **2004**, *264*, 1-12.
- [31] J. E. Rekoske, M. A. Barteau, *Ind. Eng. Chem. Res.* **1995**, *34*, 2931-2939.
- [32] Z. Wang, M. L. Larsson, M. Grahn, A. Holmgren, J. Hedlund, *Chem. Commun.* **2004**, 2888-2889.
- [33] J.-D. Grunwaldt, M. Caravati, A. Baiker, *J. Phys. Chem. B* **2006**, *110*, 25586-25589
- [34] A. F. Lee, K. Wilson, *Green Chem.* **2004**, *6*, 37-42
- [35] D. Ferri, C. Mondelli, F. Krumeich, A. Baiker, *J. Phys. Chem. B* **2006**, *110*, 22982-22986.
- [36] C. Keresszegi, D. Ferri, T. Mallat, A. Baiker, *J. Catal.* **2005**, *234*, 64-75.
- [37] C. Keresszegi, D. Ferri, T. Mallat, A. Baiker, *J. Phys. Chem. B* **2005**, *109*, 958-967.
- [38] A. Villa, D. Ferri, S. Campisi, C. E. Chan-Thaw, Y. Lu, O. Kröcher, L. Prati, *ChemCatChem* **2015**, *7*, 2534-2541.
- [39] P. A. Christensen, S. W. M. Jones, A. Hamnett, *Phys. Chem. Chem. Phys.* **2013**, *15*, 17268-17276.
- [40] E. A. Monyoncho, S. N. Steinmann, C. Michel, E. A. Baranova, T. K. Woo, P. Sautet, *ACS Catal.* **2016**, *6*, 4894-4906.
- [41] Y.-Y. Yang, J. Ren, Q.-X. Li, Z.-Y. Zhou, S.-G. Sun, W.-B. Cai, *ACS Catal.* **2014**, *4*, 798-803.
- [42] Z.-Y. Zhou, Q. Wang, J.-L. Lin, N. Tian, S.-G. Sun, *Electrochim. Acta* **2010**, *55*, 7995-7999.
- [43] E. Groppo, G. Agostini, A. Piovano, N. B. Muddada, G. Leofanti, R. Pellegrini, G. Portale, A. Longo, C. Lamberti, *J. Catal.* **2012**, *287*, 44-54.
- [44] G. Agostini, E. Groppo, A. Piovano, R. Pellegrini, G. Leofanti, C. Lamberti, *Langmuir* **2010**, *26*, 11204-11211.
- [45] A. M. Bradshaw, F. M. Hoffmann, *Surf. Sci.* **1978**, *72*, 513-535.
- [46] A. Ortega, F. M. Huffman, A. M. Bradshaw, *Surf. Sci.* **1982**, *119*, 79-94.
- [47] E. Groppo, S. Bertarione, F. Rotunno, G. Agostini, D. Scarano, R. Pellegrini, G. Leofanti, A. Zecchina, C. Lamberti, *J. Phys. Chem. C* **2007**, *111*, 7021-7028.
- [48] I. V. Yudanov, R. Sahnoun, K. M. Neyman, N. Rösch, J. Hoffmann, S. Schaueremann, V. Johánek, H. Unterhalt, G. Rupprechter, J. Libuda, H.-J. Freund, *J. Phys. Chem. B* **2003**, *107*, 255-264.
- [49] N. W. Alcock, V. M. Tracy, T. C. Waddington, *J. Chem. Soc., Dalton Trans.* **1976**, 2243-2246.
- [50] D. Rivera, P. E. Poston, R. H. Uibel, J. M. Harris, *Anal. Chem.* **2000**, *72*, 1543-1554.
- [51] H. Idriss, E. G. Seebauer, *J. Mol. Catal. A: Chem.* **2000**, *152*, 201-212.
- [52] T. Moriyoshi, Y. Uosaki, K. Takahashi, T. Yamakawa, *J. Chem. Thermodyn.* **1991**, *23*, 37-42
- [53] G. Agostini, R. Pellegrini, G. Leofanti, L. Bertinetti, S. Bertarione, E. Groppo, A. Zecchina, C. Lamberti, *J. Phys. Chem. C* **2009**, *113*, 10485-10492.
- [54] R. Pellegrini, G. Leofanti, G. Agostini, L. Bertinetti, S. Bertarione, E. Groppo, A. Zecchina, C. Lamberti, *J. Catal.* **2009**, *267*, 40-49.

Entry for the Table of Contents

The interaction of gaseous as well as liquid ethanol over Pd/Al₂O₃ catalysts was studied by FT-IR and ATR-IR spectroscopies, respectively. We identified acetates and carbonyls as decomposition products and potential surface poisoning. Particular care is devoted to the rationalization of the catalysts properties affecting such phenomenon. This would allow for the design of systems able to minimize the unwanted poisoning.